# Etude numérique et expérimentale d'un cycle combiné de production de froid et d'électricité basé sur la technologie à absorption NH3/H2O

Simone Braccio

# THÈSE

Pour obtenir le grade de

## DOCTEUR DE L'UNIVERSITÉ SAVOIE MONT BLANC

Spécialité : **Énergétique et Génie des Procédés**

Arrêté ministériel : 25 Mai 2016

Présentée par


# Simone BRACCIO


Thèse codirigée par **Nolwenn Le Pierrès, Nicolas Tauveron et Hai Trieu Phan**

préparée au sein du
**Laboratoire L2TS/SSETI/DTCH/CEA Liten**
Et du **Laboratoire LOCIE UMR CNRS 5271**

dans **l'École Doctorale SIE**

# Numerical and experimental study of a $NH_3/H_2O$ absorption based combined power and cooling production cycle

Etude numérique et expérimentale d'un cycle combiné de production de froid et d'électricité basé sur la technologie à absorption $NH_3/H_2O$

Thèse soutenue publiquement le **Mercredi 01 Février 2023**,
Devant le jury composé de :

**M. Remi REVELLIN**
Professeur, INSA de Lyon, Rapporteur et président du jury

**M. Maurizio DE LUCIA**
Professeur, Università di Firenze, Rapporteur

**Mme. Nathalie MAZET**
Directrice de recherches CNRS, PROMES, Examinatrice

**Mme. Alessia ARTECONI**
Maître de conférences, KU LEUVEN, Examinatrice

**Mme. Nolwenn LE PIERRÈS**
Professeure, Université Savoie Mont Blanc, Directrice de thèse

**M. Nicolas TAUVERON**
Directeur de recherches CEA, CEA-Liten, Co-Directeur de thèse

**M. Hai Trieu PHAN**
Docteur-ingénieur, CEA-Liten, Co-Directeur de thèse

et avec l'expertise de :

**Mme. Luisa CABEZA FABRA**
Professeure, Universitat de Lleida, Rapporteure pour le Label Européen


NUMERICS

This project has received funding from the European Union's Horizon 2020 research and innovation programme under grant agreement No 800945 — NUMERICS — H2020-MSCA-COFUND-2017

# Acknowledgments

Je souhaite avant toute chose remercier mes directeurs de thèse. Je commencerais par Nicolas, que j'ai contacté au (désormais lointain) printemps 2019 à la recherche d'un stage, et qui m'a suggéré de postuler pour une thèse qui s'est révélée être une merveilleuse aventure. Merci donc Nicolas pour ta disponibilité constante, ton expertise reconnue, tes conseils et encouragements et pour les connaissances que tu m'as transmises. Toutes les discussions que nous avons eues ont été pour moi une source inépuisable d'idées et d'inspiration. Merci aussi Nolwenn, pour ta bonne humeur et ta pédagogie, pour ton immense investissement dans la réussite de cette thèse, merci pour chaque ligne que tu as relue de manière si attentive. Merci aussi pour ton exigence, tes idées toujours originales et pour la rigueur scientifique que tu as su me transmettre au cours de ces trois années. Et finalement, merci Mimo pour ton soutien au quotidien et ta disponibilité sans faille. Je sais qu'il n'a pas toujours été facile de m'encadrer, mais ta patience a été remarquable. Tu as été pour moi un véritable mentor : tu as toujours essayé de me faire grandir en tant que personne, tu as toujours été à l'écoute de mes aspirations professionnelles, pour lesquelles tu m'as soutenu, et tu as essayé de me transmettre ta grande expérience. Merci donc à mes (3 !) directeur de thèse, ce fut un réel plaisir de mener ce travail doctoral sous votre tutelle d'apprendre à vos côtés !

Thank you also to Alessia Arteconi, for having accepted to host me during my secondment at KU Leuven for what proved to be an extremely enriching experience, both personally and for the outcome of this thesis. Thank you for your support, your patience and for initiating me to the field of exergetic analysis.

Je veux remercier aussi les rapporteurs Luisa Cabeza, Remi Revellin, Maurizio De Lucia et les membres du jury Alessia Arteconi et Nathalie Mazet, d'avoir accepté d'évaluer ma thèse, d'avoir pris le temps de relire le manuscrit et pour vos commentaires et conseils.

Merci à Bertrand Chandez, un point de référence tout au long de ma thèse, toujours disponible et prêt à fournir son soutien pour surmonter les obstacles que l'on rencontre inévitablement au cours du parcours doctoral. Et même si la qualité de ton formidable travail technique a été indispensable pour la réussite de ma thèse, je souhaite te remercier surtout pour les bons moments partagés au travail et en dehors. Tu as été un vrai ami pour moi.
Je remercie aussi Fabien Bruyat pour sa bonne humeur et pour la qualité de son travail et pour tout le temps qu'il a passé à m'aider dans la réalisation de la partie la partie expérimentale de mes travaux de recherche.
Je tiens à remercier chaleureusement aussi Florent Lefrançois, Romain Joubert, Hélène Desmales et toute l'équipe abso et technique pour votre motivation et pour les moments joyeux passées ensemble.

Merci à Nathan Guillou, les mois passés à co-encadrer ton stage ont été parmi les plus riches, animés et productifs de ma thèse. Ta joie et ta passion pour la recherche scientifique ont été pour moi une source d'inspiration et de grande motivation. Et même si je n'ai pas su apprendre à prononcer correctement le mot "éjecteur", je reste très fier du travail que nous avons accompli, et surtout que tu as accompli. Je suis sûr que l'avenir te réserve d'incroyables opportunités.

Un grand merci à mes collègues de bureau avec qui j'ai partagé une grande partie de ces trois années. Merci à Mathilde Wirtz, qui m'a guidée au début de mon parcours et qui m'a beaucoup aidée et soutenu tout au long de ma thèse. Je t'admire depuis le jour de mon arrivée pour ta force, indépendance et détermination. La qualité de ton travail m'a incité à m'améliorer chaque jour, et ta proactivité dans la recherche de nouveaux défis et de nouvelles opportunités m'a inspiré à faire de même. Le résultat final de mon travail n'aurait pas pu être le même si le tien n'en avait pas été la base. Merci à Angela Disdier pour nos journées au labo, pour toutes les discussions que nous avons eues et d'avoir toujours un bon conseil à donner à tout le monde. J'espère te revoir en Italie bientôt ! Enfin, merci à Jana Sleiman d'avoir rendu plus agréables mes derniers mois au CEA et pour avoir toujours été prête à faire de blagues avec moi. Le fait que tu as pu me supporter et la qualité de ton travail que j'ai constaté dans les mois passés ensemble, ne me laissent aucun doute sur la réussite de ta thèse.

Merci à Valery Vuillerme, Nicolas Lamaison, Nicolas Vasset, Thibaut Wissocq, Joseph Brisson, Yann Berton, Estelle Le Baron, Françoise Burgun, Quentin Blondel, Guillaume Lhermet, Houssame Boujjat, à tout le labo L2TS du CEA à l'INES et à Grenoble, et à tous les collègues de PUMA 3 d'avoir partagé de bons moments de convivialité
Merci à Nathalie Dupassieux, cheffe de labo attentive aux doctorants, pour ton suivi et ton soutien. Merci aussi à Raphaël Couturier, chef de service toujours disponible, et à Jean-François Fourmigué, coordinateur scientifique, pour ton réel intérêt pour les doctorants et doctorantes.

Merci au labo LOCIE pour votre accueil, pour les journées du doctorant, les séminaires annuel et pout les autres rassemblements, toujours agréables. Merci à Taini, Hasan, Cedric, Hafsa, Ben, Maria, Karine et tous les doctorants, avec qui j'ai partagé un bout de chemin.
Je veux remercier tout particulièrement mes amis avec lesquels j'ai partagé des moments mémorables. Muchas gracias Jaume, por el tiempo que hemos pasado juntos, por nuestras cenas y paseos en los que hemos hablado de todo y nos hemos enriquecido mutuamente. Espero que sigamos en contacto y nos veamos pronto amigo. Merci à Simon de m'avoir fait découvrir une autre façon de regarder la vie, que j'emporterai toujours avec moi. Les discussions que nous avons eues ensemble, nos rires et ta disponibilité sincère et constante font que je me sens chanceux de pouvoir me considérer ton ami.
Infine, grazie mille a Fabio, il cui buon umore e disponibilità mi hanno dato forza durante questo percorso. Grazie per la tua amicizia sincera, e a presto spero!

Grazie mille a Gianluca Rossiello, che è stato per me un supervisore aggiunto. Grazie per la tua costante disponibilità e per le innumerevoli ore passate insieme a discutere, riflettere e cercare soluzioni. Grazie per avermi trasmesso il tuo rigore e metodo, la tua esperienza. Il risultato finale di questa tesi di dottorato è tanto merito mio quanto tuo.

Questo percorso sarebbe stato impossibile da portare a termine senza il sostegno immancabile della mia famiglia. Nonostante tutti abbiano fatto sentire le loro presenza e vicinanza un pensiero speciale va alla mia cara nonna Lisetta, che ha condiviso con me ogni singolo giorno di questo dottorato, e alla mia cara nonna Maria, che purtroppo non ha potuto esserci, ma che spero ci guardi da lassù e sia fiera di noi.
Grazie mille ai miei fratelli. Grazie a Jacopo che, nonostante tutti gli impegni, tante volte mi ha aiutato in questi tre anni senza mai farmelo pesare. Una forza calma, che diventa un punto di riferimento per chi gli sta attorno. Grazie a Tommaso, per la sua leggerezza e spensieratezza che tanto mi hanno aiutato a superare i momenti più difficili di questi anni. E infine grazie ai miei genitori, che mi hanno incoraggiato e sostenuto durante i miei studi. Grazie mamma, la gratitudine e riconoscenza che ho verso di te sono infiniti perché sei e sarai il miglior sostegno che si possa mai sognare. Ed infine un ringraziamento speciale al mio papà, a cui devo tutto. Mi dispiace se troppo spesso ho proiettato le mie ansie e paure su di te, che ti sei preso in carico di condividere questo percorso con me. Poco o nulla di quello ho raggiunto e di dove sono oggi sarebbe stato possibile senza di te, e per questo sono e te ne sarò per sempre grato.
Lastly, a special thanks goes to Svenja, who like nobody else knows what these three years have been like and what obstacles I have faced (and too often put in my way). I am grateful that you chose to stay by my side and share this load with me. Your support was invaluable and indispensable and your presence the highlight of this journey.

# Partners

### Commissariat à l'Énergie Atomique et aux Énergies Alternatives

Project financed by the CEA and carried out at "Laboratoire des Technologies Thermodynamiques et Solaires" (L2TS) of the CEA-LITEN in Bourget-du-Lac. Under the supervision of Hai Trieu PHAN and Nicolas TAUVERON.

### CEA Numerics program


This project has received funding from the European Union's Horizon 2020 research and innovation programme under grant agreement N° 800945 - NUMERICS - H2020-MSCA-COFUND-2017.

### LOCIE laboratory of Université Savoie Mont Blanc


Thesis carried out with the support of LOCIE, research laboratory of the Université Savoie Mont Blanc. Under the supervision of Nolwenn LE PIERRÈS.

# Table of contents

# Abstract

In view of increasing global energy demand and concern for the environment, one particular issue is the increasing demand for cooling, which is expected to triple from 2016 until 2050 due to climate change and increasing population. In this context, absorption systems, which have been a relatively niche technology so far, are well suited to the recovery of low temperature energy for the production of cooling. Research has focused on improving the performance of heat driven cooling systems by merging them with power cycles. Hence, system performance is increased by producing power and cooling simultaneously. Additionally, a combined absorption system producing refrigeration and electricity could be better adapted to the whole range of energy demand, from only power to only refrigeration modes with intermediate operation modes producing different ratios of the two useful products.

The work carried out in the present PhD thesis regards the experimental and numerical investigation of an absorption-based combined cooling and power production cycle using low temperature heat (80-150 °C). The architecture is that of a single stage ammonia-water absorption chiller to which a power production line, including a turbine for the production of electricity, is integrated in parallel to the cooling production line.

The present document presents first an overview of available heat driven thermodynamic cycles for the production of cooling and power. Absorption machines and organic Rankine cycles are identified as mature and efficient technologies and their combination is envisaged to achieve higher efficiencies and to increase the operating flexibility. Then, the development of a prototype is undertaken by integrating an impulse axial turbine into an existing absorption chiller rig. The special characteristics of the expander as well as the simplified architecture of the absorption cycle make the prototype unique. Despite challenges encountered in the development of the system, first experimental results have been obtained giving important insights on the functioning of the cycle.

Experimental data from the prototype was also used for the development of accurate numerical models. First, a detailed model of the absorption chiller is developed based on the use of heat and mass exchangers' effectiveness, modelled using dimensionless operating parameters, and adjusted on experimental measures. Subsequently, a 1D real-gas turbine model is developed including a description of the supersonic expansion in the injector and a simplified rotor loss model, whose coefficients were adjusted based on CFD simulations. Experimental tests on the turbine with fluids other than ammonia have proved to model to be robust and applicable to different working fluids. The turbine 1D model is then integrated into the cycle model for parametric analysis of the operating conditions. Since the cycle produces two different useful products, particular attention is paid to its study from an exergetic point of view. Exergoeconomics was used to calculate separately the cost of each product generated by the system, understanding the cost formation process and optimising the overall system. Finally, different possibilities for improving the system are addressed. In particular, its scale-up with the size effect and various architectures that could increase its flexibility such as the use of an ejector for a better regulation of the mass flow.

**Keywords**: combined absorption cooling-power cycle; ammonia-water mixture; low grade heat; axial impulse micro turbine; exergy; exergoeconomics; ejector

# Résumé

Les systèmes à absorption, jusqu'à présent une technologie de niche, se prêtent bien à la valorisation d'énergie à basse température pour la production de froid. Les scientifiques se sont intéressés à l'amélioration des performances des systèmes de refroidissement tri-thermes (utilisant de la chaleur pour fonctionner) en combinant les cycles à absorption et les cycles de puissance. Ainsi, les performances du système sont améliorées par la production simultanée d'électricité et de refroidissement. En outre, un système à absorption combiné produisant de la réfrigération et de l'électricité pourrait être mieux adapté pour répondre à différents types de besoins, en fonctionnant en mode de production d'électricité seul ou réfrigération seul, ou dans des modes de fonctionnement intermédiaires produisant des ratios différents des deux productions.

Le travail mené dans cette thèse concerne l'étude expérimentale et numérique d'un cycle de production combiné de froid et d'électricité basé sur la technologie des machines à absorption utilisant de la chaleur à basse température (80-150°C).
L'architecture est celle d'une machine à absorption ammoniac-eau simple étage, auquel est intégrée une ligne de production d'électricité, comprenant une turbine pour la production de travail mécanique, en parallèle à la ligne de production de froid.

Le présent document présente premièrement une synthèse des principaux cycles thermodynamiques existants pour la production de froid et d'électricité. Les machines à absorption et les cycles organiques de Rankine sont identifiés comme des technologies matures et efficaces et leur combinaison est envisagée pour atteindre des rendements plus élevés et augmenter la flexibilité opérationnelle. Sur la base de cette constatation, le développement d'un prototype est entrepris en intégrant une turbine axiale à action dans une machine à absorption existante. Les caractéristiques très particulières de la turbine ainsi que l'architecture simplifiée du cycle à absorption rendent le prototype unique. Malgré les difficultés rencontrées dans le développement du système, les premiers résultats expérimentaux ont été obtenus, donnant des informations importantes sur le fonctionnement du cycle.

Les données expérimentales du prototype ont également été utilisées pour le développement de modèles numériques fiables. D'abord, un modèle détaillé de la machine à absorption est développé, en utilisant des efficacités des échangeurs de chaleur, modélisé en utilisant des paramètres de fonctionnement adimensionnels, et ajusté sur les résultats expérimentaux. Ensuite, un modèle 1D gaz réel de turbine est développé. Ce modelé inclut une description de l'expansion supersonique dans l'injecteur et un modèle simplifié des pertes dans le rotor dont les coefficients ont été ajustés sur la base de simulations CFD réalisées sur la turbine. Des tests expérimentaux sur la turbine avec des fluides autres que l'ammoniac ont prouvé que le modèle est robuste et applicable à différents fluides de travail. Le modèle de la turbine est intégré dans le modèle du cycle à absorption et utilisé pour effectuer une analyse paramétrique sur les conditions de fonctionnement. En particulier, puisqu'il y a deux produit utiles différents, une attention particulière est accordée à l'étude du cycle d'un point de vue exergétique. La méthode de l'analyse exergo-économique a donc été utilisée pour calculer séparément le coût de chaque produit généré, comprendre le processus de formation des coûts et optimiser le système dans sa globalité. Finalement, les possibilités d'amélioration du système sont traitées. En particulier, sa mise à l'échelle et variations d'architecture qui pourraient augmenter sa flexibilité sont examinées. Parmi celles-ci, la possibilité d'intégrer un éjecteur dans le système est considérée, en développant un modèle détaillé d'éjecteur et en le couplant au mode de cycle complet.

**Mots clés** : cycle combiné de production de froid et électricité ; mélange eau-ammoniac; chaleur à basse température ; micro turbine axiale à action ; exergie ; exergo-économie ; éjecteurs

# Résumé étendu en français

## Contexte

Compte tenu de la demande mondiale d'énergie toujours croissante et de l'attention portée aux questions environnementales et au changement climatique, des recherches se développent de plus en plus sur de nouvelles technologies de production de froid plus efficaces basées sur des sources renouvelables ou de récupération [1–3] Cette demande de refroidissement et rafraichissement est actuellement principalement couverte par les technologies conventionnelles, notamment les très énergivores machines à compression mécanique de vapeur, ce qui entraîne une forte augmentation de la demande d'électricité. Au total, environ 1.6 milliard de systèmes de refroidissement à compression de vapeur sont installés dans le monde, consommant plus de 2,000 térawattheures (TWh) d'électricité par an soit près de deux fois et demie la consommation d'électricité de l'Afrique et environ 4 fois l'énergie électrique utilisée en France en 2018 [4].
L'industrie du froid joue un rôle de plus en plus important dans l'économie mondiale, notamment dans les domaines de l'alimentation, du bâtiment ou de la santé. Elle est également au cœur des transitions écologique et digitale. Dans ce contexte, les systèmes à absorption [5] ont toute leur place. Jusqu'à présent limité à des applications de niche, leur marché est en croissance, notamment grâce à une réduction de leurs coûts. L'avantage de ces machines est que la compression mécanique est remplacée par une compression thermochimique qui utilise de la chaleur. Le seul apport d'électricité se situe au niveau d'une pompe, mais il est inférieur d'environ 10 à 30 fois par rapport à celui nécessaire pour le compresseur d'un cycle à compression mécanique. L'intérêt de ces machines est également dû à leur grande fiabilité, leur longue durée de vie et leur faible besoin de maintenance en raison de l'absence de pièces mobiles (à l'exception de la pompe à solution), ce qui signifie également une absence de vibrations et de bruit. De plus, les machines à absorption permettent la production de froid à partir de fluides non émetteurs de gaz à effet de serre, comme l'ammoniac ou l'eau. Les deux couples de fluides de travail les plus courants sont effectivement l'ammoniac/eau et l'eau/bromure de lithium, ce dernier dominant largement le marché des machines à absorption en raison de sa simplicité et de ses performances supérieures. En fait, l'ammoniac et l'eau étant deux fluides très volatils, la séparation des deux phases est compliquée et nécessite l'utilisation d'un composant supplémentaire (le rectifieur) réduisant l'efficacité du cycle. Cependant, des travaux récents ont conduit au développement de composants combinés de production et purification de vapeur d'ammoniac [6] qui simplifient l'architecture des machines à absorption ammoniac/eau et améliorent leurs performances. Ceci est très important car le couple ammoniac/eau permet (contrairement au couple l'eau/bromure de lithium) de produire du froid à des températures négatives. De plus, étant donné que la vapeur de réfrigérant produite est dans des conditions de pression et de température relativement élevées, elle peut être détendue dans un organe qui produit du travail mécanique. Cela ouvre la porte au développement de systèmes combinés très ambitieux, basés sur l'exploitation de l'énergie thermique à basse température, dans lesquels les énergies électriques et de refroidissement peuvent être produites dans le même cycle. Un tel système permettrait d'augmenter l'efficacité énergétique globale par rapport à une production séparée et de mutualiser certains composants.

Le présent travail se concentre sur le développement et l'étude expérimentale et numérique d'un système combiné de production de froid et d'électricité. Ce travail est fortement lié aux études menées dans le cadre du projet Carnot Energie du Future "TRICYCLE" et a été soutenu par le programme de recherche et d'innovation Horizon 2020 de l'Union européenne sous la convention de subvention Marie Skodowska-Curie n° 800945.

L'étude est basée sur une machine existante à absorption simple effet ammoniac-eau de petite taille, d'une puissance nominale au désorbeur de 10 kW et d'une puissance de refroidissement de 7 kW. Le prototype préindustriel a été développé au CEA INES à partir de 2012 dans le but de redessiner les composants pour optimiser leurs performances et tester des architectures de cycle innovantes. En outre, les tests expérimentaux réalisés sur l'installation pilote ont servi de bases de données, précieuses pour le développement et la validation des modèles numériques. Le prototype utilise de la chaleur à basse température (85-115 °C), simulant ainsi l'utilisation d'énergie solaire ou de chaleur.

Ce banc d'essai a été modifié par l'ajout en parallèle à la ligne de production de froid d'une ligne avec une micro-turbine axiale pour la production d'électricité. Cette architecture est caractérisée par le fait qu'une forte interaction existe entre les deux lignes de production, d'où la nécessité d'étudier le fonctionnement de la machine lorsque la part des deux produits varie.

Les objectifs globaux du travail comprennent :
- la compréhension approfondie du fonctionnement du cycle par des études expérimentales et numériques ;
- l'identification des avantages, des inconvénients, des limites d'exploitation et des défis techniques de la technologie ;
- l'évaluation de la performance et le positionnement de la technologie.

Les résultats de l'étude expérimentale ont permis de recueillir moins de données que prévu en raison des problèmes rencontrés lors du développement du prototype. Pour cette raison, des sources alternatives de données de validation ont été utilisées (analyse CFD pour la validation du modèle de turbine, données déjà disponibles de la machine à absorption, etc.) Cependant, les activités expérimentales se sont concentrées sur :
- le développement du prototype expérimental, y compris une collaboration pour le développement de l'expandeur, le choix de composants et d'architecture, etc ;
- la caractérisation de la turbine (influence des conditions d'entrée sur le débit massique traité et ses performances, influence de la vitesse de rotation, etc.) ;
- la caractérisation du cycle complet (étude des conditions stationnaires, transitoires, démarrage, changement de mode, etc.) ;
- l'analyse et le traitement des données ;
- l'identification des limites et des améliorations possibles de l'installation expérimentale.

Les activités numériques réalisées, d'autre part, ont inclus :
- le développement d'un modèle de turbine utilisé pour l'analyse de ses performances ;
- le développement d'un modèle du cycle combiné comprenant un modèle détaillé de la machine à absorption ;
- la réalisation d'une simulation en régime permanent du cycle pour caractériser le comportement dans différentes conditions de fonctionnement ;
- l'identification des limites du cycle et l'évaluation des améliorations possibles, notamment pour accroître la flexibilité de fonctionnement ;
- la réalisation d'une analyse technico-économique et exergoéconomique de la machine ;
- l'optimisation de la conception des composants et des paramètres opérationnels ;
- l'évaluation de la mise à l'échelle du système.

La combinaison d'études expérimentales et numériques a permis de renforcer la profondeur de l'analyse en tirant parti de leur complémentarité.

# Etat de l'art

Dans le contexte actuel, la récupération de chaleur à basse température est devenue une priorité. Un grand nombre d'études ont été menées dans ce domaine, couvrant une très large gamme d'applications.
En ce qui concerne la production d'électricité et de refroidissement, la recherche a conduit au développement de technologies efficaces prêtes à être produites et utilisées à grande échelle. Pour la production d'électricité à partir de chaleur à basse température, deux technologies semblent particulièrement intéressantes : les cycles de Kalina et les cycles organiques de Rankine. Les cycles organiques de Rankine ont connu un grand succès dans les dernières années et sont désormais une technologie mature. Les cycles de Kalina présentent un avantage théorique en termes d'efficacité par rapport aux ORC, mais n'ont pas gagné la faveur du marché en raison de leur plus grande complexité (due à l'utilisation du mélange ammoniac-eau et à la nécessité d'un plus grand nombre de composants). En outre, les défis de la conception d'un expandeur adapté à la corrosivité du mélange ammoniac-eau ont été mis en évidence.
Pour produire du froid, les technologies à sorption, et en particulier les machines à absorption, sont très en raison de leur flexibilité, de la possibilité d'utiliser différentes sources de chaleur, de leur faible consommation électrique et de leur fiabilité.

Plusieurs auteurs ont envisagé la combinaison des ORC et des cycles à sorption pour obtenir des rendements énergétiques plus élevés. Les cycles de coproduction (ou cycles hybrides) suscitent un vif intérêt car la mutualisation de composants peut conduire à des solutions moins coûteuses et à des performances plus élevées. Cependant, ces cycles sont encore des concepts émergents avec un faible niveau de maturité technologique.

Ce travail se concentre sur les cycles de production combinée de froid et d'électricité à absorption. Une grande variété d'architectures différentes a été proposée dans la littérature, privilégiant généralement la production d'électricité (comme dans le cycle Goswami [7]) plutôt que la production de froid. Les architectures peuvent être

partagées en fonction du mécanisme de production de froid : les architectures produisant du froid en utilisant la chaleur sensible (principalement le cycle Goswami) et les architectures utilisant la chaleur latente (comme les combinaisons parallèles d'un cycle d'absorption et d'un cycle moteur). Le mélange de travail le plus couramment utilisé dans ce type de cycles est le mélange ammoniac-eau.
La génération de deux produits utiles complique l'évaluation de la performance des systèmes combinés à absorption et nécessite l'utilisation d'une analyse exergétique.
Bien que plusieurs analyses aient été réalisées sur les cycles de génération combinés d'électricité et de refroidissement, la plupart d'entre elles se limitent généralement à des températures élevées de la source de chaleur [8–10] ou à des architectures complexes [10]. La plupart des études disponibles dans la littérature impliquent une modélisation simple de l'expandeur, en supposant généralement des rendements isentropiques fixes et la possibilité de réguler le ratio entre la production de froid et d'électricité. En outre, il existe très peu d'études expérimentales sur ces types de cycles, la plupart concernant le cycle de Goswami. Des études expérimentales sont également nécessaires afin de recueillir davantage de données pour une sélection appropriée de l'expandeur. Pour les applications à petite et moyenne échelle, le développement d'un organe de détente approprié est nécessaire, en particulier pour les expandeurs fonctionnant à l'ammoniac.
Ainsi, d'après la revue de la littérature ci-dessus, le besoin de plus d'études expérimentales et d'une modélisation plus détaillée de l'expandeur, en particulier pour mieux comprendre ses interactions avec le cycle qui l'intègre, est fort.

Dans ce contexte, ce travail fournit des données expérimentales jusqu'à présent manquantes sur le fonctionnement d'un cycle combiné de refroidissement et de production d'électricité à absorption avec une architecture parallèle. Les mesures expérimentales de l'installation pilote ont permis d'accéder à des données concernant le fonctionnement et les performances du cycle et de ses composants qui ont été utilisées pour le développement de modèles numériques détaillés de la machine à absorption et de la turbine.
Ces modèles ont ensuite été utilisés pour réaliser une étude approfondie du fonctionnement du cycle, en mettant en évidence ses avantages et ses limites, comme présenté dans les chapitres suivants.

# Description du cycle

Les machines de froid absorbent l'énergie nécessaire au changement de phase d'un fluide frigorigène à basse pression et donc à basse température et la rejettent dans le milieu extérieur via une condensation à pression plus élevée. Par conséquent, elles nécessitent deux niveaux de pression différents pour fonctionner et donc un organe de compression de vapeur, qui est le compresseur mécanique dans une machine classique à compression de vapeur. Les machines à absorption utilisent une compression dite "thermochimique" en fonctionnant avec un mélange de deux fluides (un absorbant et un réfrigérant), et se basent sur le fait que le fluide le plus volatil (le réfrigérant) peut être séparé du reste du mélange lors du processus de désorption. L'absorbant sert donc juste à transporter le fluide réfrigérant de la basse à la haute pression à l'état liquide. La séparation du réfrigérant a lieu grâce à un apport de chaleur au générateur où la vapeur du réfrigérant sort à haute température et haute pression et peut donc être utilisée pour produire du froid ou être détendue à travers un organe de détente pour produire de l'électricité.

Le cycle considéré dans cette étude est schématisé sur la **Fig. I.** Le fonctionnement est celui d'un cycle à absorption ammoniac-eau simple effet auquel est intégré un organe de détente de type turbine, en parallèle du circuit de production de froid. Côté circuit de solution, un débit de solution riche en ammoniac circule de l'absorbeur vers le générateur et est pressurisé par une pompe. Une seconde ligne comprenant une vanne de détente ramène la solution pauvre à l'absorbeur. Un économiseur permet de préchauffer la solution riche grâce à la solution pauvre sortant du générateur où un apport de puissance thermique $\dot{Q}_g$ à basse température (80-200°C) permet la désorption de la vapeur, principalement constituée d'ammoniac, de la solution. Le faible écart de volatilité entre l'absorbant (l'eau) et le réfrigérant (l'ammoniac) induit la présence de traces d'eau dans la vapeur en sortie du générateur, qu'il faut éliminer pour assurer le bon fonctionnement de la machine [11]. Cela se fait normalement avec un composant supplémentaire, le rectifieur, qui conduit cependant en général à une diminution du coefficient de performance (COP) de la machine. Afin de garantir une configuration compacte et efficace, le générateur utilisé dans la machine est un nouveau composant « combiné » (**Fig. III**) capable de générer la vapeur dans sa partie basse et de la purifier dans sa partie haute par réabsorption partielle de celle-ci dans la solution ammoniac-eau [6]. Pour la production d'électricité, un surchauffeur fournit une puissance $\dot{Q}_{sh}$ pour augmenter la température de l'ammoniac afin de garantir qu'il reste à l'état de vapeur tout au long de la détente, qui se produit à l'intérieur de la turbine. Pour la production de froid, l'ammoniac est condensé grâce à l'échange d'une puissance thermique $\dot{Q}_c$ avec une source à température intermédiaire (en général, l'air ambiant). Avant de refroidir la source froide à

l'évaporateur en absorbant une puissance $\dot{Q}_e$, l'ammoniac est détendu jusqu'à la basse pression. Un sous-refroidisseur permet de pré-refroidir l'ammoniac avant sa détente en échangeant avec l'ammoniac sortant de l'évaporateur. Les débits des deux lignes de production se mélangent et sont finalement absorbés dans la solution pauvre. L'absorption est exothermique et une puissance $\dot{Q}_a$ est cédée à la source à température intermédiaire, en général l'air ambiant, comme au condenseur.

Le cycle présenté est flexible car aussi bien la ligne turbine que la ligne de production de froid (condenseur et évaporateur) peuvent être fermées. Cela signifie que la machine peut fonctionner soit en mode combiné, soit comme une machine simple de production de froid ou de production d'électricité.

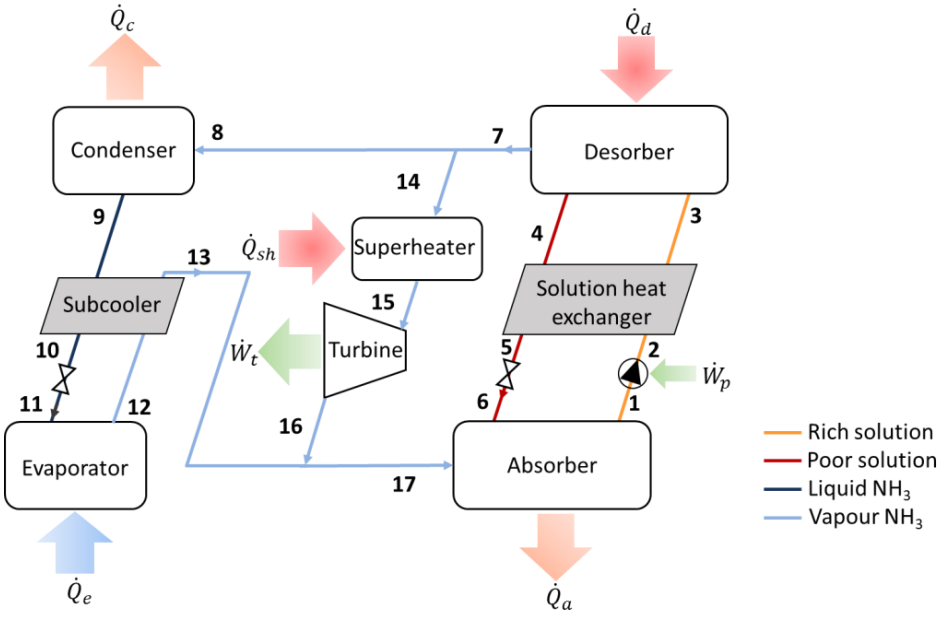


**Fig. I** – Schéma du cycle combiné.

L'organe de détente à intégrer dans l'installation pilote, qui est de petite taille, présente plusieurs défis techniques (débit massique très faible, impact de pertes par fuites, environnement corrosif, etc.) qui rendent délicats des composants tels que les détendeurs scroll ou les turbines radiales. Une turbomachine à action à admission partielle a été donc considérée. Le fait que dans ce type de turbine toute la détente a lieu dans l'injecteur limite l'influence des fuites et garantit une bonne production de travail [12]. La turbine considérée dans la présente étude est une micro turbine avec un seul injecteur comme distributeur (**Fig. II**). Compte tenu du très faible débit de vapeur disponible, le choix d'une machine à admission partielle permet d'éviter des dimensions trop petites ou des vitesses de rotation excessives.
Toutefois, en raison du comportement intrinsèque de la machine, une attention particulière doit être portée aux interdépendances entre la physique régissant la turbine et le cycle qui l'intègre.

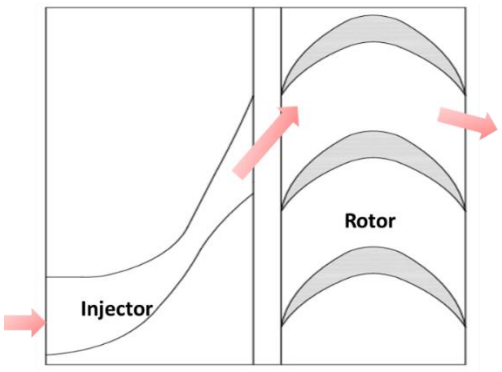


**Fig. II** – Schéma de la turbine.

# Résultats expérimentaux

Le prototype expérimental à simple effet est présenté sur la **Fig. III**. Il est principalement composé de : six échangeurs à plaques, une pompe de solution, une vanne de détente de solution, un détendeur, un surchauffeur, une turbine, un réservoir de stockage de solution, un réservoir de stockage de réfrigérant et deux réservoirs de séparation de phase liquide-vapeur. Il est instrumenté avec des capteurs de grandes précisions pour mesurer les températures, les pressions, les débits, les densités ainsi que les niveaux de liquide dans les réservoirs.
Étant donné que l'ammoniac est très corrosif pour de nombreux matériaux, un soin particulier a été apporté pour sélectionner uniquement des composants compatibles avec l'ammoniac. Seuls des échangeurs de chaleur à plaques brasées ont été utilisés pour avoir un système compact. Trois réservoirs en acier inoxydable servent de séparateur vapeur-liquide à la sortie de ces échangeurs.
La pompe de solution étant le principal composant consommateur d'électricité du prototype (donc influant directement sur le coefficient de performance électrique), une attention particulière a été portée à ses spécifications au regard des contraintes hydrauliques, environnementales, et électriques [13]. De plus, une étanchéité de haut niveau est requise, en raison de la forte toxicité de l'ammoniac pour les êtres humains, ainsi qu'un contrôle précis du débit de circulation sur une large plage de fonctionnement. La solution liquide entrant dans la pompe provenant de l'absorbeur, sa température est relativement proche de la saturation. Si un échauffement par frottement se produit, il y a un risque de désorption autour des pièces mobiles, ce qui peut gravement altérer la durée de vie. Par conséquent, la pompe sélectionnée doit présenter très peu d'échauffement, même localement sur ses parties internes. Ces considérations ont conduit à la sélection d'une pompe à diaphragme comme pompe de solution.

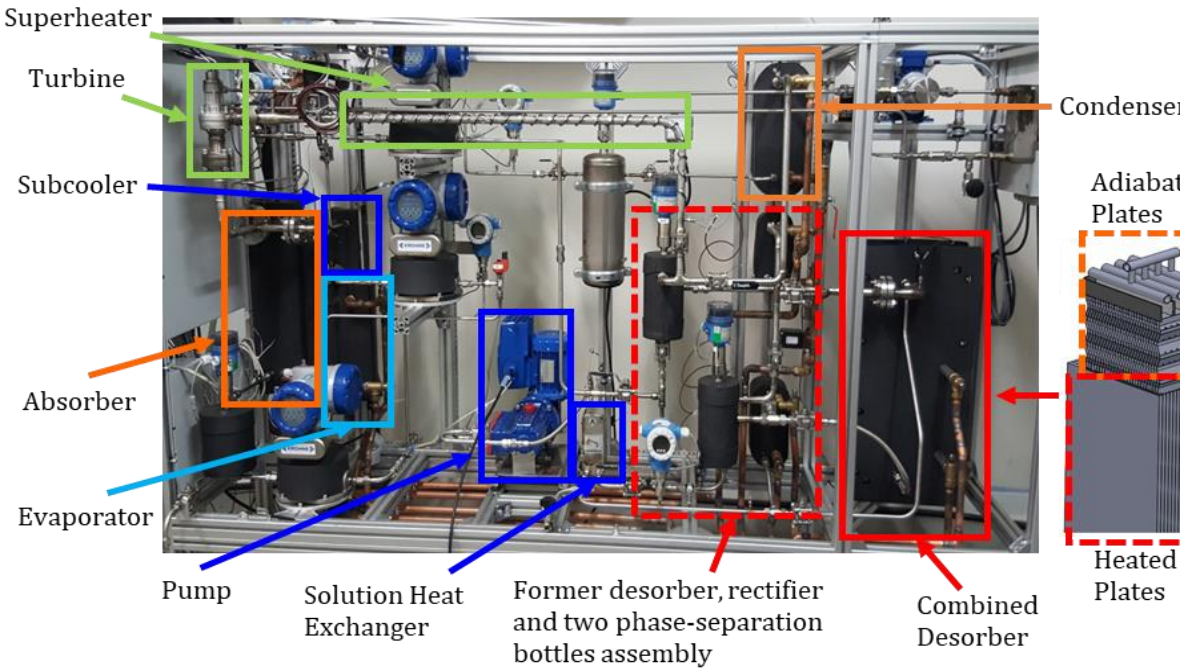


**Fig. III** – Installation pilote.

Différentes campagnes d'essais ont été réalisées sur la machine à absorption, la turbine (à l'extérieur et à l'intérieur de la boucle d'absorption) et le cycle combiné.
En ce qui concerne les essais sur la machine à absorption, il a été démontré qu'il faut faire attention à atteindre un fonctionnement stable de l'installation pilote, pour lequel la régulation du niveau dans les réservoirs et l'ouverture des vannes pilotables (les vannes en amont de l'absorbeur et de l'évaporateur) sont cruciales. Le désorbeur combiné intégré dans l'installation pilote, en plus d'éviter l'utilisation d'un rectifieur séparé, simplifie la gestion de l'installation par rapport à l'utilisation de l'architecture classique d'échangeur de chaleur à ébullition et permet d'atteindre un COP thermique supérieur à 0.7 dans les conditions de fonctionnement étudiées. Cependant, dans certaines conditions de fonctionnement le désorbeur peut fonctionner noyé, ce qui réduit l'efficacité de ce composant et affecte la performance globale du cycle.

Concernant la turbine, compte tenu du rapport entre la section de sortie et le col de l'injecteur, une très faible chute de pression est suffisante pour obtenir des conditions soniques. Par conséquent, dans le cycle combiné, la turbine

fonctionne pratiquement en permanence dans des conditions blocage sonique, dans lesquelles le débit massique traité dépend linéairement de la pression d'entrée. La prise en compte d'un comportement en gaz réel est pertinente pour le calcul du débit massique de la turbine pour l'ammoniac, alors qu'elle est négligeable pour les autres gaz testés (**Fig. IV**). Finalement, en raison de la petite taille de la turbine et des pertes importantes de la turbine et de la génératrice électrique, le rendement électrique maximal atteint était de 7%.

Les limites en termes de plages de fonctionnement du pilote et en particulier de la turbine (définition inappropriée du point de conception, faible rendement de génération électrique, faible rendement à petite échelle) n'ont pas permis une caractérisation complète du cycle. Cependant, les connaissances et l'expérience acquises lors des essais sont très importantes pour le futur développement de la technologie.

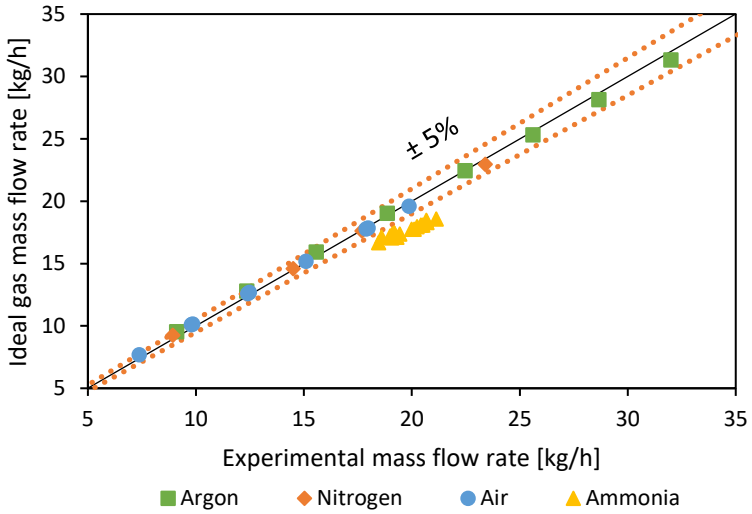


**Fig. IV** – Comparaison à l'expérimentation du débit massique de la turbine pour de simulations en modélisant les fluides comme des gaz parfaits.

Les tests effectués apportent des observations intéressantes sur le fonctionnement du cycle : tout d'abord, le fait que le débit massique de la turbine soit fixé pour des pressions de travail données entraîne des conséquences importantes sur le cycle, car il n'est pas possible de modifier le rapport entre la production de froid et d'électricité à moins de changer la pression en amont de la turbine. De plus, le détournement d'une partie de la vapeur désorbée vers la ligne de production d'électricité a des effets importants sur la ligne de production de froid du cycle, en modifiant les efficacités des échangeurs de chaleur et donc les pressions du cycle ainsi que le débit massique total de la vapeur en circulation.

# Modèles numériques

Compte tenu de ces considérations, une étude plus approfondie de la technologie a été réalisée, à partir des données de l'installation pilote. Un modèle 1D compressible de la turbomachine a d'abord été créé. Un bilan énergétique, prenant en compte les frottements dans l'injecteur et les pertes par recompression en sortie de celui-ci à travers deux rendements, permet de calculer la vitesse d'entrée dans le rotor. Celle-ci est utilisée pour calculer le travail échangé par le fluide avec les aubes mobiles grâce à l'équation d'Euler et à la connaissance du triangle des vitesses. Dans l'étude, l'approche suivie consiste à soustraire des termes de perte à ce travail théorique maximal pouvant être produit à partir de l'énergie cinétique d'entrée, pour prendre en compte les phénomènes de perte à l'intérieur du rotor. A cet effet, les termes de pertes sont écrits sous la forme d'une différence d'enthalpie, et en particulier sont considérés :

- les pertes de passage, dues au frottement dynamique du fluide sur les pales mobiles et à l'angle d'incidence non optimal du jet entrant dans le rotor
- les pertes de frottement, dues à la résistance au mouvement rencontrée par les surfaces sans aubes du rotor
- les pertes de fuite dues au fluide qui s'échappe des aubes actives et n'échange pas de travail dans le rotor
- les pertes d'admission partielle causées par la forte partialisation.

Les turbines à admission complète ont généralement des rendements plus élevés que les turbines à admission partielle, mais dans des circonstances qui ne permettent pas une admission complète, comme pour des débits massiques très faibles, des turbines à admission partielle sont utilisées. Leur utilisation entraîne des diminutions de performance qui peuvent être importantes et sont principalement dues aux aubes non alimentées. Lorsque la turbine est fortement partialisée, ces phénomènes dissipatifs peuvent devenir la principale source de perte. Les corrélations pour les différents termes de perte ont été formalisées grâce à la littérature scientifique existante et les coefficients ajustés pour être en accord avec des simulations CFD effectuées sur la turbine. Un écart moyen inférieur à 7% a été obtenu entre le modèle 1D et la puissance de sortie CFD, démontrant que les termes de perte sélectionnés sont bien adaptés. Les résultats dans le cas de l'ammoniac pur sont montrés en **Fig. IV**. On voit une courbe de puissance en cloche typique d'une turbine axiale et une vitesse de rotation optimale fonction de la pression d'entrée avec des valeurs comprises entre 40 et 55 ktr/min aux pressions d'entrée d'intérêt pour le cycle. La validation à partir des résultats expérimentaux n'a été possible que pour le débit massique traité puisque le rendement expérimental de la génératrice électrique n'était pas connu. Enfin, la possibilité d'utiliser le modèle pour prédire les performances de la turbine lors de la réduction du taux d'admission partielle a été démontrée.

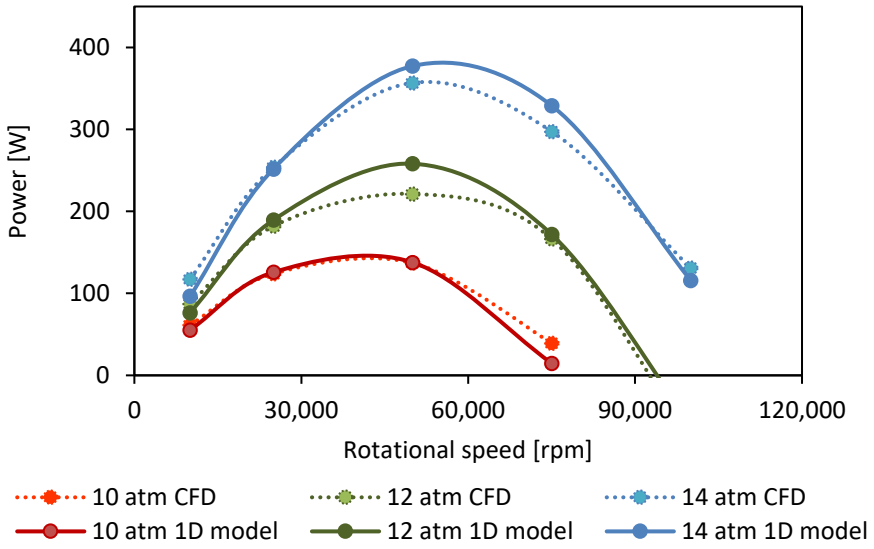


**Fig. IV** – Caractéristique de puissance de la turbine pour différentes pressions d'entrée, une température d'entrée de 120 °C, et une pression de sortie de 5 bar dans le cas de l'ammoniac pur.

Ensuite, un modèle numérique détaillé du cycle à absorption simple, décrit dans [14] a été développé et validé sur les résultats expérimentaux du prototype. Les données recueillies au cours des campagnes expérimentales ont été analysées de manière critique afin d'obtenir toutes les propriétés thermo-physiques nécessaires, et les points expérimentaux non fiables ont été exclus de la suite de l'analyse. Pour chaque composant du cycle, des équations de bilan d'énergie et de masse sont formulées sous l'hypothèse d'un état stationnaire. Le mélange est à saturation en sortie de chaque échangeur (sauf une surchauffe imposée en sortie d'évaporateur). Par conséquent, la haute pression et la basse pression du cycle sont déterminées respectivement par la température du condenseur et de l'évaporateur.

Un modèle simplifié basé sur des pincements de température fixes et sur l'efficacité massique de l'absorbeur (estimée à partir des essais expérimentaux) a été développé. Ce modèle fournit de bons résultats au point de fonctionnement nominal, mais pas dans des conditions différentes de ce point.

Par conséquent, un autre modèle a été développé sur la base des efficacité thermique, massique et d'espèce, reliant le fonctionnement des composants à celui de composants idéaux. Des mesures expérimentales ont été utilisées pour caractériser les efficacités des composants dans différentes conditions de fonctionnement et des corrélations ont été trouvées pour les modéliser sur la base de 3 paramètres adimensionnels : le nombre d'unités de transfert, le ratio énergétique et le nombre de Jakob. Le modèle intégrant les corrélations pour chaque composant a montré un très bon accord avec les résultats expérimentaux, avec une erreur maximale inférieure à 6% pour le COP et 15% pour la puissance de refroidissement sur toute la gamme de fonctionnement expérimentée (**Fig. V**).

Le modèle ajusté a été utilisé pour effectuer une analyse paramétrique sur la dimension des composants, mettant en évidence l'absorbeur, le desorbeur et l'évaporateur comme étant les composants les plus critiques de l'installation et donc ceux ayant la plus grande marge d'amélioration. L'utilisation de paramètres adimensionnels rend cette approche bien adaptée à l'analyse à plus grande échelle et à la réalisation d'optimisations thermo-

économiques. Néanmoins, des études expérimentales supplémentaires sont nécessaires pour confirmer la validité du modèle pour différentes tailles de machine.

Pour terminer le développement du cycle combiné, le modèle de la turbine est intégré au modèle de machine à absorption. Le couplage est réalisé en imposant que le débit massique traversant la ligne de production de froid soit égal au débit de vapeur désorbée moins le débit traité par la turbine.
Pour compléter le modèle de cycle, une représentation simplifiée du surchauffeur est incluse. Ce composant est modélisé comme un échangeur de chaleur à plaques ayant un coefficient de transfert de chaleur global fixe.
Enfin, la possibilité de réaliser un laminage avant la turbine a été introduite. En effet, le fait que le débit massique traité par la turbine soit fixe pour une pression d'entrée donnée impose des limites strictes au cycle en termes de plage d'opérabilité et de flexibilité. Par conséquent, l'introduction d'une vanne de laminage pourrait ajouter un degré de liberté supplémentaire au système aux prix d'une diminution de son efficacité, puisqu'en réduisant la pression en amont de la turbine, le débit massique traité par l'injecteur peut être réduit.
Le modèle de cycle combiné a été développé à partir de l'intégration des modèles ajustés de machine à absorption et de turbine, et donc il présente les limites des deux modèles sur lesquels il est basé. En particulier, les résultats ont été ajustés pour une température de source chaude comprise entre 85 et 115 °C, une température de source intermédiaire de 22 à 30 °C et une température de source froide de 8 à 20 °C. En outre, le modèle fait référence à l'utilisation d'échangeurs à plaques et, en particulier, à l'utilisation d'une technologie de desorbeur très spécifique.

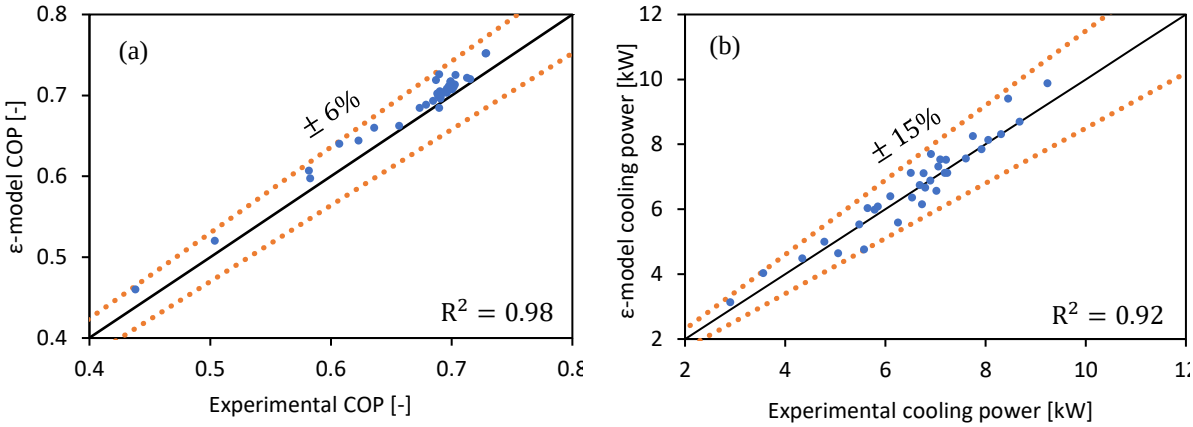


**Fig. V** – Résultats du modèle d'efficacité comparés aux résultats expérimentaux.

En ce qui concerne la turbine, les limites incluent le fait que l'ammoniac pur a été utilisé dans les simulations CFD (alors que des traces d'eau sont présentes dans la vapeur entrant dans la turbine). De plus, les simulations CFD impliquent d'autres approximations, telles que le fait que certains jeux et certaines pertes mécaniques ne sont pas représentés et des limitations liées à la discrétisation du maillage, à la description de la couche limite et de la turbulence. La condensation possible du fluide de travail pendant l'expansion doit également être étudiée plus en détail. Enfin, le modèle ne peut être utilisé pour simuler le fonctionnement en mode cycle à absorption simple et cycle combiné, mais pas en mode de génération d'électricité pure. Dans ce cas, le cycle fonctionnerait comme un cycle de Kalina, et des modifications du modèle doivent être faites.

# Résultats de simulations

Afin d'évaluer correctement l'efficacité de la production combinée de froid et d'électricité, une approche exergétique et exergoéconomique a été poursuivie, conduisant à la définition d'une efficacité exergétique globale ainsi que du coût par unité d'exergie des produits. Dans un premier temps, des simulations du fonctionnement du prototype expérimental ont été réalisées, afin d'étudier l'effet d'une variation des températures des sources.
Ensuite, un cas d'étude de base, représentant une application typique de réfrigération industrielle, a été défini pour évaluer l'intérêt d'un tel cycle. Pour la turbine, l'optimisation de la section de sortie de l'injecteur pour éviter les phénomènes de chocs entre le stator et le rotor, et une mise à l'échelle jusqu'à l'admission complète ont été réalisées. Pour les échangeurs de chaleur, le mise à l'échelle correspondante a été réalisée en augmentant les surfaces d'échange, puis une optimisation a permis de minimiser le coût unitaire de l'exergie des produits.

L'augmentation de 25 fois de la taille de l'installation permet d'utiliser une turbine à admission totale, produisant environ 90 kW de froid à environ 7 °C et environ 9 kW d'électricité, avec un rendement énergétique de 23% (**Fig. VI**).

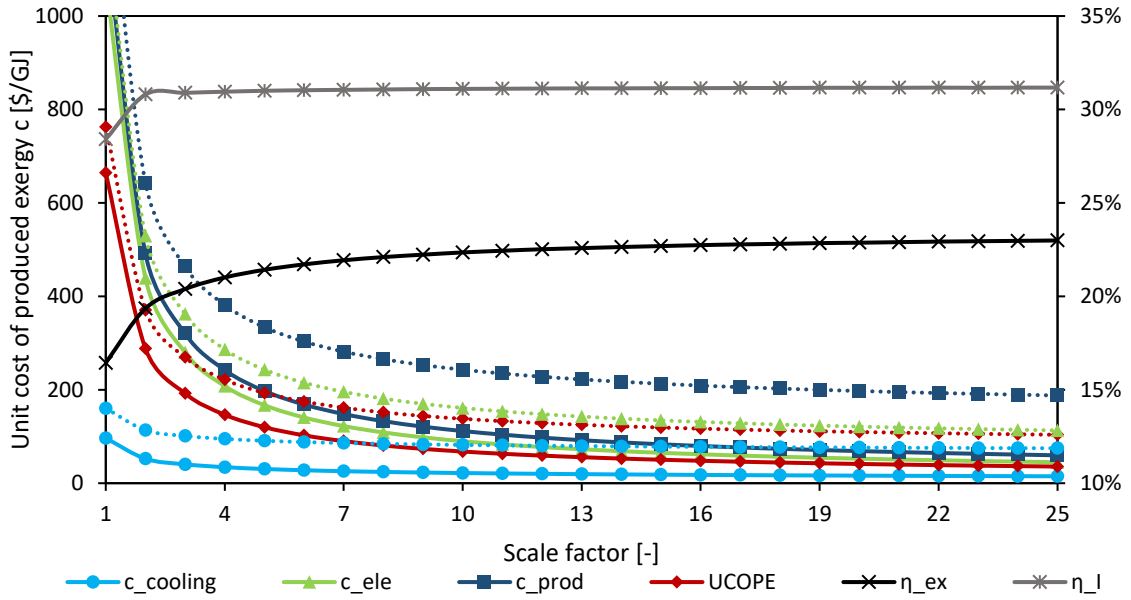


**Fig. VI** – Variation de l'efficacité énergétique $\eta_I$, de l'efficacité exergétique $\eta_{ex}$ et du coût unitaire de l'exergie $c_{fuel}$ produite (lignes en gras pour le cas de $c_{fuel}$ = 0 $/GJ, lignes en pointillés pour le cas de $c_{fuel}$ = 15 $/GJ) en augmentant la taille de l'installation par rapport à la taille du prototype expérimental.

Les limites à la flexibilité du cycle imposées par la turbine supersonique conduisent à la proposition d'une architecture alternative du cycle (**Fig. VII**). Cette disposition utilise un éjecteur entre les lignes de refroidissement et de production d'électricité, augmentant ainsi la flexibilité du système. Ceci est une solution très intéressante, car on constate qu'une augmentation de la flexibilité peut être obtenue avec une connexion plus intime des deux lignes de production grâce à l'utilisation d'un organe tel que l'éjecteur, qui permet de réguler plus efficacement le débit massique traité par la turbine.

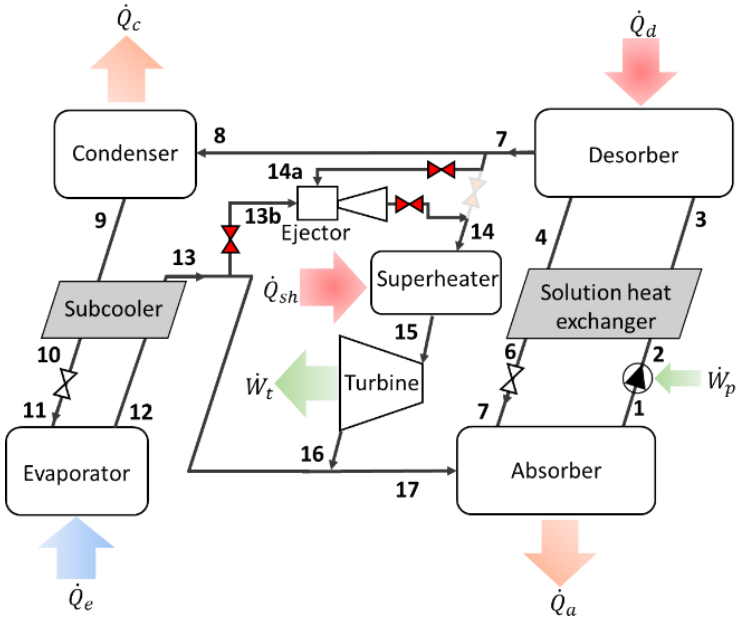


**Fig. VII** – Nouvelle architecture de cycle avec un éjecteur.

Enfin, une première analyse technico-économique sur un cas réel d'application a montré l'intérêt du cycle pour optimiser l'efficacité de la récupération de chaleur (**Fig. VIII**), mais a mis en évidence que l'intérêt économique effectif doit être évalué en fonction du coût des composants, en particulier de la turbine, et de l'électricité. Cette étude préliminaire a montré qu'un coût minimum de l'électricité de 0.15 €/kWh et des réductions importantes du coût de la turbine sont nécessaires (**Fig. X**).

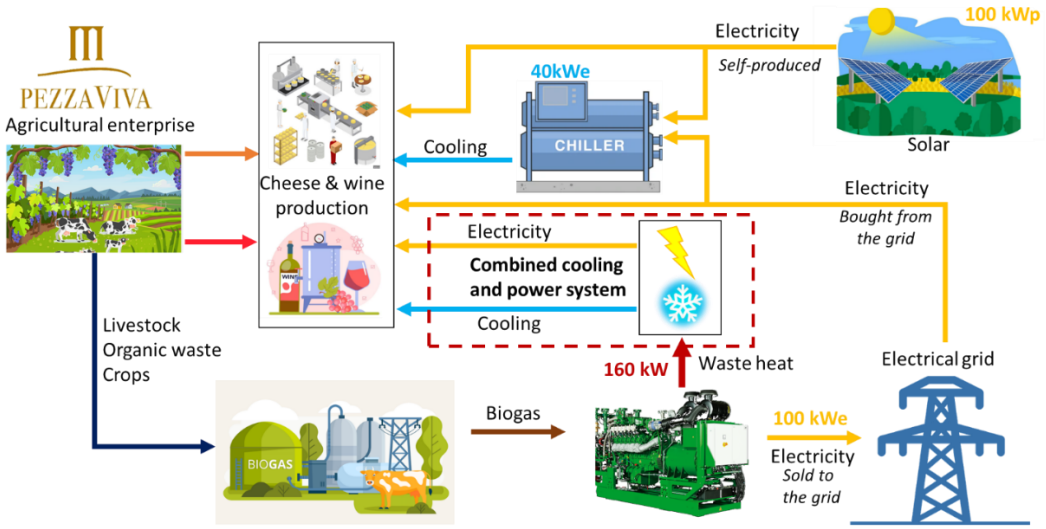


**Fig. IX** – Cas d'étude : intégration énergétique envisagée pour le cycle combiné.

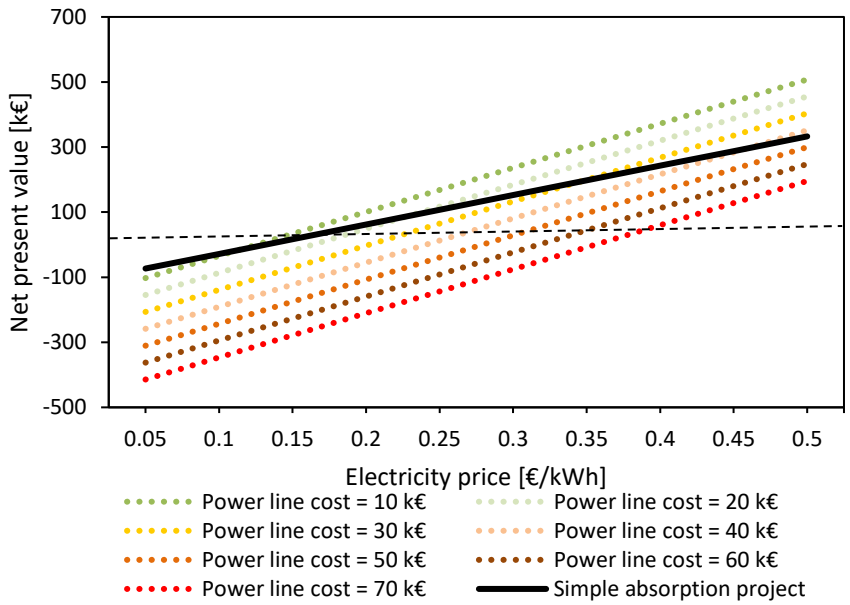


**Fig. X** – Valeur actuelle nette du projet d'intégration du cycle combiné en fonction du cout de l'électricité et du cout de la ligne de production d'électricité.

# Conclusions

En conclusion, les résultats expérimentaux présentés dans cette étude ont permis de mieux comprendre fonctionnement du cycle et d'en étudier les performances, et ces retours d'expériences seront très importants pour un futur développement de démonstrateur à taille réelle.
L'approche de modélisation développée basée sur l'utilisation de l'efficacité pour les échangeurs de chaleur et de modèles de pertes 1D pour les turbines s'est avérée efficace pour l'étude approfondie de ce type de cycles.
Globalement, l'utilisation d'une turbine axiale semble être un choix approprié pour ce type d'application, à condition d'utiliser des taux d'admission partielle raisonnables (supérieurs à 0.2) et ajustables.

Enfin, la possibilité de produire les deux types d'énergies dans le même cycle a été prouvée, avec la possibilité de passer de la génération de froid à la génération d'électricité par des architectures alternatives, mais l'intérêt économique réel du système doit être évalué en comparant le coût des produits avec leur valeur marchande.
En effet, l'évaluation de l'utilisation du cycle combiné dans une application industrielle réelle a mis en évidence que cette technologie peut augmenter considérablement l'efficacité de la récupération de chaleur des cycles à absorption, mais la rentabilité économique dépend fortement du coût de l'électricité et du coût des composants de la machine. Néanmoins, le cycle a un fort potentiel et peut représenter une solution intéressante, notamment dans le contexte actuel de la crise énergétique et du changement climatique.

# List of Figures

# List of tables

# Nomenclature

*Variables*

| | | |
|---|---|---|
| $a$ | sound speed | *[m. s$^{-1}$]* |
| $A$ | surface | [m$^2$] |
| $b$ | blade height | [m] |
| $c$ | cost per unity of exergy | [\$.J$^{-1}$] |
| $C$ | absolute velocity | [m. s$^{-1}$] |
| $\dot{C}$ | cost rate | [\$.s$^{-1}$] |
| $cp$ | heat capacity | [W.m$^{-2}$K$^{-1}$] |
| $D$ | diameter | [m] |
| $E_s$ | annual savings | [€/year] |
| $ex$ | specific exergy | [J.kg$^{-1}$] |
| $\dot{Ex}$ | exergy flow rate | [W] |
| $f$ | exergoeconomic factor | [-] |
| $h$ | specific enthalpy | [J.kg$^{-1}$] |
| $i_r$ | interest rate | [-] |
| $I_{rad}$ | solar radiance | [W/m$^2$] |
| Ja | Jakob number | [-] |
| $k$ | coefficient, constant, component | depending on the coefficient |
| K | overall heat transfer coefficient | [W.m$^{-2}$K$^{-1}$] |
| L | latent heat | [J.kg$^{-1}$] |
| $\dot{m}$ | mass flow rate | [kg. s$^{-1}$] |
| $M$ | Mach number, molar mass | [-] |
| $n$ | system lifetime | [years] |
| $P$ | pressure | [bar] |
| $P_c$ | ejector backpressure | [bar] |
| $Q$ | vapour quality, heat | [-] |
| $\dot{Q}$ | thermal power | [W] |
| $r$ | expansion ratio | [-] |
| R | ideal gas constant | [J. K$^{-1}$ mol$^{-1}$] |
| $R_{en}$ | energetic ratio | [-] |
| $R_{th}$ | throttling ratio | [-] |
| $r_s$ | split ratio | [-] |
| $s$ | specific entropy | [J. K$^{-1}$. kg$^{-1}$] |
| $S$ | heat exchangers area | [m$^2$] |
| $Sv$ | Savings | [€/year] |
| $T$ | Temperature | [K] |
| u | velocity | [m. s$^{-1}$] |
| $U$ | rotational speed | [m. s$^{-1}$] |
| $W$ | relative velocity, specific work | [m. s$^{-1}$] |
| $\dot{W}$ | mechanical power | [W] |
| $x$ | ammonia mass fraction | [-] |
| $Y$ | rate of exergy destruction (loss) to total fuel exergy | [-] |
| $Y^*$ | rate of exergy destruction (loss) to total exergy destruction | [-] |
| $Z$ | capital cost | [\$] |
| $\dot{Z}$ | capital cost rate | [\$.s-1] |

*Greek letters*

| | | |
|---|---|---|
| $\alpha$ | absolute angle, off-design mixing efficiency coefficient | [°] |
| $\beta$ | relative angle | [°] |
| $\gamma$ | maintenance factor | [-] |
| $\gamma_a$ | adiabatic index | [-] |

| | | |
|---|---|---|
| $\Delta$ | variation | [-] |
| $\varepsilon$ | Heat exchangers effectiveness, partial admission ratio | [-] |
| $\eta$ | efficiency | [-] |
| $\varphi$ | mixing efficiency coefficient | [-] |
| $\rho$ | density | [$kg.m^{-3}$] |
| $\tau$ | operating hours | [h] |
| $\omega$ | rotational speed, entrainment ratio | [rpm] |
| $\Psi$ | passage loss coefficient | [-] |

## *Acronyms*

| | | |
|---|---|---|
| *ACs* | air condition systems | |
| *APC* | *absorption power and cooling* | |
| *CEPCI* | chemical engineering plant cost index | |
| *CFC* | chlorofluorocarbon | |
| *CFD* | computational fluid dynamics | |
| *CCP* | combined cooling and power | |
| *COP* | coefficient of performance | |
| *CRF* | capital recovery factor | |
| $D_S$ | specific diameter | |
| *GWP* | global warming potential | |
| $H_2O$ | water | |
| *HC* | hydrocarbon | |
| *HCFC* | hydrochlorofluorocarbon | |
| *HEX* | heat exchangers | |
| *HFC* | hydrofluorocarbon | |
| *HFO* | hydrofluoroolefin | |
| *HTF* | heat transfer fluid | |
| *LCOE* | levelized cost of energy | [€/kWh] |
| $NH_3$ | ammonia | |
| *NPV* | net present value | |
| *NTU* | number of transfer units | |
| $N_S$ | specific speed | |
| *ODP* | ozone depletion potential | |
| *ORC* | organic Rankine cycles | |
| *PBP* | payback period | |
| $r_s$ | split ratio | |
| *R290* | propane | |
| *R600a* | isobutane | |
| *R717* | ammonia | |
| *SERS* | single ejector refrigeration system | |
| *SI* | international system | |
| *TRL* | technology readiness level | |
| *UCOPE* | unit cost of produced exergy | [$.GJ^{-1}$] |

## *Subscripts and superscripts*

| | |
|---|---|
| *a* | absorber |
| *ad* | adapted |
| *amb* | ambient |
| *ax* | axial |
| *c* | condenser, cooling |
| *cooling* | cooling |
| *CH* | chemical |
| *CI* | capital investment |
| *cri* | critical point ejector |
| *cv* | control volume |
| *d* | desorber |

| | |
|---|---|
| *D* | destroyed |
| *e* | evaporator, energy |
| *eff* | effective |
| *ele* | electric |
| *en* | energetic |
| *equip* | equipment |
| *ex* | exergetic |
| *exp* | expansion |
| *f* | friction |
| *F* | fuel |
| *fr* | friction |
| *gen* | generator |
| *H* | high |
| *HTF* | heat transfer fluid |
| *id* | ideal |
| *i* | inlet |
| *is* | isentropic |
| *I* | first principle, intermediate |
| *KN* | kinetic |
| *L* | Loss, limit, low |
| *lk* | leaking |
| *liq* | liquid |
| *lm* | logarithmic mean |
| *LF* | limiting fluid |
| *m* | mean |
| *mass* | mass |
| *max* | maximum |
| *mech* | mechanical |
| *min* | minimum |
| *n* | nozzle |
| *net* | net |
| *nom* | nominal |
| *NLF* | non-limiting fluid |
| *o* | outlet |
| *OM* | operating and maintenance |
| *p* | Pump, passage |
| *P* | product |
| *pa* | partial admission |
| *pass* | passage |
| *PH* | physical |
| *power* | power |
| *prod* | products |
| *proj* | project |
| *PT* | potential |
| *P&t* | piping and tanks |
| *rec* | recompression |
| *rect* | rectifier |
| *Q* | thermal |
| *ref* | refrigerant |
| *refvalv* | refrigerant throttling valve |
| *sat* | saturated |
| *se* | shock exit section |
| *sh* | superheater |
| *shx* | solution heat exchanger |
| *sol* | solution |
| *solvalv* | solution throttling valve |
| *sp* | poor solution |
| *species* | species |
| *sr* | rich solution |
| *sub* | subcooler |

| | |
|---|---|
| *th* | thermal |
| *t* | turbine, time |
| *throat* | throat |
| *u* | tangential |
| *vap* | vapour |
| *sh* | superheater |
| *t* | turbine |
| *tot* | total conditions |
| *throat* | throat |
| *u* | tangential |
| *vap* | vapour |
| *VCC* | vapour compression chiller |
| *w* | work |
| * | sonic conditions |
| *0* | reference state |
| *1,2,..* | system state points |

# Content of the thesis

*Chapter 1* of this document is dedicated to the description of the context in which the study is positioned, including a general introduction of the increasing energy demand worldwide with a focus of cooling. The interest of using thermally driven technologies in general, and combined power and cooling cycles in particular is presented. The boundaries and objectives of the work are also presented.

*Chapter 2* introduces an overview of heat driven technologies for power and cooling production. Given their relatively higher maturity, the focus is on thermodynamic cycles, and specifically on those of interest for the present study. However, the chapter simply provides a cartography of the available technologies without covering the topics developed in more details during the thesis work.
Concerning power production cycles, the organic Rankine and the Kalina cycles are presented first. Different expanders available for low-temperature heat recovery and expander selection process are also examined. Subsequently, cooling production thermodynamic cycles are discussed. The overview includes ejector and adsorption cycles, but particular attention is paid to absorption cycles, object of this work. Finally, combined cooling and power architectures are presented, with a focus on absorption bases cycles. Performance evaluation parameters are introduced for all the technologies reviewed. The chapter is concluded by a description of the scientific challenges tackled in this work.

*Chapter 3* details the development of the experimental prototype and the experimental tests carried out. The architecture as well as the setting-up of the prototype, including technological aspects are presented in details. Challenges encountered during the development of the machine as well as its limitations are discussed. The experimental campaigns carried out included different types of tests: tests on the simple absorption machine, tests on the turbine in isolation and tests on the combined cycle. The amount of information that can be obtained from experimental tests is limited, but they still provide interesting insights into the operation of the turbine and its interactions with the cycle that integrates it. Feedback from experimental tests is given at the end of the chapter.

*Chapter 4* contains details on the development of a numerical model of the cycle. A model of the absorption chiller is developed first, characterising exchangers through semi-empirical effectiveness modelled on dimensionless parameters and adjusted on experimental results. Subsequently, a model of the partial admission turbine is built, tuning loss model coefficients based on CFD simulations carried-out on the expander. Finally, the turbine model is integrated in the absorption cycle model, providing a reliable tool for the simulation of the combined production cycle. Scale-up evaluation using the models is also briefly discussed.

*Chapter 5* presents the investigation of the combined cooling and power cycle using the developed numerical models. Energy and analyses at the pilot plant scale are presented first, followed by an evaluation of the plant-scale up. To this end, the exergoeconomic methodology is applied to allocate costs to the products of the system based on their exergetic value. An optimisation on the heat exchangers area is then performed to minimise the overall exergetic cost of products.
Since strong limitations imposed by the turbine to the cycle were highlighted during the investigation, a new architecture integrating an ejector is presented and its advantages in terms of increased flexibility assessed.
Finally, a preliminary techno-economic assessment of the use of the technology in a real life industrial application is performed in the last part of the chapter.

*Chapter 6* summarizes the main achievements and conclusions of this work, coming both from numerical and experimental investigations. Perspectives and proposals for the pursuit of the work are discussed in the end.

Finally, *Chapter 7* includes all the appendixes containing additional information concerning some parts of the study. In particular, thermodynamic modelling of ejectors for refrigeration systems and comparison between numerical and experimental results concerning the turbine power production are presented.

# Chapter 1

# General introduction

*Worldwide energy demand growth, and in particular the steep increase of energy needs for cooling considerably complicate the necessary greenhouse gases reduction task. The spreading of heat driven systems, including absorption machines, could represent one of the pillars to ensure a sustainable global diffusion of cooling system. Combined cooling and power production appears to be a very interesting solution to overcome the problems related to the strong fluctuations of cooling demand, limiting the diffusion of absorption cycles due to the low utilization rate. In this context, the focus of this thesis is the development and investigation of an absorption based cooling and power cycle using low-temperature thermal energy. The objectives of the thesis are stated in this chapter and the structure of the present document is described.*

# 1.1 Context

Climate change is one the most critical challenges humanity has ever been confronted with. The warming of the planet threatens food security, freshwater supply, human health and political stability worldwide. The effects of climate change, including sea level rise, droughts, floods, and extreme weather, will be more severe if utmost actions are not taken to reduce drastically emissions of greenhouse gases into the atmosphere.

This task is complicated by a growing world population, increased from 6 billion in the beginning of the century to 8 billion in 2022 and expected to reach 9.7 billion in 2050 [15]. This together with a continuous development of global economy results in an energy demand growing worldwide at unrestrained rates. Indeed, researchers forecasted global energy demand to double or even triple or until 2050 [16].

Although a shift in paradigm is already visible, 80% of all the energy used in 2019 was still provided by fossil fuels. Hence, the scientific community all over the world is focusing its attention on the search for new energy conversion technologies that are increasingly efficient and based on renewable sources [1–3].
The decarbonisation of the energy sector is based on the introduction of distributed technologies using renewable energy sources and on the increase in energy efficiency, to achieve which waste energy recovery plays a role of paramount importance. Moreover, recent geopolitical events have highlighted the threats faced by Europe to guarantee reliable and low-cost energy provisioning and the need for increased self-sufficiency. Indeed, until recently, energy was considered as a commodity whose small cost had a limited influence on the industrial and manufacturing sector. However, things have changed drastically over the last months and the high cost of energy could be catastrophic for many companies. To address this critical situation, the European community has launched several programs (e.g. REPowerEU [17]) aiming at reducing dependence on foreign fossil fuels by accelerating the transition towards clean energy, thus achieving a more resilient energy system and a true Energy Union. The pillars of these programs are to save energy, diversify supplies, substitute fossil fuels by accelerating Europe's clean energy transition and smartly combine investments and reforms.

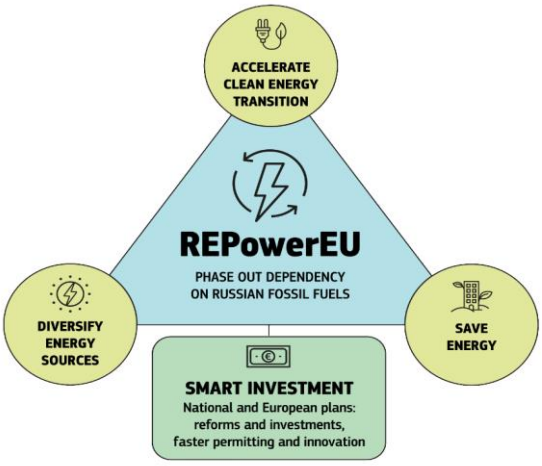


**Fig. 1.1** – RepowerEu plant [17].

This interest involves all sectors starting from the best known ones such as power production and transport but also heating and cooling [18,19]. In the European Union, heating and cooling (in both buildings and industrial sectors) account for half of the final energy consumption [20]. The REPowerEu plan sets ambitious objectives with particular emphasis put on the diffusion of heat pumps, setting the objective of 20 million units installed in the EU by 2026 and about 60 million installed by 2030. The plan includes 56 M€ of investments and measures to accelerate and encourage the introduction of these systems, such as more severe requirements on energy efficiency in buildings and a possible ban on fossil fuel boilers sales by 2029.
Worldwide, heating and cooling requirement in buildings was covered for about 10.7%, by renewable sources in 2019, while this figure was 7.9% in 2009. Renewable sources include, both direct renewable heat (from biomass, solar and geothermal) and indirect renewable heating and cooling (provided by renewable electricity and cogenerative networks of district heating and cooling). As for Europe, this percentage is of about 13%, but some countries, such as France, Italy and Germany, while still depending heavily on natural gas, have seen rapid growth in the installations of heat pumps. This contributed to the increase in renewable heat shares in buildings, reaching a value of 24.1% in France, 22% in Italy and 19% in Germany. United States and the United Kingdom are around

10%, China around 15% (reflecting the solar thermal and geothermal increase), while both Turkey (geothermal) and Brazil (biomass) have also shares above 10%.

The tripling of global energy demand for cooling between 1990 and 2016 (**Fig. 1.2**) in the residential sector [21] shows that this end use is growing much faster compared to other uses, resulting in an ever increasing demand for electricity. This demand of cooling is mainly covered using conventional technologies through air conditioners that supply about 75% of the world cooling demand.
More specifically, since 1990, global sales of ACs (Air Conditioners) have grown steadily and significantly and have almost quadrupled thus reaching in 2016 values of approximately 135 million units sold per year. Altogether, around 1.6 billion cooling systems are installed worldwide, with more than half only in two countries: the People's Republic of China and the United States.
These ACs, which vary enormously in terms of energy efficiency and operation, consume over 2,000 terawatt hours (TWh) of electricity per year [21], which is nearly two and a half times the total electricity consumption of Africa and about 4 times the electric energy used in France (which was approximately 478 TWh in 2018 [4]).
The global outlook in the coming years foresees a continuous increase in the spread of cooling systems, especially in emerging countries such as India, China and Brazil. Moreover, it is worth to note that compared to an installed power of around 850 GW worldwide, in 2016, this power is expected to quadruple thus reaching an installed power of around 3,500 GW in 2050.

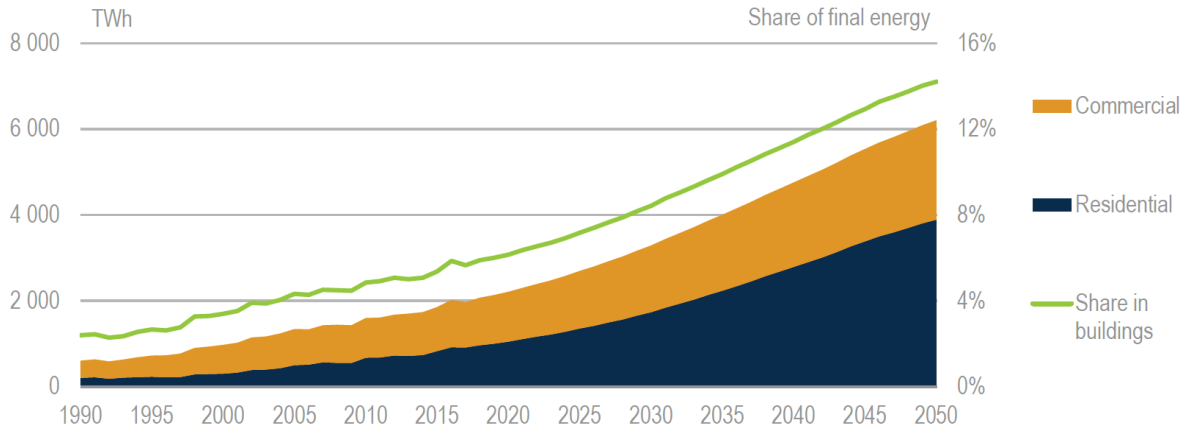


**Fig. 1.2 -** World energy use for space cooling by subsector in the 2016 IEA Baseline scenario [21].

The foreseen performance improvement of ACs systems will only partially offset the impact of the energy consumption of the rising number of AC units owned. Energy consumption for space cooling is predicted to rise from 2020 TWh in 2016 to 6,200 TWh in 2050, representing a further threefold increase with respect to 1990 values (**Fig. 1.2**). Almost 70% of this increase comes from the residential sector, projected to account for 65% of the space cooling demand in 2050.

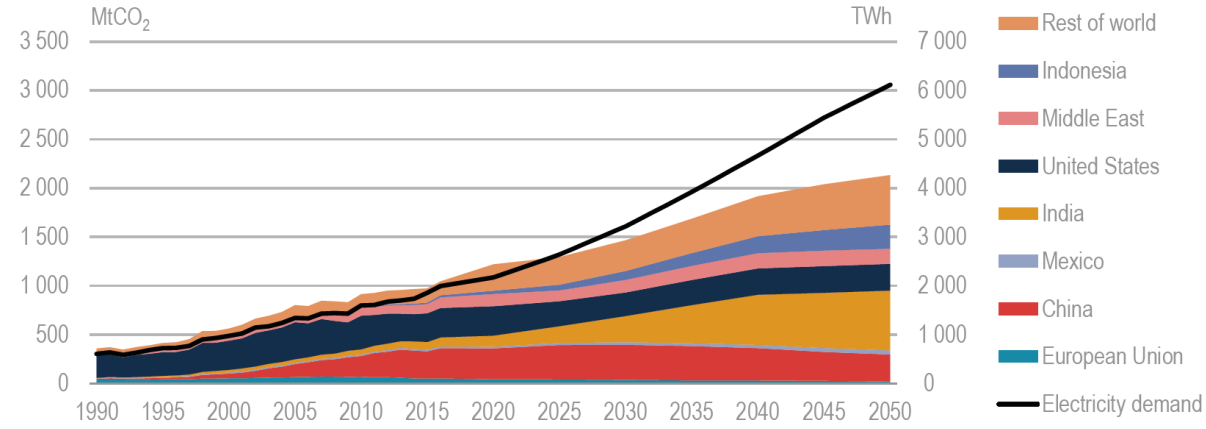


**Fig. 1.3 -** Electricity demand for space cooling and resulting $CO_2$ emissions in the 2016 IEA Baseline Scenario [21].

This will greatly influence the $CO_2$ emissions (**Fig. 1.3**), bringing their current contribution of about 1,135 $MtCO_2$ equivalent in 2016 to about 2,070 $MtCO_2$ in 2050 (under the IEA scenario of continuous use of current technologies). Additionally, despite partial decoupling with electricity use, ACs loads will tremendously increase power needs, putting strain on electricity systems in many countries jeopardizing their capacity to meet peaks of demand.

For this reason, in recent years, much attention has been paid to both research programs and national incentives for energy efficiency. The countries with higher energy demands in Europe are Germany, France and Italy.
With reference to energy consumption in domestic applications, space heating and domestic hot water represent the largest share (79%) of the total final energy consumption (192.5Mtep) [20]. Although space cooling in Europe represents a rather small percentage of the total final energy consumption, the demand in both the residential sector and in the food industry is constantly increasing especially during the summer months, showing a similar increase trend with air pollution and global warming.
While for France the percentage of final energy demand for heating and cooling attributable to space and process cooling is only the 3-4% (**Fig. 1.4**), for other countries in the Mediterranean area (Italy, Spain, Greece) this percentage is the order of 10-12%, with a tendency to increase strongly expected in the coming years.

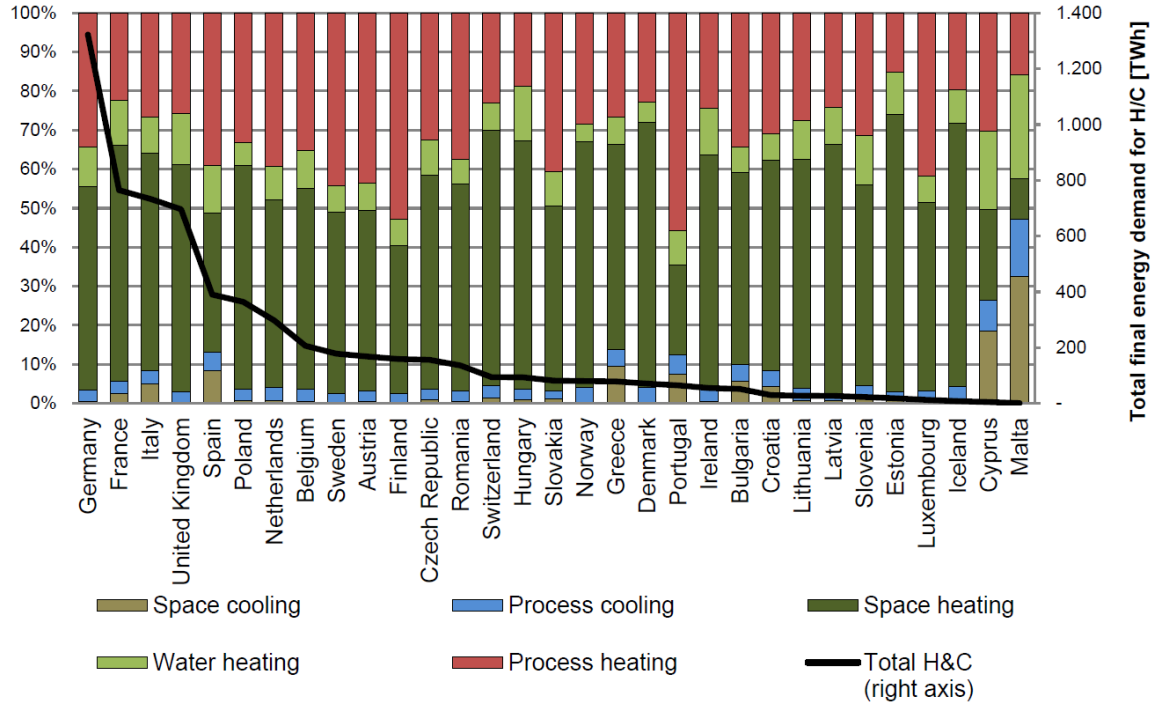


**Fig. 1.4 -** Final energy demand for heating and cooling per end-uses in Europe in 2012 [20].

The interest in the study of new cooling technologies is always growing in terms of both increasing conversion efficiency and versatility in the use of waste energy and in the use of renewable sources.
An interesting possibility is represented by heat driven cooling technologies that use thermal energy, like solar or geothermal energy and waste heat rather than electricity to produce cooling. These systems can produce significant energy savings, have low global warming and ozone depletion potential, and also ensure higher indoor air quality [22]. The spreading of these cooling systems represents one of the pillars to ensure a sustainable global diffusion of cooling systems and, at the same time, reduce the necessary electrical power, and contain climate-changing emissions.

Concerning the industrial sector, researchers estimated that approximately 20-50% of the energy consumed by industry is lost [23]. A data of 1,130 PJ/year (313 TWh/year) of waste heat was accounted for [24] in the temperature interval below 200 °C for four significant industrial sectors (food, paper, chemical and refining) among the most energy intensive **(Fig. 1.5**).

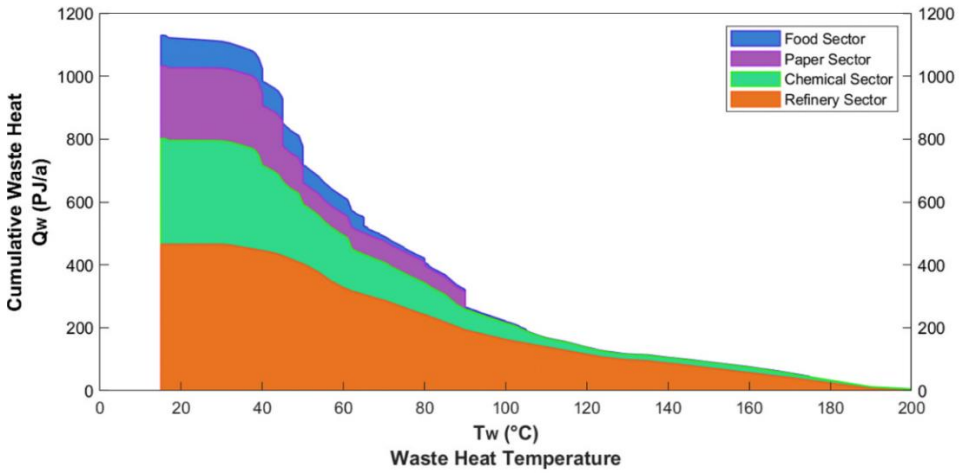


**Fig. 1.5** - Cumulative waste heat <200 °C in EU28 identified in four significant industries [24].

This interest is increasing not only towards isolated systems but also towards integrated systems such as district heating and cooling [25]. Presently, district heating networks are mainly widespread in Europe in Nordic countries, such as in Denmark where they already cover values above 60% of users. District cooling networks are present mainly in the USA, Japan and UAE (United Arab Emirates) where they already cover values of 22% of users with a target of reaching 28% by 2030. In Europe district heating and cooling are on the agenda of many strategic tables (SET Plan, Horizon 2020, Mission Innovation, EU Energy Efficiency Directive) [26] and several EU pilot projects have also been funded to demonstrate these applications on a city scale.
The recovery of waste heat from waste and sewage water for example is an emerging practice that is already used in many European cities based on already established and mature technologies that can help reduce primary energy demand. Heat can be used to generate cooling and examples of cities where heat driven chillers (generally absorption chillers) are used in the district cooling plants are Barcelona, Gothenburg, Vienna, Halmstad and Copenhagen. Very often, these cooling systems use a combination of sources allowing them to have high flexibility and very high efficiencies.

Additionally, thermally driven cooling technologies open the way to the attractive possibility of solar cooling, which combine heat driven chillers with solar thermal collectors [27]. The main advantage in this case is the good matching of solar global irradiation and cooling demand (**Fig. 1.6**), particularly advantageous in sunny and hot climates.

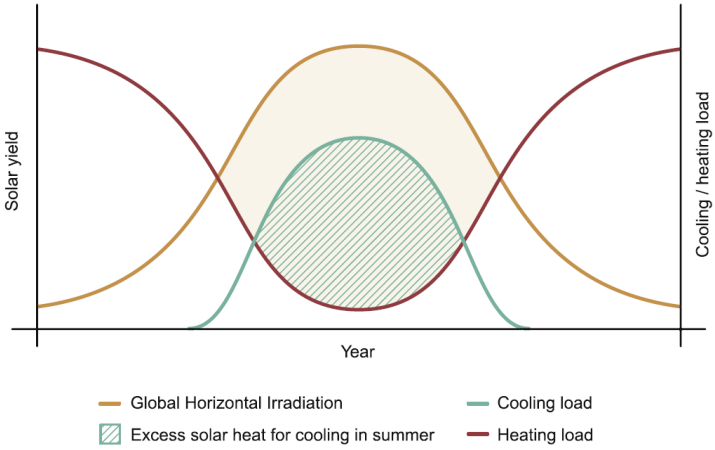


**Fig. 1.6** - Solar resource versus cooling demand [27].

According to the IEA 2012 solar heating and cooling roadmap scenario, solar energy could produce annually 1.5 EJ (417 TWh/year [27]) of solar cooling (**Fig. 1.7**), nearly 17% of total energy use for cooling prospected for 2050.

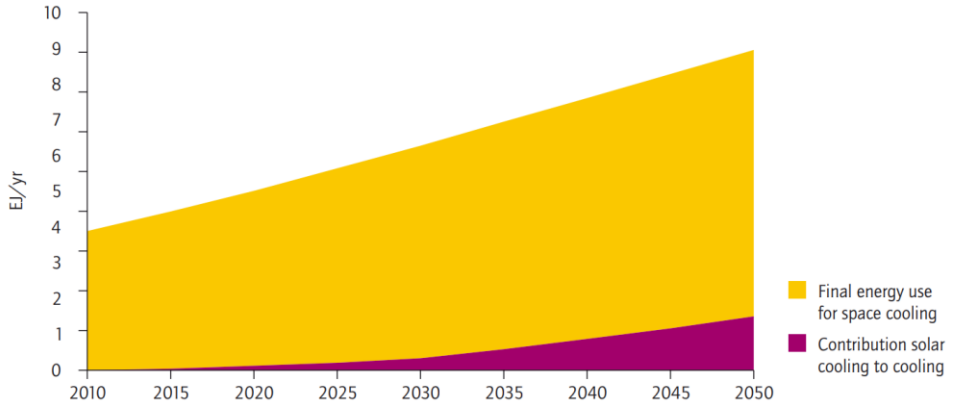


**Fig. 1.7** - IEA roadmap vision for solar cooling in relation to total final energy use for cooling by 2050 [28].

Although a rising demand for solar thermal cooling has been reported [29] only 1,350 solar cooling systems were estimated to be installed worldwide by the end of 2015 [30], of which around 80% were in Europe, mainly in Spain, Germany and Italy. Of these, 84% were closed systems (producing cold water) with absorption machines accounting for 71% and adsorption machines for 13% of installed units [27], while open systems (producing air conditioning) like desiccant evaporative cooling (DEC), both solid and liquid, accounted for 16% of the units.

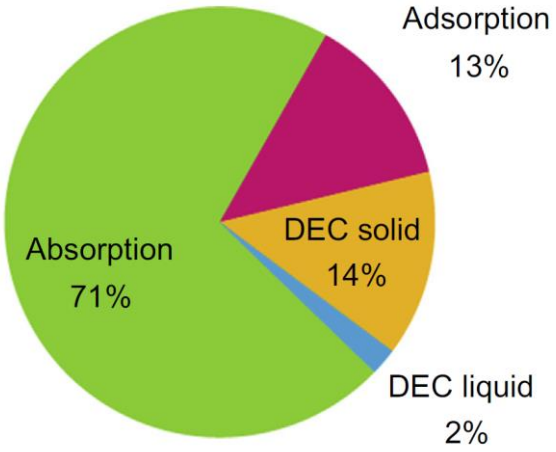


**Fig. 1.8 -** Market share of heat driven solar cooling systems in 2009 [27].

Hence, heat driven cooling technologies in general and in particular absorption cooling systems have so far been relatively niche technologies. Nevertheless, their market is growing with a reduction in their costs. During the period from 2007 to 2016, (even though not as rapidly as the cost of other technologies like solar photovoltaics) the costs of absorption pumps have been more than halved [25].
The main problem that these systems have is the variability of the availability of thermal energy to be used, as well as the variation of the required cooling demand. The number of hours energy is required is extremely variable on a seasonal and daily level, which greatly affects the economy of these systems, often making the economic comparison with compression systems extremely difficult. Moreover, these systems remain bulky and heavy and are more costly than traditional vapour compression systems. Clearly, further cost savings and efficiency improvements are needed to implement the technology on a much larger scale compared to the current level. Innovations are also needed to provide cooling solutions integrated with thermal storage and for their integration in district heating and cooling.

Many absorption pairs have been investigated [31], but two pairs are more commonly encountered: water-lithium bromide and ammonia-water. The first pair generally dominates the market (used in 98% of absorption machines around the world [29]) since it allows higher COP to be reached while the latter allows the production of cooling at negative temperatures and development of innovative new cycles for combined production of cooling and electricity [32].

Indeed, although characterized by low TRL, Technology Readiness Level, a possible ambitious solution to the problem of the variability of the required cooling load is represented by the use of integrated systems, in which mechanical, thermal and cooling power are produced within the same cycle, using binary mixtures.
This trend is confirmed by the implementation plan of ETIP SNET (European Technology and Innovation Platform for Smart Networks for the Energy Transition) in which heating and cooling and flexibility represent two of the 12 objectives to be implemented by 2030, within "Efficient energy use" block.
Research has focused on improving the performance of thermal cooling systems by combining power cycles, such as the Kalina cycle [33] or the Rankine cycle [34], with absorption cycles to produce both cooling and power using only one heat source rather than coupling two cycles in cascade. This can lead to an increased system efficiency and more effective usage of the heat source [35], as well as the mutualisation of components for vapour generation, condensation, pumping, etc. A combined absorption system producing not only refrigeration but also electricity could be better adapted to the whole range of energy demand, from only power to only cooling modes with intermediate operation modes producing different rations of the two products
Furthermore, the use of binary mixtures, has been reported to achieve high conversion efficiencies [36] thanks to an improved thermal matching with heat sources and sinks, reducing exergetic losses with respect to traditional heat exchange processes [37].

Ayou et al. [38] reviewed the main combined cooling and power architectures described in literature and distinguished two main categories: series [39,40] and parallel [41,42] architectures.
The first series architecture was proposed by Goswami et al. [7] as modification of the Kalina power cycle, improving the efficiency by the simultaneous production of power and cooling effect. On the other hand, parallel cycle architectures have not yet been widely investigated. Although possibly less efficient for simultaneous production of cooling and electricity, they should enable more flexibility to switch between production modes and be easier to implement.

In considerations of the above, research activities carried out in the framework of present doctoral thesis at the CEA INES in collaboration with the LOCIE appear to be particularly relevant and timely. Indeed, the work is focused on the development and on the experimental and numerical investigation of an absorption based cooling and power production cycle, using low temperature thermal energy.

## 1.2 Objectives of the work and methodology

The present thesis is focused on the development and on the experimental and numerical investigation of a thermodynamic cycle for the combined production of cooling and electricity. The work is strongly connected with the studies carried out within the framework of the project Carnot Energy of the Future “TRICYCLE” and has been supported by the European Union Horizon 2020 research and innovation program under the Marie Skłodowska-Curie grant agreement No 800945.

The study is based on an existing small capacity ammonia-water single stage absorption chiller of nominal desorber power of 10 kW and cooling power of 7 kW. The pre-industrial prototype was developed at CEA INES starting from 2012 [13] with the goal of redesigning components to optimize their performance and test innovative cycle architectures [43]. In addition, experimental tests conducted on the pilot plant served as a valuable source of data for the development and validation of numerical models [44]. The absorption chiller, extensively investigated in previous studies [29,45], uses low-temperature thermal energy (85-115 °C) thus simulating the use of medium-temperature solar energy achievable using low-concentration solar or waste heat from recovery systems.

The plant initially designed for solar cooling applications, has been modified by adding a parallel line feeding an axial micro turbine, for the production of electricity. This architecture is characterized by the fact that a strong interaction exists between the two production lines, hence the need to investigate the functioning of the machine as the two products output varies.

The overall objectives of the work encompass:
- in depth understanding of the functioning of the cycle through both experimental and numerical studies
- identification of the advantages, disadvantages, operating limits and technical challenges of the technology
- performance evaluation and positioning of the technology

The activity plan comprises experimental and numerical activities, both preceded by a comprehensive review of heat driven technologies and in particular of absorption cooling and power combined production architectures. This includes a theoretical analysis on the fundamentals of combined power and refrigeration absorption cycles and a reflection on the various performance criteria used in literature for the energetic and exergetic performance evaluations of these types of systems.

Results of the experimental study have allowed gathering less data than expected due to setbacks encountered during the development of the prototype. For this reason, alternative validation data sources have been used (CFD analysis for the validation of the turbine model, already available data from the absorption chiller prototype, etc.) However, experimental activities have focused on:

- setting up of the experimental prototype, including collaboration for the development of the expander, components and architecture choices, etc.
- characterisation of the turbine (influence of inlet conditions on treated mass flow rate and performance, influence of rotational speed, etc.)
- characterization of the complete cycle (study of stationary conditions, transient, start-up, mode switch, etc.)
- data analysis and treatment
- identification of limitations and possible improvements of the experimental plant

Performed numerical activities, on the other hand have included:

- development of a turbine model used for its performance analysis
- development of model of the combined cycle including a detailed model of the absorption chiller
- performance of steady-state simulation of the cycle to characterise the behaviour under different operating conditions
- identifications of limitations of the cycle and evaluation of possible improvements, particularly to increase flexibility of operation
- performance of a technical and exergoeconomic analysis of the machine
- optimization of components designs and of operational parameters
- evaluation of the scale-up of the system

The combination of experimental and numerical studies has enhanced the depth of the analysis by leveraging on their mutual complementarity.

# Chapter 2

# Low temperature power and heat driven cooling thermodynamic cycles

*Low temperature heat recovery could play a major role in achieving decarbonisation of energy systems. This chapter reviews electricity and cooling production technologies driven by thermal energy. Attention is drawn on Organic Rankine cycles and Kalina cycles for the production of cooling and absorption, adsorption and ejector refrigeration cycles for the production of cooling. Their combination could allow achieving higher performances and mutualising common components thus reducing the size and costs of the system. Combined production cycles may also represent a solution to the problem of the variability of the cooling demand throughout the year. The focus of this work is on absorption-based technologies of which different architectures are presented. The chapter is concluded by a discussion of research and technical challenges that need to be investigated for a successful development and diffusion of this technology.*

# 2.1 Introduction

Energy in the form of heat is present everywhere around us and is directly necessary in countless processes (direct heating, steam or hot water production and various industrial applications). Additionally, it can be converted in other forms of energy, like electricity or mechanical work.
The second law of thermodynamics dictates that all processes using energy to generate work must reject some waste heat. Sources of waste heat can vary in size and rejection temperatures, from small sources at low temperature like natural organisms, light bulbs or refrigeration systems, to larger sources like internal combustion engines and power stations. Waste heat has a lower value (i.e., a lower exergy) than the original energy source and hence is very often discarded. The same is valid for the heat obtained as a by-product in industrial processes.

However, waste heat recovery has a significant potential to increase the overall efficiency of systems. The use of residual heat improves the utilisation of the primary energy source, thus reducing the necessary energy input.
Possible end-uses of waste heat include electricity generation, cooling production, combined heat and power or combined cooling and power production and trigeneration. It should be highlighted that not only waste heat can be used in these applications, but also renewable heat, coming from solar and geothermal sources or biomass.

The potential electricity generation from the recovery of waste heat in energy intensive industries in Europe is between 13,000 and 20,000 GWh/year (depending on the operating hours) [46].
According to a study conducted on the industrial energy consumption in 2008 [47] most of the waste heat is discharged at low temperature (66%) below 200 °C (**Fig. 2.1**). Concerning France, the ADEME (French Environment and Energy Management Agency) estimated that the industrial waste heat available in France represents 109.5 TWh annually, corresponding to 36% of the thermal needs the industrial sector itself. According to this estimate, 51.6% of this waste heat is available at temperatures below 100 °C and 24.1% at temperatures between 100 and 200 °C. Hence, low temperature heat utilisation has become a priority.

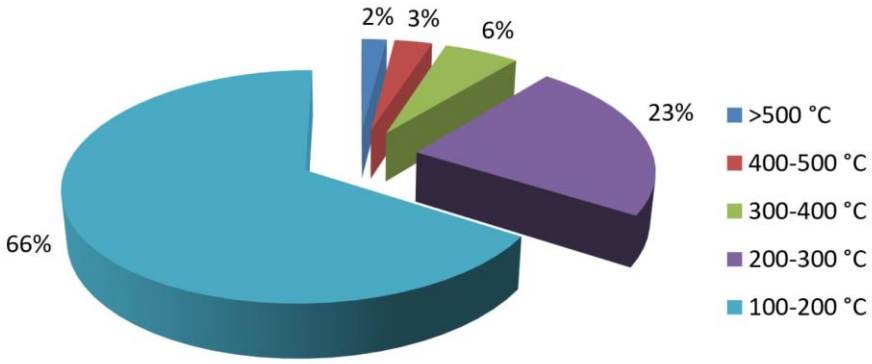


**Fig. 2.1 -** Waste heat temperature distribution in industry in 2008 in France (60TWh) [48].

This chapter presents low temperature power and cooling production cycles driven by low temperature thermal energy. Power production thermodynamic cycles are presented first, followed by cooling and combined cooling and power production cycles.

# 2.2 Low temperature power production cycles

The conversion of low temperature heat into electricity, generally using renewable or waste energy is currently object of intense study for its implications on energy efficiency and distributed energy production.
Many systems are available to generate electricity directly from heat [49]. These technologies include the use of thermoelectric, piezoelectric, thermionic and thermo-photovoltaic devices for electricity generation [49]. Stirling engines appear less suited for heat recovery below 300 °C [50]. Despite the fact that a few of the aforementioned

technologies have already undergone the prototype phase with encouraging results, none of these is already widely used in industry [51].
On the other hand, the use of thermodynamic cycles enables a cost effective [52] and proven way to convert heat into mechanical work, which can be then used to generate electricity. With this purpose, the two most promising cycles are arguably the well-known Organic Rankine Cycle (ORC) and the Kalina Cycle (KC).

In this section these two cycles, possible fluids to drive and expander characteristics and selection criteria are discussed.

### 2.2.1 Organic Rankine cycles

The Organic Rankine Cycle (ORC) works on the principle of the Rankine cycle, but instead of steam, the system uses organic substances with low boiling points and high vapour pressures as working fluid to generate power. This cycle consists of two adiabatic transformations, the first in the pump and the second in the expander, and by two isobar transformations, one in the evaporator and the other in the condenser as shown in **Fig. 2.2**.

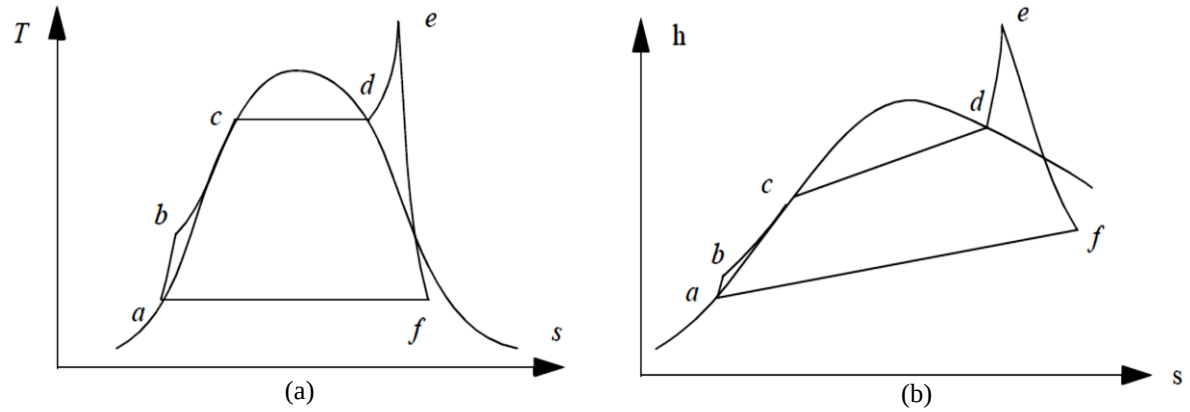


**Fig. 2.2 -** T-s (a) and h-s (b) diagram of a Rankine cycle. Adapted from [53].

Classic Rankine cycle steam plants, introduced in the second half of the nineteenth century, were mainly applied for the production of electricity in the form of large power plants. These plants can reach remarkable performances thanks to the small compression work of a liquid with reduced specific volume, transformed into vapour with a high specific volume, thus providing a considerable expansion work.
The motor fluid of this cycle is notoriously water and the temperatures and pressures involved are very high, in the range of around 40-100 bar and 350-620 ° C at the turbine inlet.
The ORC is a technology that uses organic fluids to perform the same cycle presented in **Fig. 2.3** However, working pressures and temperatures are lower and do not exceed 40-50 bar and 200-300 °C, and ORCs can also be used to exploit heat at much lower temperatures (80-100°).
Multi MWe ORC installations exist, using heat from a geothermal source, biomass or recovery waste energy from industrial processes [53], but these ORCs are also available at the scale of kilowatts, making them suitable for applications in both domestic and small industries [54]. Moreover, being less complex and requiring less maintenance than classical steam cycles, the use of these systems for small and very small scales is favoured.

The advantage of ORC cycles lies in the additional degree of freedom that the choice of fluid allows. Given the wide range of fluids available, it is possible to tailor the cycle to the available heat source (**Fig. 2.4)**.
The layout of the Organic Rankine Cycle is usually simpler than the traditional Rankine steam cycle due to the working fluids used in this cycle. Fluids can be classified as dry, isentropic, or wet fluid depending on the slope of the saturation vapour curve on a T-s diagram (**Fig. 2.4**). Vapour saturation curve of wet fluid (e.g., water or ammonia) has a negative slope, a dry fluid (e.g., n-pentane) has a positive slope, while an isentropic (e.g., R245fa) has an almost vertical slope. Since most of the fluids used in ORCs are either dry or isentropic (with no risk of having a two-phase mixture after expansion), usually there is no steam super heater and a single heat exchanger can be used to carry out the three evaporation phases: preheating, vaporization and overheating. Since also the bleeding from the turbine are not generally solutions used for ORC, the variations on the architecture of the cycle are rather limited. The basic cycle configuration is shown in **Fig. 2.3** and is very similar to the traditional steam cycle.

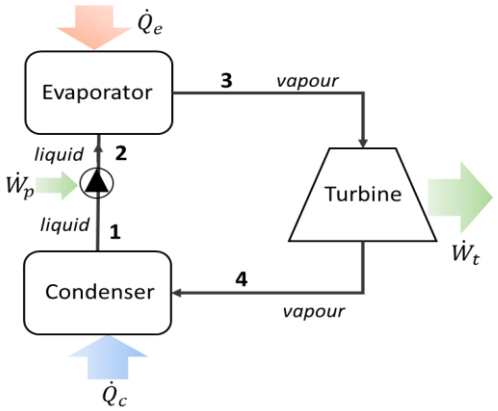


**Fig. 2.3 -** ORC working principle.

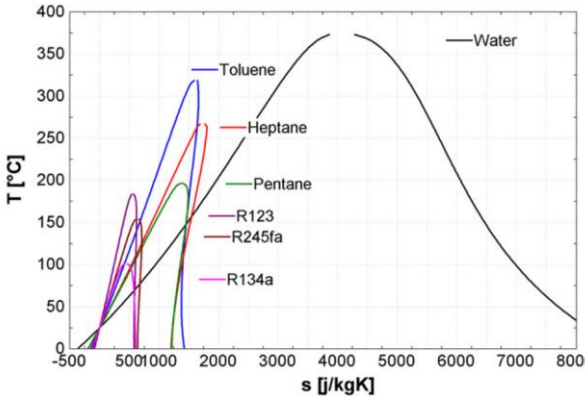


**Fig. 2.4 -** T-s diagram of water and various common ORC fluids [55].

A simple modification to the standard configuration leads to the configuration of the regenerative cycle [56]. This design includes the use of an internal heat exchanger, the purpose of which is to recover heat from the turbine outlet to heat up the working fluid before the evaporator inlet. If other parameters are constant, this simple change of layout (only one heat exchanger is added) allows a considerable increase of the cycle efficiency.

## *Transcritical Organic Rankine cycle*

In the main current industrial applications, the steam is saturated or slightly overheated; however, supercritical cycles have been gaining popularity. A transcritical (sometimes also referred to as supercritical) cycle (**Fig. 2.5)** is a cycle with a maximum pressure higher than the critical one [57]. The efficiency of a thermodynamic cycle is directly linked to the efficiency of the heat exchange processes. In supercritical cycles, the absence of a biphasic region in the evaporation phase, allows a better match with the heat source, leading to an increase in the overall exergetic efficiency.

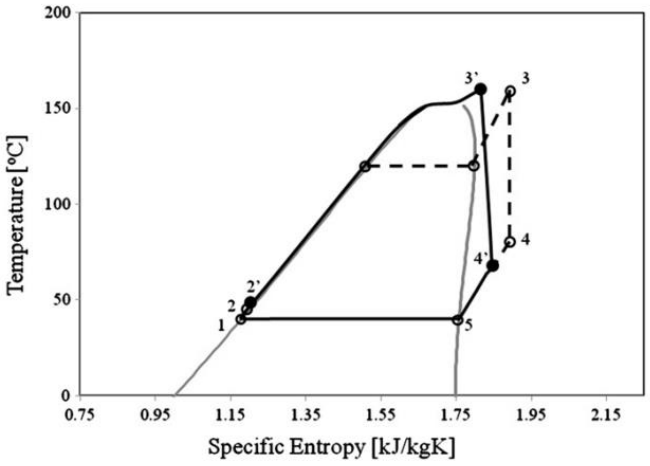


**Fig. 2.5 -** Subcritical (dotted line) and transcritical (bold line) ORC. Example of R245fa [58].

For supercritical Rankine cycles, organic fluids such as isobutene, propane, propylene, R134a and R245fa have been suggested [59], but $CO_2$ also has interesting qualities such as: low critical temperature, safety, thermal stability, low environmental impact and low cost [60].
Despite the higher attainable efficiencies, supercritical cycles generally have higher pressures than the subcritical cycles and more expensive devices are required in addition to the need of a greater pump work.

### *Working fluids for ORCs*

The possibility of selecting the most appropriate working fluid for a specific application is one of the key features of the Organic Rankine Cycle technology [61]. The best performances of ORC cycles are obtained by using isentropic and dry fluids [62].
The choice of the organic fluid is based not only on its thermo-physical properties, but also on the safety requirements and on the costs of use. The main selection criteria are [63]: good thermodynamic and physical properties (high density, low liquid specific heat and high latent heat), thermal stability, low ozone depleting potential (ODP) and global warming potential (GWP), safety, availability and cost.
More than 50 working fluids have been suggested in literature [63], some of which have already been phased out due to environmental regulations. Such a wide range of candidates is a proof of the fact that no best fluid meeting all the criteria aforementioned exists and compromise must be made when selecting working fluids.

Typical working fluids are represented by low-boiling refrigerants such as chlorofluorocarbons (CFC), hydrofluocarbons (HFC), hydro-chlorofluorocarbons (HCFC). Montreal Protocol (1987), Kyoto Protocol (1997), Paris agreement (2015) and Kigali amendment (2016) have forced the phase-down of CFCs, HCFCs and more recently of most HFCs. EU's F-gas regulation (EU regulation n° 517/2014) imposes GWP limits for the fluids used in different applications. Possible replacements fluids include:

- Natural fluids: HCs (hydrocarbons) such as R290 (propane), R600a (isobutane) and R1270 (propylene) and inorganic refrigerants such as $CO_2$ (carbon dioxide) and R717 (ammonia).
- HFOs (hydro-fluoro-elements) that are unsaturated HFCs, such as R1234yf and R1234ze(Z).
- HFEs (hydrofluoroether) such as HFE7000, HFE7100
- Fluoroketones such as NOVEC649
- Blends like HFC/HC blends, HC/HC blends or HFC/HFO blends.

In particular, a way to improve an existing ORC performance is the use of zeotropic mixture as the working fluid, a blend of two or more pure fluids, characterized by a non-isothermal phase-change at constant pressure.
This temperature variation during the phase change process, also called the temperature glide, could decrease the temperature difference between the working fluid and the heat source and heat sink, thus increasing the exergetic efficiency of the cycle [12]. Despite the advantages achievable with mixtures, their use in ORCs is still extremely limited [57] because of a number of difficulties which make their use less practical and affordable than the use of a pure fluid. These include the change of composition of the mixture if leakage occurs or the fractionating of the zeotropic mixture during heat transfer limiting the allowable temperature glide and hence reducing the first law efficiency of the system.

## 2.2.2 Kalina cycles

Similar to the Organic Rankine cycle, the Kalina cycle (named after the Russian engineer Alexander Kalina), is a thermodynamic cycle used to convert thermal energy into mechanical power. The basic Kalina cycle is essentially a modified Rankine cycle that uses the mixture of at least two different compounds as the working fluid: generally, a mixture of ammonia and water, a zeotropic mixture.

**Table 2.1 -** Properties of ammonia and water.

| Fluid | Molecular weight [kg/kmol] | Critical temperature [°C] | Critical pressure [bar] | Boiling point at 1.013 bar [°C] | Freezing point at 1.013 bar [°C] | Latent heat at 10 °C [kJ/kg] |
|---|---|---|---|---|---|---|
| Ammonia | 17 | 101,1 | 40,59 | -33,3 | - 77,7 | 1226.1 |
| Water | 18 | 373,9 | 220,64 | 100,0 | 0,0 | 2477.2 |

Water and ammonia have similar molecular weight, but quite different thermo-physical characteristics as presented in **Table 2.1**. For example, ammonia is a more volatile component than water, having a lower boiling temperature. Hence, for this mixture, temperature and composition vary continuously during the evaporation and condensation process. The diagram in **Fig. 2.6** shows that, depending on the mixture original composition, the temperature glide during evaporation can be very important. Additionally, the vapour produced at lower temperatures in the first phases of the evaporation process (point b) is purer than the vapour produced at higher temperature in the last stages of the evaporation process (point f). More details on the ammonia water mixture will be given in *Section 2.3* when discussing ammonia-water absorption machines.

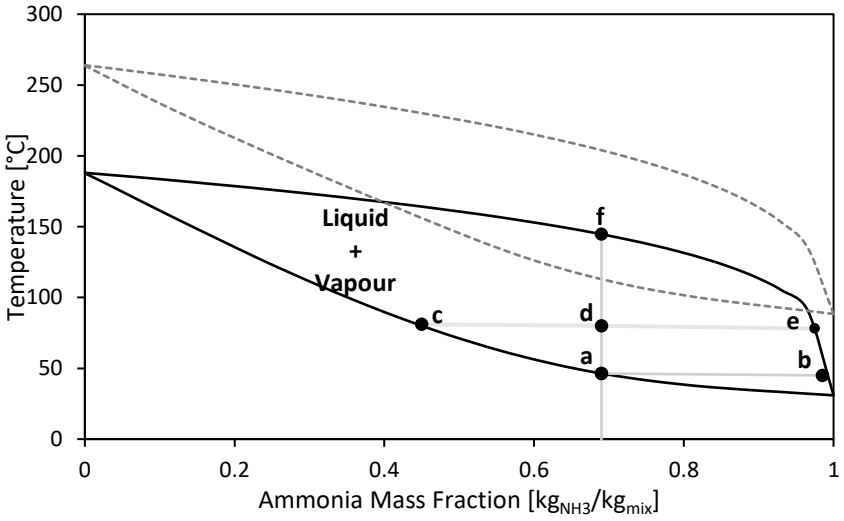


**Fig. 2.6 -** Isobaric phase transition of a zeotropic mixture (ammonia-water).

A family of unique Kalina Cycle systems (KCSs) exist, each designed for specific applications and is identified by a unique system number such as KCS5 (for direct fuel-fired plants), KCS34 (for low-to-medium temperature geothermal resources, as a topping thermodynamic cycle prior to district heating), etc. [38].
**Fig. 2.7** shows a simplified diagram [64] of the Kalina cycle. The mixture of ammonia and water passes through the heat recovery unit before reaching the generator. Here the fluid is separated in an ammonia rich vapour at high pressure and temperature, and a poor liquid mixture. The generator also includes a distillation column or a similar device, to achieve the require purity of the ammonia vapour. The desorbed vapour enters then the superheater, where its temperature is increased before the expansion in the turbine to generate mechanical work. After leaving the turbine, the vapour enters the absorber where it is absorbed in the poor solution with an exothermic reaction. The rich solution produced is pumped again through the heat recovery unit and the cycle continues in this manner.

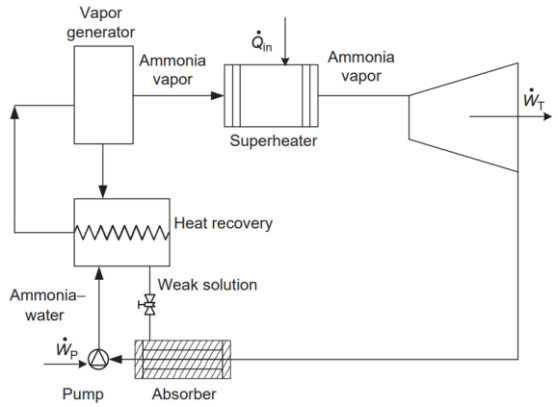


**Fig. 2.7 -** Kalina cycle diagram [64].

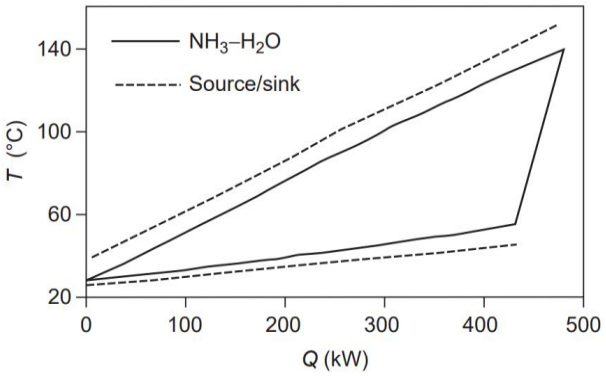


**Fig. 2.8 -** Kalina cycle temperature profile [64].

As explained before, the use of zeotropic mixtures produces a better thermal match between heat sources and working fluid **Fig. 2.8**. The thermal performances of steam Rankine and Kalina cycles when both are used as bottoming cycles (using waste heat from another cycle) with the same thermal boundary conditions were compared [65]. Using the Kalina cycle leads to 10–20% improvement in the thermal efficiency, while Kalina et al. [66] reported a possible increase of 20%.
However, compared to the Rankine cycle, the Kalina cycle is more complex and requires more components (distillation column, internal heat exchangers, etc.). Hence, although the Kalina cycle presents some theoretical advantages when compared to the Rankine cycle, and it has been intensively studied [67], this technology has not gained market favor yet.

### 2.2.3 Expanders for power cycles

In both Organic Rankine and Kalina cycles the expansion device is of fundamental importance for the performance and efficiency of the cycle [68]. Expanders are generally divided into two categories: volumetric expanders and

turbomachines. Volumetric expanders comprise reciprocal piston, screw, roots and scroll expanders, while turbomachines include axial turbines, radial inflow turbines and radial outflow turbines.

Volumetric or positive displacement expanders operate on a principle of force application on a movable mechanical component to extract power. The pressurized fluid is introduced into a chamber and the chamber volume is increased as the compressed fluid applies a net force. When the chamber reaches its maximum expansion volume, the low-pressure fluid is released out of expander. Most of the positive displacement expander technologies usually exhibit a built-in volume ratio (i.e., a fixed ratio between the volume of the chamber at the beginning and at the end of the expansion) characterising the volume expansion rate. Volumetric machines are often equipped with valves to control the inlet and outlet flow of fluid and synchronization with expanding chamber.

In turbomachine type expanders, the work exchange is brought about by dynamic action, without a closed boundary preventing the free flow of the fluid [69]. Essentially, a rotating blade row, a rotor, reduces the stagnation enthalpy (closely related to the pressure changes) of the fluid moving through it by subtracting work from the flow, depending upon the effect required of the machine. Turbines are currently the most common expander choice of typical ORC and Kalina cycles. The specific properties of organic fluids with respect to water and ammonia result in unconventional configurations of ORC turbines [70]. In general, the enthalpy drop during expansion is inversely proportional to the molecular weight and hence the specific work exchanged by organic fluids with turbines is relatively small with respect to water or ammonia. Additionally, in the case of organic fluids, larger mass flow rates can be used resulting in acceptable sizes with respect to the miniaturized configurations corresponding to water. Given its high latent heat, the same is not valid for ammonia.
Finally, because expansion ratios are generally high in these cycles the occurrence of shock waves and choked flow is very common, further complicating the design of expanders.
Major technologies of expanders and selection criteria are discussed in this section.

## *Axial turbines*

For larger power outputs (from a few hundred $kW_{el}$ to a few $MW_{el}$) axial turbines are generally the preferred choice [71]. In axial turbines the flow of the working fluid is parallel to the shaft. A set of static guide vanes or nozzle vanes accelerates and adds swirl to the fluid and directs it to the rotor, where enthalpy drop of the fluid is converted into rotating mechanical energy. With reference to **Fig. 2.9** Euler's equation [69] enables to calculate the ideal work of a turbine stage can be written as:

$$Work_{id} = U_2 \cdot C_2 \cdot sin(\alpha_2) - U_3 \cdot C_3 \cdot sin(\alpha_3) = U \cdot (C_{u,2} - C_{u,3}) \quad (2.1)$$

Here state point 2 and 3 indicate respectively the rotor inlet and outlet, U is the blade speed, C is the absolute velocity, $\alpha$ its angle and $C_u$ is the tangential component of the absolute velocity. Since for a radial turbine the radius remains the same between rotor inlet and outlet, hence $U_2 = U_3 = U$.

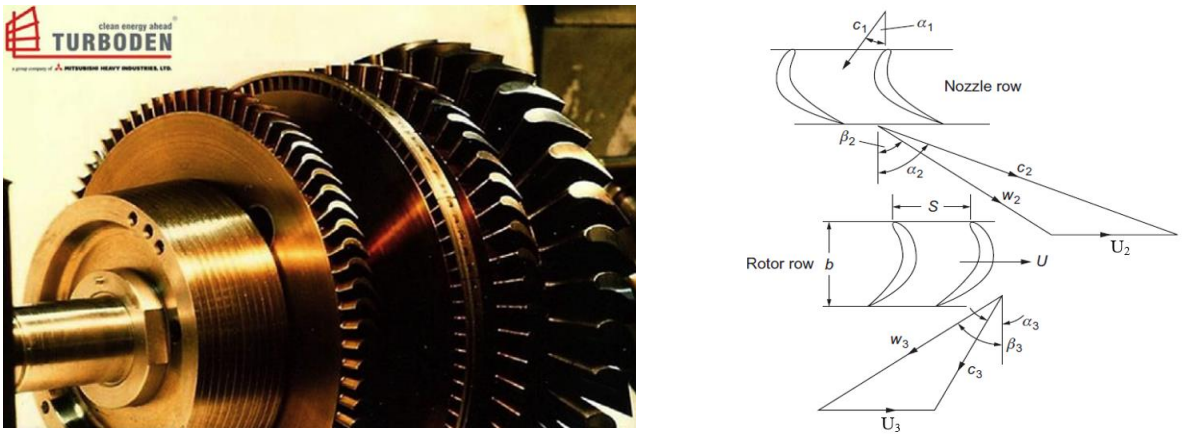


**Fig. 2.9 -** Example of ORC axial turbine [71] and velocities triangle [69].

Axial turbines are used to drive most of the generators producing electricity world-wide and were the first type of expanders used in ORCs [71]. However, when working with fluids other than water, these turbines require important modifications in their design. Fewer stages are required and single-stage turbines are often encountered.

ORC fluids tend to have the low speed of sound, consequently high Mach numbers can be reached, highly increasing irreversibilities.

### *Radial turbines*

For low electric power output (from tens to hundreds of $kW_{el}$) the choice of single-stage radial inward turbines (**Fig. 2.10**) is widely suggested [70]. They consist of volute, stator vanes and rotor blades and, in some applications, a diffuser recovering kinetic energy at the rotor exit and converting it into static pressure.
The flow enters the volute where it is accelerated before entering the nozzle vanes due to the reduced cross-section area and is distributed evenly around the periphery of the stator inlet. After leaving the volute, the flow enters the stator vane where it is further expanded and turned to enter the rotor blades in the optimum direction with the necessary tangential velocity.
In application where expansion ratios are relatively low and cost and simplicity are important, turbines without stator vanes (relying only on the volute) are often used. For turbines operating at higher expansion ratios the necessary rotor inlet speed becomes so large that nozzle vanes are essentials.

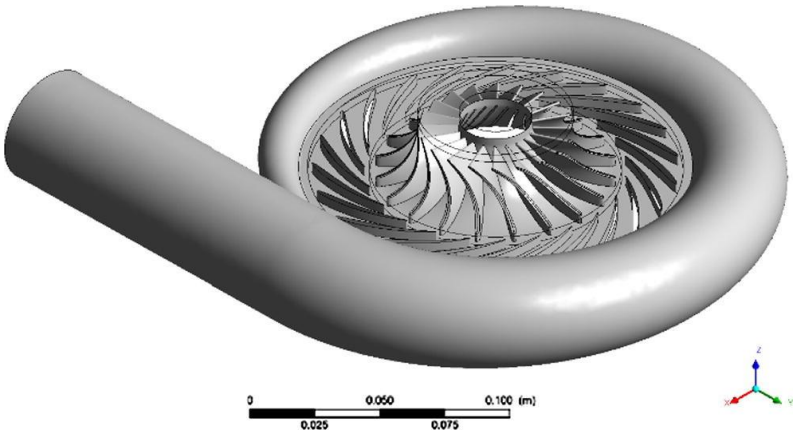


**Fig. 2.10 -** Radial inflow turbine [72].

Reasons to prefer a radial turbine over an axial machine may be the cost (a radial turbine rotor can be manufactured as a one-piece casting while an axial turbine often demand separate blades and disks). Additionally, a radial turbine can deliver higher specific power than an axial machine thus probably implying smaller or fewer stages. The reason for this can be found in **Eq.**(**2.1**). Indeed, since in a radial inflow turbine the radius at outlet is smaller than the radius at inlet, $U_3$ is smaller than $U_2$, allowing to increase the specific work production.

More recently, the use of radial outflow turbines has also been proposed to overcome some of the limitations of working with non-conventional fluids. Some studies suggest that these configuration could guarantee good aerodynamic performance at nominal point and flexibility at partial loads with a low mechanical complexity [73]. However, development of optimal blade geometries is still ongoing and further studies are needed.

### *Screw expanders*

The screw expander (**Fig. 2.11**) consists of two helical rotors with reverse pitch that rotate at a certain distance from one another inside a casing. As they rotate, the volume trapped between the rotors and the casing changes. If fluid is admitted into this space at one end of the rotors, its volume will increase until it is finally expelled from the opposite side of the rotors. Power is transferred between the fluid and the rotor shafts by pressure on the rotors, which changes with the fluid volume.
The presence of liquid in the expander has little effect on its mode of operation or efficiency. However, these machines require a gearbox to couple them to the generator and normally require a somewhat complex oil lubrication system. A further obstacle is posed by the difficulty to obtain very small clearances between the rotors to avoid excessive leakage losses. In the 70- 450 mm diameter range, it is possible to use available machine tools

designed specifically for rotor manufacture, but for greater diameters, the machining operation becomes too complex [74]. Consequently, few examples of use of this device exist in small ORC systems [75].

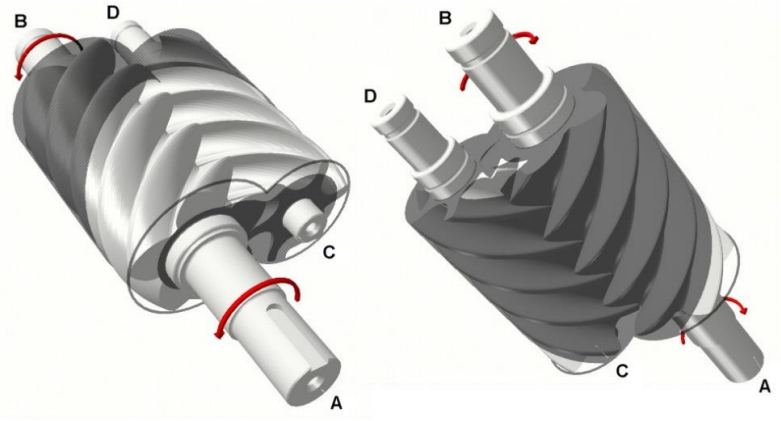


**Fig. 2.11 -** Screw expander [74].

## *Rotary expanders*

Rotary vane expanders (**Fig. 2.12**) consist of a cylindrical housing (stator) in which a rotor is in motion eccentrically with respect to the stator [76]. Slots are spread out all over the rotor and allow the insertion of vanes that are pushed out by a spring or similar mechanisms. The vanes, pressed against the housing, define the working chambers. When that chamber is no longer in contact with the inlet suction port, the expansion process begins, and ends when the chamber faces the outlet exhaust port.

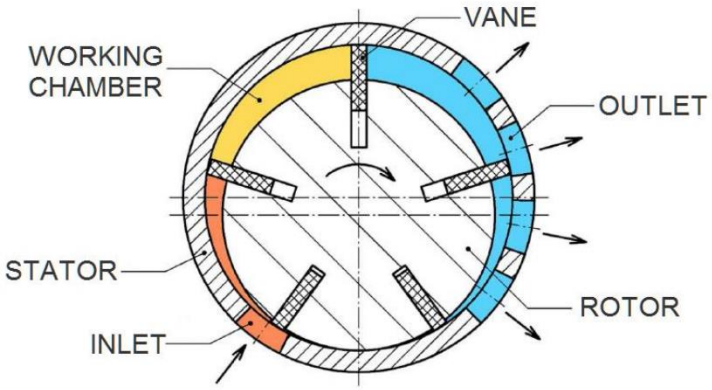


**Fig. 2.12 -** Rotary vane expander [77].

The design of this expander is very simple and of low production costs compared to other expander concepts [78]. Some advantages of these machines are flat operating efficiency curves over a wide range and the ability to operate in the presence of liquids and wet vapours and little lubrication requirements [79]. Built-in volume ratios commonly encountered are in the range of 2-8.5 [79].
Generally, on these machines, the maximum tolerable pressure is about 10 bar and the rotation speed is around 3-4,000 rpm due to the high inertia brought by the offset of the rotor [76]. Additionally, similarly to most volumetric expanders, vane machines are often limited in temperatures and suffer from high leakage and friction losses.

## *Piston expanders*

The crank train mechanism (**Fig. 2.13**), used in radial piston expanders, is similar to the mechanism used in internal combustion engines and relies on the use of a crankshaft connected to pistons. Steam enters the chambers by turns and expands in order to generate mechanical work. The flow into the cylinder is controlled by gliding valves.

Piston (or reciprocating) expanders can achieve larger volume ratios (typically ranging from 6 to 14) than other volumetric expanders [32] and operate under high supply pressures and temperatures [80]. Indeed, the possibility of using automatic adjusting flip valves allows variating the volume ratio to adapt it to the actual expansion ratio. They also tolerate well the presence of wet vapour and for this reason they have been often used when variability of the source does not allow to control the wetness of the vapour entering the expander, as is the case for ORCs for on-road-vehicle applications where reciprocating engines have often been used [68].
Studies [81] have demonstrated that reciprocating expanders can perform efficiently under large pressure ratios where they have better performances than other volumetric expanders like scroll expanders.
However, piston expanders are complex devices, with high friction losses due to a large number of interacting surfaces. Since lubrication is difficult, reliability is often an issue and manufacturing costs are relatively high.

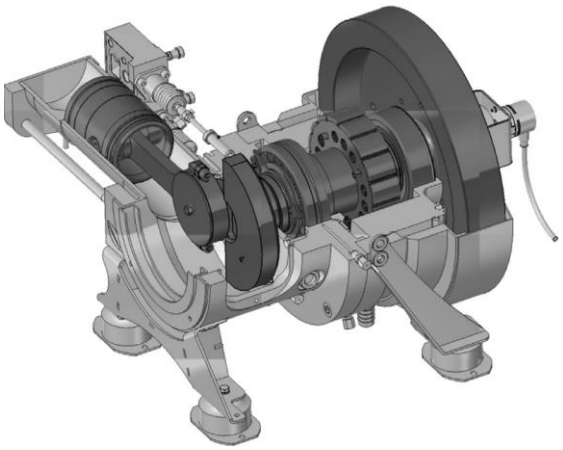

**Fig. 2.13 -** Piston expander [82].

## *Scroll expanders*

A scroll expander is composed of two involute spirals, or scrolls (a moving and a fixed one), having the same shape and rotated of 180 degrees with respect to each other (**Fig. 2.14)** [83].
In operation, one scroll remains fixed while the other is attached to an eccentric that drives a generator shaft.
The moving scroll orbits without rotation around the fixed one, creating gas pockets where the high-pressure working fluid is trapped. The small pockets formed when the gas enters the expander follow the spiral outward moving towards the periphery and enlarge in size until the discharge port.
Absence of valves, few moving parts, low rotational speeds and the low cost of scroll expanders are some of the reasons why they have gained significant interest. Additionally, these machines have high reliability and smooth, continuous and quiet working.

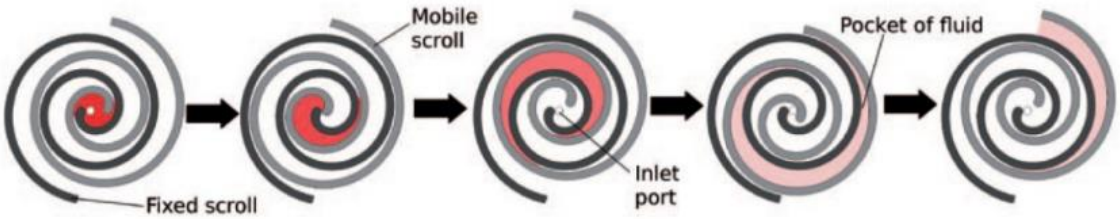


**Fig. 2.14 -** Scroll expander working principle [83].

However, scroll expanders present the typical drawbacks of volumetric expanders. In addition to a complex geometry and a demanding machining process, scrolls expanders require a tight manufacturing tolerance to minimise leakage area and avoid very strong performance penalizations. Indeed, leakages are, together with mechanical friction, the primary source of loss in scrolls [33]. Scroll expanders usually have moderate built-in volume ratios, between 3.5 and 5 and hence are more adapted to organic fluids than to water [76].

## *Expander selection*

Many parameters need to be considered when selecting an expander such as high isentropic efficiency, pressure ratio, power output, lubrication requirements, complexity, rotational speed, dynamic balance, reliability and cost [68]. Other important selection criteria are working temperatures and pressures, leakages, noise and safety.

Turbines are used in a wide range, from a few $kW_{el}$ to more than a $MW_{el}$ guaranteeing high performance but are complex to design. On the other hand, volumetric machines received a large interest for small-scale applications since volumetric compressors can be adapted to work as expanders [84], avoiding dedicated design phase.

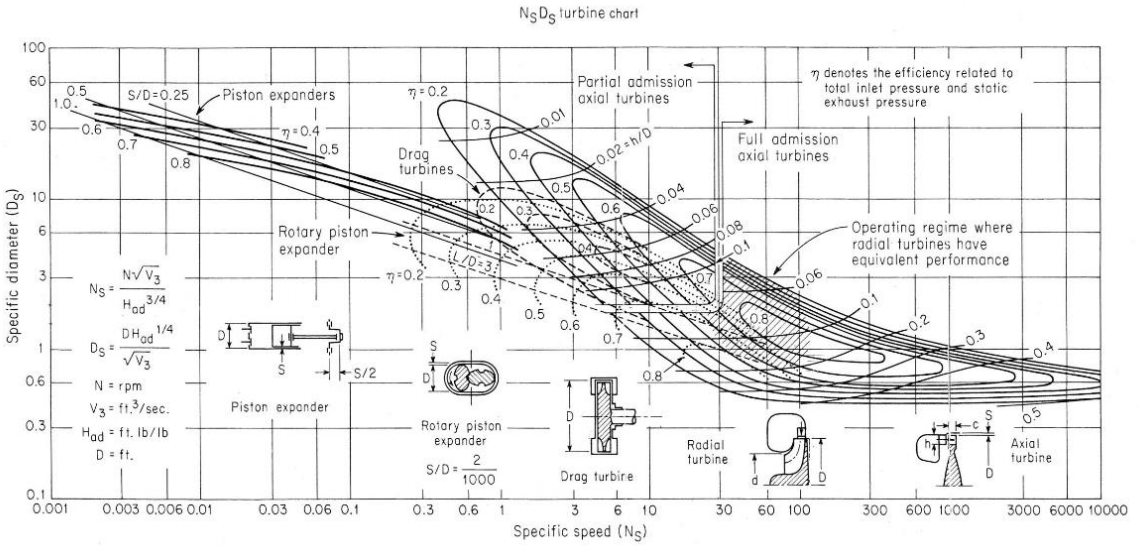


**Fig. 2.15** – Balje's $N_s$-$D_s$ turbine chart [85].

The similitude theory and Balje's performance chart can help with the choice of expander for a specific application. Similitude considerations show that only four parameters are needed to fully describe the characteristics of turbomachines handling compressible fluids; namely, the Mach number, the Reynolds number, and the specific speed and diameter of the machine [85]. Fully turbulent flows ($Re > 10^6$), generally occurring in turbomachines, make it possible to neglect the effects of the Reynolds number on turbomachinery efficiency while the effect on efficiency of the Mach number can only be neglected for Mach < 0.49.
The Balje diagram, illustrated in **Fig. 2.15**, provides the specific speed $N_s$ and diameter $D_s$ range at the design operation point for different types of expanders. The selection process requires a preliminary evaluation of $N_s$ and $D_s$ whose calculation implies knowledge of the type of fluid, mass flow rate, inlet temperature and pressure and outlet pressure as shown in **Eq. (2.2)** and **Eq. (2.3)**:

$$N_s = \omega \cdot \frac{\sqrt{\dot{m}/\rho_{\text{fluid}}}}{(\Delta h_{is})^{3/4}} \tag{2.2}$$

$$D_s = D \cdot \frac{(\Delta h_{is})^{1/4}}{\sqrt{\dot{m}/\rho_{\text{fluid}}}} \tag{2.3}$$

Landelle and Tauveron [86] developed and open-access database collecting more than 100 ORC experimental facilities from about 175 scientific literature references. The database shows that in the reviewed experimental installations, turbomachines cover almost all range of power scale, but particularly at small scale, require high rotational speed. Volumetric expanders have much lower rotational speed and are generally found only at smaller scale, rarely above 10 $kW_{el.}$ While they all have similar rotational speed and power output (**Fig. 2.16**), significant differences in the pressure ratio range are found, in accordance with technical limitations highlighted in their description. Expanders' efficiency strongly increases with their scale. Turbines are the preferred choice for larger applications, screw expanders are found in the range of 5-50 $kW_{el}$, while rotary and scroll are common below 5 $kW_{el}$, with scrolls achieving higher performances, as shown in **Fig. 2.17**.

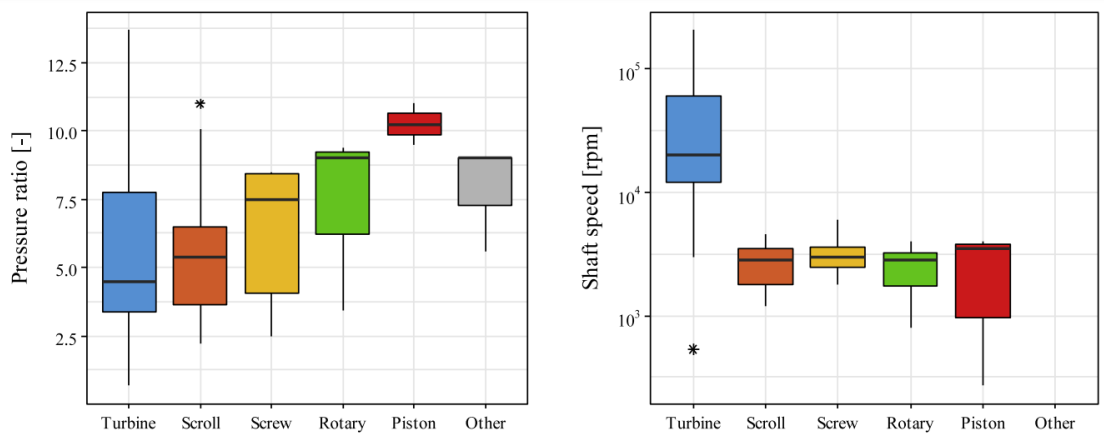


**Fig. 2.16** Pressure ratio and shaft speed of expanders used in experimental facilities [87].

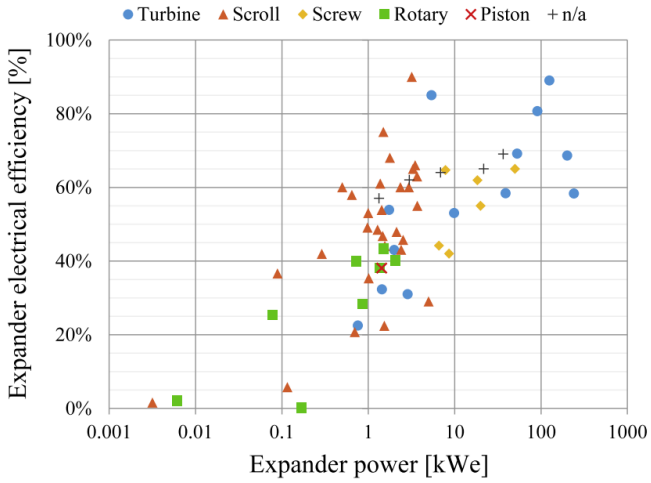


**Fig. 2.17** Electric power and efficiency map of expanders used in experimental facilities [87].

Not many examples of Kalina cycles exist in industrial applications, but they are however of particular interest to this work given the use of the ammonia-water mixture as a working fluid. Almost all existing cycles integrate a turbine and are applied to big geothermal installation of the size of the $MW_{el}$. Canoga Park was the first large scale Kalina plant commissioned in 1989 and integrating a radial inflow turbine, preferred to an axial one because of the low volumetric flow rate. The only major materials challenge reported was with the labyrinth seals for the steam turbine and the plant operated for more than 5 years.
Probably the most famous Kalina power plant is, however, the Husavik geothermal plant [88], opened in the year 2000. From its start-up, the plant experienced severe corrosion problems affecting the turbine and the nozzle vanes, causing repeated shutdowns of the plant. The original turbine was replaced in 2004 and no further corrosion problem was experienced until 2008 when, for unclear reasons, the turbine failed catastrophically. Poor water quality control and not compliance with operational guidelines have also been identified as significant contributors to the operational difficulties.
This example shows that, even if there are precedents of long-term successful implementation of Kalina cycles, the corrosiveness of the ammonia water-mixture requires the development of adapted solutions and the use of appropriate materials for all the parts of the turbine.

### 2.2.4 Performance parameters

In the case of power production cycles, first law efficiency is defined as the ratio of net useful power production over the available thermal input at the evaporator:

$$\eta_{I,power} = \frac{\dot{W}_{t,elec-}\dot{W}_{p,elec}}{\dot{Q}_e} \tag{2.4}$$

The definition of **Eq. (2.4)** does not take into account the real value of the thermal power input at the evaporator. To do so, a second law efficiency can be defined as:

$$\eta_{II} = \frac{\eta_{I,power}}{\eta_{I,Carnot}} \tag{2.5}$$

where $\eta_{I,Carnot} = 1 - T_c/T_e$. A very similar concept is that of exergetic efficiency defined as:

$$\eta_{ex} = \frac{\dot{W}_{t,elec} - \dot{W}_{p,elec}}{\dot{E}x_e} \tag{2.6}$$

The concepts of second law efficiency, exergy and exergetic efficiency will be detailed in *Section 5.2*.
Additionally, in the case of power production cycles, the characterization of the performance of the expander is of particular importance. Normally the isentropic and adiabatic power produced by an expander are defined respectively as:

$$\dot{W}_{is} = \dot{m} \cdot [h(T_{in}, P_{in}) - h(s_{in}, P_{out})] \tag{2.7}$$
$$\dot{W}_{ad} = \dot{m} \cdot [h(T_{in}, P_{in}) - h(T_{out}, P_{out})] \tag{2.8}$$

The adiabaticity approximation is generally valid for large turbo-expanders, but this is normally not the case for volumetric expanders [89] or micro-turbines [87]. Hence, the electrical efficiency is more adapted than isentropic efficiency for the comparison of different expanders.

$$\eta_{is} = \dot{W}_{t,ad} / \dot{W}_{t,is} \tag{2.9}$$
$$\eta_{elec} = \dot{W}_{t,elec} / \dot{W}_{t,is} \tag{2.10}$$

### 2.2.5 Applications and market

As previously stated, only few examples of Kalina plant exist around the world. On the other hand, ORCs are a well-known technology since the early 1970s.
This technology becomes more profitable than steam Rankine cycles for limited electrical power (generally below 1 $MW_{el}$) and low temperatures (85-450 °C). In December 2016, total installed capacity of ORC technology was approximately 2,701 MW, distributed over 1754 units (**Fig. 2.18**) [90]. The largest number of plants are installed for biomass waste heat recovery applications (1,073 plants for a total power of 376 MW), followed by geothermal (337 plants for a total power of 2,021 MW) and biomass (332 plants for a total of 301 MW).

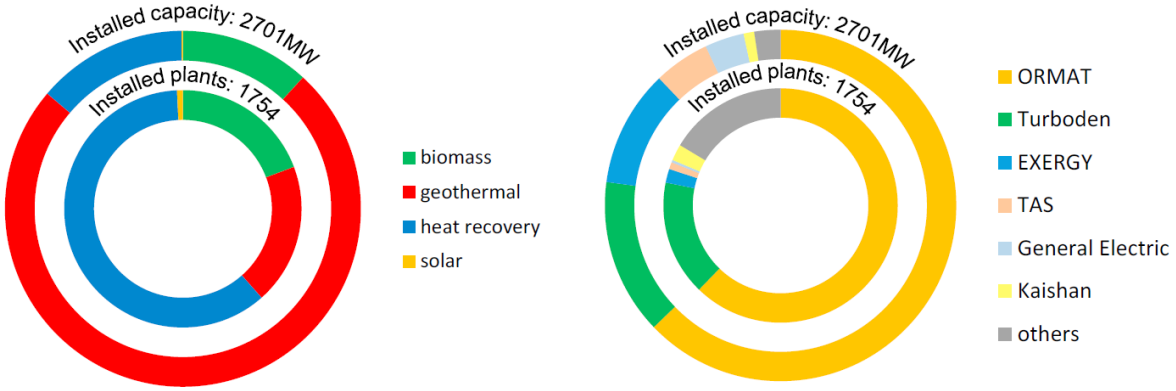


**Fig. 2.18** – Total ORCs installed capacity per application and per manufacturer [90].

With respect to 2016, at the end of 2020 overall ORC market had increased by 40% in terms of installed capacity, (4.07 GW) and by 46% (+851) in terms of installed plants. Regarding the capacity increase between 2016 and 2020, the largest increase is due to geothermal application (+970 MW, +45%), while waste heat systems have the largest growth concerning the number of installed systems (628 plants, + 207%) [91].
The market is dominated by few companies (ORMAT, Turboden, Exergy and TAS) with high capital intensity and consolidated know-how. Most other manufacturers focus on small energy recovery applications with products ranging from 10 to 150 $kW_{el}$. Two French companies are currently active in the ORC market, Enogia operating on small sizes and Enertime offering machines of several megawatts. Very few examples of solar applications exist.

## 2.3 Absorption refrigeration cycles

The term "heat pump" refers to a device or a machine able to allow the transfer of heat from a source at a lower temperature to one at higher temperature by resorting to the use of an external energy source. The vast majority of refrigerating systems operating in the world are based on vapour compression technology, exploiting the mechanical work of a compressor to create the pressure difference necessary for the correct functioning of the cycle.

However different refrigeration systems exist some of which are driven not by mechanical work, but rather by heat. These systems work on various principles: gas based (like Stirling cycles, reverse Brayton cycles, etc.), thermoelectric, elastocaloric, etc. Nevertheless, most of them remain relegated to niche applications and for refrigeration and cooling the preferred choice remain vapour cycles, based on the heat necessary for phase change, like in the case of classical vapour compression machines. These cycles include absorption, ejectors and adsorption cycles. The presence of this high temperature heat source means that, these systems interface to operate with three temperature levels (hence an additional heat source is present with respect to vapour compression machines).
These machines have a much longer history than their current diffusion would suggest (the first prototype of absorption machine was developed for example in 1858 [29]). Their initial success was however ephemeral, and they were soon replaced in the market by compression systems, benefiting from the low cost of electricity.

Due to their particular relevance to this work, absorption machines are discussed more in detail in this section. Vapour compression cycles are discussed first as a term of comparison. Subsequently, the absorption process and single stage absorption chillers are presented, concluding with a brief review of more complex cycle architectures. Choice of the working mixtures for these cycles is discussed at the end of this section.

### 2.3.1 Classical vapour compression cycles

Vapour compression refrigeration technology is based on the physical principle of the energy required for the phase change: a liquid needs to absorb heat to evaporate, while vapour releases it when condensing. Cooling systems exploit this principle by forcing natural or chemical compounds (refrigerants) to evaporate and condense repeatedly in a closed circuit.
The majority of refrigerants in use today are man-made fluids (the same as the ones presented in *Section 2.2.1*), with significant heating/cooling potential and properties that allow them to change states at relatively low temperatures.

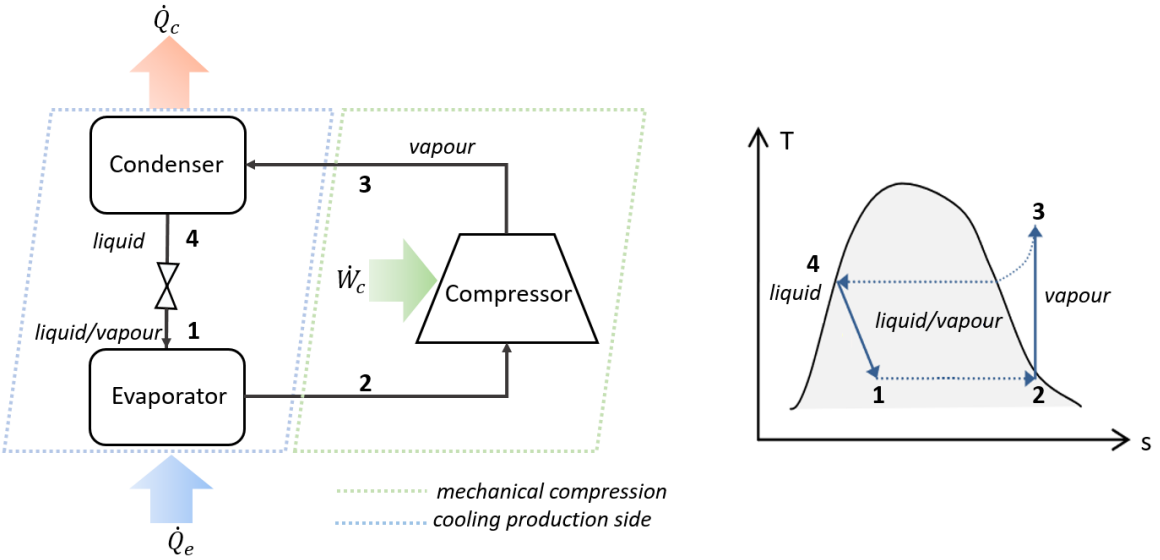


**Fig. 2.19** – Vapour compression chillers schematic layout and T-s diagram.

The basic diagram of the cycle (**Fig. 2.19**), also called reverse Rankine cycle, is very simple and shows indeed many similarities with the Rankine cycle shown in **Fig. 2.3**. The low-pressure refrigerant fluid passes through the evaporator where it produces the useful evaporating effect by absorbing heat from the low temperature source.

Subsequently it passes through a compressor where it is compressed up to a higher pressure. This high pressure and temperature fluid then passes through the condenser, where it transfers heat to the environment, returning to the liquid state. To close the cycle, this liquid passes through a throttling valve where its pressure is reduced, and returns to the evaporator, restarting the cycle.
The cooling coefficient of performance for vapour compression chillers is defined as:

$$COP_{cooling} = \frac{\dot{Q}_e}{\dot{W}_c} \tag{2.11}$$

The maximum theoretical COP achievable by a vapour compression chiller is defined by the theoretical "Carnot process", function of the heat source (the low temperature source) and heat sink (here referred to as intermediate temperature source) temperatures:

$$COP_{cooling,rev} = \frac{T_L}{T_I - T_L} \tag{2.12}$$

Increasing the temperature difference between the intermediate source ($T_I$) and the cold source ($T_L$) causes lower performances. Real performance of heat pumps ($COP_{cooling}$) has increased considerably in recent years and have reached the level of approximately 6 – 7 for ground-source heat pumps, but with values varying greatly by region and specific installation [92].
In addition to the problems of high global warming potential (GWP) of most currently used refrigerant fluids, the other main problem is related to the large electricity consumptions and problems connected to the network overload. Fully electrified heating and cooling services could have an important impact on electrical systems especially during peak periods. Their diffusion could lead to a 22% increase in peak power [92]. A possible alternative is the use of thermally driven technologies, like absorption machines, using much less electricity.

### 2.3.2 Physical process of absorption

In absorption chillers, the working fluid consists of the binary (or ternary) solution of a component called refrigerant (or coolant) and one called absorbent. **Fig. 2.20** shows two reservoirs connected by a duct on which a two-way valve is installed. The container on the right contains a refrigerant fluid; the one on the left is the solution of the same refrigerant and the absorbent fluid. When the valve in **Fig. 2.20(a)** is open, the vapour refrigerant from the right container passes through the duct and is absorbed by the solution. This causes a pressure reduction in the same container, immediately compensated by a new evaporation of refrigerant. During the vaporization, migration and absorption process, the temperature of the liquid refrigerant that remains in the right container is reduced due to its partial vaporization (the latent heat of evaporation is subtracted).

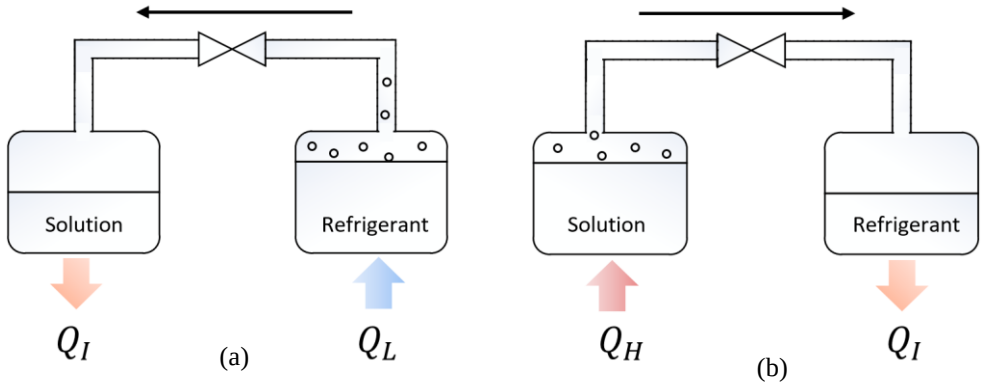


**Fig. 2.20 -** The absorption (a) and desorption (b) processes.

At the same time, the solution present in the container on the left becomes richer in refrigerant. This phenomenon, properly called absorption process, is generally exothermic. Hence, the simple communication between two containers with different concentrations of refrigerant can produce a cooling effect on one side and the release of heat on the other. When the solution in the left container can no longer continue to absorb additional quantities of refrigerant, since it has reached the saturation concentration, the system can be said to be in equilibrium.
For the separation process of the components, the saturated solution must be heated (the refrigerant being more volatile it evaporates first as explained in *Section 2.2.2*). The supply of heat to the solution contained in the left

container **Fig. 2.20(b)**, allows the reversal of the process and, therefore, the transfer of a quantity of refrigerant in the state of steam to the right tank. When in contact with the liquid at room temperature, the vapour condenses releasing $Q_I$. To keep the refrigerant temperature constant in the right tank it is therefore necessary to subtract $Q_I$. With the system shown in **Fig. 2.20**, it is impossible to carry out simultaneously the processes of absorption and separation. To carry out a continuous process is necessary to connect the four reservoirs, in which individual transformations happen.

### 2.3.3 Single stage absorption chillers

The working principle of absorption chillers is very similar to that of vapour compression chillers, with which they share many components. However, they replace the mechanical vapour compression of standard air conditioners by a thermochemical compression, driven by any type of heat source.
In fact, to guarantee the two different pressure levels a pump, consuming a modest amount of electricity, is used in these cycles. For ammonia for example, the ideal work of compression has been calculated to be around 96 times higher when using a compressor (in the case of a vapour) than when using a pump (in the case of a liquid) [45].
Clearly, the use of a pump is only possible if the phase of the fluid whose pressure has to be increased is liquid. Absorption systems overcome this problem using mixtures is which the refrigerant is in a solution with the absorbent during the pumping process and is then separated from it with a desorption in order to perform the cooling cycle.

The schematic diagram of a basic (also called single stage) absorption machine is represented in **Fig. 2.21**. In its simplest configuration, it is composed of four heat exchangers: absorber, desorber (or generator), condenser and evaporator. It can be observed that the absorption cycle consists of two subsystems:

- the first subsystem (cooling production side) consisting of the condenser, a lamination valve and an evaporator, unchanged with respect to the traditional compression refrigeration cycle;
- the second subsystem (solution loop) consisting of the desorber, lamination valve, absorber and circulation pump. This subsystem performs the thermal compression of the refrigerant through the thermal power exchanged with the external environment in the absorber and in the desorber and through the modest mechanical power supplied in the circulation pump.

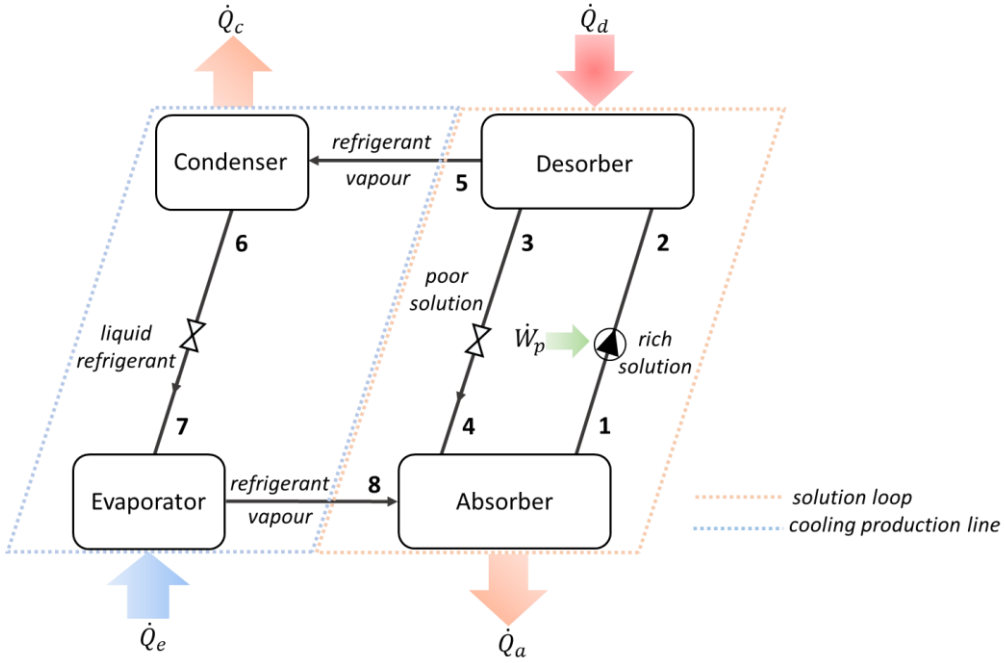


**Fig. 2.21** – Schematic diagram of an absorption chiller.

The working principle is hence rather simple. On the solution circuit loop, a first line of solution rich in refrigerant is pressurized by a pump and circulates from the absorber to the desorber. Here a power supply $\dot{Q}_d$ at high

temperature allows the desorption of steam, mainly consisting of refrigerant, from the solution. A second line comprising an expansion valve returns the solution, poor in refrigerant, to the absorber.
The desorbed refrigerant vapour enters the cooling production side of the circuit which remains unchanged with respect to a vapour compression cycle (**Fig. 2.19**). The refrigerant vapour is condensed through the exchange of thermal power $\dot{Q}_c$ with an intermediate temperature source. Before cooling the low temperature heat source at the evaporator by absorbing power $\dot{Q}_e$, the fluid is expanded in a valve to reach the low pressure. The vapour flow is finally absorbed in the poor solution due to cooling by an intermediate temperature source (usually the same used in the condenser) to which a power $\dot{Q}_a$ is transferred in the absorber.
Other components can be added in order to increase the performance of the absorption chiller, by reusing waste heat within the cycle, enabling to minimise thermodynamic losses. The biggest opportunity for internal heat exchange is represented by the solution heat exchanger (SHX), to be located between the absorber and the generator in order to pre-heat the rich solution entering the generator by cooling the poor one before the absorber. This reduces the heat supplied to the desorber, consequently increasing the COP, and reduces the power to evacuate at the absorber. The Dühring plot and the enthalpy-concentration diagram of a water-lithium bromide absorption chiller integrating a solution heat exchanger are shown in **Fig. 2.22**. Other internal heat recovery opportunities are presented in the discussion of ammonia-water absorption machines and in the presentation of more complex architectures.

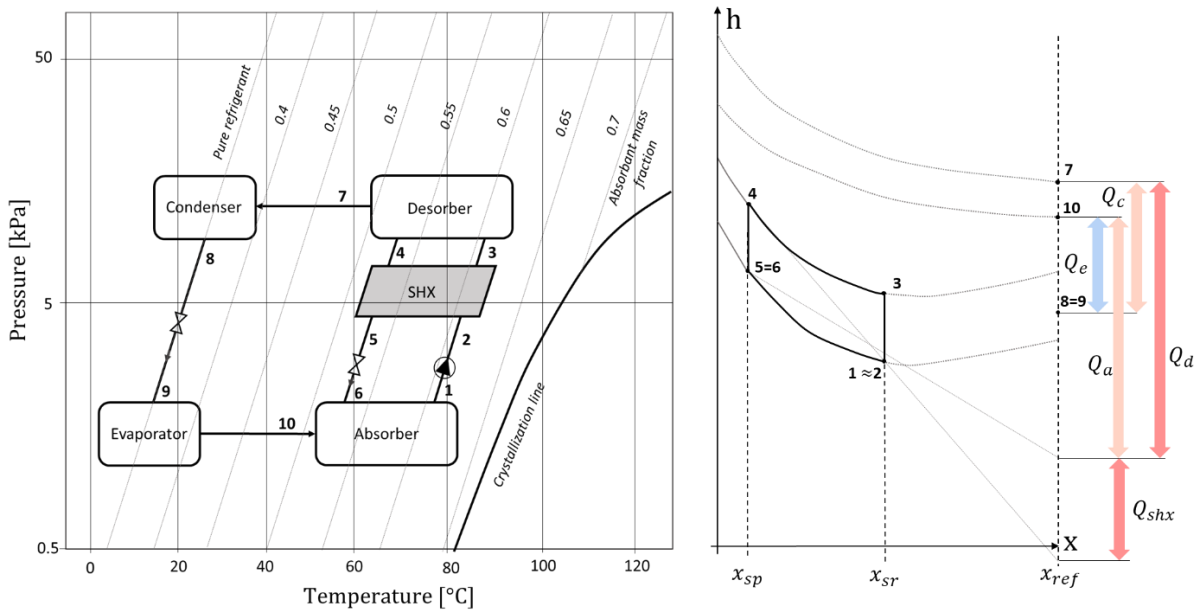


**Fig. 2.22 –** Dühring plot and enthalpy-concentration diagram of a water-lithium bromide absorption chiller integrating a solution heat exchanger, adapted from [93].

## *Idealized absorption cycle*

An ideal absorption cooling cycle can be seen as the combination of two Carnot cycles (**Fig. 2.23**), a power generation and a refrigeration cycle. Considering a high temperature $T_H$, a medium temperature $T_I$ and a low temperature $T_L$, it is necessary to operate the power Carnot cycle between $T_H$ and $T_I$, and the refrigeration cycle between $T_I$ and $T_L$. Thus, if the high and low temperature sources are needed to extract from them $Q_H$ and $Q_L$ respectively, the intermediate temperature heat source absorbs $Q_I'$ and $Q_I''$. The work W produced by the power cycle is used by the refrigeration cycle so that the latter can operate the transfer of heat from the low to the intermediate temperature level [94].

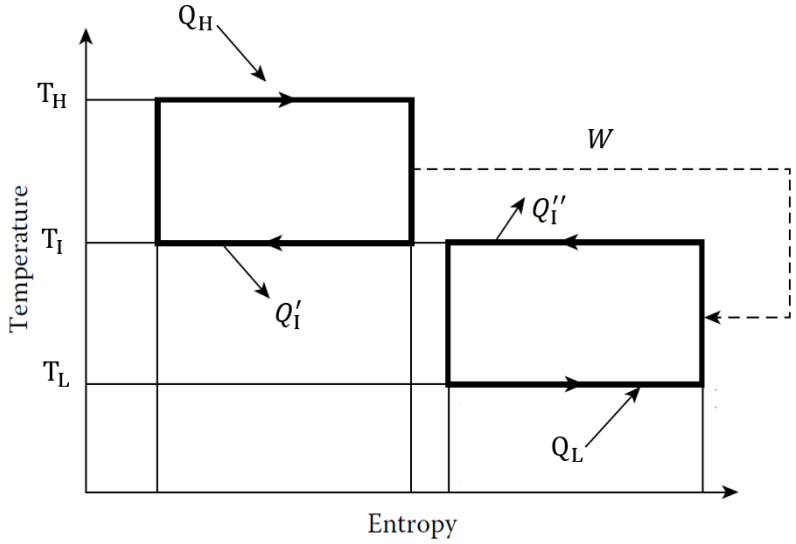


**Fig. 2.23 -** Idealized representation of an absorption chiller as the combination of a Carnot power cycle and a Carnot refrigeration cycle [5].

In the case of chillers, $Q_H$ is the heat powering the absorption cycle while the useful effect is the heat $Q_L$ subtracted from the low temperature source. The ideal coefficient of performance of the system $COP_{cooling,rev} = Q_L/Q_H$ can be then calculated as the product of the Carnot efficiency of the power and refrigeration ideal cycles:

$$COP_{Carnot,cooling} = \frac{T_H - T_I}{T_H} \cdot \frac{T_L}{T_I - T_L} \tag{2.13}$$

Performance of real absorption cycles deviates considerably from that of an ideal one. To begin with, it is necessary to include a contribution, albeit usually extremely small, of external mechanical energy to allow the pump to circulate the solution of the working fluids between the absorber and the generator. In most practical applications it is found that the mechanical power $\dot{W}$ required by the pump is negligible (from a first principle perspective) in comparison to the thermal power values involved [95]. This constitutes a first factor of misalignment of real absorption cycle from the ideal one.
Other factors of misalignment from ideal cycles include: the viscous friction within the working fluid, the mechanical friction between the system boundaries and the fluid contained therein, the mixing between the refrigerant and the solution in the absorber, the imperfect adiabaticity of the system, the uncontrolled expansion of the liquid fluid occurring through each lamination valve. These irreversibility factors, increasing the entropy of the system, are the cause of lower energy efficiency of real thermodynamic cycles.

### 2.3.4 Working mixtures

The correct and safe operation, as well as the efficiency of an absorption chiller, strongly depend on the thermodynamic properties of the working fluids chosen for the application. A fundamental requirement of each refrigerant/absorbent solution proposed for use in an absorption system lies in the miscibility of its components in the liquid phase within the entire temperature range in which the thermal cycle is intended to operate. The solution must necessarily be chemically stable. Furthermore, the characteristics listed below, even if they do not constitute a fundamental requirement for the use of the solution, are still desirable [96]:

- the difference between the boiling points of pure refrigerant and solution at the same pressure must be as high as possible;
- the refrigerant must have a high latent evaporation heat and must be able to be absorbed at high concentration in the absorbent, in order to reduce the flow rates of the solution elaborated between the generator and the absorber with the same useful cooling effect;
- the transport properties involved in the heat exchange processes, such as viscosity, thermal conductivity and diffusivity, should be favourable;
- both the refrigerant and the absorbent should be as little corrosive, explosive, toxic to people and the environment as possible, and as cheap as possible.

Literature offers numerous binary or ternary solutions having to a greater or a lesser extent, the characteristics listed above [31,96]. Working mixtures can be divided into different categories depending on the refrigerant used: ammonia, water, alcohol, halogenated hydrocarbons or other medium [96]. Various absorbents have been proposed for each of the refrigerant mentioned. However, the most common solutions are still represented by water-lithium bromide and ammonia-water.

### *Water-lithium bromide*

The water-lithium bromide working pair is generally preferred to all other working pairs in refrigeration applications because of the higher performance it guarantees [31,97]. Indeed, currently, 98% of absorption machines around the world function with $H_2O$–LiBr and only 2% with $NH_3$–$H_2O$ [29]. Lithium bromide absorption chiller represent the main competing technology of vapour compression chillers, and the choice between the two depends strongly on economic factors (e.g., the cost of electricity).

Lithium bromide is not a volatile absorbent. Therefore, unlike in the case of the ammonia water mixture presented in *Section 2.2.2*, the vapour desorbed when evaporating the water-lithium bromide mixture can be considered pure refrigerant. This is a great benefit compared to ammonia-water absorption systems, because purification of the refrigerant vapour is not needed. Other advantages of the mixture lie in the extremely high latent heat of vaporization of water, in the strong affinity between the components, the high degree of safety and chemical stability. However, the use of water as a refrigerant limits the achievable refrigeration temperature to values above 0°C to avoid freezing.
Besides the limitations of using water as a refrigerant, crystallization and corrosion problems can arise. Lithium bromide is in solid state at low temperature and, when in solution with water, crystallization can occur even at relatively low concentration. Crystallization risk, especially for high ambient temperatures [31], is one of the major challenges posed by the water-lithium bromide pair, thus further reducing the operational range of the machine.
Moreover, in presence of dissolved oxygen in the mixture, the water-lithium bromide couple is aggressive towards copper as much as the ammonia-water couple and, in addition, towards carbon steel. Corrosion not only shortens the life of the machine but also drastically reduces the COP. However, it should be noted that, the refrigeration circuit being almost completely airtight, the percentage of oxygen present in the working solution is very low.
Even if the problem of corrosion is less relevant than for ammonia-based solutions, for the water/lithium bromide mixture there is the disadvantage of working with sub atmospheric pressures. For example, for the evaporation process to take place at 5 °C, a pressure of about 0.009 bar is required for water.
Such reduced pressure values entail the need to use components of large dimensions, to have hermetic joints between the various elements of the circuit and achieve reduced pressure drops within the low-pressure components so as not to further reduce the required pressure [98]. The relatively high viscosity of this pair with respect to ammonia-water increases pumping requirements and reduces heat and mass transfer [31].

The coefficient of performance of these machines in the case of chiller (i.e., the ratio between cooling power output and thermal power input), typically varies over the range 0.7-1.2, depending on the cycle configuration. They require specific maintenance procedures, and ignoring these procedures often leads to early failure.

### *Ammonia-water*

Both ammonia and water are highly stable fluids in a wide range of temperatures and pressures. $NH_3$ has a high latent evaporation heat and a reduced solidification point (-77 °C), so that it can be used in refrigeration applications at very low temperatures. More generally, the ammonia-water couple can be used in a very large range of working temperatures (-60/+377 °C ) and pressures (0/400 bar) [99]. However, since both ammonia and water are volatile substances, the refrigerant circuit requires the installation of a device that allows further separation between the substances leaving the desorber. Indeed, an important difference in the case of the ammonia-water mixture is that the absorbent, water, has a vapour pressure that is not negligible relative to that of ammonia, the refrigerant. Therefore, the vapour generated in the desorber contains a certain amount of water (typically in the order of 5% water). The mass fraction of water in the vapour depends on the mass fraction of the liquid mixture in the desorber, the temperature, and the desorber design. Any water contained in the desorbed vapour is detrimental to the performance of the system. A presence even as low as 1% of water in the ammonia vapour entering the evaporator of the refrigeration system produces a temperature glide so high as to significantly reduce the cooling capacity and performance of the machine (potential COP reductions over 30% [11]). Furthermore, the deposit of water in the evaporator produces considerable increases in pressure in the component and in the absorber, ultimately, leading to their breakage [5].

Problems with the use of ammonia are its toxicity, its corrosive action on copper and its alloys and the high pressures necessary in the generator to separate it from the water. On the other hand, the low environmental impact and the reduced cost of the entire mixture are guaranteed. Furthermore, there is no danger of crystallization of the solution, which allows easier control of the cooling circuit.
The disadvantages in danger, however, do not stop the use of $NH_3/H_2O$ mixtures because of the multiple advantages, like the fact that unlike water-lithium bromide, ammonia-water machines allow temperatures of evaporation enormously lower at greatly higher pressures. This entails the possibility of adopting pipes with a reduced diameter and exchangers of limited dimensions.
Machines are available in capacity ranging from 10 to 90 kW with COP typically around 0.4-0.7 [5]. Additionally, a multi-effect or a desorber-absorber heat exchange (GAX) [100] cycle can be used to achieve higher efficiency [14]. They require a higher hot source temperature, but it is possible to reach cooling COP around 1-1.2 and heating COP around 1.8-2.0 [102].
These units have a niche market because there are few competing gas-fired technologies suitable for many applications. Custom ammonia/water applications in industry for waste heat utilization are an interesting application of this technology [5].

A variant of ammonia-water systems is the one operating with an auxiliary gas, very often-molecular hydrogen or helium. Chillers based on this technology, direct descendant of the Swedish patent of von Platen and Munter [103], allow achieving only very low COPs. On the other hand, they do not use electricity for their functioning, they do not have any rotating or mobile mechanical components and produce very low acoustic impacts. Their most extensive use is in food refrigeration in the domestic, recreational and hotel sectors.

### *Other working mixtures*

Ammonia-water and water-lithium bromide are not the two working pairs well adapted for absorption systems. Ammonia and water present however several attributes, making their use as refrigerants very convenient. For this reason, efforts have focused mainly on the search for new absorbents.
Many salts have been studied as possible alternatives of lithium bromide for example. Lithium iodide has been proposed as a viable absorbent ($H_2O$-LiI) [104], particularly as an element of multi-component absorbents [96].
Another proposed pair is water-lithium chloride ($H_2O$-LiCl) which, depending on the studied operating conditions, can have higher COPs and exergetic efficiency than $H_2O$-LiBr systems [105,106]. Additionally, this mixture is characterised by long-term stability and a lower cost than $H_2O$-LiBr, but presenting a higher risk of crystallization which has so far complicated the its use [31]. Ionic liquids (IL) have also been proposed as absorbents in water-based mixtures [107]. Numerical studies on these systems yielded slightly lower COP values with respect to the $H_2O$-LiBr mixture. This was confirmed by experimental results which have also highlighted that when using $H_2O$-IL the cooling capacity was considerably lower due to the higher viscosity of the mixture.
Many other binary mixtures have been proposed (e.g. $H_2O$-NaOH), but $H_2O$-LiCl appears to be the most promising alternative to $H_2O$-LiBr if crystallization problems are overcome [31].

Concerning ammonia-based working mixtures, researchers have focused on the identification of absorbents replacing water capable of avoiding the need for a rectifier and, at the same time improving the properties of the mixture (such as a reduced corrosion risk). Salts seem to be a suitable solution also in the case of ammonia, with lithium nitrate ($LiNO_3$) and sodium thiocyanate (NaSCN) appearing as the most promising alternatives, both showing COPs about 10% higher than when using $H_2O$ as an absorbant. The $NH_3$- $LiNO_3$ mixture was discovered first and hence is more studied than $NH_3$- NaSCN, possibly also because of its wider range of working conditions. Experimental studies showed some disadvantages such as low heat and mass transfer in the desorber and in the absorber, resulting in lower performances than expected [108]. The $NH_3$-NaSCN has very similar performances, but its use is limited to temperatures above -10 °C to avoid crystallization [109]. Moreover, the higher vapour pressure difference between the absorbent and the refrigerant, allows these two alternative mixtures to operate with lower desorber temperatures, and to have better performances at negative evaporator temperatures. However, the increased viscosity compared to $NH_3$-$H_2O$ generates greater pressure drops, requiring higher circulation rates and more powerful pumps.
Ionic liquids have been proposed as absorbents also for ammonia-based systems but risks concerning the life cycle of the systems like presence of impurities, degradation of properties overtime and need for recycling have been highlighted by several authors [110,111].

Numerical comparison of the COP of different water-based and ammonia-based binary mixtures is shown in **Fig. 2.24** [112], referring to an evaporator temperature of 8 °C and two different intermediate source temperature: 30 °C

(**Fig. 2.24(a)**) and 44 °C (**Fig. 2.24(b)**). In the case of water-based systems, $H_2O$-LiBr continues to be the best choice given the similar performances but more limited operating range of $H_2O$-LiCl systems. For ammonia-based working pairs, $LiNO_3$ and NaSCN seem to be good candidates to substitute water as absorbents. However, improvements are still needed to avoid the lower-than-expected experimental performance on these systems.

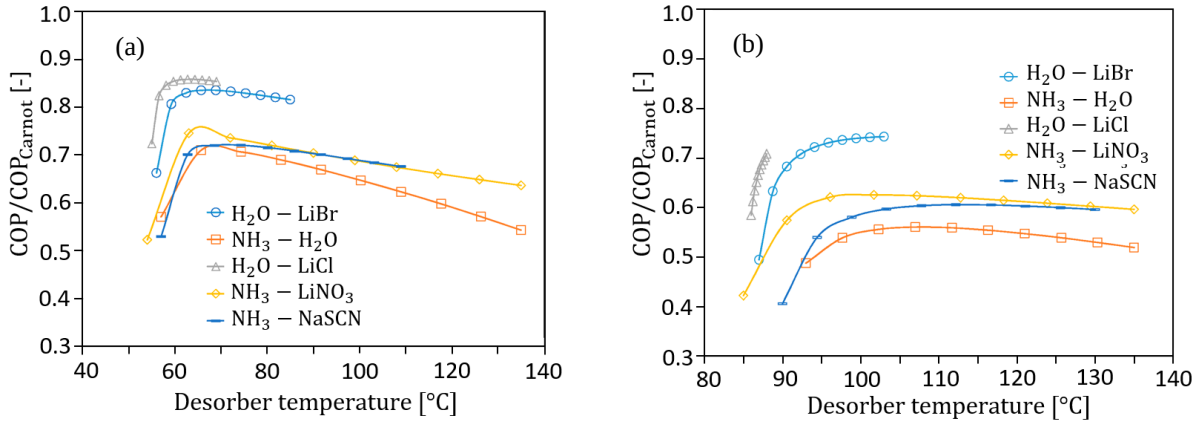


**Fig. 2.24 –** Comparison of the COP of different water-based and ammonia-based binary mixtures against desorber temperature for an intermediate source temperature of 30°C (a) and 44 °C (b) and cold source temperature of 8 °C. Adapted from [112].

Ternary mixtures have also been object of several studies [113]. For example, the ternary mixture $NH_3$-$H_2O$-$LiNO_3$ has been studied in order to reduce the absorbent viscosity with pure $LiNO_3$, resulting in better COP with reference to $NH_3$-$H_2O$ [114], but requiring higher desorber temperatures.

Finally, the use of other refrigerants like alcohols or environmentally acceptable hydrofluorocarbons (HFC) has been developed for special applications like harvesting of underground heat.
From the above review, it is evident that more studies are needed on the improvement of systems working with innovative mixtures and that the most reliable pairs remain $H_2O$-LiBr and $NH_3$-$H_2O$. In particular the latter is of particular interest for its increased operation range with respect to the $H_2O$-LiBr couple (limited to above zero cooling temperatures and ambient temperatures below 35 °C), its lower cost and the possibility to develop reversible machines or combined cycle for the production of cooling and electricity [43].

For these reasons, the development of this technology is in progress at INES since 2011 [13,29]. Given their central role in this work, specific issues related to single stage ammonia-water absorption chillers are discussed in the next section.

### 2.3.5 Ammonia-water single stage absorption chillers

A typical single stage ammonia-water system presents very little differences with respect to the already discussed basic layout of an absorption chiller (**Fig. 2.21**). The main difference is the presence of a refrigerant purification component at the desorber outlet, the rectifier. As discussed in the previous section, the presence of water in the desorbed vapour, however small, causes drastic performance reduction and malfunctioning of the system, eventually leading to its breaking. The rectifier cools down the vapour, condensing a fraction of it mainly composed of water, thus increasing the purity in refrigerant of the vapour. However, the refrigerant vapour mass flow rate towards the condenser is reduced, hence affecting the efficiency of the cycle.
Minimization of thermodynamic losses by reusing heat within the cycle, usually leads to the use of the already discussed solution heat exchanger, which uses hot rich solution leaving the desorber to preheat the cold poor solution, reducing the external heat required and increasing the COP. This solution heat exchanger is the biggest opportunity for internal heat exchange in most cycles, but other interesting opportunities exist. For example, a subcooler (also called condensate precooler or refrigerant heat exchanger) is shown in **Fig. 2.25**.

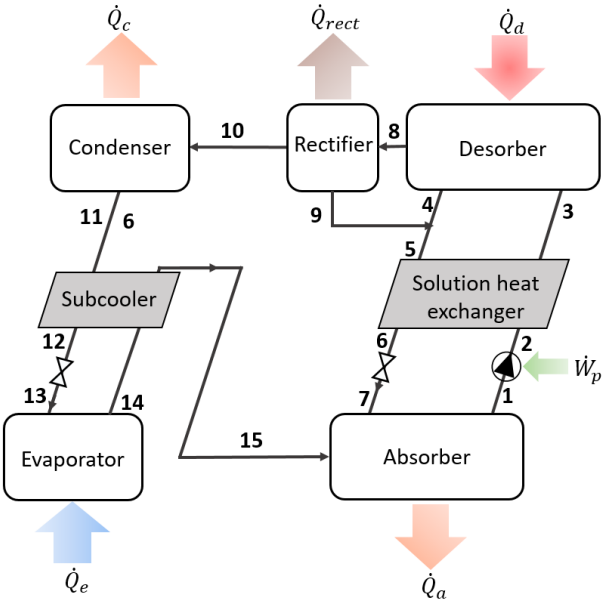


**Fig. 2.25** – Schematic diagram of an ammonia-water absorption chiller with internal heat recovery.

This exchanger cools down the liquid refrigerant leaving the condenser using the cooler stream leaving the evaporator. In the case of ammonia-water systems, this has two benefits. First, the enthalpy at the evaporator inlet is reduced, thus increasing the cooling capacity per unit mass of refrigerant, improving the performance of the cycle. The second benefit is related to the management of the presence of water in the evaporator. As discussed, the presence of water in the refrigerant generates very high temperature glides in the evaporation process. This can be reduced by allowing the presence of some liquid at the evaporator outlet. However, this would reduce the performance of the cycle since energy would be used to desorb the refrigerant, but part of it would not provide refrigeration. The best option is hence to evaporate the remaining liquid after the evaporator in the subcooler, which hence improves the performance of the cycle and helps with water management in the evaporator.
However, the presence of the subcooler increases the enthalpy of the vapour entering the absorber (whose size must be increased to maintain the same performance) and causes additional pressures losses. Nevertheless its presence in ammonia-water systems is generally advantageous [5].
The condensation heat rejected at the rectifier represents another possibility of internal heat recovery in the case of ammonia-water systems. Recovery is possible by using the rich solution leaving the absorber (point 2 in **Fig. 2.25**) as coolant in the rectifier. In this way, the poor solution is preheated before entering the solution heat exchanger. This can be an important means of performance improvement since the rectifier heat is used within the system instead of being rejected to a heat sink outside of the absorption system. In addition, this heat recovery can help to balance the mismatch between the heat capacity rates of the poor solution leaving the desorber and the rich solution entering it. Indeed, since the mass flow rate leaving the desorber is smaller, its heat capacity rate is also normally smaller than the one of the rich solution [5].

Many other possibilities of internal heat recovery exist. For example, solution recirculation can be used in the absorber or in the desorber. Considering the absorber solution recirculation, the rich solution after passing through the pump enters again in the absorber through a separate pipe and exchanges heat with the solution. In this way, the solution is preheated using the heat rejected by the absorber. However, a three-path heat exchangers, a device generally difficult to manufacture, must be employed. Alternatively, another potential option is to use two separate heat exchangers (one cooled by an external fluid and one cooled by the solution exiting the pump) in parallel to replace, the absorber. This poses considerable control challenges and increases the costs and size of the system.
The importance of these additional heat recovery measures depends on the specific operating conditions and not all of them are always beneficial. Additionally, in many cases their combination is not feasible since, for example, the rich solution has a limited need for energy. Hence, the configuration shown in **Fig. 2.25** is one of the most commonly used, being a good compromise between performance improvement and architecture complexity.

Recently, several studies have focused on the combination in the same component of a desorber and a rectifier section, a concept anticipated to have several advantages like improved heat transfer coefficients, reduced costs and size. The desorber and the rectifier are normally separate components, but they can be combined. Several technologies have been proposed [115–117]. A combined plate heat exchanger desorber was recently developed at INES [29] using flat corrugated plates to reduce size, cost and complexity of the system.

This heat exchanger is composed of a distribution system dividing uniformly the rich solution at inlet, a lower part where vapour is generated exchanging heat with the hot source, and an adiabatic upper part allowing the purification of the vapour generated by partial reabsorption of the latter in the ammonia-water solution entering the exchanger. Experimental tests [29] showed that the combined desorber is highly efficient and guarantees very high purity of the ammonia vapour (above 98% [118]) with a lower heat supply, thus improving the COP of the cycle. Additionally, the functioning of the machine is more stable and steady conditions are reached faster.

A final note on ammonia-water systems concerns material considerations. Ammonia is very corrosive to most common materials including copper and carbon steel, so stainless steel is normally used. It should be kept in mind however that the thermal conductivity is about ten times lower than that of copper. Additionally, although a natural fluid commonly used in several applications, ammonia is very toxic for humans, so it needs to be handled with great care. A peculiar characteristic of ammonia is its very pungent odour, which can be easily detected by humans in concentrations of few parts per million, before representing a risk for health.

### 2.3.6 Advanced architectures

Multi-stage and multi-effect systems are interesting solutions offering the possibility to reach higher COPs or increased temperature difference between the intermediate and cold source temperature (lift). Around 30 different classes of two-stage absorption systems have been proposed in literature [5]. Normally, the term multi-stage refers to the presence in the cycle of more than one solution circuit, while the term multi-effect refers to the use of a quantity of heat more than once to generate vapour.
An example of a two-stage (two solution circuits), double effect system is shown in **Fig. 2.26**. The first stage has the same configuration as the cycle shown in **Fig. 2.25,** with the difference that a second solution circuit is added in parallel to the first. Hence, the vapour from the evaporator is divided between the two absorbers and the vapour desorbed by both desorbers is sent to the condenser. The two solution circuits are coupled by an internal heat exchange, so that the heat rejected by the second absorber and rectifier constitutes the power supplied to the first desorber.

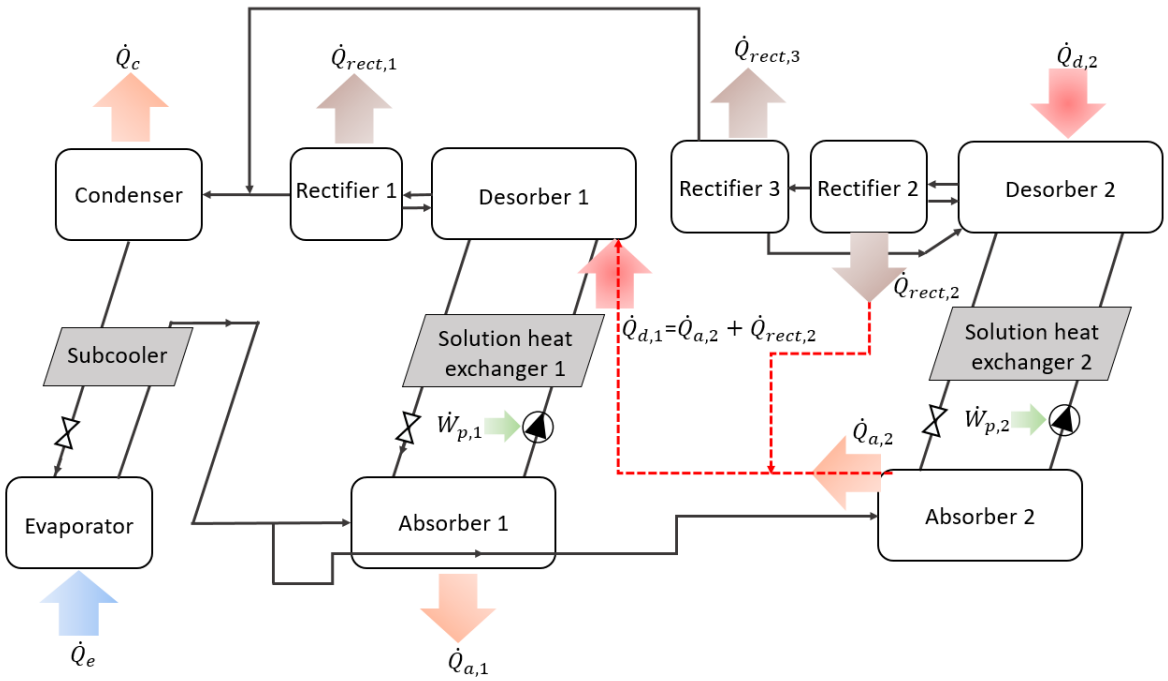


**Fig. 2.26** – Two-stage, double-effect ammonia water absorption system, adapted from [5].

The advantage of this configuration lies in the possibility of using a higher temperature heat at the desorber with respect to a single stage configuration, thus increasing the COP.
Nevertheless, for the system to operate in steady state, the mass fraction of the vapour produced by both rectifiers should be the same. This is difficult to achieve in practise, and several modifications to the scheme presented in **Fig. 2.26** are needed to ensure the control of the system, considerably reducing the advantages of the architecture.

Many other different architectures exist like the two-stage triple effect, double lift, half stage, etc. Arguably, the most noteworthy is the generator/absorber heat exchange (GAX) cycle, coming from a development of the architecture shown in **Fig. 2.27**. GAX cycles are only feasible using the ammonia-water mixture, but the simplicity of the solution makes them a suitable candidate from commercial products.

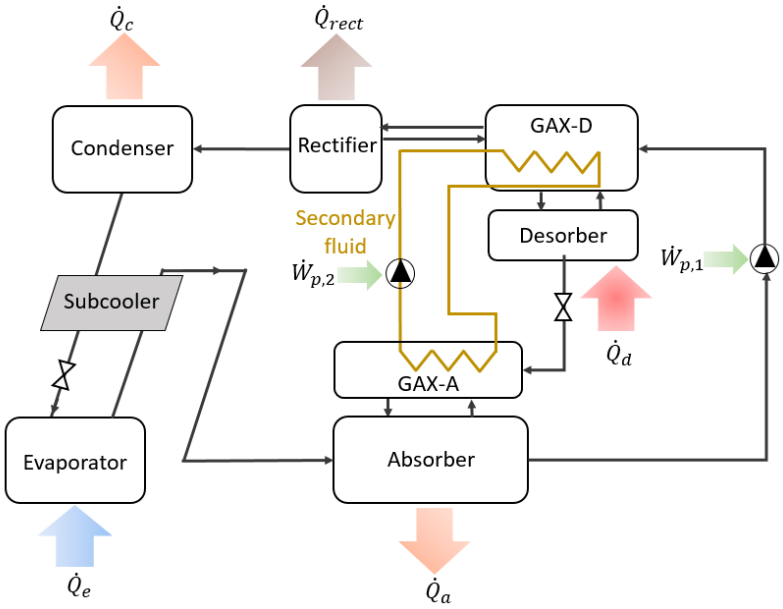


**Fig. 2.27 –** GAX cycle working and basic layout, adapted from [5].

The GAX (or DAHX, "desorber/absorber heat exchange") cycle, introduced and patented in 1914 by Altenkirch and Tenckhoff, has many interesting characteristics. The GAX-A and the GAX-D exchange heat through a secondary fluid circuit. In the GAX-A a first absorption phase takes place, whose rejection heat is recovered by the secondary fluid. The absorption is then completed in the main absorber, exchanging heat with the intermediate source. The GAX-D instead operates a first separation process using the heat extracted from the GAX-A. The separation is then completed in the desorber where more refrigerant vapour is produced using heat from the hot temperature source. The vapour desorbed in the GAX-D and in the desorber eventually mix before entering the rectifier. Many systems use a single component containing both the GAX-A and GAX-D.

GAX cycles can achieve very high COPs (1.5-2) thanks to the very effective internal heat exchange. Additionally, this system is very similar to a single-stage cycle and is therefore characterised by similarly low complexity and cost. Variation to the architecture presented in **Fig. 2.27** are possible, including absorber recirculation or branched GAX cycles. However, these systems significantly exceed the single stage performance only for high hot source temperatures. Additionally, the realization of these systems poses numerous challenges and commercial solution are not yet diffused.

### 2.3.7 Performance parameters

Absorption heat pumps performance parameters are defined in a very similar ways as for vapour compression (*Section 2.3.1*). In general, also absorption heat pumps can be used to produce cooling or heating. In the first case (of interest in this study), the cooling coefficient of performance ($COP_{cooling}$) is defined as the ratio between the useful power absorbed by the evaporator ($\dot{Q}_e$) and the sum of the thermal power supplied by the generator ($\dot{Q}_d$) and the mechanical power consumed by the pump $\dot{W}_P$ [5]:

$$COP_{cooling} = \frac{\dot{Q}_e}{\dot{Q}_d + \dot{W}_p} \tag{2.14}$$

A thermal and an electrical performance coefficient $COP_{cooling,ele}$ can also defined as:

$$COP_{cooling,th} = \frac{\dot{Q}_e}{\dot{Q}_d} \tag{2.15}$$

$$COP_{cooling,ele} = \frac{\dot{Q}_e}{\dot{W}_p} \tag{2.16}$$

Given the focus of the study on refrigeration applications, in the following, COP will be used to indicate the $COP_{cooling}$ (defined in **Eq. (2.14)**) except explicitly otherwise indicated. The coefficients of performance presented in **Eq. (2.14)-(2.16)** refer to the system shown in **Fig. 2.25**. They represent first law (or energy) performance parameters. The COP of an ideal cycle was expressed in **Eq. (2.13)**. Hence, a second law efficiency of the cycle can be expressed as:

$$\eta_{II} = \frac{COP}{COP_{Carnot}} \tag{2.17}$$

A very similar concept is represented by the exergetic efficiency of the system defined as:

$$\eta_{ex} = \frac{\dot{E}x_e}{\dot{E}x_d + \dot{W}_p} \tag{2.18}$$

In **Eq. (2.18)** the numerator represents the useful output of the systems in terms of exergy streams, while the denominator represents the input exergy streams at the desorber and pump. The concepts of second law efficiency, exergy and exergetic efficiency will be discussed in more details in *Section 5.2*, presenting the energy, exergy and exergoeconomic analysis of the system under investigation.

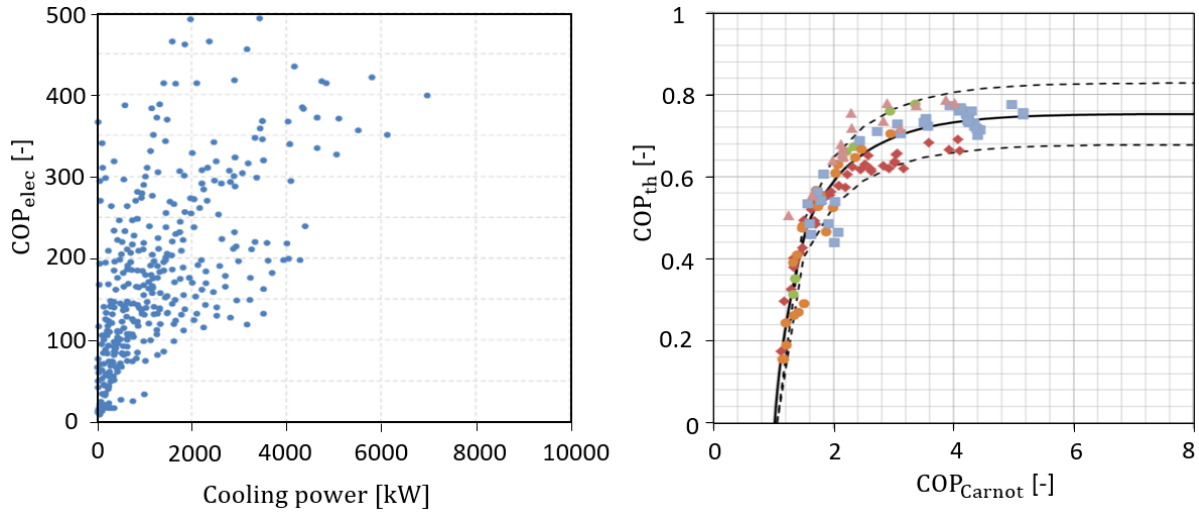


**Fig. 2.28 –** Performance of over 600 single-effect absorption machines references [119].

An internal database integrating more than 600 single-effect machines references (**Fig. 2.28**) was developed at INES [29]. The available data shows that the electrical COP quickly exceeds 100 for large scales machines. This values is lower for small machines, very likely due to poor performance of the circulations pumps at smaller scales [120]. Nominal thermal COP declared by manufacturers is generally around 0.6-0.7, but it varies depending on the temperature of the sources. The maximum achievable performance for fixed temperatures of the sources is given by the $COP_{Carnot}$ , hence comparing this value with the actual thermal COP of a machine is important to estimate the irreversibilities taking place within the cycle.

### 2.3.8 Applications and market

Absorption chillers are used nowadays mostly in building cooling application [5]. They are diffused mainly in large buildings, like hotels, where they are particularly appreciated for characteristics like the absence of noise and vibrations, the low operating and maintenance costs, and the possibility of using different energy sources. Indeed, a peculiar characteristic of absorption chillers is that they operate with the use of thermal energy together with a small rate of electricity. Their use, therefore, can be very convenient in areas where the electricity network is absent or not very extensive. In many cases, they can be economically advantageous to use instead of mechanical compression chillers to avoid exceedance of the subscribed maximum power established in the supply contracts or to not overload the network.

Absorption machines also play an important role in the industrial heat recovery, especially in sectors having subprocesses operating at different temperatures (e.g., in the food industry, distillation process, etc.) where it is very interesting to use the heat rejected by a process to produce the cooling needed in another process. Given the still relatively high capital costs needed for the implementation of these solutions, their economic interest strongly depends on the cost of electricity, very low in the past years.
The use of renewable sources and in particular that of solar energy to cool an environment, known as solar cooling, is one of the most interesting applications [101,121,122]. Another interesting use of absorption machines is that of polygeneration. It is usually applied when the energy requirements are, with a variable contemporaneity factor depending on the case, together electric, thermal and cooling. The polygeneration can takes place with a single integrated plant, having a much increased energy conversion efficiency compared to separate productions. In addition to the most common ones mentioned so far, there are numerous other applications of absorption refrigeration technologies. An example is the use of the single stage cooler as an air conditioner on internal combustion engine vehicles [5].
Then main players in the ammonia-water absorption refrigeration are relatively small companies like the Italian Robur (**Fig. 2.29**) or the Dutch Colibrì. More companies are active in the water-lithium bromide sector.

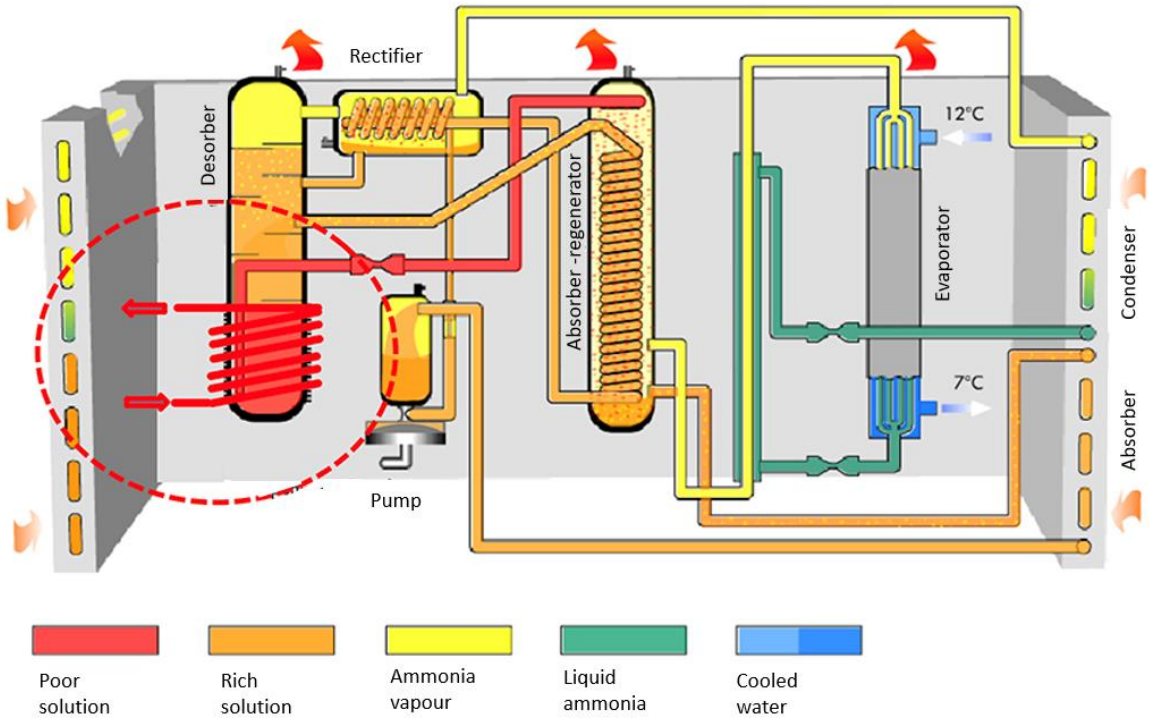


**Fig. 2.29** – Schematic diagram of the Robur ARS, Robur © [123].

## 2.4 Other heat driven cooling technologies

Other heat-driven technologies that have been demonstrated include adsorption (solid/vapour), Stirling cycle, ejector refrigeration, and magnetic refrigeration. Many other ideas have appeared in literature. Because of their relevance to this work, particularly in the development of combined cooling and power cycles, adsorption chillers and ejector refrigeration systems are presented in this section. They share many similarities with the previously discussed absorption chillers, notably the fact that they are trithermal cycles. Additionally, the definition of the thermal COP remains unchanged with respect to the one defined for absorption chillers. The domains of application of these systems are often common to those of absorption machines from which they differentiate for some specific features, like a simpler architecture (ejector refrigeration cycles) or their thermal storage capacity (adsorption cycles). However, they generally present lower COPs.

### 2.4.1 Ejector refrigeration cycles

The fundamental working principle of an ejector is to use a high-pressure flow (referred to as primary flow) to entrain and compress a low-pressure flow (referred to as secondary flow). The high-pressure primary flow enters a usually converging-diverging (though sometimes converging-only) primary nozzle inside of which it undergoes an expansion to high velocity and low pressure. The resulting low-pressure and high velocity primary flow is used to entrain the secondary flow from the suction chamber into the mixing chamber. In the mixing chamber, the two flows fully mix, and the high-speed mixed flow is decelerated in a diffuser, where it recovers pressure before leaving the ejector. **Fig. 2.30** shows a typical ejector geometry, giving a visual representation of the flows within the component.

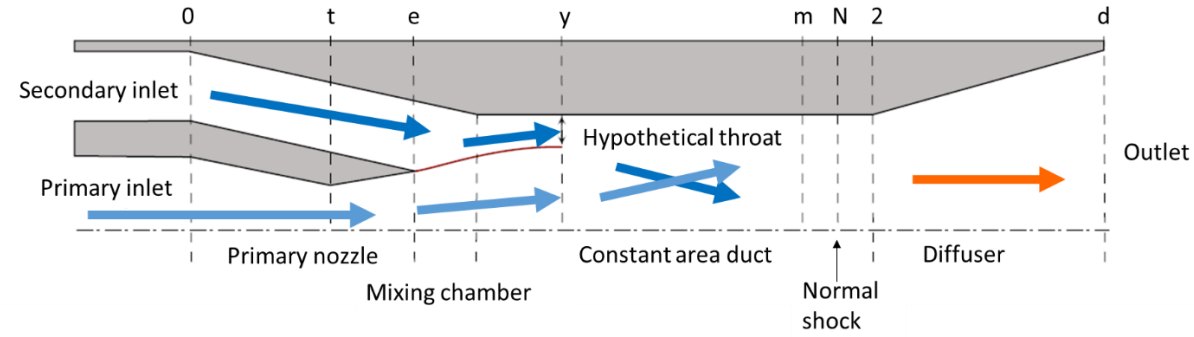


**Fig. 2.30** – Schematic diagram of an ejector.

Ejectors can be used in various low-grade heat refrigeration cycles [124]. The most basic design of such cycles is the standard SERS (single ejector refrigeration system) presented on **Fig. 2.31**. In this cycle, the ejector is combined with three heat exchangers (condenser, evaporator and generator), a pump and an expansion valve. Low-grade heat allows the production of high-pressure primary vapour in the generator used to entrain the low-pressure secondary vapour leaving the evaporator. This cycle is the most commonly described and studied ejector cycle in literature because of its simplicity. Indeed, a large number of experimental and theoretical studies have been performed on this cycle, and their results used to improve ejector design and validate numerical models.

This cycle presents many similar advantages as absorption cycles, most importantly the very low electricity consumption of the circulation pump. In addition, since they have no moving parts, ejectors are very robust, reliable and are characterized by a very simple geometry involving low-maintenance and low costs.

The SERS cycle has generally lower performance than absorption cycles, even if relatively high COPs (reaching 0.9 [125]) have also been reported, indicating strong improvements possibilities. However, one of the main barriers to a widespread usage of ejectors in refrigeration cycles resides precisely in their relatively narrow range of use due to the absence of control moving parts. When operating outside of their design conditions, ejectors suffer significant performance reductions and might even stop working.
The fluids normally applied in these systems (i.e., HFC, HC, $CO_2$, etc.) are the same refrigerants described in *Section 2.2.1* when discussing fluids for organic Rankine cycles.

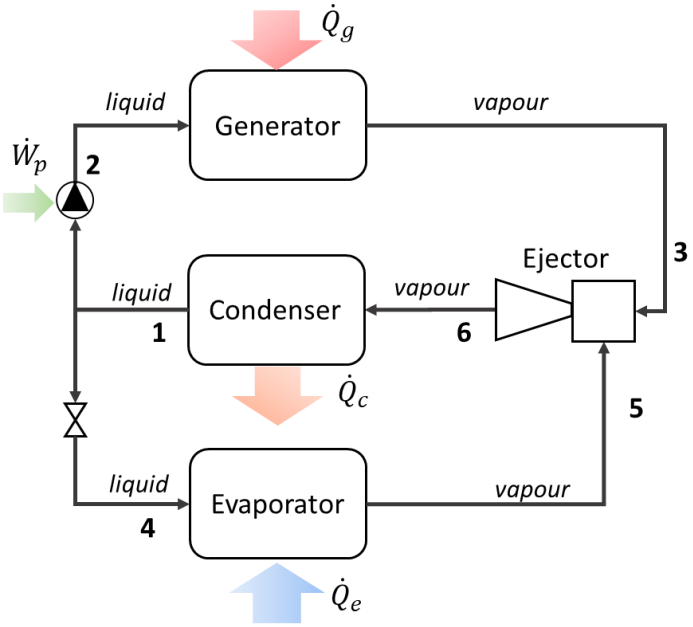


**Fig. 2.31** – Schematic diagram of a simple ejector refrigeration cycle.

Several different ejector refrigeration systems have been commercialized in recent years [126]. Their interest with respect to absorption machines resides in their increased simplicity and lower costs. Hence, interesting applications are represented by light commercial and household refrigeration, automotive and residential air conditioning, as well as the combination in cascade with classical vapour compression chillers. However, given the complicated regulations of these systems, appropriate control strategies need to be devised for a diffusion of this technology.

## *Ejectors and absorption machines*

The integration of ejectors in absorption cycles has been proposed by several authors [124]. In principle, the addition of an ejector can improve significantly the COP of the systems at a very low additional cost and with almost no complexification of the architecture.
In light of the fact that the absorber is the bottleneck component in absorption cycles [45], improving its operating pressure can be highly beneficial for the absorption process. This can be done by placing an ejector on the poor solution line instead of a lamination valve [127] **(Fig. 2.32(a)**). This configuration has been shown to have not only higher COPs but also lower activation temperatures.
The same advantages can be obtained by placing the ejector between the desorber and the condenser **(Fig. 2.32(b)**). In this case, the performance of the cycle is increased because not all the vapour producing the cooling effect in the evaporator has to absorbed in the poor solution, but instead part of it recirculates in the cooling production line.

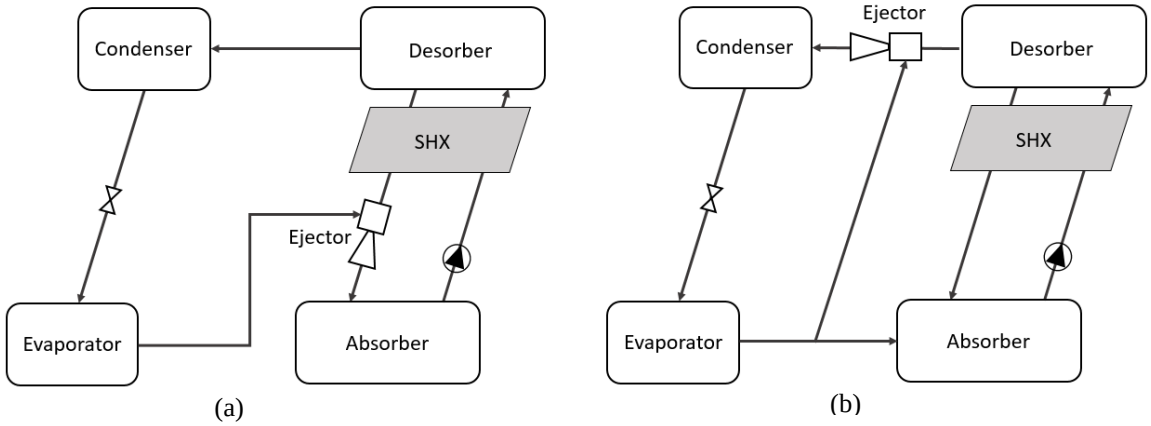


**Fig. 2.32** – Combined ejector-absorption refrigeration systems.

Both numerical and experimental studies [128,129] have shown that the second configuration is more efficient than the first.

Several other solutions have been proposed in literature, including the use in more complex absorption cycles (e.g. double effect absorption cycles [130]), but problems related to the malfunctioning of the ejector in off-design points remain.

### 2.4.2 Adsorption and thermochemical cycles

The absorption machines previously described are part of a larger family generally referred to as sorption technologies. Sorption is the phenomenon of capture or fixation of a gaseous phase, called sorbate, by a condensed phase (solid or liquid), called sorbent [131]. The reverse phenomenon, by which the gaseous phase is extracted from the solid or liquid substrate, is called desorption.

While absorption chillers are based on a liquid-gas sorption process, adsorption or thermochemical cooling systems are based on the properties of certain solids of reacting with or adsorbing large quantities of vapour due to their very large superficial area and porosity. The adsorbed refrigerant can then be released by means of heating. These machines share many similarities with absorption machines. They are both based on a trithermal thermodynamic cycle. Furthermore, they work using the same physical principle of involving the generation of a difference in the concentration of a refrigerant fluid in a sorbent by supplying thermal energy to and from the outside. The desorption and absorption processes in general take place with a similar sequence and for the same purposes: the first allows the separation of the refrigerant from the absorbent and takes place at high pressure before the condensation process, while the second allows the sorption of the refrigerant vapour in the absorbent and occurs after the evaporation process.
However, the two technologies also present important differences. First, the adsorption process is produced by trapping the refrigerant in a solid, making adsorption systems intrinsically intermittent. Indeed, while in an absorption process the fluid can move within the machine, the solid sorbent cannot in adsorption machines. The desorber and the absorber are therefore replaced by adsorbent beds, containing a porous matrix. Production of a continuous useful effect requires the use of several adsorption beds (at least 3 [132]). Nevertheless, a two-bed adsorption chiller is already sufficient to provide a cooling effect for 90% of the time and for this reason most of commercial systems are integrate at least two beds.
However, it is worth mentioning as well that the discontinuous functioning gives solid-gas adsorption and thermochemical cooling production system an intrinsic storage capacity.

The most common adsorption working pairs are water-silica gel, water-zeolite, methanol-activated carbon, and ammonia-activated carbon among others. Numerous solid-gas reactive couples can be used in thermochemical cycles, involving various types of chemical reactions. They cover a wide range of operating temperatures. The four main types are: hydrides-$H_2$, metal oxide-$O_2$, hydrates-$H_2O$ and metal halides-$NH_3$ [133].

The maximum achievable COPs are low, of the order of 0.1-0.3 [134] and the systems currently marketed are more expensive than other comparable size systems. However, this type of system allows to be operated without using electricity and has very low activation temperatures, even below 70 °C.
One market niche within which adsorption systems can effectively compete relates to vaccine refrigeration or ice production in areas, especially in undeveloped countries, not reached by the network electricity.

## 2.5 Combined cooling and power cycles

With the rapid development of distributed energy supply systems, combined cooling and power systems (CCP), combined heating and power (CHP) and, combined cooling heating and power (CCHP) systems have become a very interesting solutions to improve the energy efficiency and to reduce greenhouse gas (GHG) emissions [135]. Many studies focused on the energy savings of this systems. Wu [136] showed that, compared to the traditional energy supply mode, the CCHP system can improve the overall efficiency from 59% to 88%. This is owed to the cascade utilization of different energy carriers and the adoption of the thermally activated technologies.

The development of a combined production system is generally based on the combination of several technologies independently or within the same process, to generate the desired output products. When the target is the use of a low temperature heat source, the technologies presented in *Sections 2.2-2.4* are well suited to be integrated together for the production of cooling and power.
For the production of power using low temperature heat, it was highlighted that ORCs have achieved technological maturity and guarantee satisfactory performances. For the production of cooling, sorption technologies, and in particular absorption chillers, currently appear to be the most promising alternative. Hence, the combination of ORCs and sorption cycles is envisaged to achieve higher energy efficiencies.
The independent use of these technologies is presented first, followed by integrated combined cycles. Integrated (or hybrid cycles) are in particular object of strong interest in recent years because the pooling of common components of power and cooling production cycles in a single cycle, can lead to more compact and less expensive solution than configurations providing the same functionalities separately. These cycles have also been demonstrated to achieve higher performances [137], but are still emerging concepts with a low technology readiness level (TRL).

### 2.5.1 ORC coupled to vapour based chillers

The combination of power cycles and vapour based chillers (mechanical compression chillers, absorption machines, ejector refrigeration cycles etc.) has been object of several studies [138].
Liang [139] investigated a heat driven cooling system that combined an ORC to a vapour compression chiller (VCC), aiming to provide a more compact alternative to absorption chillers in applications where size constraints are very limiting.

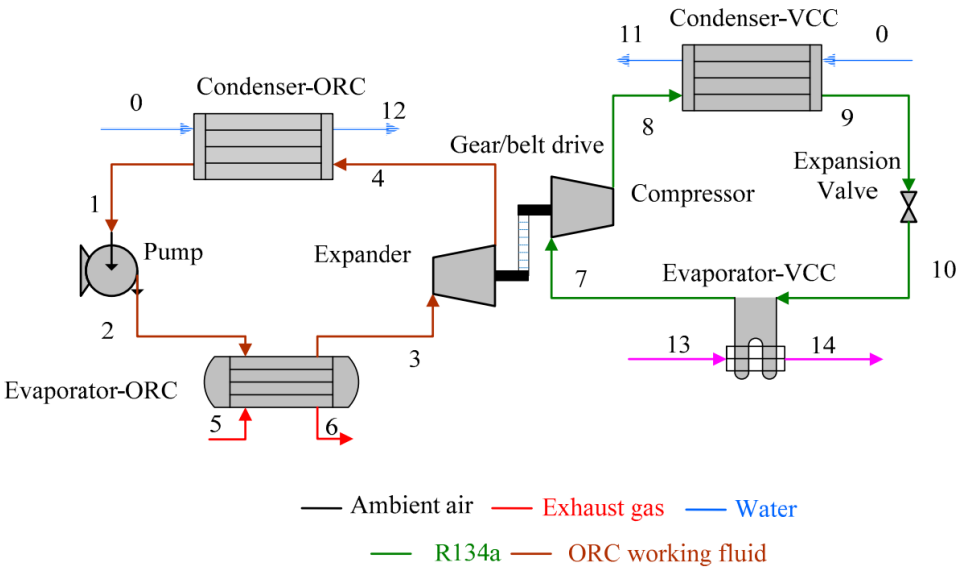


**Fig. 2.33 –** Organic Rankine cycle-vapour compression cycle systems for waste heat recovery [139].

Bao [140] compared four different systems based on single-fluid and dual-fluid combination of ORC and VCC. Both single-fluid and dual-fluid systems showed good COP, increasing with the temperature of the hot source up to around 0.5 at 150 °C.

Cao [141] proposed the combination of a Kalina cycle (**Fig. 2.7**) and an absorption cycle in cascade (**Fig. 2.25**). In the proposed configuration, geothermal heat is supplied to the Kalina cycle and the heat contained in the poor solution at the outlet of the vapour generator is used to drive in cascade an absorption cycle. Results showed that the exergetic efficiency and net power output of Kalina-based CCP were higher than those of separate generation system were.
Zare et al. [36] compared two serial configurations, consisting of a power cycle (ORC and Kalina), a single stage absorption chiller and a heat exchanger for providing domestic hot water. The exergetic efficiency of the configuration using a Kalina cycle (50.36%) was found to be slightly higher than the one integrating an ORC (46.51%). Pastor-Martinez et al. [142] compared the energy and exergetic efficiency of several polygeneration arrangements driven by low and medium temperature source (80-150 °C) for the production of cooling, heating and electricity. The polygeneration systems consisted of an ORC, an absorption chiller (single or half-effect) and heat exchangers producing simultaneously power, cooling and useful heat. Eight possible configurations were studied (serial cascade, parallel and hybrid series-parallel configurations) showing that there is a threshold temperature at which there is a shift in the configuration with the highest performance. Additionally, it was observed that the configurations in which ORC and absorption cooling were placed at the first thermal level were the ones with the highest energetic and exergetic performance.

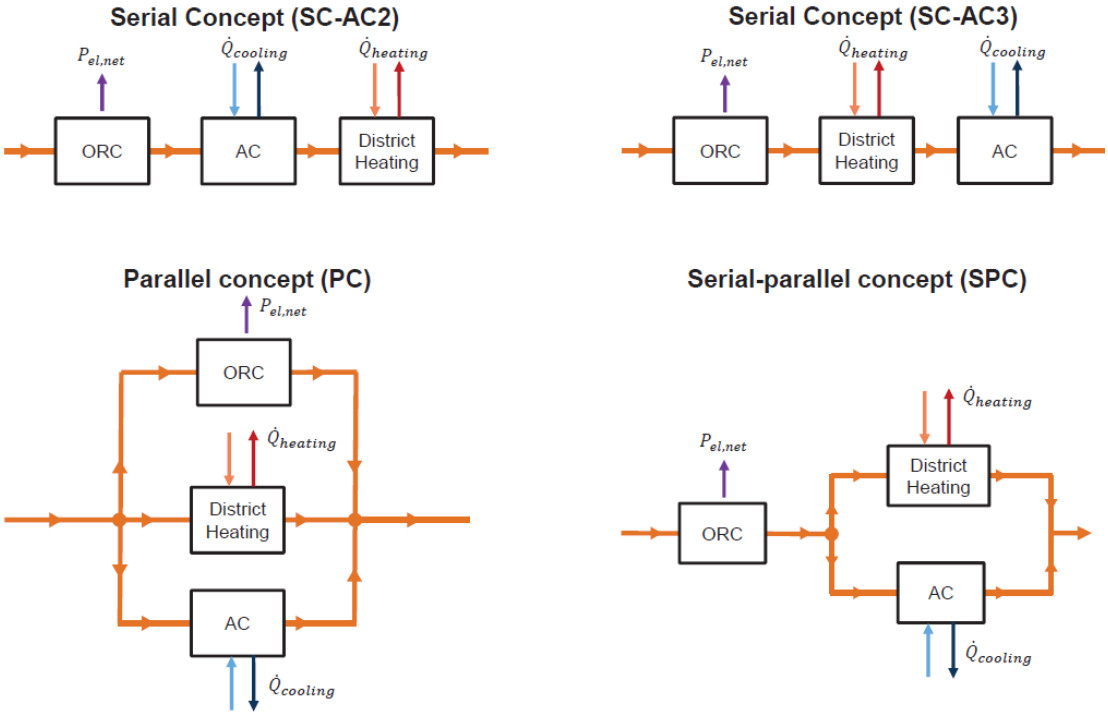


**Fig. 2.34 -** Simplified visualization of different power, cooling and heating configurations [143]. (AC: Absorption Chiller).

Schifflechner et al. [144] investigated different plant configurations focusing on part load effects of the ORC system, but only considered a standard LiBr-$H_2O$ absorption chiller for cooling. In a following study [143], the analysis was extended to different absorption chiller concepts (single stage, double effect and double lift) applied in the four configurations shown in **Fig. 2.34**. The calculations were carried out for a hot source temperature of 130 °C and taking into account partial load behaviour. The highest annual net power output was obtained using a serial configuration with the absorption chiller in third position working with a desorber temperature of 45 °C only. On the other hand, in the case of serial-parallel and parallel configurations the standard absorption chiller was the optimal choice to maximise net power production of the Rankine cycle.
Combinations of ORC and ejector refrigeration systems have also been proposed [145].

### 2.5.2 Thermochemical combined cycles

Based on the same working principle as adsorption cycles, hybrid cycles involving a solid-gas sorption process (adsorption or thermochemical) also function in discontinuous-mode operation and for this reason have the advantage of being able to address storage issues.
Thanks to the great diversity of reactive solids available, thermochemical cycles can cover a very wide range of operating conditions.
Wang et al. [146] investigated a combined cooling and power thermochemical cycle using two solid reactants implemented in two separate fixed-bed reactors. The thermodynamic study showed that COP and exergetic efficiency reached 0.77 and 0.9 respectively for a heat source temperature in the range 100-400 °C. An experimental study performed by the same authors highlighted the difficulties to guarantee a stable power production due to fluctuations in the kinetics of the solid-gas chemical reaction [147].
Another technical limitation of hybrid thermochemical cycles is the fact that ammonia is a wet fluid, causing problems during expansion. To overcome the issues of liquid droplets at the expander outlet, Bao et al. included a superheater upstream of the expander [148].
Jiang et al. [10] proposed a novel system, integrating internal heat recovery to improve energy performances. For heat source temperatures in the range 200–360 °C and cooling effect at 0 °C, results showed a very high COP of 1.3 and exergy efficiencies between 0.41 and 0.74 [149].

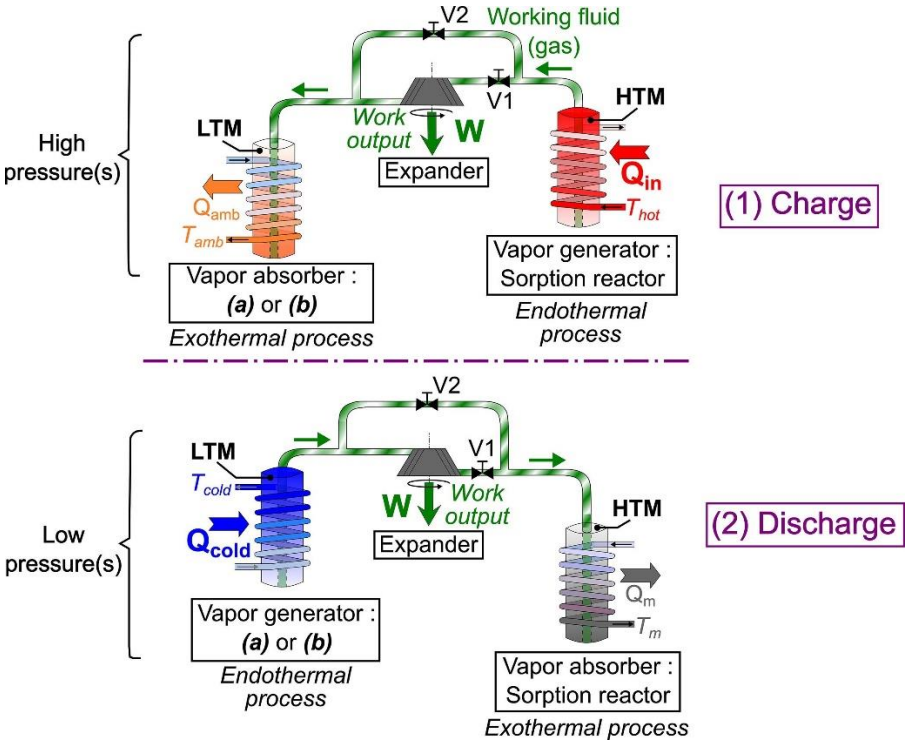


**Fig. 2.35 -** Resorption hybrid thermochemical cycle for power and cold combined production [150].

The general working principle of hybrid thermochemical working cycles (**Fig. 2.35**) is described by Godefroy et al. [150]. These cycles have two time-shifted operating phases (providing and intrinsic storage function), each of which involves a steam generator component and a steam consumer component. The two steps are a charging phase when the heat source is available and then a discharging phase. The expander present in the cycle can be used to generate mechanical work during the charging or discharging phase or during both phases. This kind of hybrid cycle can therefore function in three different modes: separated power and cooling production mode (the expander operates in the charging step, while cooling is produced in the discharging step), simultaneous cooling and power production mode (the expander operates in discharging together with the cooling production), and combined mode (the expander operates in both steps and cooling is produced in the discharging step).
The energy efficiencies of the cycle in **Fig. 2.35** where in the range 0.24-0.61 [150], while exergy efficiencies were in the range 0.06-0.4.

### 2.5.3 Ejector based combined cooling and power cycles

Ejector-based refrigeration cycles are another interesting option for CCP applications. Wang et al. [151] proposed the integration of an ejector in an ORC cycle. A similar concept was studied by Chen et al. [152]. In this system, a steam bleeding from the turbine (point 3 in **Fig. 2.36**) is used as primary fluid in the ejector to entrain a secondary fluid coming from the evaporator. The primary and secondary fluids, fully mixed at the ejector outlet, reach the condenser where they meet the remaining fully expanded vapour from the turbine outlet, rejecting heat to the environment. Among the different fluid studied, for a heat source temperature of 120°C, evaporator temperature of 10°C and condenser temperature of 35°C, methanol showed the highest thermal efficiency of 0.195, followed by ethanol and water (0.173).

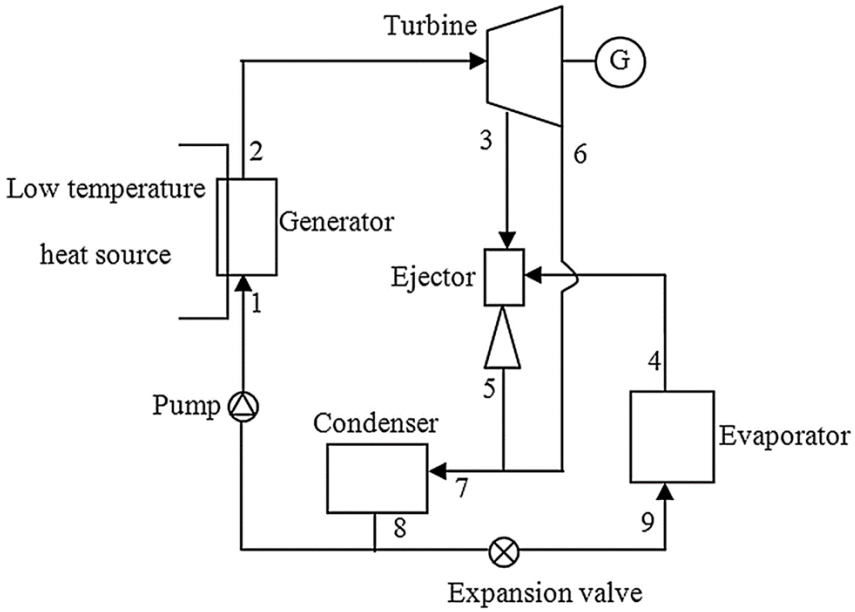


**Fig. 2.36 -** Schematic diagram of the combined power and ejector cooling system [152].

Zhao et al. [153] applied the ORC-based ejector refrigeration cycle to a flash/binary power generation system. Ghaebi et al. [154] proposed a Kalina-based ejector refrigeration cycle CCP system in which the poor solution is divided into two streams, one of which is much expanded to reduce its temperature. The low-temperature ammonia-water mixture produces the cooling effect at the evaporator, and then is mixed with the turbine outlet stream by the ejector. In a following work [155], the same authors proposed a modified system in which a two-stage turbine and two vapour-liquid separators are used with multiple internal heat exchangers. The optimum thermal and exergy efficiencies calculated were 15% and 47.8%, respectively.

### 2.5.4 Absorption based combined cooling and power cycles

As previously discussed, while cooling demand is often seasonal, power demand is more constant throughout the year. A combined absorption system producing not only power as is the case for Kalina or ORC cycles but also cooling, could be capable of functioning in a wide range of operating conditions from power only to cooling only, including different ratios of the two outputs.

The most commonly used mixture for absorption cooling and power production systems is ammonia-water, even if other mixtures can also be used [38].
Literature depicts various architectures of absorption cooling and power (ACP) production cycles. A first overview of the systems studied was proposed by Ayou et al. [38]. Two main families stand out: series architectures [39,40,156] and parallel architectures [41,42,157]. The former generally privilege the production of electricity while the latter offer more flexibility between the different production modes and are easier to implement. In addition, series architectures generally produce the cooling effect using sensible heat (e.g. the Goswami cycle) while parallel architectire use latent heat (e.g. hybrid Rankine and absorption chiller cycles).
Regardless of the architecture, cooling can be produced through absorption chillers [41,156,157] or ejectors [39]. The combination of both technologies was also considered in several studies [42,158]. Electricity is produced by

the expansion of the working fluid in an expander (volumetric [157] or turbine type [158]) coupled to a generator [86]. Some noteworthy architectures are described in the following.

### *Series architectures*

Goswami [7] proposed a modification of the Kalina cycle, improving the efficiency by the simultaneous production of power and cooling effect (**Fig. 2.37**). This cycle shares remarkable similarities with the Kalina cycle and an ammonia-water absorption cycle. In particular the three cycles share the same solution circuit, but the Goswami cycle integrates both an expander (for example a turbine in **Fig. 2.37)** and a refrigeration heat exchanger in the refrigerant side of the cycle.

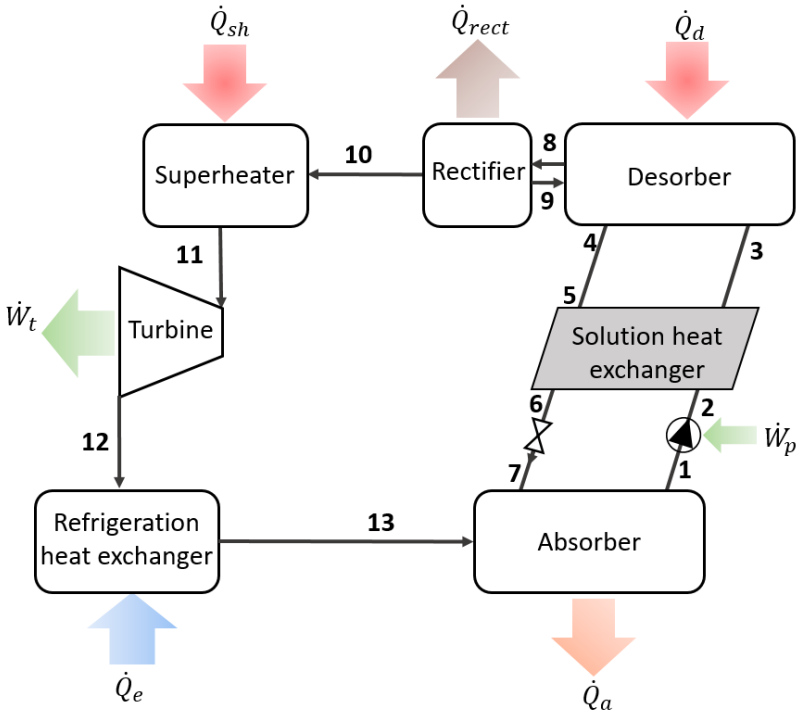


**Fig. 2.37** –Schematic diagram of the Goswami cycle.

The purified vapour exiting the rectifier is superheated and expanded in the expander to generate power. Expanding the vapour below the ambient temperature can simultaneously provide power and refrigeration. The refrigeration effect is obtained by sensible heating of the vapour at the turbine outlet. Indeed, the cooling effect is possible because the condensing temperature of an ammonia-rich vapour can be significantly lower than the saturation temperature of a lower concentration ammonia–water mixture. The vapour is then reabsorbed in the poor solution in the absorber.
Expanding the vapour to low temperature in the expander requires a vapour with a high ammonia purity, which due to the necessary rectification process, does not favour power production. Superheating of the rectified vapour increases power production but it degrades cooling production.

Goswami and co-workers studied the proposed cycle extensively [159]. Simulations of the cycle resulted in a maximum first law efficiency of 23.54% with the working fluid entering the turbine at 137 °C and 30 bar and exiting at 2 bar. Tamm and Goswami [160] experimentally demonstrated the feasibility of the Goswami cycle highlighting the potential for combined turbine work and refrigeration output in system operation. Their results showed that vapour generation and absorption condensation exhibited the expected trends but with deviations from ideal and equilibrium modelling.
Hasan at al. [161] performed the optimization of the same cycle from the perspective of the second law of thermodynamics. The authors obtained a maximum second law efficiency of 65.8% at 147 °C heat source temperature while the maximum irreversibility was found to take place in the absorber (44% of total irreversibility) with the rectifier and the solution heat exchanger also contributing significantly (16% and 24% respectively). Zare et al. [162] conducted a thermoeconomic optimization of the Goswami cycle obtaining a 18.6% and 25.9%

reduction in the sum of the unit cost of the system products compared to the cost of the cycle products obtained through at the cycle optimized from the first and second law of thermodynamics viewpoint respectively.

## *Parallel architectures*

Among the Combined Cold and Power production (CCP) cycle architectures under development, those in parallel are the most versatile and easiest to implement but they have not been widely investigated yet.

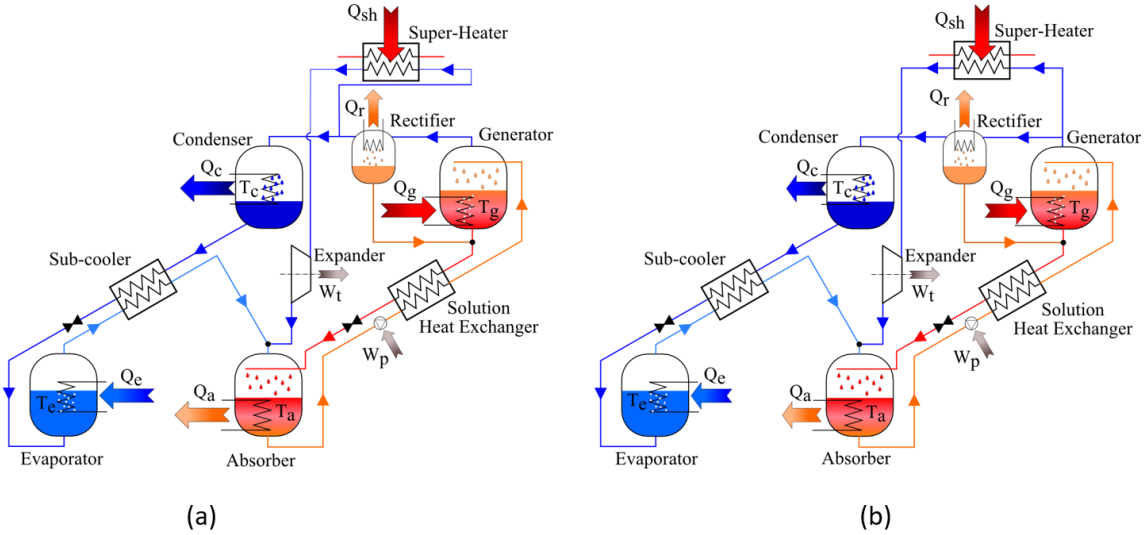


**Fig. 2.38 –** Schematic diagram of a CCP cycle with two different rectifier configurations [33].

An example is shown **Fig. 2.38**. It consists of a water-ammonia absorption cycle in parallel with power production line using part of the desorbed ammonia vapour to feed an expander for electricity production. While in the case of **Fig. 2.38(a)** the rectification is effective for both the cooling and the power production lines, in the configuration shown in **Fig. 2.38(b)** the ammonia expended to generate power is not rectified as the switch valve directing the flow between the two production lines is positioned before the rectifier. The two variations of the cycle exist in different architectures present in the literature [41,157].
The results found by Voeltzel et al. [33] using a scroll expander confirmed the relevance of the rectifier to improve the performance of cooling production. In addition, the COP is relatively unaffected by the cycle configuration since in both configurations the rectifier is always upstream of the cooling production line, but the rectification of ammonia before the expander results in a significant decrease of the expander efficiency. This trend does not occur when the ammonia entering the expander is not rectified. Thus, the loss of performance attributable to the presence of water vapour in the working fluid is less significant than that due to the reduction in flow rate caused by the rectification in the case of a scroll expander.

Also employing parallel architecture, Zheng et al. [163] introduced an absorption combined power and cooling cycle operating at a maximum pressure of 50 bar with high and intermediate temperatures of 350 °C and 137 °C. The cycle consisted of two boilers, two absorbers, two heat exchangers, a condenser, evaporator, rectifier, separator (at intermediate pressure) and turbine for work production. The amount of refrigerant to the power and cooling lines could be adjusted to get the desired power and cooling output using a splitter. The reported overall thermal efficiency of the system was 24.2%, while its exergetic efficiency was 37.3%.
Mendoza et al. [157] focused on the integration in parallel of a scroll expander in absorption cycles for the simultaneous production of cooling and power. A parametric cycle study was performed using three different working fluids, $LiNO_3$, NaSCN and a mixture of ammonia and water. The results demonstrated that using soluble solid absorbents performs competitively in comparison to the ammonia-water mixture. The maximum exergetic efficiency and first law efficiency obtained (43% and 11% respectively) decrease when increasing the power production of the cycle. Villada et al. [164] compared the Goswami cycle with the same parallel single- stage combined absorption cycles studied by Mendoza et al. [157]. They concluded that if the main interest is power production, the Goswami cycle offers the best first and second law efficiencies, while if the main interest is cooling the in-parallel architecture is the best option despite relatively low efficiency.

Wang et al. [42] proposed a new combined power and ejector–absorption refrigeration cycle combining the Rankine cycle and the ejector–absorption refrigeration cycle, to generate both power and refrigeration output simultaneously. The introduction of an ejector between the rectifier and the condenser, provided a performance improvement without greatly increasing the complexity of the system. For 25 bar pressure and 285 °C temperature at inlet of turbine and 1.2 bar pressure and 96 °C temperature at the exit of turbine, thermal and exergy efficiencies of the system were 20.97% and 35.77% respectively.
Mohmoudi and Kordlar [165] proposed the combination of a Kalina cycle with a double effect absorption cycle for harvesting geothermal energy. The cycle was optimized for both maximum exergetic efficiency and minimum total product cost showing that in the second case the total product unit cost is around 17% lower than in the first, with a highest exergetic efficiency found of 34.8%.
Shokati et al. [8] investigated two different configuration of a double effect absorption refrigeration-Kalina cogeneration cycle for the recovery of heat from high temperature heat sources. Seyfouri [166] analysed a cogeneration system consisting of an organic Rankine cycle and a hybrid GAX cycle using geothermal hot water at 133 °C to generate power and cooling at -50 °C obtaining a maximum exergetic efficiency of 42.8%.

### 2.5.5 Performance parameters

In addition to the cooling and electrical power outputs, both first and second law based performance criteria are important to evaluate a combined cycle performance.
The system first law efficiency $\eta_I$ (sometimes referred to as energy utilization factor [167]) is defined as the ratio of useful outputs (cooling and net electrical power) to the total driving thermal energy inputs [168]:

$$\eta_I = \frac{\dot{W}_{ele,net} + \dot{Q}_e}{\dot{Q}_d + \dot{Q}_{sh}} \tag{2.19}$$

In **Eq. (2.19)** the net electrical power generated by the turbine is calculated as: $\dot{W}_{ele,net} = \eta_{gen} \cdot \eta_{mech} \cdot \dot{W}_t - \dot{W}_p = \dot{W}_{t,ele} - \dot{W}_p$ [169], where $\eta_{gen}$ is the electric generator efficiency, $\eta_{mech}$ is the mechanical coupling efficiency [170] and $\dot{W}_p$ is the overall power consumption of the pump (including isentropic, mechanical and electric efficiencies).
However, as observed in [171], **Eq. (2.19)** overestimates the efficiency of the cycle by giving the same value to the cooling and electrical power outputs of the system. To avoid misleading results, the authors suggested the use of a modified first law efficiency, replacing cooling power output $\dot{Q}_e$ with the exergy associated with the refrigeration output $\dot{E}x_{P,e}$:

$$\eta_{I,eff} = \frac{\dot{W}_{ele,net} + \dot{E}x_{P,e}}{\dot{Q}_d + \dot{Q}_{sh}} \tag{2.20}$$

Also the modified expression of **Eq. (2.20)** fails to account for the quality of the thermal input, thus not reflecting all the losses due to irreversibility in a cycle. Hence, to evaluate the true value of useful outputs of a combined cooling and power cycle, exergetic efficiency must be used [172]. The exergetic efficiency of the system can be written as [173]:

$$\eta_{ex} = \frac{\dot{W}_{ele,net} + (\dot{E}x_{e,o} - \dot{E}x_{e,i})}{(\dot{E}x_{d,i} - \dot{E}x_{d,o}) + (\dot{E}x_{sh,i} - \dot{E}x_{sh,o})} = \frac{\dot{W}_{ele,net} + \dot{E}x_{P,e}}{\dot{E}x_{F,d} + \dot{E}x_{F,sh}} \tag{2.21}$$

For parallel architectures, in which the desorbed vapour is divided between the cooling and the electrical power production lines, another very important parameter is the split ratio used to measure the fraction of refrigerant vapour passing through the cooling production line over the total desorbed refrigerant vapour.

$$r_s = \frac{\dot{m}_{ref,cooling}}{\dot{m}_{ref}} \tag{2.22}$$

The absolute values of efficiencies defined in **Eq. (2.19)-(2.21)** for parallel architectures depends on the split ratio with which a cycle operates. Therefore, although optimisation of these parameters is often sought, this is not always possible if a value of $r_s$ is imposed.

## 2.6 Synthesis

In the current context, low temperature heat recovery has become a priority. A large number of studies has been carried out in this field covering a very wide range of applications.
Concerning the production of electricity and cooling, research has led to the development of efficient technologies ready to be produced and used on a large scale. For the production of electricity, two technologies in particular have attracted interest: Kalina cycles and organic Rankine cycles. Organic Rankine cycles have experienced great success in recent years and are now a mature technology. Kalina cycles present a theoretical efficiency advantage over ORCs but have not gained market favour because of their higher complexity (due to the use of the ammonia-water mixture and the need for more components). Additionally, the challenges of designing an expander adapted for the corrosiveness of the ammonia water-mixture has been highlighted.
To produce cooling, sorption technologies, and in particular absorption machines, hold great promise for the future because of their flexibility, possibility to use different heat sources, low electricity consumption and reliability.

Several authors have envisaged the combination of ORCs and sorption cycles to achieve higher energy efficiencies. Co-production cycles (or hybrid cycles) are object of strong interest because the mutualisation of common components, can lead to less expensive solutions and higher performances. However, these cycles are still emerging concepts with a low technology readiness level (TRL).

The focus of this work is on absorption-based cooling and power combined production cycles. A wide variety of different architectures has been proposed in literature, generally favouring the power output (as in the Goswami cycle [7]) rather than the cooling output. In general, architecture can be divided based on the cooling producing mechanism: architectures producing cooling using sensible heat (mainly the Goswami cycle) and architectures using latent heat (like parallel combinations of an absorption and a power cycle). The most commonly used fluid in this type of cycles is the ammonia water mixture.
The dual-output nature of combined absorption systems complicates their performance evaluation and requires the use of an exergy analysis. For parallel architectures, the split ratio (i.e., the ratio between the vapour passing through the cooling production line and the total vapour mass flow rate) appears to be another important parameter.

While several analyses have been performed on combined power and cooling cycles, most of them are generally limited to high heat source temperatures [8–10] or complex architectures [10]. Most of the studies available in literature involve simple modelling of the expander, usually assuming fixed isentropic efficiencies and the possibility to regulate the split ratio.
Additionally, there are very few experimental studies investigating these types of cycles, most of them regarding the Goswami cycle. Experimental studies are also needed in order to gather more data for an appropriate selection of the expansion device. Especially for small and medium scale applications, the development of a suitable expansion device is necessary, in particular for expanders working with ammonia.
Hence, from the above literature review, the need for more experimental studies and for a more detailed modelling of the expander in particular to better understand its interactions with the cycle integrating it, is strong.

In this context, this work provides so far missing experimental data on the operation of an absorption combined cooling and power production cycle with a parallel architecture. Experimental measures from the pilot plant allowed access to data concerning the functioning and performance of the cycle and of its component that have been used for the development of detailed numerical models of the absorption chiller and turbine.
These models have been subsequently used to carry out an in-depth investigation of the functioning of the cycle, highlighting its advantages and limitations, as presented in the next chapters.

# Chapter 3
# Experimental investigation

*The literature review presented in the previous chapter highlighted the lack of experimental studies on absorption combined cooling and power production cycles. These studies are however necessary for an in-depth understanding of their functioning and of the interactions between power and cooling production sides of the circuit. For this reason, the integration of an expander into a single stage ammonia water absorption chiller was undertaken. The peculiar characteristics of the expansion device, as well as the use of a newly developed combined desorber avoiding the presence of a rectifier make the prototype built unique. Design and integration of the expander proved to be very challenging, mainly due to the small size of the application and corrosiveness of the ammonia water mixture. Despite these difficulties, first experimental measurements have been obtained, giving interesting insights on the functioning of the cycle. Feedback from the pilot plant will be very useful for the further development of the technology.*

# 3.1 Introduction

The literature review presented in the previous chapter highlighted the lack of experimental studies on absorption based combined refrigeration and electricity production cycles. Most of these studies were performed on series architectures and in particular on the Goswami cycle [38]. Tamm et al. [160] constructed a prototype (details about the size are not available) to demonstrate the feasibility of the Goswami cycle and to compare the experimental results with the theoretical simulations. Deviations from ideal modelling were highlighted, but the potential for combined power and refrigeration output was demonstrated.
Han et al. [174] built an experimental rig for combined refrigeration and power production using a parallel architecture. The system, using the ammonia-water mixture could work in simple absorption refrigeration mode and absorption refrigeration and power production mode. The design cooling capacity in refrigeration mode was 10 kW and the design power capacity in power generation mode 2 kW. However, the authors claimed that no expander was available on the market for the small-scale experimental prototype. Hence, they simulated the expander using a throttling valve and a vapour heat exchanger. The same method of simulating the expander was also used in the aforementioned Goswami cycle prototype developed by Tamm et al. [160].
The expander selection is crucial for the efficiency of the system, but it is complicated by the small scales of experimental prototype (less than1 $kW_{el}$) and by the use of the ammonia-water mixture, a very corrosive fluid. This requires the development of suitable expansion devices for absorption based combined cycles and complicates the development of experimental prototypes. Nevertheless, experimental studies are crucial in order to fully understand this technology and, in particular, the interactions between the expander and the cycle that integrates it. Considering the strong interconnections between the two production lines, it is important to investigate the functioning of the machine as the two products output varies, as well as during transient operation and functioning in different operating modes.

To bring an advancement on the subject, one of the objectives of the present work was the development of a suitable expander for a small-scale absorption combined cooling and power (ACP) cycle and its integration in an existing single stage ammonia water absorption chiller. The particular characteristics of the developed expander (a supersonic partial admission axial micro-turbine) as well as the use of a newly developed component able to desorb and purify the ammonia vapour make this prototype unique. Even though the technical challenges and the problems encountered in the setting up of the pilot plant did not allow a complete characterisation, the analyses carried out and the feedback from the prototype give important insights on the functioning and limitations of this cycle and will play an important role for the future improvement of the technology.

# 3.2 Description of the architecture of the cycle

The combined cooling and power cycle under investigation is shown schematically in **Fig. 3.1**. The functioning is based on a water-ammonia absorption machine with an expander coupled in parallel to the cold production circuit. This type of architecture was chosen because of the greater flexibility it allows in choosing between cooling and electricity production [38]. With respect to the diagram shown in **Fig. 2.38** the architecture is simplified by the absence of the rectifier.
On the solution loop, a first line of solution rich in ammonia circulates from the absorber to the desorber and is pressurised by a pump. A second line comprising an expansion valve returns the poor solution to the absorber. In the desorber a supply of heat at high temperature enables both the desorption and the purification of steam, mainly consisting of ammonia, from the solution. On the electricity production line, the expander selection process (*Section 2.2.3*) leads to the choice of an axial partial-admission impulse turbine for production of the power $\dot{W}_T$ (presented in *Section 3.3.2*). Before the turbine, a superheater provides power $\dot{Q}_{sh}$ to increase the temperature of the fluid to ensure that it remains in the gas state throughout the expansion which occurs inside the turbine. Indeed, condensation of the mixture during the expansion would be detrimental to the functioning of the expander and could lead to its rupture.

On the cold production line, ammonia is condensed through the exchange of thermal power $\dot{Q}_c$ with an intermediate temperature source. Before cooling the cold source at the evaporator by absorbing a power $\dot{Q}_e$, the fluid is expanded in a valve to achieve low pressure. A sub-cooler is used to pre-cool the ammonia before it expands using the ammonia coming out of the evaporator. The ammonia flows of the two production lines of cold and power mix and are ultimately absorbed in the poor solution in the absorber.

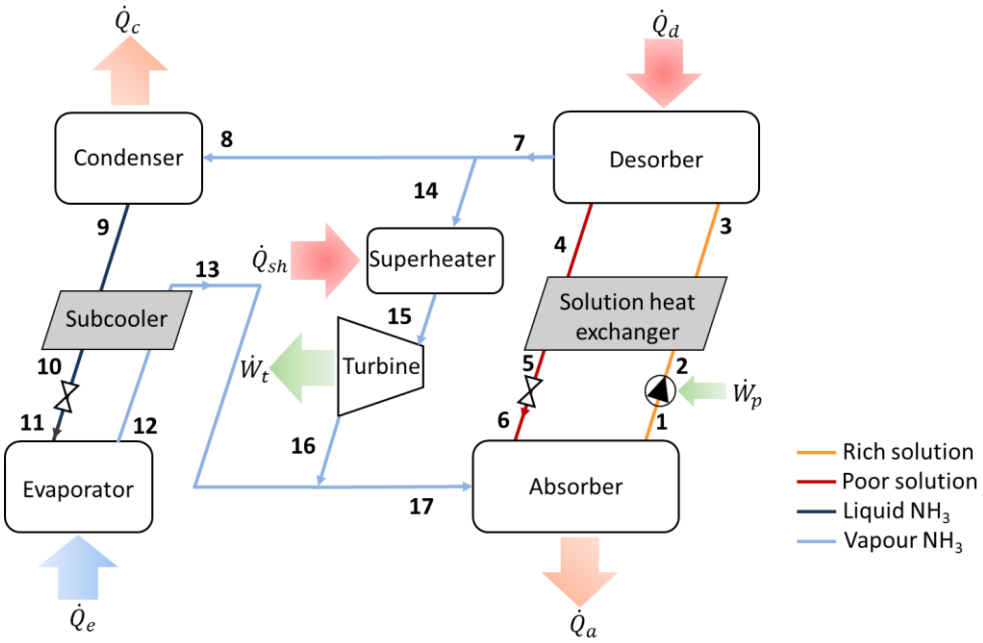


**Fig. 3.1 -** Schematic diagram of the combined cooling and power production cycle.

## 3.3 Experimental prototype

### 3.3.1 Absorption chiller prototype

The cooling and power production prototype (**Fig. 3.2**) is based on an existing single-effect ammonia-water absorption chiller of 7 kW cooling capacity developed by CEA INES since 2011.

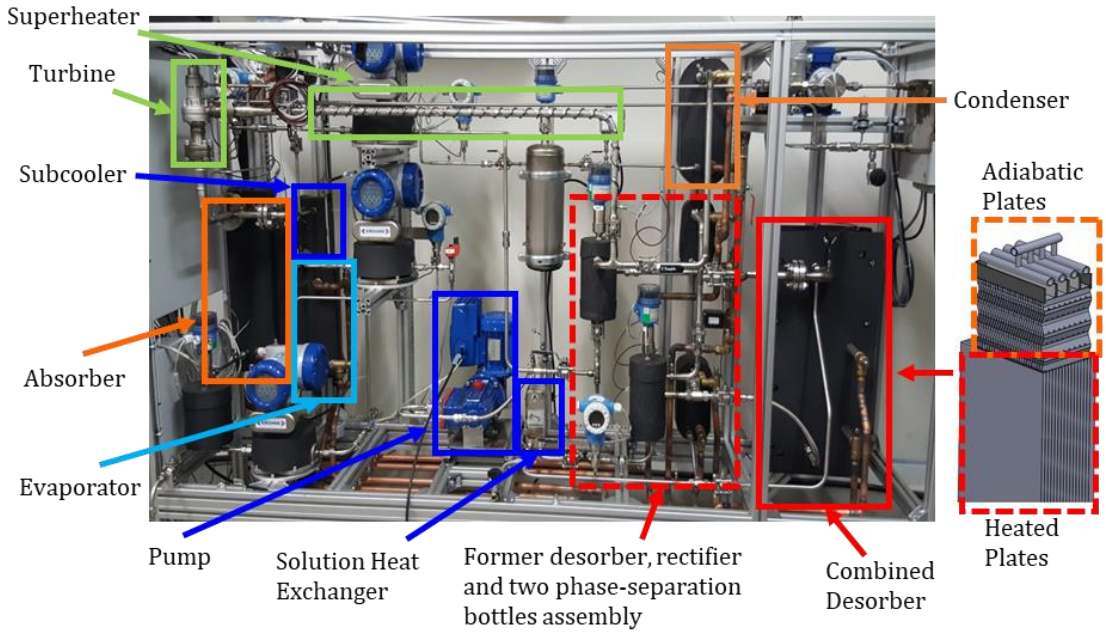


**Fig. 3.2 -** Picture of the prototype of the $NH_3/H_2O$ combined cycle.

Since the ammonia-water mixture is corrosive to most common materials, only stainless steel and EPDM or PTFE for seals and membranes were used in the prototype. In order to increase the compactness and reduce the cost of the prototype, only commercial brazed/welded plate heat exchangers are used. Particular attention was paid also

to the selection of the pump, the main electricity consuming component of the cycle. Since the liquid solution entering the pump comes from the absorber, its temperature is relatively close to saturation and desorption around the moving parts might occur in the presence of frictional heating. As this could severely reduce its lifespan, the pump must show very little heating, even locally. These considerations lead to the selection of a *Hydra-Cell* diaphragm triplex single-acting pump, driven by an induction motor coupled to a variable frequency drive for flow control. Detailed performance evaluation of the pump integrated in the cycle was performed by Landelle et al. [120].
The chiller [13] was originally composed of seven heat exchangers. The five main ones were external heat and mass exchangers: desorber, absorber, evaporator, condenser and rectifier. Among these, the most critical is certainly the absorber, extensively studied and characterised in the absorption chiller prototype by Triché et al. [175]. Two internal heat exchangers, the solution heat exchanger and the subcooler are used to improve the performance of the cycle. Four reservoirs were present in the original absorption chiller: two phase separation tanks (each of 1 L volume) at the outlet of desorber and rectifier, needed to separate the ammonia vapour from water condensate, and two buffer tanks before the pump (0.7 L volume) and subcooler (5.2 L volume). Piping (internal diameter of 10 mm for liquid piping and 17.3 mm for vapour piping) and separation tank design was done in-house to meet operating conditions requirements specific to the prototype.
Usual control components for ammonia-water systems (thermostatic expansion valves, time regulated valves, etc.) could not be found in an adapted size for the prototype [13]. Electronically actuated expansion valves are hence present in the loop, one before the evaporator, regulating the temperature glide during the evaporation process, and the other before the absorber, on the poor solution line, controlling the level of the reservoir upstream of the pump. Volume of the components determines the quantity of water and ammonia needed, which in the case of the prototype are around 1 kg of water and 2.5 kg of ammonia. Filling of the machine is performed by first injecting water in a low point of the prototype close to the reservoir upstream of the pump, and then injecting ammonia in a high point of the machine, near the reservoir downstream the condenser.

Wirtz et al. [29] recently designed and tested a new combined falling-film desorber/rectifier (**Fig. 3.3**), performing an internal purification of the desorbed vapour with the rich solution at inlet. This heat exchanger is composed of a distribution system dividing uniformly the rich solution at inlet, a lower part where vapour is generated exchanging heat with the hot source, and an adiabatic upper part allowing the purification of the vapour generated by partial reabsorption of the latter in the ammonia-water solution entering the exchanger. The combination of the heated and adiabatic sections enables replacing two plate heat exchangers used for the desorber and the rectifier as well as two associated phase-separation bottles by only one component, thus helping to reduce costs and overall dimensions. The high purity of the ammonia vapour at the desorber exit eliminates the need for further purification, making this solution particularly interesting in terms of compactness and performance.

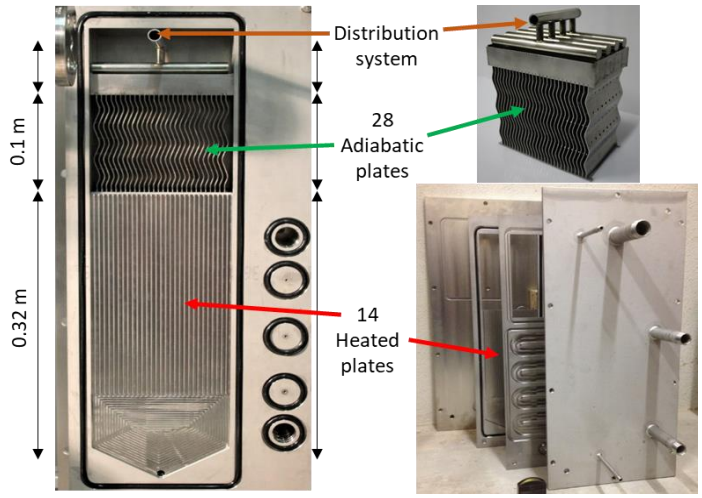


**Fig. 3.3** - Exploded view of the combined desorber/rectifier [29].

Experimental studies [29] showed that the combined desorber/rectifier is highly efficient and guarantees very high purity of the ammonia vapour (above 98% [118]) with a lower heat supply needed, thus improving the COP of the cycle. Additionally, the functioning of the machine is more stable and steady conditions are reached faster. Hence, this component was used in this work. The geometry of the desorber as well as that of the other stainless steel corrugated plate heat exchangers is given in **Table 3.1.** Another smaller reservoir (0.2 L) is placed at the poor solution side desorber outlet, to detect possible flooding of the component and recover vapour trapped in the poor solution. Studies have however shown this contribution is negligible.

**Table 3.1 -** Dimensions of the heat exchangers of the cycle.

| | Absorber | Condenser | Desorber heated (adiabatic) part | Evaporator | Solution Heat Exchanger | Subcooler |
|---|---|---|---|---|---|---|
| Plate width [mm] | 96 | 111 | 320 (100) | 111 | 72 | 72 |
| Plate length [mm] | 668 | 310 | 150 (90) | 310 | 187 | 187 |
| Plate thickness [mm] | 0.5 | 0.5 | 6 (0.8) | 0.5 | 0.5 | 0.5 |
| Number of plates [-] | 16 | 40 | 16 (28) | 24 | 25 | 20 |
| Total surface [$m^2$] | 0.89 | 1.30 | 0.67 (0.23) | 0.75 | 0.31 | 0.24 |

The chiller is connected to a characterization bench, in which independent hydraulic loops fix the temperatures and the mass flow rate of the external heat transfer fluids (HTF) inside the generator, condenser, absorber and evaporator. The temperatures and mass flow rates of HTFs, the rotational speed of the pump (controlling the rich solution mass flow rate) and the opening of the actuated expansions valves (controlling the temperature glide in the evaporator and the level of the buffer tank before the pump) are the only control parameters available. They are used to modify the operating conditions of the chiller to perform the tests necessary for the characterization of the machine. Nominal point and operating range of components are given in **Table 3.2**. It can be noted that the nominal cold source inlet temperature is relatively high, 18 °C (corresponding to a cooling production around 13 °C), due to the pre-existing design of the prototype for air-conditioning applications. However, within these ranges, tests give trustworthy insights on the operation of the machine and can be used to validate numerical models that could be able to extrapolate results at lower cooling production temperatures.

**Table 3.2 -** Nominal point and operating range of components.

| | | Absorber | Condenser | Desorber | Evaporator | Pump |
|---|---|---|---|---|---|---|
| Temperature [°C] | Nominal | 27 | 27 | 95 | 18 | 32 |
| | Minimal | 22 | 22 | 80 | 10 | - |
| | Maximal | 30 | 30 | 106 | 22 | 50 |
| Pressure [bar] | Nominal | 7 | 12 | 12 | 7 | 7/12 |
| | Minimal | 5 | 11 | 11 | 5 | - |
| | Maximal | 8 | 14 | 14 | 8 | 5/20 |
| HTF and pump mass flow rate [kg/h] | Nominal | 1,200 | 1,200 | 1,600 | 1,100 | 150 |
| | Maximal | 1,300 | 1,300 | 1,800 | 1,200 | 250 |
| | Minimal | 200 | 200 | 200 | 200 | - |
| Power [kW] | Nominal | 9 | 7 | 10 | 7 | 0.55 |

### 3.3.2 Turbine

Starting from the existing experimental rig described in the previous section, a power production line was added in parallel to the cooling production line. Indeed, part of the pressurised steam produced at the desorber can be fed to an expander coupled to an electrical generator to produce electricity. Expanders for combined cooling and power cycles benefit from the recent developments of Organic Rankine Cycles (ORC) [176]. However, since combined production systems are quite complex, only a few experimental investigations have been conducted. Voeltzel et al. [33] proposed the integration of a scroll expander in the testing rig. The model developed by Lemort et al. [89] was adjusted on experimental results from a 1 kW Air Squared scroll expander mounted on an ORC rest rig developed at CEA Grenoble [120] using R245fa and adapted to use ammonia as a working fluid as detailed by Mendoza et al. [177].
Results highlighted that the leakage area determined for the expander on the ORC rig (5.7 $mm^2$) would have resulted in quasi-a nil production of the scroll in the investigated ammonia-water absorption chiller prototype. Indeed, given the small size of the prototype and the very low mass flow rates (around 20 kg/h), a much higher volumetric efficiency of the expander would have been required (leakage area around 1 $mm^2$). Additionally, no supplier of scroll expanders working with ammonia was found.
A different power generation technology was therefore investigated for the prototype, that of a turbo-expander.

The expander selection process, described in *Section 2.2.1* and based on Balje's Turbine chart (**Fig. 2.15**), requires a preliminary evaluation of $N_s$ and $D_s$. In this application, the conditions defined (in a previous work) for the design of the turbine were: inlet pressure of 16 bar, inlet temperature of 120 °C, outlet pressure of 4 bar, mass flow rate of 20 kg/h. The calculated $N_s$ and $D_s$ of around 2-5 and 10-14 (depending on the different rotational speed and diameter supposed) suggested the partial admission axial turbine to be the best choice (with a total to static

maximum efficiency of around 40-50%. As a reminder total to static efficiency is calculated as the ratio of the turbine work output to the enthalpy drop). It should be noted that design conditions are quite different from actual operating conditions of the prototype (**Table 3.2**.), generating increased losses, as discussed in the following.
The expander integrated in the cycle is hence a partial admission supersonic impulse axial turbine, characterised by 27 rotor blades and a stator composed of a single converging-diverging injector is shown in **Fig. 3.4**. This choice of expander allows avoiding excessively small and unfeasible dimensions or too high and impracticable rotational speed, at the cost of increased partial admission losses. The diameter of the rotor is of 60 mm, the throat and exit section of the injector are respectively around 2.7 $mm^2$ and 4.6 $mm^2$, while the design rotational speed is 75,000 rpm. In addition, the fact that all the expansion takes place in the injector means that there is no pressure drop in the rotor, therefore reducing losses due to leakage. This proves to be very beneficial for the application since leakage losses cause major performance reductions for machines of this size.
However, despite a design rotational speed of 75,000 rpm, mechanical tests performed powering electrically the turbine showed an abrupt increase of vibration for rotational speed above 32 500 rpm, advising against the use of the turbine above 30,000 rpm.

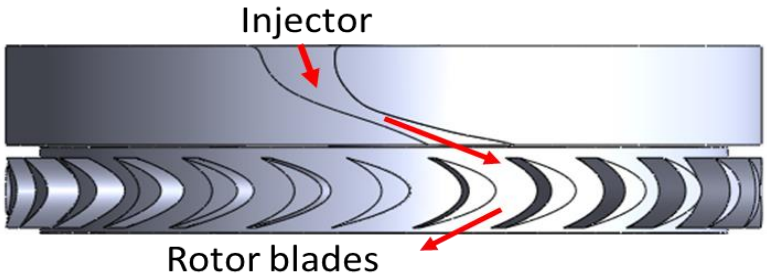


**Fig. 3.4 -** Schematic diagram of the turbine.

The turbine rotor is made of titanium to reduce its weight and increase the maximum attainable rotational speed, while the rest of the expander is made of stainless steel.
The production of electricity is achieved using a 1950/10 brushless *LMT* electrical motor used as an electrical generator. The output current is three-phase with a variable voltage which is measured by a voltmeter. The electricity produced by the generator is thermally dissipated on an electrical resistance rig composed of 3 electrical resistances (R1=1.2 ohm, R2=2.4 ohm and R3=4.9 ohm respectively) that can be either used individually or arranged in parallel/series to change the total resistance.
The resistance rig allows the expander to evacuate the electricity produced and regulates the rotational speed of the expander which is estimated using the frequency of the electrical power output measured with a frequency meter. Increasing the electrical resistance allows reaching higher rotational speeds.
To increase the efficiency of power production and avoid condensation of the working fluid (of wet type), an electrical superheater of 1 kW nominal power is placed before the turbine inlet. Indeed, given the high speed of the flow at the injector outlet, the presence of droplets colliding with the rotor blades could lead to the breaking of the moving parts of the turbine. However, the maximum turbine inlet temperature must be kept below 130 °C, and an additional cooling circuit is installed to keep the temperature of the electrical generator below 60 °C to avoid demagnetization of the permanent magnets of the electric generator.
Finally, the prototype is completed by a line, comprising a variable opening manual valve, allowing to by-pass the turbine to ensure that the steam conditions are appropriate before allowing its inlet in the turbine. By varying the valve opening, the by-pass line can also be used to assess the impact on the cycle of diverting a variable mass flow rate towards the power production line.

### 3.3.3 Experimental measurement apparatus

The ammonia-water absorption chiller is fully instrumented with high precision sensors as shown in **Fig. 3.5**. Measures of temperature (with T-type thermocouples for the working fluid and platinum resistance thermometer for heat transfer fluids), density and mass flow rate (with Coriolis flow meters) and pressure are available at the inlet and the outlet of the main components. Liquid level sensors are placed in each reservoir to monitor the fluid distribution in the prototype and, in the case of the reservoir upstream of the pump, ensure safety of operation. The turbine test bench is also equipped with measures of tension and frequency, allowing to calculate its rotational speed and the electrical power output. The chiller sensors are described in **Table 3.3.**

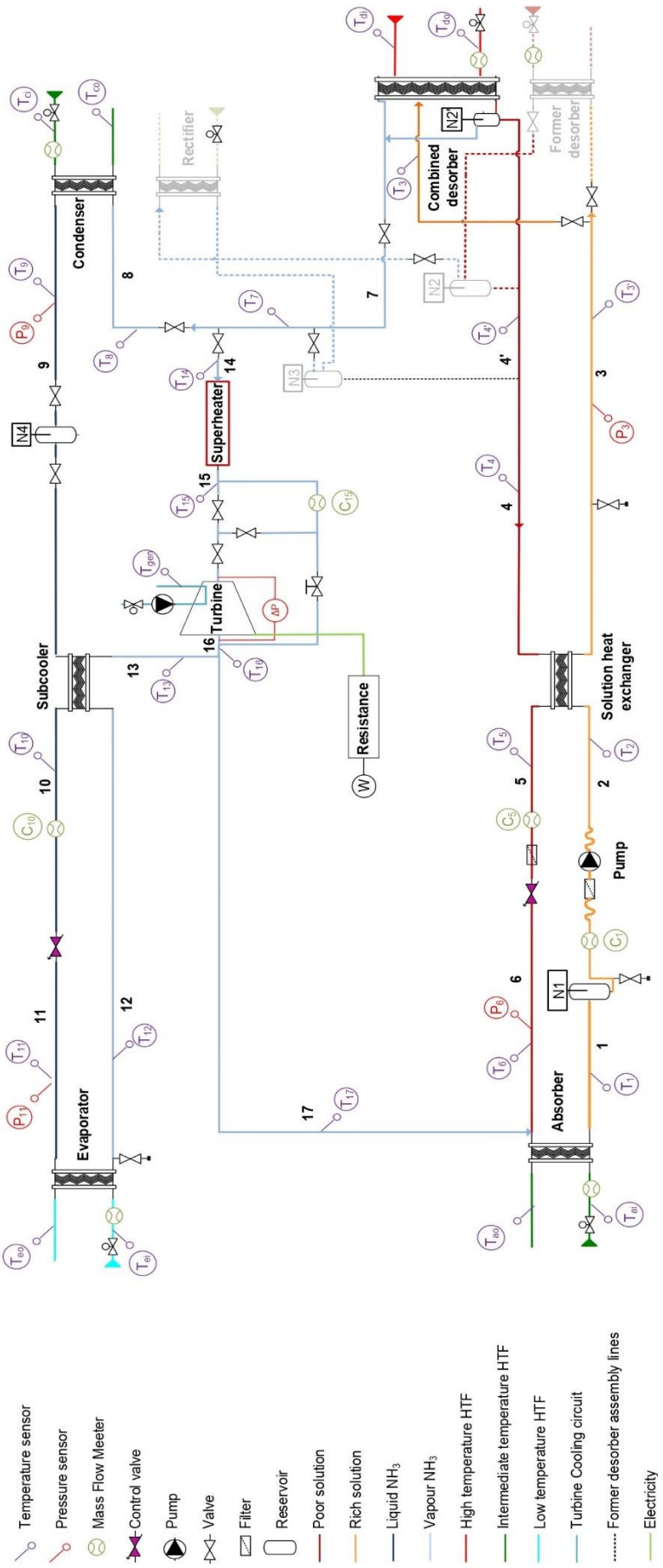


**Fig. 3.5 -** Schematic process flow diagram of the machine (created in Microsoft Visio).

With this instrumentation, it is possible to calculate both the mass fraction in the different lines of the circuit and evaluate energy balances for each component. The power exchanged by each external heat exchanger is calculated through an energy balance on the HTF side knowing the temperature at the inlet and outlet of the exchanger and the HTF mass flow rate. The electrical power produced by the turbine is calculated from the value of voltage and electrical resistance ($\dot{W}_t = V^2/R$).

**Table 3.3** - Sensor number and measurement characteristics.

| Sensor Type | Number | Uncertainty (±) |
|---|---|---|
| P-Type cooling or heating fluid temperature | 8 | 0.15 K |
| T-type refrigerant and solution temperature | 12 | 0.18 K |
| Low pressure (0-10 bar) | 2 | 0.48% |
| High pressure (0-20 bar) | 2 | 0.90% |
| Coriolis flow meter (Mass flow rate and density) | 3 | 0.3% - 2.3 kg/m$^3$ |
| Electromagnetic flowmeter | 4 | 0.5% |
| Liquid level sensors | 4 | 5% |
| Frequency meter | 1 | 1.7% |
| Tension | 1 | 0.1% |

# 3.4 Experimental tests

The absorption chiller rig described in *Section 3.3.1* was tested and characterised in previous investigations [29], proving to be reliable and capable of achieving good performances (*Section 3.4.1*). However, several problems were encountered in the combined cycle set-up not allowing an in-depth characterisation of the prototype.
A first start-up of the turbine conducted in the framework of the present PhD thesis failed due to corrosion problems of the electrical generator. The resin with which the stator coils were initially covered was found to be insufficient to protect against the ammonia-water mixture.
A re-design of the electricity generation part of the turbine was hence undertaken, leading to the use of a protective casing in titanium separating the rotor and the stator of the electrical motor, protecting it from corrosion. However, the presence of the casing is likely to have greatly reduced the efficiency of the electrical generator.
A second start-up of the plant failed as the turbine stopped functioning in the first hours of tests. The presence of a damaged bearing was revealed by posterior analysis. One of the possible causes can come from excessive efforts on bearings, highly solicited in partial admission turbines [178]. Indeed, the injection of fluid in an unevenly distributed way causes a radial force on the turbine rotor that, even if below the allowable load of bearings, can increase vibrations. Possible condensation of the working mixture in the absorption cycle loop could increase the already high stress on bearings because of the high velocity of the droplets colliding with the rotor blades. Hence, it was decided to test the turbine outside the loop using nitrogen, argon and compressed air for its characterisation (*Section 3.4.2*).
In this section, tests performed on the absorption chiller are discussed first. Subsequently tests performed on the turbine alone and on the combined cycle are presented.

## 3.4.1 Absorption cycle

The absorption chiller prototype integrating the new combined desorber/rectifier was investigated by Wirtz [29] as part of her doctoral thesis with the main goal of characterising the behaviour in the cycle of the newly developed component. Subcooling of the solution at the inlet of the combined generator was studied, showing that it enables production of a purer ammonia vapour, but affects the COP significantly, due to the need of a higher thermal input at the desorber. Therefore, the solution subcooling was not recommended. In addition, two operating modes of the combined desorber/rectifier were investigated: partially flooded and unflooded working mode. The partial flooding of the combined desorber/rectifier degrades the performance of the machine, by up to 33% for the COP and by 38% for the cooling capacity, suggesting the unflooded configuration to be favourable.

For this reason, only results from [29] concerning the unflooded working mode are presented in this document. Experimental tests were conducted varying the main operating parameters that influence cycle performance, namely the temperature of the sources and the mass flow rate of the rich solution circulating in the loop. Stable

operating conditions (pressures, temperatures and tanks level constant) were reached for each test point and the quantities measured were averaged over the period of steady functioning of duration of at least 15 minutes, to obtain the time-averaged points shown in **Table 3.4**. The interval of variation is 80-106 °C for the desorber HTF temperature, 600-1,800 kg/h for the desorber HTF mass flow rate, 22-30 °C for the intermediate temperature HTF, 80-110 kg/h for the rich solution temperature and 10-22 °C for the HTF temperature entering the evaporator. The temperature glide in the evaporator is set constant in all the tests at 5 °C as well as the mass flow rate of the other components' HTF.

**Fig. 3.6** shows the variation of the cooling power output and COP of the chiller extracted from **Table 3.4** for different desorber HTF inlet temperatures (**Fig. 3.6(a)**, corresponding to points 1-9), intermediate source HTF temperatures (**Fig. 3.6(b)**, corresponding to points 10-16), evaporator HTF inlet temperatures (**Fig. 3.6(c)**, corresponding to points 17-21), solution mass flow rates (**Fig. 3.6(d)**, corresponding to points 22-28) and, desorber HTF mass flow rates (**Fig. 3.6(e)**, corresponding to points 29-35).

**Table 3.4** – Absorption chiller experimental campaign matrix [29,118].

| Point | High temperature source [°C] | Desorber HTF mass flow rate [kg/h] | Intermediate temperature source [°C] | Low temperature source [°C] | Rich solution mass flow rate [kg/h] | Cooling power output [kW] | COP [-] |
|---|---|---|---|---|---|---|---|
| 1 | **106.1** | 1,600 | 26.9 | 17.7 | 100 | 8.68 | 0.67 |
| 2 | **102.2** | 1,600 | 27.2 | 17.8 | 100 | 8.06 | 0.68 |
| 3 | **100.2** | 1,600 | 27.0 | 17.8 | 100 | 7.93 | 0.69 |
| 4 | **98.2** | 1,600 | 27.1 | 17.8 | 100 | 7.61 | 0.69 |
| 5 | **95.2** | 1,600 | 27.0 | 17.8 | 100 | 7.24 | 0.69 |
| 6 | **92.2** | 1,600 | 27.0 | 17.8 | 101 | 6.80 | 0.69 |
| 7 | **90.2** | 1,600 | 27.0 | 17.8 | 101 | 6.54 | 0.69 |
| 8 | **85.2** | 1,600 | 26.9 | 17.7 | 99 | 5.48 | 0.69 |
| 9 | **80.2** | 1,600 | 27.0 | 17.8 | 100 | 5.06 | 0.68 |
| 10 | 95.2 | **1,800** | 26.7 | 17.7 | 100 | 7.06 | 0.68 |
| 11 | 95.2 | **1,600** | 26.8 | 17.7 | 100 | 7.19 | 0.69 |
| 12 | 95.2 | **1,400** | 26.7 | 17.7 | 99 | 6.90 | 0.69 |
| 13 | 95.1 | **1,200** | 26.7 | 17.7 | 100 | 7.03 | 0.70 |
| 14 | 95.1 | **1,000** | 26.7 | 17.7 | 99 | 6.73 | 0.70 |
| 15 | 95.0 | **800** | 26.6 | 17.7 | 99 | 6.26 | 0.69 |
| 16 | 94.9 | **600** | 26.7 | 17.7 | 99 | 5.58 | 0.70 |
| 17 | 95.2 | 1,600 | **30.2** | 17.7 | 101 | 4.34 | 0.58 |
| 18 | 95.2 | 1,600 | **28.2** | 17.7 | 101 | 5.79 | 0.65 |
| 19 | 95.2 | 1,600 | **26.2** | 17.7 | 99 | 7.21 | 0.69 |
| 20 | 95.1 | 1,600 | **25.3** | 17.7 | 100 | 8.32 | 0.71 |
| 21 | 95.1 | 1,600 | **22.5** | 17.7 | 100 | 9.24 | 0.72 |
| 22 | 95.2 | 1,600 | 27.0 | 17.7 | **110** | 5.85 | 0.60 |
| 23 | 95.2 | 1,600 | 27.0 | 17.7 | **105** | 6.10 | 0.63 |
| 24 | 95.2 | 1,600 | 27.0 | 17.7 | **100** | 6.69 | 0.67 |
| 25 | 95.2 | 1,600 | 27.1 | 17.7 | **95** | 6.76 | 0.68 |
| 26 | 95.2 | 1,600 | 27.1 | 17.7 | **89** | 7.10 | 0.69 |
| 27 | 95.2 | 1,600 | 27.0 | 17.7 | **85** | 6.91 | 0.70 |
| 28 | 95.2 | 1,600 | 27.1 | 17.7 | **80** | 6.72 | 0.69 |
| 29 | 95.2 | 1,600 | 26.9 | **21.7** | 100 | 8.45 | 0.72 |
| 30 | 95.2 | 1,600 | 27.1 | **19.7** | 99 | 7.75 | 0.71 |
| 31 | 95.2 | 1,600 | 27.0 | **17.7** | 100 | 6.51 | 0.69 |
| 32 | 95.2 | 1,600 | 27.0 | **15.7** | 100 | 5.65 | 0.62 |
| 33 | 95.2 | 1,600 | 27.0 | **13.7** | 101 | 4.78 | 0.58 |
| 34 | 95.2 | 1,600 | 27.0 | **11.7** | 100 | 3.57 | 0.50 |
| 35 | 95.2 | 1,600 | 27.0 | **9.8** | 100 | 2.91 | 0.43 |

Cooling capacity and COP are plotted versus the desorber HTF inlet temperature in **Fig. 3.6(a)** (all the graphs presented in this document are produced using Microsoft Excel), while holding all other inputs constant at the nominal values listed in **Table 3.2** and **Table 3.4**. The desorber temperature is a very influencing parameter in the functioning of absorption machines and can vary depending on the heat source or control system. Theoretical analysis performed by Herold et al. [5] showed that the cooling capacity varies approximately linearly with the

desorber HTF inlet temperature, while the COP exhibits a relatively flatter curve with a maximum determined by several competing factors (design parameters, thermal operating conditions, heat transfer irreversibilities, etc.). Indeed, experimental tests showed that in general, cycles have a specific desorber temperature, called optimal generation temperature, that maximises the COP [118].
Experimental results on the pilot plant confirm theoretical analysis, showing a cooling power output linearly increasing with the desorber temperature (passing from around 5 kW at 80 °C to more than 8.5 kW at 106 °C) and a relatively flat COP curve, with a maximum of 0.7 around 85 °C. Below 80 °C the functioning becomes very unstable, and eventually the machine stops working.

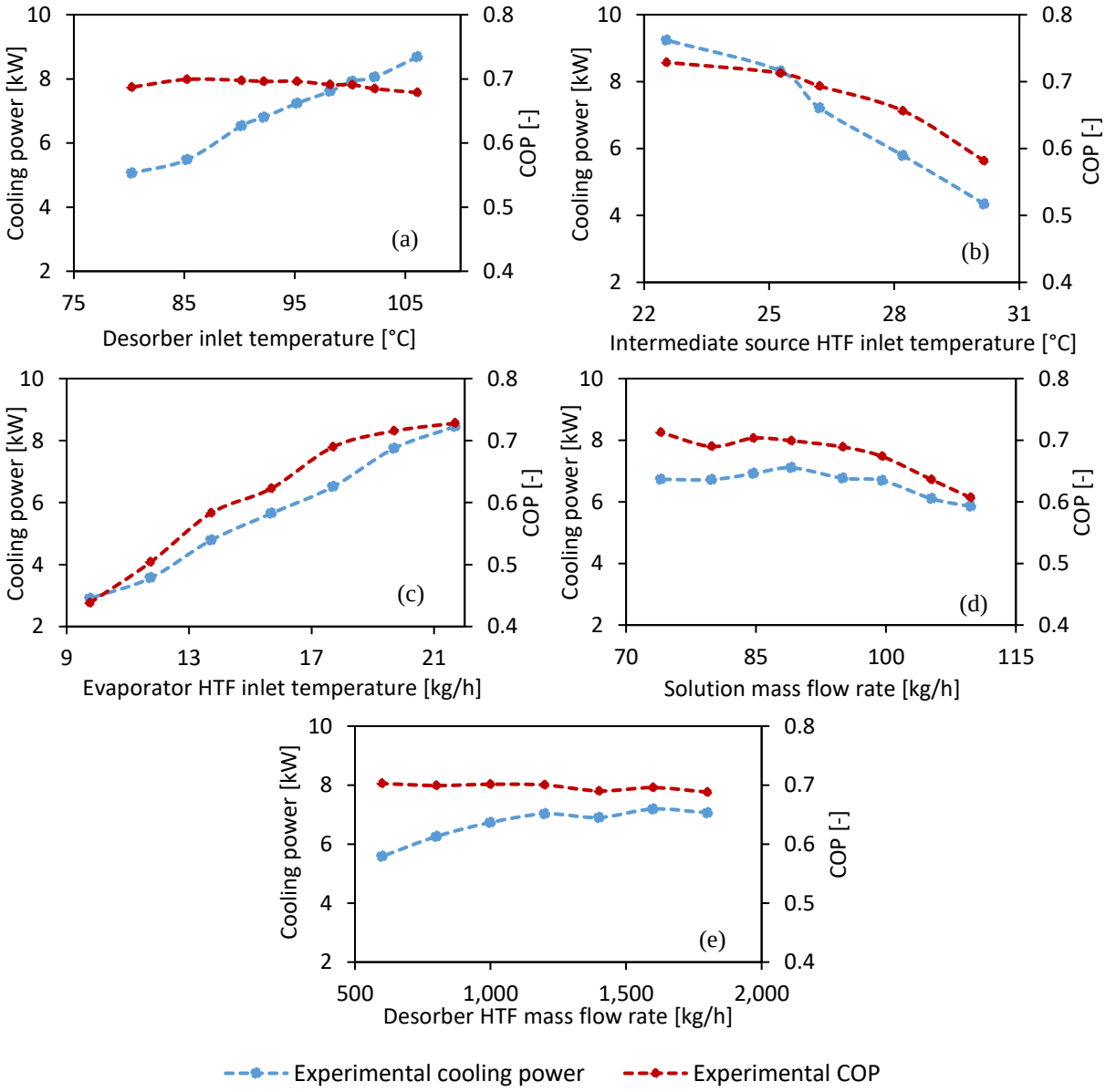


**Fig. 3.6 –** Experimental performance of the absorption chiller.

The effect of the intermediate source temperature, to which heat is rejected, is shown in **Fig. 3.6(b)**. Since the HTF flows in parallel to the condenser and to the absorber, this temperature represents both the condenser and absorber HTF inlet temperature. The condensation temperature determines the high pressure of the cycle. Increasing this temperature results in a higher pressure, with some benefits concerning the ammonia vapour purity. On the other hand, the temperature of the fluid entering the evaporator increases, reducing the COP of the cycle.
Concerning the absorber, since the absorption process is exothermic, better performances are achievable at lower temperatures. Additionally, higher pressures and lower temperatures increases the vapour mass flow rate absorbable (since the ammonia concentration of the saturated liquid increases). For this reason, reducing the

absorption temperature can strongly improve the COP. This is confirmed by experimental results showing that the cooling power and COP pass respectively from 9.2 kW and 0.73 for an intermediate source temperature of 23 °C to 4.3 kW and 0.58 for an intermediate source of 30 °C.

The evaporation temperature determines the low pressure of the cycle, hence when it decreases, also the low pressure is reduced, with a negative effect on the absorption process and a COP reduction. Indeed, in experimental tests (**Fig. 3.6(c)**), the COP passes from 0.7 for an evaporator HTF inlet temperature of 22 °C to 0.43 for an HTF temperature of 10 °C. In the same temperature range, the cooling output is reduced from 8.45 kW to less than 3 kW.

The effect of the rich solution mass flow rate is plotted in **Fig. 3.6 (d)**. Wirtz [29] highlighted that a low solution mass flowrate (75 kg/h) makes it possible to reduce the energy consumption of the pump by approximately 15% but it requires a higher temperature for the heat source. The increase of the solution mass flowrate up to 100 kg/h slightly degrades the performance but enables the machine to run with a low heat source (85-95 °C) and leads to the self-regulation of the machine for air-conditioning applications. Finally, the effect of the external HTF is plotted in **Fig. 3.6 (e)** in the case of the desorber. The curves show very little COP sensitivity and only moderate capacity sensitivity. Similar trends are reported for all HTF mass flow rates also by Herold et al. [5]. It can be noted that for low values of the HTF mass flow rate, the controlling side of the heat exchange may be the heat transfer fluid but, for mass flow rated higher than 1200 kg/h an asymptote is approached, indicating that the solution becomes the limiting fluid.

The values of the COP versus $COP_{Carnot}$ (**Eq. (2.13)**) are plotted in **Fig. 3.7** for the tests in which the temperature of the sources was changed. Test points relative to the intermediate and cold source temperature variation have an asymptotical tendency typical of absorption machines, as shown in **Fig. 2.28**. However, this is not the case when the desorber temperature is varied because of the specific functioning of the combined desorber/rectifier. Increasing the temperature of the desorber influences the internal rectification process in the adiabatic part of the exchanger increasing the temperature difference between the exiting vapour and the solution at inlet. Additionally, the temperature of the solution at inlet is higher, thus resulting in a reduced capacity to purify the refrigerant vapour. Imperfect vapour purification can have a very negative impact on COP, suggesting the need to increase the solution mass flow rate or adding a rectifier to further purify the vapour when the desorber HTF temperature increases.

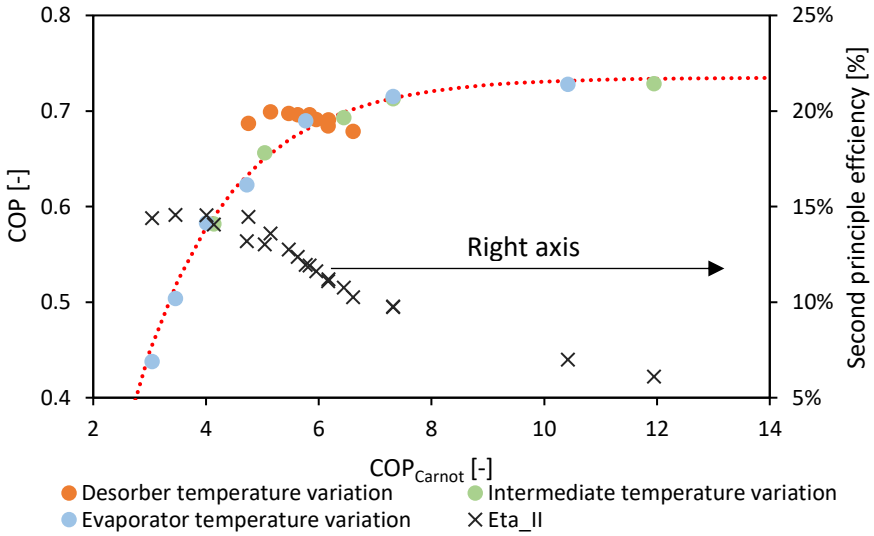


**Fig. 3.7 –** COP versus $COP_{Carnot}$ for the absorption chiller prototype.

## *Ammonia concentration calculation*

Experimental data lack the direct measures of concentration within the loop, which is very difficult to achieve and not practicable. These data are necessary for calculation of the thermodynamic properties of the mixture and characterization of the functioning of the evaporator, desorber, and absorber and therefore need to be deduced from other direct measures. Indirect evaluation of the concentration is possible, using the thermodynamic

properties (*h*, *T*, *P*, etc.) of ammonia-water solution obtained from the Engineering Equation Solver, based on the mixture equation of state developed by Ibrahim and Klein [179]. The correlations are applicable for temperatures between 230 K and 600 K at equilibrium pressures between 0.2 and 110 bar with an average deviation of less than 5% with respect to reported experimental data.
Ammonia concentration inside the loop can be calculated in several ways. For example, one possibility is to use the available measures of pressure and temperature together with the density measured by the Coriolis flowmeter (C1 and C5) on the rich and poor solution side respectively (**Fig. 3.5**):

$$x_{sr} = x\,(T_1, P_6, \rho_1) \tag{3.1}$$
$$x_{sp} = x\,(T_5, P_3, \rho_5) \tag{3.2}$$

The values of ammonia concentration in the vapour refrigerant $x_{ref}$ calculated with a mass balance on the desorber were often exceeding unity for the test points and therefore this procedure was not retained. An alternative is to calculate the ammonia concentration of the refrigerant vapour from an energy balance formulated on either the condenser (**Eq.(3.3)**) or the evaporator (**Eq.(3.4)**):

$$\dot{Q}_c = \dot{m}_{ref} \cdot h\left(T_8, P_8, x_{ref}\right) - \dot{m}_{ref} \cdot h\left(T_9, P_8, x_{ref}\right) \tag{3.3}$$
$$\dot{Q}_{evap} = \dot{m}_{ref} \cdot h\left(T_{12}, P_{11}, x_{ref}\right) - \dot{m}_{ref} \cdot h\left(T_{11}, P_{11}, x_{ref}\right) \tag{3.4}$$

Knowing this value, the other two concentrations can be calculated either by assuming that the solution leaving the desorber is saturated liquid (**Eq.(3.5)** and **Eq.(3.7)**), or by performing an energy and mass balance on the desorber (**Eq.(3.6)-(3.7)**) or on the absorber (**Eq.(3.8)-(3.9)**):

$$x_{sp} = x_{liq,sat}\,(T_4, P_3) \tag{3.5}$$

$$\dot{Q}_d = \dot{m}_{ref} \cdot h\left(T_7, P_3, x_{ref}\right) + \dot{m}_{sp} \cdot h\left(T_4, P_3, x_{sp}\right) - \dot{m}_{sr} \cdot h\,(T_3, P_3, x_{sr}) \tag{3.6}$$
$$\dot{m}_{sr} \cdot x_{sr} = \dot{m}_{sp} \cdot x_{sp} + \dot{m}_{ref} \cdot x_{ref} \tag{3.7}$$

$$\dot{Q}_a = \dot{m}_{ref} \cdot h\left(T_{17}, P_{11}, x_{ref}\right) + \dot{m}_{sp} \cdot h\left(T_6, P_6, x_{sp}\right) - \dot{m}_{sr} \cdot h\,(T_1, P_6, x_{sr}) \tag{3.8}$$
$$\dot{m}_{sr} \cdot x_{sr} = \dot{m}_{sp} \cdot x_{sp} + \dot{m}_{ref} \cdot x_{ref} \tag{3.9}$$

The concentrations calculated with the different procedures were used to calculate the power exchanged by the working mixture in each exchanger and compared to the power exchanged by the HTF, considered to be the effective power exchanged by the component. This is calculated as the HTF mass flow rate multiplied by HTF enthalpy variation across the exchanger. Calculation of the refrigerant vapour concentration through an energy balance on the evaporator (**Eq.(3.4)**) and assuming the poor solution leaving the desorber to be saturated liquid (**Eq.(3.5)** and **Eq.(3.7)**), was found to have the smallest average error between the power calculated on the solution side and the HTF side (**Fig. 3.8**).
Power balance errors on components higher than 5% between the power calculated on the solution side and on the HTF side were not accepted and points 17-22-33-34-35 were discarded for the following numerical models adjusting as they were not considered to be sufficiently reliable.

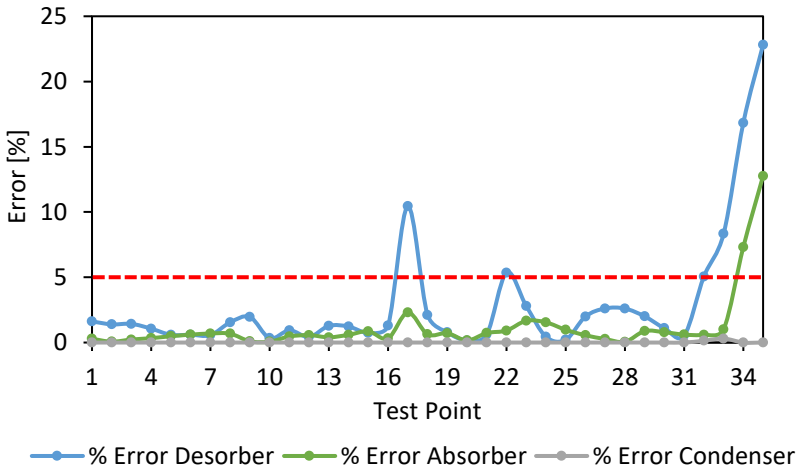


**Fig. 3.8 –** Power balance error for different key components (working fluid side/HTF side).

As a validation check, refrigerant ammonia concentration was used to calculate the saturated liquid pressure at the condenser outlet and evaporator inlet temperature which are normally used to model the high and low pressure in the loop [5]. A comparison with experimentally measured pressure shows a difference of less than 3% for the high pressure (**Fig. 3.9(a)**) and less than 1% for the low pressure (**Fig. 3.9 (b)**) thus validating the use of this hypothesis in the model of the cycle.

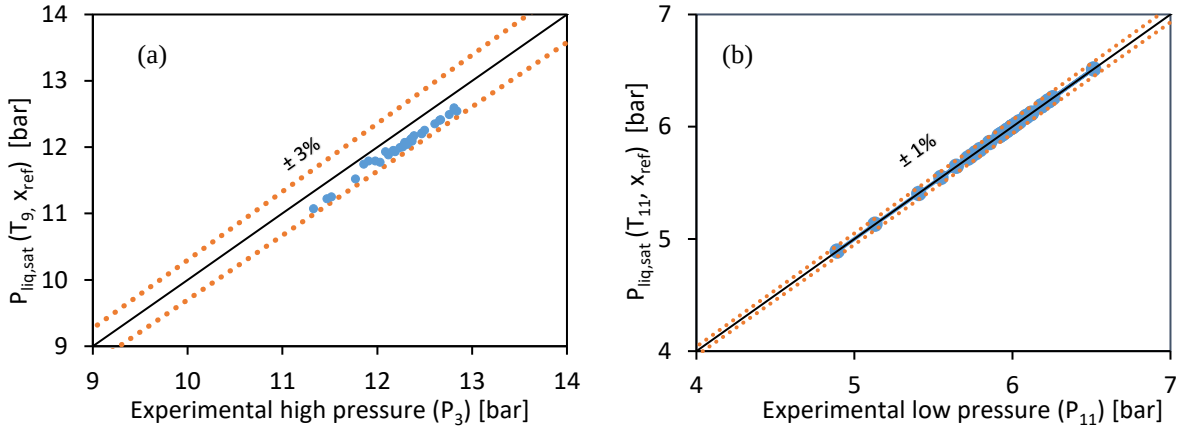


**Fig. 3.9 -** Comparison of the experimental pressure and the deduced saturated liquid pressure at the condenser outlet (a) and evaporator inlet (b).

In conclusion, experimental data analysis requires verification of energy balances on each component. In the present work operating conditions characterised by errors higher than 5% were discarded. Results showed that the combined desorber integrated in the pilot plant, in addition to avoiding the use of a separated rectifier, simplifies the plant management compared to the use of the classical boiling heat exchanger architecture. Experimental results on the pilot plant are in accordance with theory analysis on single stage absorption chillers and despite the small scale, a thermal COP higher than 0.7 is reached in the investigated operating conditions.

### 3.4.2 Turbine

Experimental tests on the turbine alone (state points 14 to 16 in **Fig. 3.5**) were carried out to characterise its functioning. The turbine was tested outside the loop using three different gases (argon, nitrogen and compressed air) and inside the loop with ammonia, using the electrical resistance R1 of 1.2 Ohm (see *Section 3.3.2*). Indeed, tests outside the loop were performed to enrich the experimental database, since tests with ammonia in the cycle were not sufficiently numerous and varied. All the tests carried out on the turbine are presented in **Table 3.5**.
Tests performed with the three gases were performed with a turbine inlet temperature always comprised between 20-22 °C, without superheating the flow. The fluid at outlet was discharged at ambient temperature; however, it was found that increasing the inlet pressure generated a back pressure at the outlet of the turbine, resulting in an outlet pressure between 1.1 and 1.8 bar, depending on the inlet pressure. For this reason, results concerning electricity production, electrical efficiency and rotational speed are presented as a function of the available pressure drop.
The points presented are stationary points (constant inlet pressure and temperature and outlet pressure), averaged over a period of about one minute during which the turbine operating conditions were stable. The measurement uncertainty is estimated to be 0.7% for the mass flow rate and 0.8% for the pressure.

Results in **Fig. 3.10** show that the mass flow rate treated by the injector increases linearly with the inlet pressure. This suggests that, in all the conditions tested, the injector was in choking conditions in which the treated mass flow rate is linearly dependent on the inlet pressure. Indeed, for an ideal gas, the mass flow rate treated by an injector in choking conditions can be written as [69]:

$$\dot{m}_{max} = \frac{P_{i,tot} \cdot A_{throat}}{\sqrt{R \cdot T_{i,tot}}} \cdot \sqrt{\gamma \cdot \left(\frac{2}{\gamma+1}\right)^{\frac{\gamma+1}{\gamma-1}}} \tag{3.10}$$

**Table 3.5 –** Experimental campaign matrix for tests carried out on the turbine.

| Test point | Fluid | Electrical resistance [Ohm] | $P_{in}$ [bar] | $T_{in}$ [°C] | $P_{out}$ [bar] | $\dot{m}_t$ [kg/h] | Frequency [Hz] | Voltage [VDC] | $\omega_t$ [rpm] | $\dot{W}_t$ [W] |
|---|---|---|---|---|---|---|---|---|---|---|
| 1 | Argon | 1.2 | 9.98 | 19.2 | 2.40 | 32.0 | 217 | 5.88 | 13,071 | 34.6 |
| 2 | Argon | 1.2 | 8.94 | 18.2 | 2.17 | 28.6 | 203 | 5.36 | 12,200 | 28.7 |
| 3 | Argon | 1.2 | 8.03 | 17.8 | 1.94 | 25.6 | 193 | 5.00 | 11,599 | 25.1 |
| 4 | Argon | 1.2 | 7.11 | 17.6 | 1.71 | 22.4 | 180 | 4.65 | 10,831 | 21.6 |
| 5 | Argon | 1.2 | 6.02 | 17.6 | 1.50 | 18.8 | 155 | 3.75 | 9,330 | 14.1 |
| 6 | Argon | 1.2 | 5.03 | 17.6 | 1.36 | 15.5 | 129 | 2.93 | 7,780 | 8.6 |
| 7 | Argon | 1.2 | 4.04 | 17.8 | 1.24 | 12.3 | 109 | 2.24 | 6,565 | 5.0 |
| 8 | Argon | 1.2 | 3.02 | 17.9 | 1.14 | 9.1 | 84 | 1.40 | 5,081 | 2.0 |
| 9 | Nitrogen | 1.2 | 9.24 | 17.8 | 2.20 | 23.4 | 223 | 6.08 | 13,405 | 37.0 |
| 10 | Nitrogen | 1.2 | 7.06 | 16.9 | 1.68 | 17.6 | 192 | 4.94 | 11,522 | 24.4 |
| 11 | Nitrogen | 1.2 | 5.84 | 16.7 | 1.45 | 14.5 | 162 | 3.94 | 9,732 | 15.6 |
| 12 | Nitrogen | 1.2 | 5.02 | 16.7 | 1.34 | 12.3 | 134 | 3.04 | 8,058 | 9.2 |
| 13 | Nitrogen | 1.2 | 3.69 | 16.8 | 1.18 | 8.9 | 101 | 2.00 | 6,111 | 4.0 |
| 14 | Air | 1.2 | 3.04 | 21.7 | 1.14 | 7.3 | 83 | 1.37 | 5,008 | 1.6 |
| 15 | Air | 1.2 | 4.02 | 22.2 | 1.23 | 9.8 | 108 | 2.17 | 6,484 | 3.9 |
| 16 | Air | 1.2 | 5.0 | 22.5 | 1.3 | 12.4 | 133 | 3.0 | 8,021 | 7.5 |
| 17 | Air | 1.2 | 7.11 | 23.2 | 1.74 | 17.9 | 188 | 4.87 | 11,333 | 19.8 |
| 18 | Air | 1.2 | 7.82 | 23.7 | 1.90 | 19.8 | 203 | 5.30 | 12,186 | 23.4 |
| 19 | Air | 1.2 | 7.08 | 23.5 | 1.72 | 17.8 | 190 | 4.93 | 11,415 | 20.3 |
| 20 | Air | 1.2 | 6.04 | 23.3 | 1.49 | 15.1 | 166 | 4.16 | 10,006 | 14.4 |
| 21 | Air | 1.2 | 5.04 | 23.1 | 1.34 | 12.4 | 137 | 3.20 | 8,275 | 8.5 |
| 22 | Air | 1.2 | 4.01 | 22.7 | 1.23 | 9.8 | 103 | 2.02 | 6,230 | 3.4 |
| 23 | Air | 1.2 | 6.94 | 22.0 | 1.76 | 18.0 | 156 | 4.48 | 9,373 | 16.7 |
| 24 | Air | 1.2 | 6.04 | 21.8 | 1.55 | 15.5 | 139 | 3.83 | 8,359 | 12.2 |
| 25 | Air | 1.2 | 5.04 | 21.6 | 1.38 | 12.8 | 117 | 3.03 | 7,029 | 7.6 |
| 26 | Air | 1.2 | 4.04 | 21.4 | 1.25 | 10.1 | 94 | 2.13 | 5,674 | 3.8 |
| 27 | Air | 1.2 | 3.03 | 21.2 | 1.16 | 7.4 | 72 | 1.33 | 4,374 | 1.5 |
| 28 | Air | 2.4 | 6.99 | 22.0 | 1.78 | 18.2 | 243 | 8.06 | 14,633 | 27.0 |
| 29 | Air | 2.4 | 6.02 | 21.6 | 1.55 | 15.5 | 216 | 7.00 | 12,976 | 20.4 |
| 30 | Air | 2.4 | 5.05 | 21.5 | 1.39 | 12.8 | 178 | 5.54 | 10,712 | 12.8 |
| 31 | Air | 2.4 | 4.04 | 21.2 | 1.26 | 10.1 | 139 | 4.06 | 8,386 | 6.9 |
| 32 | Air | 2.4 | 3.05 | 21.0 | 1.16 | 7.5 | 101 | 2.53 | 6,080 | 2.7 |
| 33 | Air | 5.9 | 7.05 | 22.1 | 1.75 | na | 372 | 13.44 | 22,363 | 36.9 |
| 34 | Air | 5.9 | 6.05 | 21.9 | 1.52 | na | 324 | 11.46 | 19,471 | 26.8 |
| 35 | Air | 5.9 | 5.1 | 21.5 | 1.3 | na | 264 | 9.0 | 15,895 | 16.7 |
| 36 | Air | 5.9 | 4.05 | 21.1 | 1.22 | na | 204 | 6.67 | 12,290 | 9.1 |
| 37 | Air | 5.9 | 3.04 | 21.0 | 1.12 | na | 142 | 4.20 | 8,561 | 3.6 |
| 38 | Air | 5.9 | 2.05 | 20.7 | 1.06 | na | 78 | 1.74 | 4,726 | 0.6 |
| 39 | Air | 8.2 | 6.82 | 22.6 | 1.71 | na | 445 | 16.42 | 26,746 | 32.9 |
| 40 | Air | 8.2 | 6.04 | 22.4 | 1.53 | na | 400 | 14.57 | 24,038 | 25.9 |
| 41 | Air | 8.2 | 5.0 | 22.0 | 1.4 | na | 332 | 11.9 | 19,921 | 17.1 |
| 42 | Air | 8.2 | 4.04 | 21.7 | 1.23 | na | 258 | 8.90 | 15,489 | 9.7 |
| 43 | Air | 8.2 | 3.03 | 21.4 | 1.14 | na | 178 | 5.68 | 10,721 | 3.9 |
| 44 | Air | 8.2 | 2.02 | 21.1 | 1.07 | na | 91 | 2.29 | 5,513 | 0.6 |
| 45 | Ammonia | 1.2 | 12.02 | 94.1 | 5.15 | 20.5 | 0 | 5.31 | na | 23.5 |
| 46 | Ammonia | 1.2 | 12.29 | 98.7 | 5.41 | 20.7 | 0 | 5.60 | na | 26.1 |
| 47 | Ammonia | 1.2 | 11.53 | 102.3 | 5.32 | 19.2 | 0 | 5.65 | na | 26.6 |
| 48 | Ammonia | 1.2 | 11.48 | 102.7 | 5.19 | 19.1 | 184 | 5.47 | 11,016 | 24.9 |
| 49 | Ammonia | 1.2 | 11.53 | 100.8 | 5.10 | 19.2 | 179 | 5.33 | 10,730 | 23.7 |
| 50 | Ammonia | 1.2 | 11.31 | 98.0 | 4.65 | 18.6 | 175 | 4.85 | 10,516 | 19.6 |
| 51 | Ammonia | 1.2 | 11.31 | 95.1 | 4.66 | 19.3 | 161 | 4.80 | 9,640 | 19.2 |
| 52 | Ammonia | 1.2 | 11.36 | 96.9 | 4.74 | 19.0 | 154 | na | 9,261 | na |
| 53 | Ammonia | 1.2 | 11.25 | 99.2 | 4.97 | 19.1 | 0 | na | na | na |
| 54 | Ammonia | 1.2 | 11.77 | 99.3 | 5.11 | 20.0 | 0 | na | na | na |
| 55 | Ammonia | 1.2 | 11.91 | 99.0 | 5.11 | 20.2 | 0 | na | na | na |
| 56 | Ammonia | 1.2 | 12.01 | 98.2 | 5.11 | 20.4 | 0 | na | na | na |
| 57 | Ammonia | 1.2 | 12.18 | 98.2 | 5.03 | 20.7 | 0 | na | na | na |
| 58 | Ammonia | 1.2 | 12.44 | 97.4 | 4.71 | 21.1 | 0 | na | na | na |
| 59 | Ammonia | 1.2 | 10.97 | 100.0 | 4.71 | 18.5 | 0 | na | na | na |
| 60 | Ammonia | 1.2 | 11.50 | 97.0 | 4.58 | 19.4 | 0 | na | na | na |
| 61 | Ammonia | 1.2 | 10.90 | 90.6 | 3.61 | 24.2 | 0 | na | na | na |
| 62 | Ammonia | 1.2 | 11.75 | 93.7 | 5.09 | 20.1 | 0 | na | na | na |

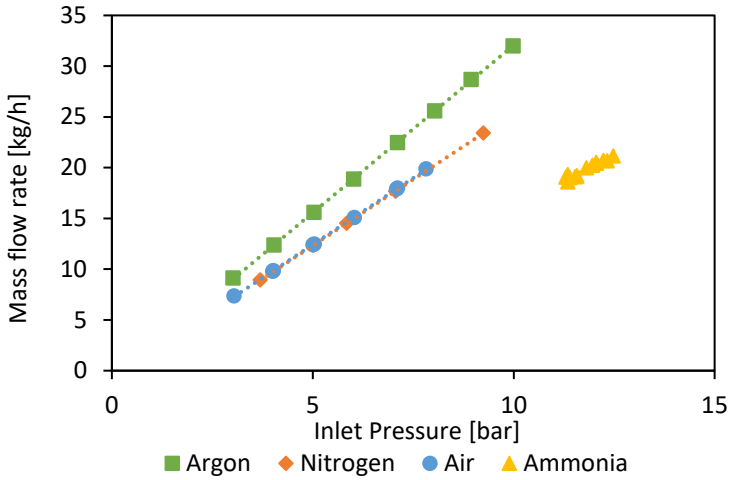


**Fig. 3.10** - Turbine mass flow rate as a function of the inlet pressure.

Using **Eq. (3.10)**, the ideal gas mass flow rate can be calculated for each test point and compared to the experimental mass flow rate as shown in **Fig. 3.11.** Considering the same injector throat section of 3 $mm^2$ for all the investigated fluids leads to very good agreements in the case of Argon, Nitrogen and Air, with an average error of 1.9% and a maximum error below 5%.
In the case of ammonia, the average discrepancy is above 10%, proving that the use of perfect gas relations in the case of a vapour like ammonia leads to non-negligible errors. The difference could also be due to condensation of the working mixture (a wet fluid) during expansion. Real gas equations should hence be used to assess whether condensation has a relevant effect or if it is real gas behaviour that plays the most important role.

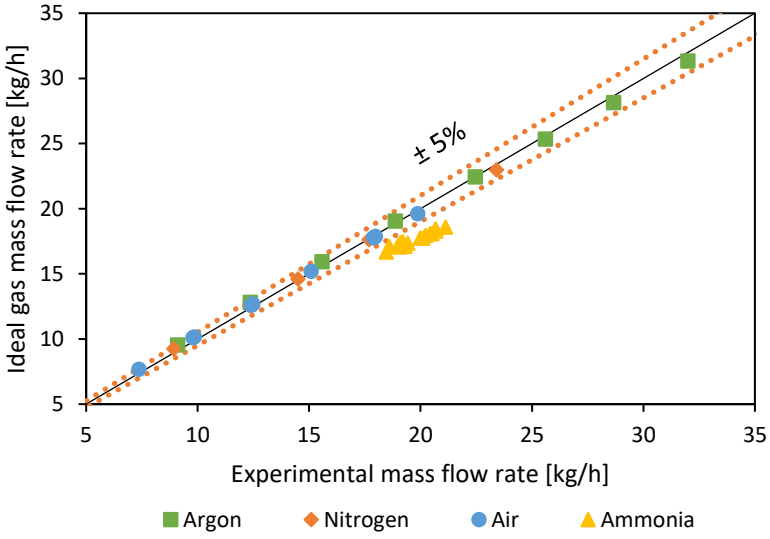


**Fig. 3.11** – Experimental vs ideal gas turbine mass flow rate.

**Fig. 3.12** shows that, as expected, when the available pressure drop on the turbine increases, the electrical power produced by the turbine also increases. In particular, the power output increases slightly more than linearly due to the combined effect of the increasing mass flow rate and of the increasing efficiency at higher rotational speed. The measurement error on the electrical power produced is estimated below 1%, while the error in measuring the rotational speed is estimated at 1.7%.
As mentioned above, the electrical power output increase also depends on the electrical efficiency increase. Increasing the pressure drop on the turbine also increases its rotational speed, as shown in **Fig. 3.13(b)**, thus bringing the turbine closer to its optimal operating point, and increasing its electrical efficiency, **Fig. 3.13(a)**.
As shown in **Fig. 3.12** and **Fig. 3.13**. The electrical power output and efficiency of the turbine are much lower than expected. This is due to several factors, including shocks taking place during the expansion, the low efficiency of the electrical generator (generally below 50-60% for these power sizes [86], but here likely much lower), the additional losses generated by the titanium casing protecting the coils and the low rotational speeds reached.

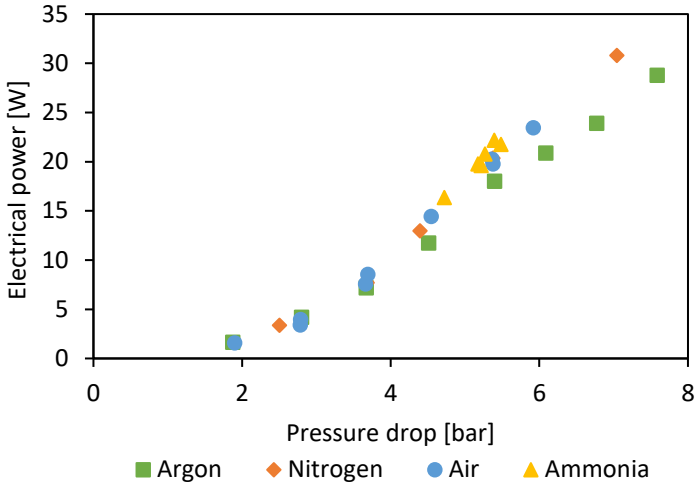


**Fig. 3.12 -** Electrical power of the turbine as a function of the pressure drop using R1=1.2 ohm.

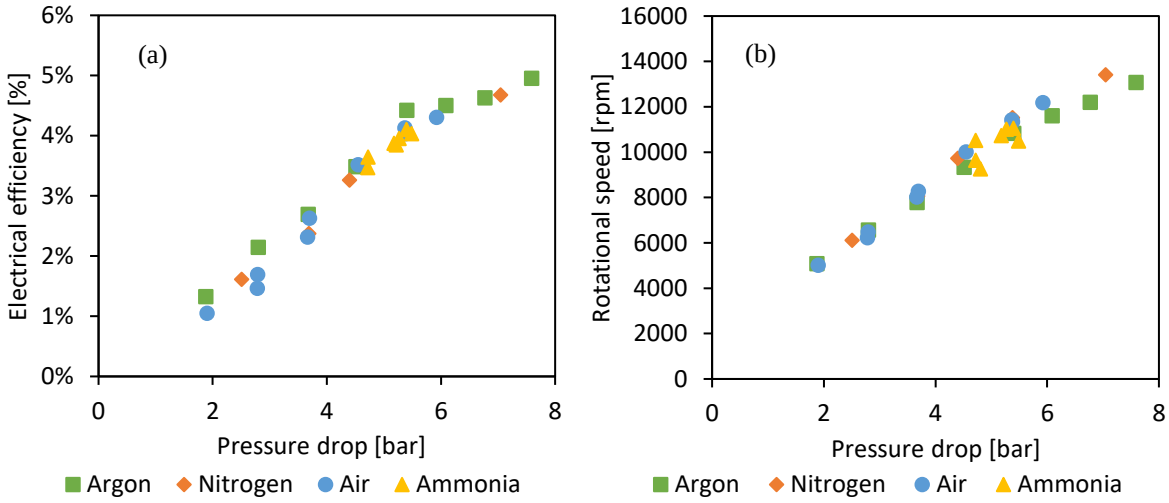


**Fig. 3.13 -** Electrical efficiency and rotational speed increase as a function of the pressure drop using R1= 1.2 ohm.

To assess the influence of the rotational speed on the performance of the turbine, additional tests were carried out using compressed air and changing the value of electrical resistance. For a given pressure drop, increasing the electrical resistance (using a higher resistance) results in a higher rotational speed of the turbine, as presented in **Fig. 3.14**.
On the other hand, increasing the rotational speed initially increases the electrical efficiency (**Fig. 3.15(a)**) and the electrical power output (**Fig. 3.15(b)**) of the turbine, but in the case of compressed air, it seems that a maximum is reached between 4.9 and 8.2 Ohm.

Calculating by interpolation the values of rotational speed, electrical power and electrical efficiency from **Fig. 3.14** and **Fig. 3.15**, for different values of the pressure drop, it is possible to draw the electrical power output and electrical efficiency characteristic of the turbine. The result are the bell-shaped curves typical of axial turbines (as detailed in *Section 4.3*), shown in **Fig. 3.16**, in which each point represents the use of a different electrical resistance. As expected, the power output and the electrical efficiency of the turbine increase when the pressure drop increases, reaching a maximum around 33 W and an electrical efficiency of 7% for a rotational speed of around 20,000 rpm when the available pressure drop is 5 bar. Additionally, it can be noted that, the optimal working point shifts at higher rotational speeds when the pressure drop is increased.

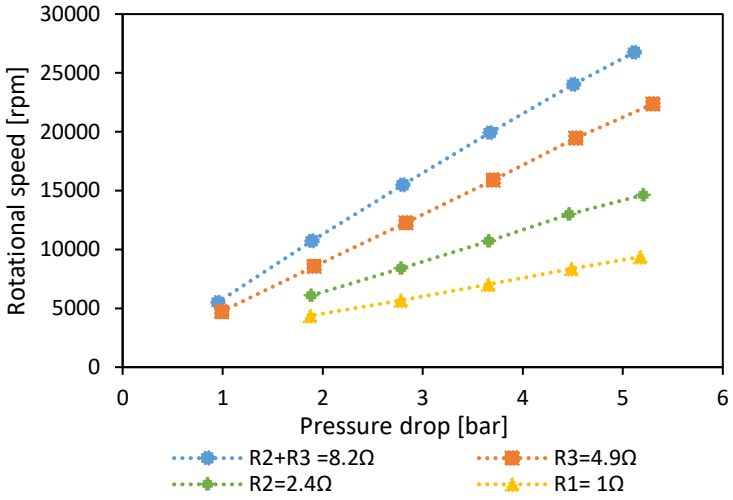


**Fig. 3.14 –** Rotational speed of the turbine as a function of the pressure drop for different values of the electrical resistance and air as a working fluid.

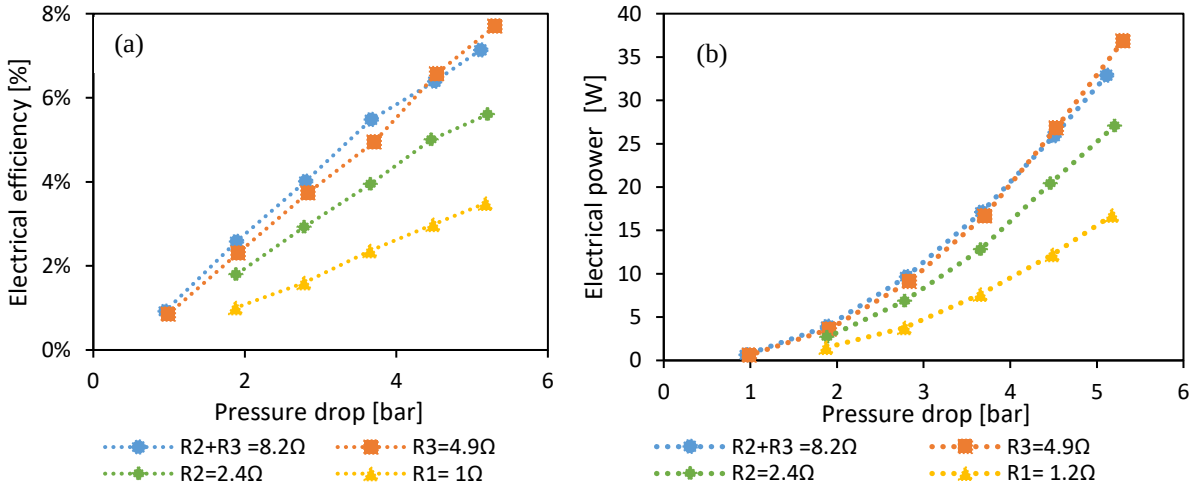


**Fig. 3.15** - Electrical efficiency (a) and electrical power output (b) of the turbine as a function of the pressure drop for different values of the electrical resistance and air as working fluid.

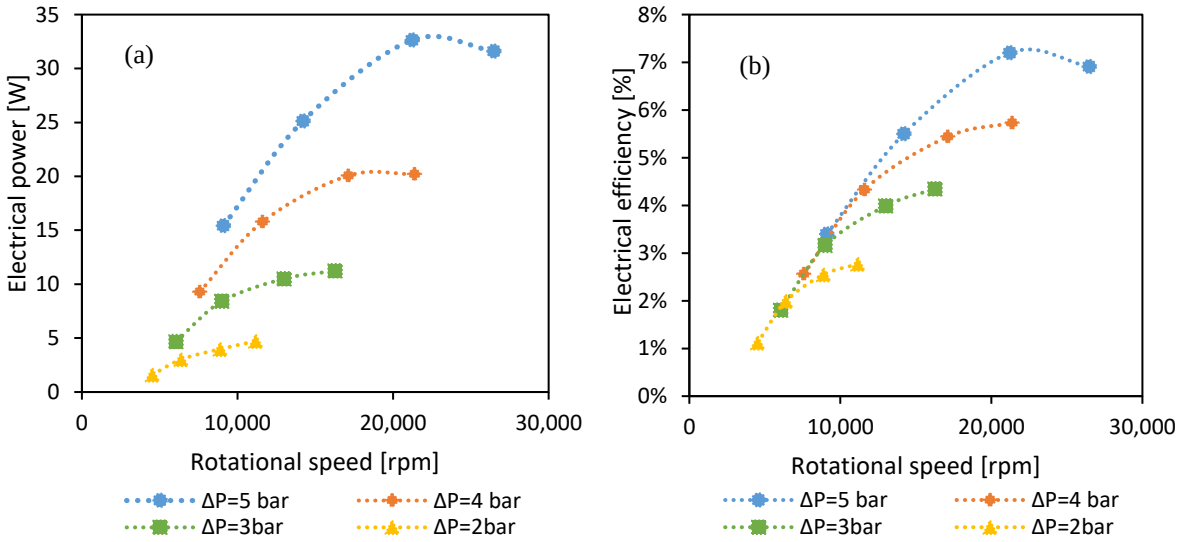


**Fig. 3.16** - Electrical power output (a) and electrical efficiency (b) of the turbine as a function of the rotational speed for different values of the available pressure drop.

Finally, the influence of the turbine inlet temperature was evaluated. Impulse turbines like the one investigated here transform a pressure difference into an increase of the velocity of the flow. Therefore, inlet and outlet pressures represent the most important variables, while temperature-related effects are secondary. This is shown in **Fig. 3.17**, referring to the use of resistance R2 (4.9 Ohm), two different inlet temperatures, 70 °C and 20 °C, are compared. Increasing the turbine inlet temperature has a negligible effect on the electrical power output. The isentropic enthalpy drop increases, passing from 96 kJ/kg for an inlet at 20 °C to 112 kJ/kg for an inlet temperature of 70 °C (inlet pressure 7 bar, outlet pressure 1.75 bar). However, this is almost completely compensated by a reduction of the turbine mass flow rate passing from 18.5 kg/h at 20 °C to 17.5 kg/h at 70 °C, due to the lower density at higher temperatures.

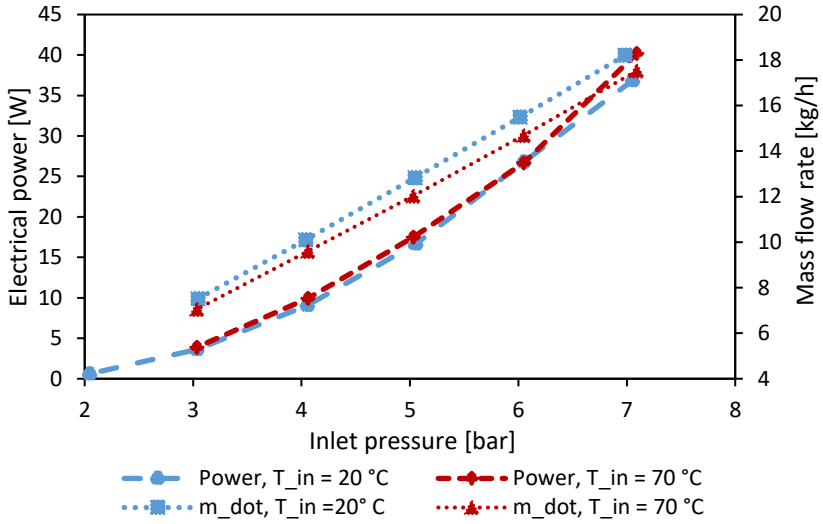


**Fig. 3.17** - Electrical power output and turbine mass flow rate as a function of the turbine inlet pressure for 2 different temperatures using the resistance R3= 4.9 Ohm.

In conclusion, tests performed on the turbine showed that in all the points tested the expander was in choking conditions. Therefore, a linear dependency reported between the turbine inlet pressure and treated mass flow rate is in accordance with theory. The real-gas assumption leads to relevant errors for the turbine mass flow rate calculation in the case of ammonia, while discrepancies are negligible for the other tested gases. The overall electrical efficiency and power production are strongly correlated to the pressure drop through the turbine and its rotational speed for all fluids tested. Finally, the turbine inlet temperature has a limited influence on the overall electrical efficiency.

### 3.4.3 Combined cooling and power production cycle

The partial admission turbine was integrated in the previously described absorption chiller prototype to evaluate the interaction between the expander and the cycle integrating it. Tests performed are listed in **Table 3.6**, where ABS indicates that the machine was working in simple absorption working mode, i.e. split ratio (defined in **Eq. (2.22)** and here equal to $r_s = \dot{m}_8/\dot{m}_7$) $r_s = 1$, ACP indicates the combined cooling and power working mode and PC indicates the power cycle working mode in which only the turbine line is open, i.e. $r_s = 0$.

**Table 3.6** – Combined cooling and power production prototype experimental campaign matrix. Points marked with an asterisk represent test points performed after the dysfunction of the turbine.

| Point | Mode | $T_{di}$ [°C] | $T_{ai}$ [°C] | $T_{ei}$ [°C] | $T_{15}$ [°C] | $\dot{m}_{10}$ [kg/h] | $\dot{m}_{15}$ [kg/h] | $r_s$ [-] | $P_3$ [bar] | $P_{11}$ [bar] | $\dot{Q}_d$ [kW] | $\dot{Q}_e$ [kW] | $\dot{W}_t$ [W] |
|---|---|---|---|---|---|---|---|---|---|---|---|---|---|
| 1 | ABS | 82.8 | 27.2 | 17.8 | 14.5 | 14.7 | 0 | 1.00 | 11.74 | 5.83 | 7.6 | 4.5 | na |
| 2 | ABS | 102.7 | 27.6 | 17.8 | 27.4 | 16.1 | 0 | 1.00 | 12.06 | 6.34 | 9.9 | 4.9 | na |
| 3 | ACP | 102.3 | 29.0 | 17.6 | 94.1 | 10.6 | 20.5 | 0.34 | 12.02 | 6.87 | 13.7 | 2.1 | 23.5 |
| 4 | ACP | 104.8 | 29.8 | 17.8 | 98.7 | 10.9 | 20.7 | 0.35 | 12.29 | 6.87 | 14.1 | 2.2 | 26.1 |
| 5 | ACP | 104.6 | 27.0 | 17.8 | 102.3 | 12.0 | 19.2 | 0.38 | 11.53 | 6.20 | 14.1 | 3.7 | 26.6 |
| 6 | ACP | 105.4 | 27.2 | 17.9 | 102.7 | 10.5 | 19.1 | 0.35 | 11.48 | 6.29 | 13.5 | 3.2 | 24.9 |
| 7 | ACP | 100.2 | 27.4 | 17.9 | 100.8 | 10.2 | 19.2 | 0.35 | 11.53 | 6.42 | 13.0 | 3.0 | 23.7 |
| 8 | ACP | 94.1 | 26.8 | 17.9 | 98.0 | 10.2 | 18.6 | 0.36 | 11.31 | 6.66 | 12.3 | 3.0 | 19.6 |
| 9 | ACP | 94.1 | 26.9 | 17.8 | 95.1 | 10.5 | 19.3 | 0.35 | 11.31 | 6.66 | 12.9 | 3.1 | 19.2 |
| 10 | ACP* | 94.1 | 27.0 | 17.8 | 96.9 | 10.6 | 19.0 | 0.36 | 11.36 | 6.62 | 12.7 | 3.1 | na |
| 11 | ABS* | 94.1 | 27.6 | 17.9 | 39.7 | 22.0 | 0 | 1.00 | 12.46 | 5.97 | 10.1 | 6.6 | na |
| 12 | ACP* | 100.3 | 26.2 | 17.7 | 99.2 | 11.4 | 19.1 | 0.37 | 11.25 | 6.29 | 13.7 | 3.6 | na |
| 13 | ACP* | 100.3 | 28.3 | 17.7 | 99.3 | 10.3 | 20.0 | 0.34 | 11.77 | 6.67 | 13.4 | 2.9 | na |
| 14 | ACP* | 100.2 | 28.9 | 17.8 | 99.0 | 10.0 | 20.2 | 0.33 | 11.91 | 6.81 | 13.4 | 2.7 | na |
| 15 | ACP* | 100.3 | 29.4 | 17.8 | 98.2 | 9.9 | 20.4 | 0.33 | 12.01 | 6.90 | 13.3 | 2.4 | na |
| 16 | ACP* | 100.2 | 30.6 | 17.8 | 98.2 | 9.8 | 20.7 | 0.32 | 12.18 | 7.15 | 13.3 | 1.7 | na |
| 17 | ACP* | 100.2 | 33.2 | 18.4 | 97.4 | 9.7 | 21.1 | 0.31 | 12.44 | 7.73 | 13.3 | 0.5 | na |
| 18 | ACP* | 100.2 | 26.6 | 14.8 | 100.0 | 12.5 | 18.5 | 0.40 | 10.97 | 6.27 | 13.5 | 2.2 | na |
| 19 | ACP* | 100.1 | 28.2 | 17.7 | 97.0 | 12.8 | 19.4 | 0.40 | 11.50 | 6.92 | 13.8 | 2.1 | na |
| 20 | PC* | 89.2 | 27.0 | 17.8 | 90.6 | 0.0 | 24.2 | 0.00 | 13.83 | 7.29 | 10.6 | 0.0 | na |
| 21 | ACP* | 99.1 | 28.3 | 17.7 | 93.7 | 10.1 | 20.1 | 0.33 | 11.75 | 6.66 | 13.2 | 2.9 | na |

Test points marked with an asterisk (point 12-21) represent tests performed after the breaking of the turbine (see *Section 3.4*). Although the turbine had stopped rotating, given the very small power extracted from the fluid by the turbine, these points give interesting insights on the effect of diverting a part of the steam mass flow rate to the turbine line. As in the case of the tests performed on the absorption cycle, also in this case the temperature glide in the evaporator was fixed to 5 °C for all points.

The effect of changing the desorber temperature, all other conditions kept constant is shown in **Fig. 3.18** (corresponding to points 6-8 in **Table 3.6**), referring to an intermediate source temperature of 27 °C, a cold source temperature of 18 °C and a solution mass flow rate of 100 kg/h. In the test shown in **Fig. 3.18**, the cycle is initially started in the simple absorption operating mode. The external circuits are started first, and once the temperature set point is approached, the cycle is started in the initialisation mode. During this 3-minute phase, the pump is started up at a reduced speed, circulating around 60 kg/h of rich solution. It can be noted that the time required to reach stable conditions is less than 15 minutes (900 s). Once stable conditions are reached, the turbine by-pass valve is opened, and the superheater is started to reach the desired turbine inlet temperature before opening the valve upstream of the turbine and closing the by-pass valve. This protocol was used as an initial precaution to ensure adequate turbine inlet conditions in terms of steam quality and temperature, in particular to avoid condensation during expansion.

Switching from the simple absorption to the combined cooling and power working mode deviates part of the vapour mass flow rate to the power production line. Consequently, passing to a combined production working mode reduces the high pressure of the cycle, while it increases the low pressure. Indeed, in the case of the condenser a smaller mass flow rate results in a lower temperature of the fluid at the condenser outlet ($T_9$), hence reducing the high pressure of the cycle. In the case of the evaporator instead, the temperature at evaporator inlet ($T_{11}$) increases, reducing the pinch with the cold source and increasing the low pressure of the cycle, as shown in **Fig. 3.18 (a)**.

Since the absorption process is favoured by a higher pressure, and desorption by a lower pressure, this results in an increase in the circulating vapour mass flow rate as shown in **Fig. 3.18 (b)**.

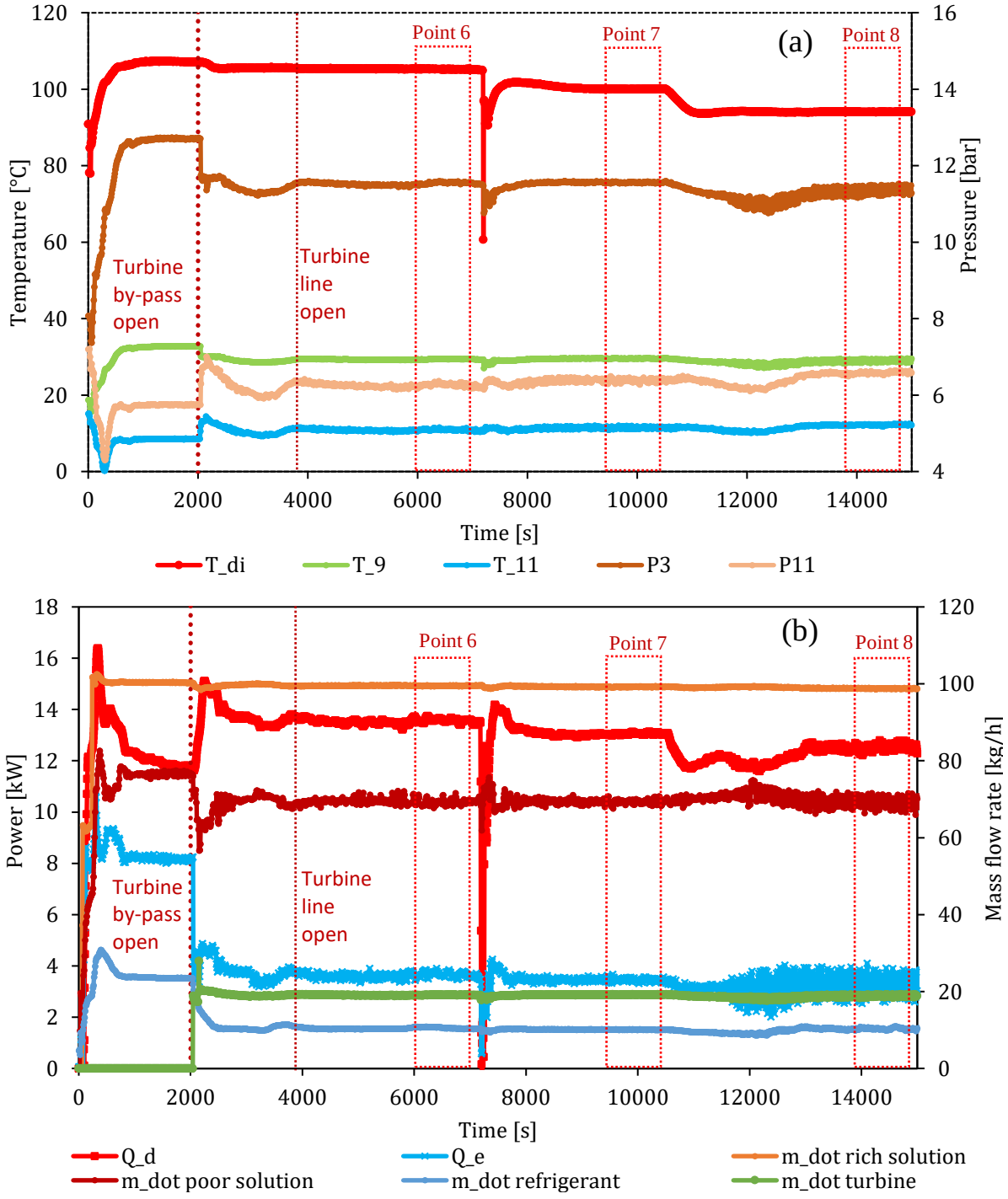


**Fig. 3.18 -** Desorber temperature variation ($T_{ai}$= 27 °C, $T_{ei}$= 18 °C).

The variation of the desorber temperature seems to have little impact on the working pressure and mass flow rates of the cycle. Indeed, while the power absorbed from the hot source decreases when reducing its temperature, the cooling power as well as the mass flow rate passing through the turbine remain unchanged, indicating the efficiency of the cycle increases (for $T_{ai}$ = 27 °C, $T_{ei}$ = 18 °C). However, the functioning of the cycle becomes unstable and it is difficult to operate the plant with a hot source below 95°C. It should be noted that the peaks seen in **Fig. 3.18** are determined by the PID control of the hot source temperature and not by the operating characteristics of the machine.

The influence of the intermediate source temperature is presented in **Fig. 3.19** (corresponding to points 12-17 in **Table 3.6**). The same tendencies discussed for the tests performed on the single stage absorption chillers can be found also in this case, with a reduction of the cooling power output when the intermediate source temperature increases. It should be noted however that, while increasing $T_{ai}$ reduces the efficiency of the cooling production cycle, it also increases the high pressure of the cycle (**Table 3.6**), passing from 11.25 bar for $T_{ai}$ =26.2 °C to 12.44 bar for $T_{ai}$=33.2 °C. This is favourable for the turbine, which can benefit from a higher ΔP and a higher mass flow rate (linearly dependent on the inlet pressure, as shown in **Eq.(3.10)**) and thus conclusions drawn in the previous section allow to say that its power output increases. However, the high pressure of the cycle increases less than linearly when increasing the intermediate source temperature, mitigating the positive effect on the production of power. Indeed, since a higher mass flow rate is deviated to the power production line, the temperature pinch on the condenser is reduced with an effect on the cycle high pressure.
Similar considerations can be made also in the case of the cold source temperature. Lowering this temperature reduces the cooling production output but increases the ΔP available to the turbine.

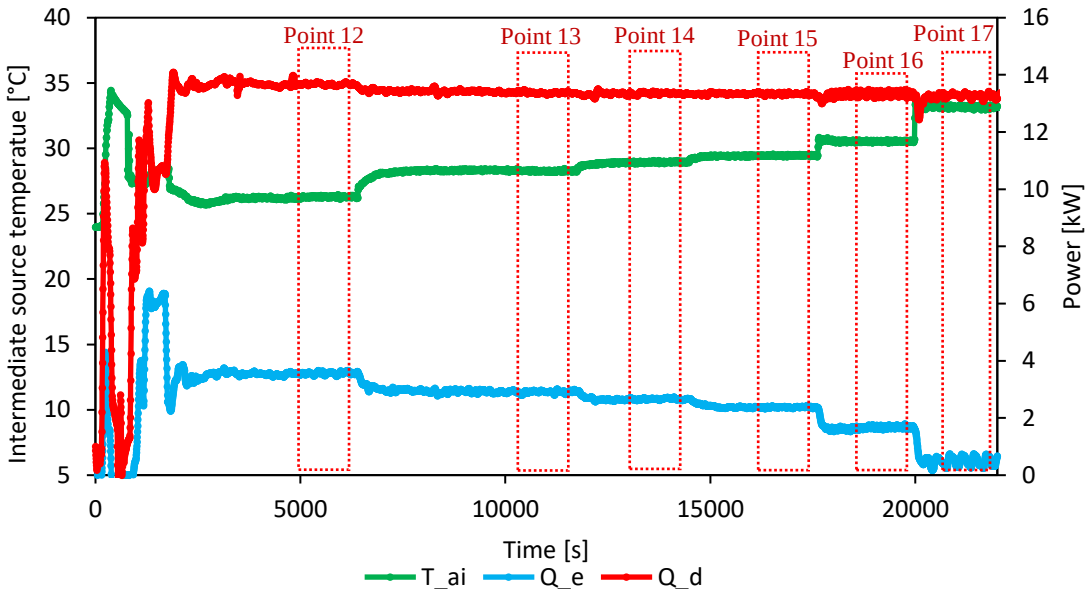


**Fig. 3.19** – Intermediate source temperature variation ($T_{di}$ = 100 °C, $T_{ei}$ = 18 °C, $\dot{m}_1$ =100 kg/h).

**Fig. 3.20** shows the transition from a stable point with the turbine line closed to a stable point with the turbine line open. The time required to reach stable functioning is below 180 s (3 minutes), but it can be notices that the turbine reaches stable functioning more quickly.

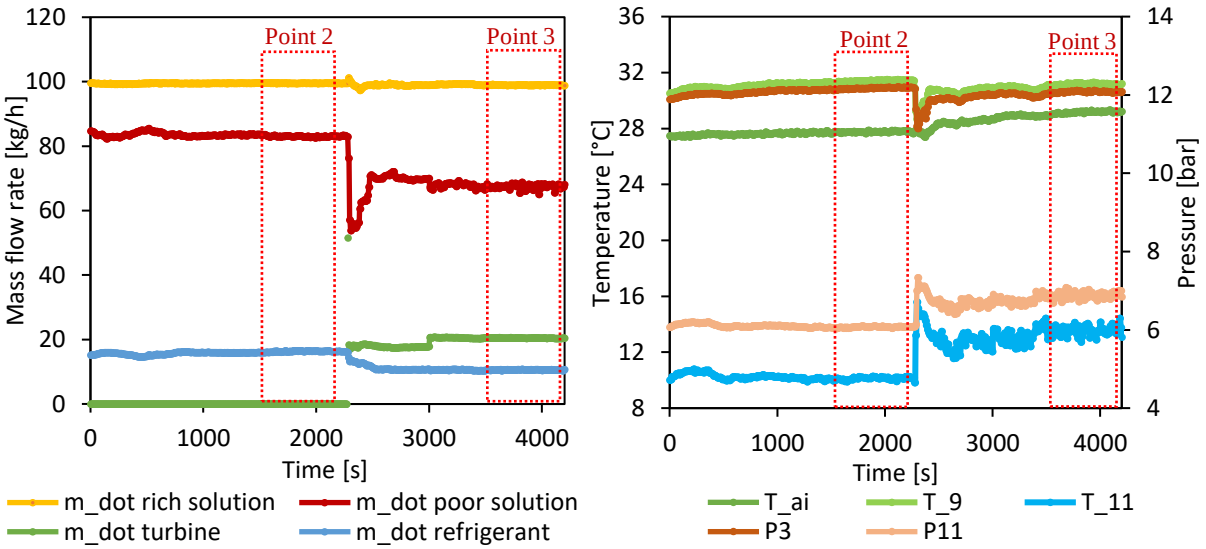


**Fig. 3.20** – Working mode switching from simple absorption to absorption cooling and power ($T_{di}$ = 102 °C, $T_{ai}$ = 18 °C).

The same considerations discussed before can be made concerning the increase in the circulating vapour mass flow rate and the variation of the working pressures when part of the circulating vapour is deviated towards the turbine. Additionally, it can be noted that, since the power absorbed by the hot source increases from 9.9 kW to 13.7 kW, it is difficult for the intermediate temperature HTF modules to reject all the power absorbed from the cycle. Hence, the absorber and condenser HTF inlet temperature increases from the set point of 27 °C to around 29 °C. Moreover, the sudden decrease in poor solution mass flow rate that takes place at the opening of the turbine line indicates that the desorber is probably capable of producing all the vapour requested, but the absorber then becomes limiting and causes the circulating vapour mass flow rate to stabilise at a lower value.

The opposite mode switch is shown in **Fig. 3.21.** Here passing from a combined production mode to a simple absorption mode decreases the mass flow rate of circulating vapour, increases the high pressure of the cycle and decreases the low pressure. In this case, since the desorber inlet temperature (94°C) is lower than in the previous case shown in **Fig. 3.20** (102 °C), the power absorbed from the hot source is smaller. Hence, the power to be rejected to the intermediate source is also smaller and it is possible to maintain the set intermediate source temperature of 27 °C also in the combined production working mode.
In general, it can be observed that, as in the case of the absorption chiller working mode, the dependency of the working pressures from the condenser outlet and evaporator inlet temperatures remains also in the combined production working mode. Additionally, it can be noted that the functioning is on average more unstable in the combined production working mode.

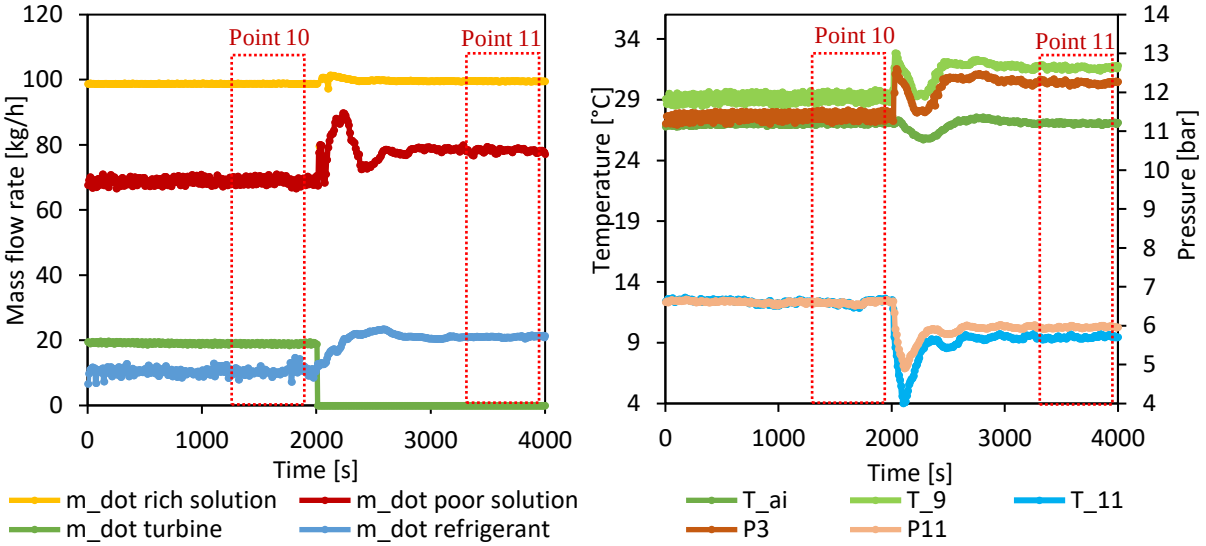


**Fig. 3.21 -** Working mode switching from absorption cooling and power to simple absorption ($T_{di}$ = 94 °C, $T_{ei}$ = 18 °C).

Functioning as power cycle (equivalent to a Kalina cycle) was also tested. In this operating mode, the high pressure of the cycle is defined by an equilibrium between the mass flow rate that can be treated by the turbine at a given pressure and the amount of steam desorbed at the same pressure. The low pressure of the cycle is instead fixed by the absorption temperature (of the intermediate temperature source), which in this case takes place in the absorber. In the case of the prototype, the safeties are set to stop the loop if a pressure of 14 bar is exceeded. Hence, stable functioning as a power cycle was only possible for low temperatures of the hot source (below 90 °C).
Starting and stopping the system have been tested in all three possible working modes showing that the plant is flexible enough to be started or stopped in any configuration, provided that adequate operating conditions are imposed.
Finally, in order to test the effect on the cycle of diverting an increasing part of the vapour mass flow rate to the power production line were carried out. Since this was not possible using the turbine, tests with variable opening of the turbine by-pass valve were conducted. Results, showed in **Fig. 3.22** show that the more the valve opening is increased, the more steam is desorbed (passing from around 20 kg/h when the valve is closed to almost 30 when it is fully open).

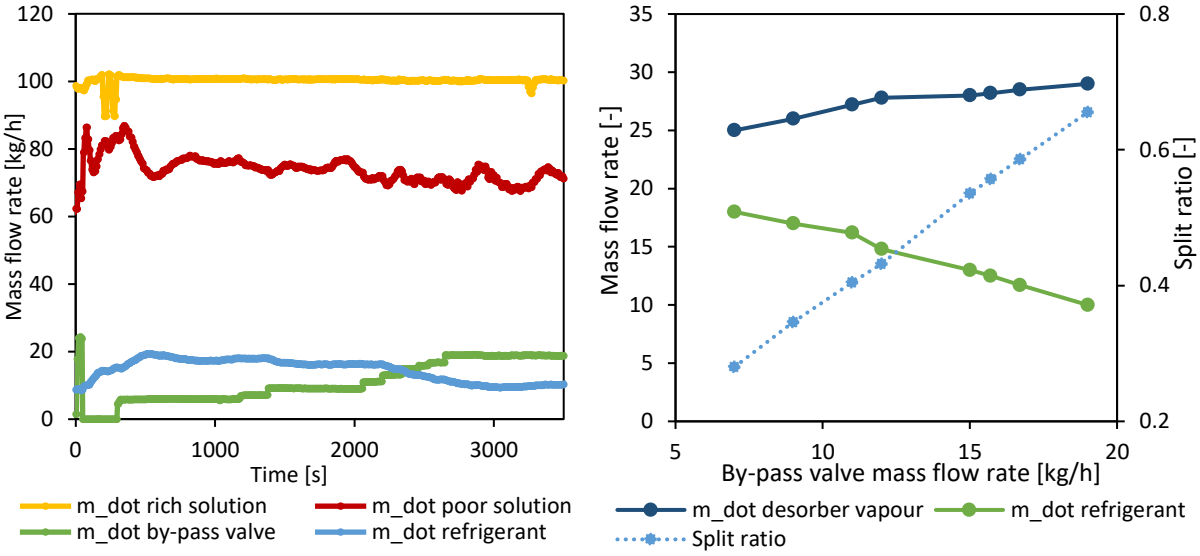


**Fig. 3.22 -** Variation of the turbine by-pass valve opening ($T_{di}$ = 100 °C, $T_{ai}$ =18 °C, $T_{ei}$ =18 °C, $\dot{m}_1$ =100 kg/h).

In conclusion, the integration of the micro-turbine into the single-stage absorption chiller plant has been analysed through an experimental campaign. Tests have been conducted only around the nominal operating point of the absorption chillers. Dynamic switching between the three possible operating modes has been tested and proved to be stable and quick to reach steady state. One of the main findings of these tests is that the lack of possibility to regulate the mass flow rate treated by turbine imposes strict limits on the cooling production side of the loop.
Moreover, the reduced mass flow rate passing through the cooling side heat exchangers (condenser and evaporator) increases their efficiency, affecting the pressures equilibrium established within the cycle and the circulating vapour mass flow rate.

## 3.5 Feedback from experimental tests on the prototype

Several experimental tests campaign were carried out on the experimental facility in the course of this thesis work, both in the absorption chiller and combined cycle configuration. These tests allowed a deeper understanding of the system's operation, its operating range and its limitations.
A first limitation worth mentioning is that the prototype is designed for a cold source temperature of 18 °C (resulting in cooling production at around 13-15 C°) and performance of the system degrades considerably at lower temperature. Also, since the HTF used is water, the cold production temperature would in any case be limited to positive temperatures.
Aspects to be given great attention are the operation of the electronically actuated valves and the level control in the tanks. It was noted that wearing of valves, could lead to instabilities in the machine's operation and strongly fluctuating behaviour. The expansion valve on the poor solution line for example needed to be replaced twice during testing. This valve, in addition to ensuring the pressure drop necessary for the functioning of the cycle, is also in charge of controlling the liquid level in the tank before the pump. This parameter also proved to be important and influential on the operational stability of the system, as it regulates the quantity of working fluid circulating in the loop. Experience on the pilot plant suggests that this level should be regulated to 60 mm when using the combined desorber/rectifier.

Another important issue is the flooding of the desorber. As previously stated, Wirtz [29] characterised the desorber both in the unflooded and partially flooded working mode. However, the flooding of the desorber is not desirable, but rather an issue due to problems of design and positioning of the component in the loop. A small reservoir is placed downstream the desorber, at the poor solution outlet. The purpose of this tank was originally to recover the part of the vapour that may have remained trapped in the poor solution. Numerical models and experimental results have shown this contribution to be negligible. However, since this tank is placed at the same height as the desorber, if the liquid level inside it exceeds 30 mm, this means that the desorber is partially flooded. The height of the tank is 146 mm, hence when the reservoir is filled with liquid it is not possible to know exactly the level of the liquid in the desorber. Avoiding flooding of the desorber can be rather challenging and specific working protocols need

to be used. Wirtz [29] reported that setting the desorber temperature initially at a higher value and then lowering it to the desired value appeared to be an effective way to avoid flooding of the desorber.
Finally, one last point concerns the choice of the temperature glide in the evaporator. When the ammonia vapour purity is not very high, the temperature glide in evaporator can be considerable. This glide can be reduced by allowing some liquid at the evaporator exit which is then evaporated in the subcooler. However, the presence of the liquid degrades the cycle performance because energy is spent in the desorber to produce vapour which provides no refrigeration. On the other hand, an excessive temperature glide leads to a reduction of the evaporator inlet temperature, with a strong impact on the pressures and performance of the cycle. The choice of this parameter can then have a strong impact on the performance of the cycle. In the experimental prototype, it is regulated (generally at 5 °C) by regulating the mass flow rate on the cooling production line through the actuated throttling valve placed before the evaporator.

All the above-mentioned features complicate the management of the plant and can reduce the repeatability of the tests. Looking for example at **Fig. 3.6**, for the nominal operating point ($T_{di}$ = 95 °C, $T_{ai}$ = 27 °C, $T_{ei}$ = 18 °C and $\dot{m}_1$ = 100 kg/h) performances can vary with a cooling power changing between 6.5-7.2 kW and a COP varying from 0.66-0.69.

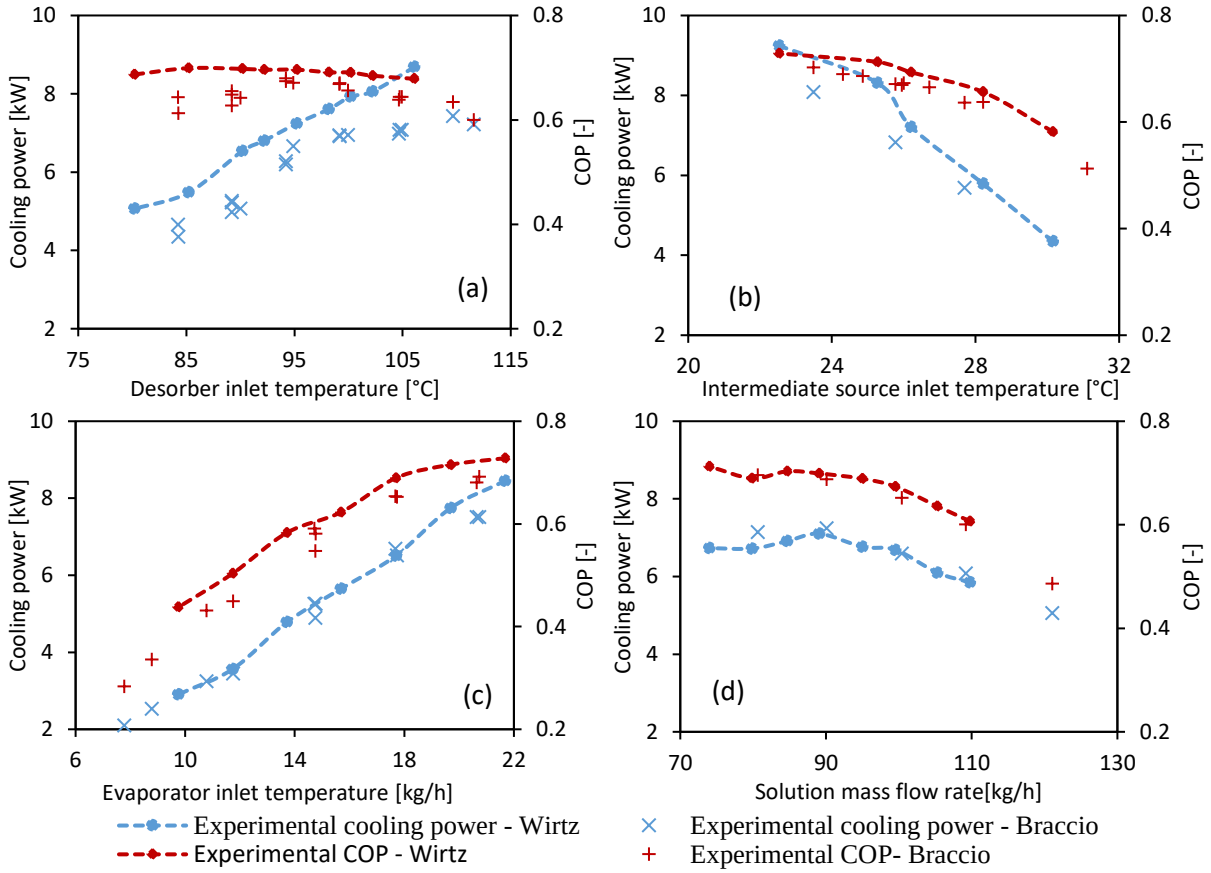


**Fig. 3.23 –** Comparison of experimental tests on the absorption chiller.

In order to check the repeatability of the experimental measures and the familiarize with the prototype prior to the combined cycle tests, experimental test campaigns on the absorption chiller were undertaken also in the framework of the present doctoral thesis. The experimental campaign matrix is shown in **Table 3.7**. It can be noted that, despite several attempts, it was not possible to achieve unflooded functioning of the combined desorber in most of the tests. To solve this problem, a re-design of the component is underway to make it easier to control and the new combined desorber/rectifier will be integrated in the loop in future works.
**Fig. 3.23** compares results of this experimental campaign with results obtained by Wirtz [29] (**Fig. 3.6**). It should be noted however that **Fig. 3.6(a)-(b)-(c)** refer to two different desorber temperatures, 100 °C and 95 °C respectively. In these three cases, the results are similar to those obtained by Wirtz. Given the temperature difference, the measured powers should be higher in the case of experimental test points shown in **Table 3.7**. The fact that the two values are very similar indicates that the efficiency is lower in the case of partially flooded desorber.

**Table 3.7** – Absorption chiller additional experimental campaign matrix.

| Point | High temperature source [°C] | Intermediate temperature source [°C] | Low temperature source [°C] | Rich solution mass flow rate [kg/h] | Temperature glide evaporator [°C] | Desorber outlet tank level [mm] | Cooling power output [kW] | COP [-] |
|---|---|---|---|---|---|---|---|---|
| 1 | **99** | 27 | 18 | 100 | 5.0 | 22 | 6.93 | 0.67 |
| 2 | **94** | 27 | 18 | 100 | 4.9 | 19 | 6.27 | 0.68 |
| 3 | **89** | 27 | 18 | 99 | 5.0 | 25 | 5.22 | 0.66 |
| 4 | **84** | 27 | 18 | 100 | 5.0 | 27 | 4.35 | 0.61 |
| 5 | **89** | 27 | 18 | 101 | 4.9 | 46 | 4.98 | 0.63 |
| 6 | **99** | 27 | 18 | 100 | 5.0 | 28 | 6.91 | 0.67 |
| 7 | **94** | 27 | 18 | 100 | 5.0 | 29 | 6.19 | 0.67 |
| 8 | **89** | 27 | 18 | 99 | 4.9 | 34 | 5.26 | 0.65 |
| 9 | **84** | 27 | 18 | 99 | 5.1 | 27 | 4.65 | 0.64 |
| 10 | **112** | 29 | 18 | 100 | 5.0 | 128 | 7.22 | 0.60 |
| 11 | **105** | 28 | 18 | 99 | 5.0 | 136 | 6.98 | 0.64 |
| 12 | **105** | 28 | 18 | 100 | 5.0 | 146 | 7.08 | 0.64 |
| 13 | **100** | 27 | 18 | 100 | 5.0 | 146 | 6.94 | 0.66 |
| 14 | **95** | 26 | 18 | 100 | 5.0 | 146 | 6.66 | 0.67 |
| 15 | **90** | 27 | 18 | 99 | 5.0 | 146 | 5.07 | 0.64 |
| 16 | **110** | 28 | 18 | 99 | 5.0 | 146 | 7.43 | 0.63 |
| 17 | **105** | 28 | 18 | 101 | 5.0 | 146 | 7.07 | 0.64 |
| 18 | 95 | **23** | 18 | 100 | 5.1 | 146 | 8.08 | 0.70 |
| 19 | 95 | **26** | 18 | 100 | 5.0 | 146 | 6.82 | 0.67 |
| 20 | 95 | **28** | 18 | 100 | 5.1 | 146 | 5.69 | 0.64 |
| 21 | 100 | **26** | 18 | 100 | 5.0 | 146 | 7.48 | 0.67 |
| 22 | 100 | **24** | 18 | 100 | 5.0 | 146 | 8.39 | 0.69 |
| 23 | 100 | **25** | 18 | 100 | 5.0 | 146 | 8.15 | 0.69 |
| 24 | 100 | **26** | 18 | 100 | 5.0 | 146 | 7.56 | 0.67 |
| 25 | 100 | **27** | 18 | 100 | 5.0 | 146 | 7.11 | 0.67 |
| 26 | 100 | **28** | 18 | 100 | 5.1 | 146 | 6.25 | 0.64 |
| 27 | 100 | **31** | 18 | 100 | 5.1 | 146 | 3.82 | 0.51 |
| 28 | 94 | 27 | **18** | 100 | 5.1 | 146 | 5.61 | 0.64 |
| 29 | 99 | 27 | **8** | 102 | 0.6 | 133 | 2.10 | 0.28 |
| 30 | 99 | 27 | **11** | 102 | 5.3 | 130 | 3.25 | 0.43 |
| 31 | 99 | 27 | **15** | 101 | 5.0 | 146 | 5.26 | 0.58 |
| 32 | 99 | 27 | **18** | 100 | 5.3 | 146 | 6.52 | 0.65 |
| 33 | 99 | 28 | **21** | 99 | 5.0 | 146 | 7.51 | 0.69 |
| 34 | 99 | 28 | **21** | 99 | 5.0 | 146 | 7.52 | 0.68 |
| 35 | 99 | 27 | **18** | 100 | 5.1 | 146 | 6.69 | 0.65 |
| 36 | 99 | 27 | **15** | 101 | 4.7 | 146 | 5.26 | 0.59 |
| 37 | 99 | 27 | **15** | 101 | 4.9 | 133 | 4.89 | 0.55 |
| 38 | 99 | 27 | **12** | 102 | 5.0 | 132 | 3.45 | 0.45 |
| 39 | 99 | 27 | **9** | 102 | 1.3 | 131 | 2.54 | 0.34 |
| 40 | 99 | 27 | 18 | **121** | 4.9 | 144 | 5.06 | 0.49 |
| 41 | 99 | 27 | 18 | 121 | **2.0** | 146 | 5.09 | 0.49 |
| 42 | 99 | 27 | 18 | 122 | **8.0** | 146 | 4.79 | 0.49 |
| 43 | 99 | 27 | 18 | **109** | 5.0 | 146 | 6.08 | 0.60 |
| 44 | 99 | 27 | 18 | 109 | **1.5** | 146 | 5.74 | 0.55 |
| 45 | 99 | 27 | 18 | **100** | 5.1 | 146 | 6.59 | 0.65 |
| 46 | 99 | 28 | 18 | **90** | 5.0 | 146 | 7.25 | 0.69 |
| 47 | 99 | 27 | 18 | **81** | 5.1 | 145 | 7.14 | 0.70 |

By contrast, much more pronounced discrepancies appear when the desorber temperature varies (**Fig. 3.6(a)**). In this case, the flooding of the desorber (and consequently the reduction of its useful exchange surface area) seem to play a more important role. In fact, the cooling power output is always lower than in the case of unflooded desorber and the COP curve has a less flat curve and a much more pronounced maximum around 95 °C (where performance is very similar to the unflooded case).

As shown in **Table 3.7**, some tests were also performed to evaluate the impact of the definition of the temperature glide in the evaporator (points 40-44). This parameter seems to have a relatively small influence on the performance of the cycle with an optimum value around 2-5 °C.
In the case of the turbine, an improper definition of the design point (inlet pressure of 16 bar and outlet pressure of 4 bar) leads to the presence of shocks and non-isentropic adjustment phenomena when the turbine is used in the cycle (with an inlet pressure usually below 12 bar and an outlet pressure usually above 6 bar). In addition, a very low efficiency of electricity generation (further degraded by the titanium casing protecting the coils), very low achievable rotational speeds and important mechanical losses result in extremely low values of electricity production of the turbine. Worth mentioning, are also the difficulties of controlling the turbine inlet temperature using the electric superheater. Finally, the problem of the condensation of the working mixture during expansion remains to be investigated.

Concerning the combined cycle, the most important limitations highlighted concern the limited operating range of the cycle. Indeed, there is a limit to the total power that can be exchanged by external circuits, which in total cannot exceed approximately 40 kW. Because of this, it is not possible to achieve desorber temperatures beyond 110 °C-115 °C. Furthermore, the maximum cycle pressure is limited to 14 bar, which did not allow the machine to be characterised in detail as a power cycle. Lastly, we point out the strict limits imposed by the turbine on the cycle. In fact, by imposing a treated flow rate, the turbine greatly reduces the flexibility of the cycle identified at the outset as its main advantage. This also has a strong impact on the pressures on the cycle and ultimately on its overall functioning.

## 3.6 Conclusions

Given the lack of experimental studies on APC cycles available in literature, one of the objectives of the present work was the development of a suitable expander for a small-scale combined cooling and power production cycle and its integration in an existing single stage ammonia water absorption chiller. The characteristics of the expander and of the cycle components bring the novelty of the present work.
However, several challenges were faced mainly related to the small size of the pilot plant. This greatly hindered the choice of expansion device and its development, which was complicated by the corrosiveness of the ammonia-water mixture. Various test campaigns were carried out on the absorption chiller, the turbine (outside and inside the absorption loop) and the combined cycle.
Concerning the absorption chiller testing, it was shown that attention must be paid to reach steady operation of the pilot plant, for which reservoirs level regulation and actuated valve opening (i.e., throttling valves upstream the absorber and evaporator) is crucial. The combined desorber integrated in the pilot plant, in addition to avoiding the use of a separated rectifier, simplifies the plant management compared to the use of the classical boiling heat exchanger architecture and allows reaching a thermal COP a higher than 0.7 in the investigated operating conditions. However, partial flooding of the desorber can occur leading to reduced efficiency of the component affecting the overall cycle performance.
The turbine integrated in the cycle is an impulse turbine, in which all expansion takes place in the converging diverging injector. Given the ratio between the exit and throat section of the injector a very small pressure drop is sufficient to achieve sonic conditions. Therefore, in the APC cycle, the turbine works practically constantly in choking conditions, in which the mass flow rate treated depends linearly on the inlet pressure. Taking into account the real-gas behaviour is relevant for the turbine mass flow rate calculation for ammonia, while it is negligible for the other tested gases. Due to the small scale of the turbine, and significant losses of the electricity generation components, the maximum electrical efficiency achieved was of 7%.
Limitations in terms of the operating ranges of the pilot and specifically of the turbine (inappropriate design point definition, low efficiency of electrical generation, low efficiency at small scales) have not allowed a complete characterisation of the cycle. However, insights and experience gained from the tests will be of paramount importance to continue the development of the technology.
The measurements bring interesting observations on the functioning of the cycle. First, the fact that the turbine mass flow rate is fixed for given working conditions has important consequences on the cycle, as it is not possible to change the split ratio between cooling and power production unless the pressure upstream of the turbine is changed. Furthermore, diverting some of the desorbed steam to the power production line has important effects on the cooling production side of the cycle, changing its efficiency and hence the pressures of the cycle as well as the mass flow rate of circulating vapour.
To go further, an assessment is needed to evaluate the relevance of the technology on a larger range of operating conditions and scales. For that, a numerical model of the cycle was developed, as presented in the following sections, based on the exploitation of experimental data along with complementary validation tools.

# Chapter 4
# Numerical models development

*This chapter presents the development of a numerical model of the cycle presented in the previous chapter. To go further on the analysis of the combined cooling and power cycle, a numerical model has been developed based on experimental data and results of CFD simulations for the turbine. A model of the absorption chiller is developed first, using data from the original absorption chiller prototype. The model is based on the characterisation of exchangers through semi-empirical effectiveness modelled on dimensionless parameters. Effectiveness coefficients are adjusted on experimental measurements from the pilot plant. Subsequently, a model of the partial admission turbine is built, including a description of the expansion taking place in the supersonic injector and a simplified rotor loss model. Loss model coefficients are tuned based on CFD simulations carried-out on the expander. Finally, the turbine model is integrated in the absorption cycle model, providing a reliable tool for the simulation of the combined production cycle. Scale-up possibility of the models is presented at the end of each subsection.*

# 4.1 Introduction

In this chapter, the development of the numerical models used for the characterisation and performance evaluation of the combined production cycle is presented. A model of the absorption chiller is developed first by characterising its exchangers trough semi-empirical effectiveness adjusted on experimental data. Subsequently, a 1D model of the turbine is built including a simplified loss model in which the expressions of the loss terms are defined based on existing literature, but their coefficients are adjusted to match CFD simulations performed on the turbine. It is important to highlight however that CFD simulations were simply used as a validation tool for the 1D turbine and not to investigate its performance. The turbine model is then integrated into the absorption cycle model to allow the simulations of the complete cooling and power cycle. Limitations on the flexibility of the cycle imposed by the turbine (described in the previous chapter and discussed more in details in the next chapter) have suggested the possibility of introducing an ejector into the cycle to allow greater flexibility without excessive performance penalty.
The evaluation of this new patented architecture [180] (presented in *Section 5.5*) required the development of an ejector model presented in *Section 7.1*. The model, based on mass flow rate maximisation, was validated on experimental data from various SERS cycles (*Section 2.4.1*) proving to be a very reliable tool to predict on-design and off-design performance of the ejector. As a first step for the assessment of the proposed novel architecture, a simplified ejector model, capable of predicting nominal (but not off-design) ejector performance was also developed (*Section 7.2*) and integrated into the combined cycle. However, since ejector modelling is not the focus of the present work, this is not presented in this chapter and details regarding these models are given in the Appendix.

# 4.2 Absorption cycle model

This section presents the development of a numerical model of the ammonia-water single-stage absorption chiller integrating a new combined desorber presented in *Section 3.3.1*.
Appropriate modelling is of fundamental importance for performance evaluation, characterization and optimization of a system. Existing models can be divided into three categories depending on their nature: physical, semi-empirical, with some degree of physical insight, and black box or empirical, when no physical insight is necessary and the model describes a dataset of experimental results [181]. Black box methods include multivariate polynomial regression and artificial neural network models [182]. Semi-empirical models were proposed as an alternative by Gordon [183] and Ziegler [184] who adapted the characteristic equation method to account for the fact that predicted cooling capacity deviates considerably from the linear behaviour, particularly at high temperatures. Despite the increased accuracy of these models, the underlying physics of cycle functioning are concealed, and the calculated performance can deviate considerably from experimental performance, especially outside nominal conditions. A more accurate approach is to implement semi-empirical effectiveness in a physical model considering heat and mass transfer processes separately [181]. Physical models provide the best results in steady state conditions but need access to the physical properties of fluids [44]. Several correlations have been proposed for the ammonia-water mixture. Thorin [185] compared the saturation properties predicted by the correlations of Stecco and Desideri [186], Ibrahim and Klein [179] and Tillner-Roth and Friend [187], showing that at low temperatures they all give very similar results and that the difference is not significant for performance calculation at low temperatures (below 250 °C). Correlations of Ibrahim and Klein [179], included into EES internal library are hence used here.
This section develops a model of the absorption machine based on semi-empirical models of the individual components tuned using experimental data. The component models are then integrated in a physical model of the cycle, capable of predicting its performance, and taking into account the size and architecture of the specific application.
A simplified process flow diagram of the absorption chiller only is presented in **Fig. 4.1**. With respect to **Fig. 3.5**, since the power production line is closed, state points 7 and 8 coincide, as well as state points 13 and 17.

Results from the experimental campaign presented in *Section 3.4.1* were analysed critically, excluding unreliable points (see *Section 3.4.1*), to be able to obtain an accurate database for numerical model adjustment. Initially a simplified physical model using fixed pinch temperatures was developed serving as a term of comparison for more detailed models.
For the simplified model, components are described by means of an average temperature pinch based on experimental tests for the external exchangers and constant effectiveness for the internal exchangers. Subsequently, a more detailed model of the pilot plant was developed based on thermal, mass and species semi-

empirical effectiveness for each exchanger. Heat exchanger effectiveness is often characterized using dimensionless parameters like the number of transfer units ($NTU$) and the energetic ratio ($R_{en}$) between the maximum and minimum heat capacity of the two fluids. In the case of absorption machines, the absorber and the desorber represent two atypical heat exchangers in which sorption processes also take place, making it necessary to include another parameter, the Jakob number ($Ja$) for their characterization [29]. The experimental behaviour of each exchanger is characterized using appropriate effectiveness, and the various correlations developed to model them were integrated in the physical model of the cycle and compared to experimental results. Finally, a parametric analysis on component size is performed to prove the robustness of the model and its capability to be used for the scale-up evaluation.

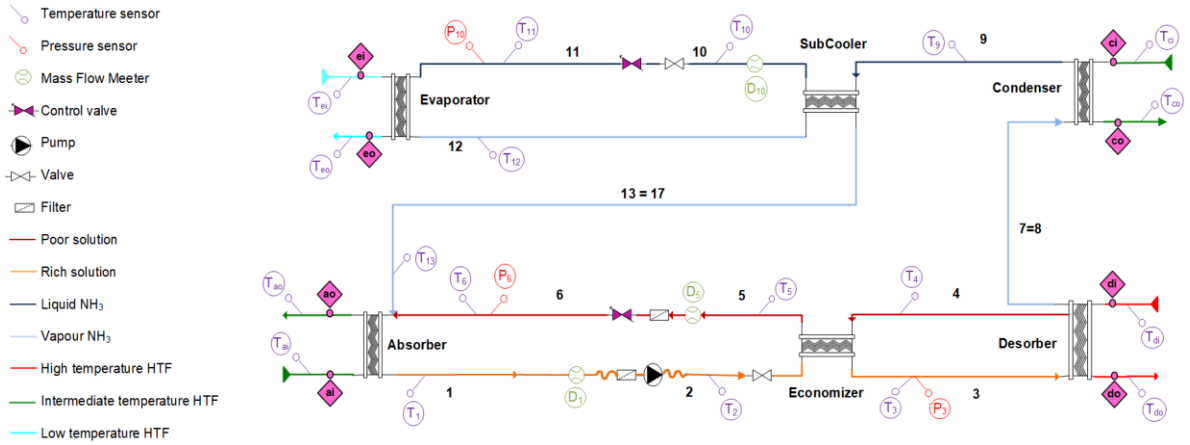


**Fig. 4.1 –** Simplified process flow diagram of the absorption chiller (created in Microsoft Visio).

The aim is also to propose a modelling method for absorption machines able to give reliable information on the performance also when changing the plant size. This is particularly useful, for example, to evaluate the scale-up of the technology, help designing the relative size of components of the cycle and perform techno-economic or exergo-economic analysis. This type of modelling can be very useful in the development of combined cooling and power cycles.

### 4.2.1 Simplified model of the cycle

A simplified steady state numerical model of the absorption cycle previously introduced was developed in EES based on the now well know description of Herolds et al. [5] with respect to which only the specific differences due to the combined desorber are highlighted here. For each component, the energy and mass conservation equations were formulated. The parameters of each heat exchanger (pinch or effectiveness) were set based on the values assessed experimentally in order to predict well the performance of the ammonia-water absorption prototype in the nominal operating point. It is assumed that the mixture is saturated at the outlet of desorber and condenser.

The desorber considered is a combined component that generates vapour and purifies it by exchanging heat with the liquid solution at the inlet (as described in *Section 3.3.1*). Therefore, in ideal conditions, the refrigerant vapour at the outlet reaches the same temperature as the solution at the inlet and its concentration is that of saturated vapour at the inlet temperature of the rich solution $T_3$:

$$x_{7,id} = x_{vap,sat}(T_3, P_3) \tag{4.1}$$

The conditions of the poor solution at the outlet can then be calculated through an energy balance on the desorber (**Eq. (3.6)**). The performance of the absorber is modelled with a mass effectiveness $\varepsilon_{\text{mass,a}} = \dot{m}_{13}/\dot{m}_{13,\max}$ fixed to 0.6 according to previous experimental tests on this prototype [175] and a temperature pinch between the HTF at the inlet and the rich solution at the outlet $\Delta T_a = T_1 - T_{a,i}$ fixed to 5 °C. A fixed temperature pinch of 5 °C is imposed between the inlet of the intermediate temperature HTF and the liquid refrigerant exiting the condenser

($\Delta T_c = T_9 - T_{c,i}$). The high pressure of the cycle is then determined as the saturated liquid pressure at the condenser outlet temperature $T_9$ and ammonia mass fraction $x_9$.
The evaporator performance is defined by the pinch between the HTF at the inlet and the refrigerant fluid at outlet ($\Delta T_e = T_{e,i} - T_{12}$) imposed equal to 5 °$C$ and a temperature glide between the inlet and outlet of the component ($\Delta T_{glide} = T_{12} - T_{11}$) also imposed equal to 5 °C, as it is a control parameter of the plant (*Section 3.4*). Since $T_{11}$ and $x_{11}$ are known, the hypothesis of an isenthalpic throttling in the valve allows calculation of the low pressure of the cycle. As highlighted by experimental results (**Fig. 3.9**) the low pressure of the cycle can also be calculated as the saturated liquid pressure at $T_{11}$ and $x_{11}$. The solution heat exchanger effectiveness $\varepsilon_{shx} = \dot{Q}_{shx}/\dot{Q}_{shx,max}$ is set equal to 0.8 and the subcooler effectiveness $\varepsilon_{sub} = \dot{Q}_{sub}/\dot{Q}_{sub,max}$ is set to 0.9. Details for the calculation of $\dot{m}_{12,max}$, $\dot{Q}_{shx,max}$ and $\dot{Q}_{sub,max}$ will be given in the following sections. Finally, no pressure drop or thermal dispersion is considered and the pump isentropic efficiency is set to 0.8 [13].

The results of the simplified model are compared to the experimental measures in **Fig. 4.2**. The model of the cycle predicts the experimental results well at the operating point near the nominal conditions (defined in **Table 3.2**). Nevertheless, considering fixed component effectiveness results in simulated points differing substantially from experimental for conditions other than nominal, with a frequent overestimation of performance. This highlights the need for more accurate modelling such that the model can be used reliably for different applications and plant sizes. The development of a model based on variable semi-empirical effectiveness is therefore presented in the following paragraphs.

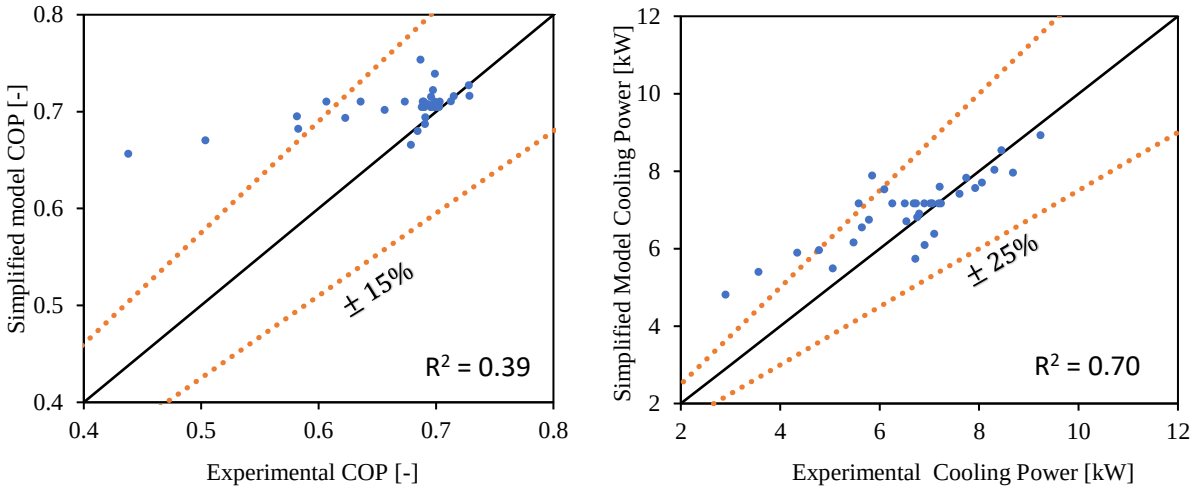


**Fig. 4.2 -** Comparison of the simplified numerical model with experimental results.

## 4.2.2 Experimental effectiveness model (ε-model)

With the goal of better describing the behaviour of the machine, a more detailed steady state model was developed by introducing variable experimental effectiveness to describe the functioning of each heat exchanger. Also in this case, the assumption is made that the fluid is at saturation at the outlet of desorber and condenser and at the inlet of the evaporator. The efficiency of the pump is assumed equal to 0.8, expansion in valves is considered isenthalpic and pressure drops and thermal dispersions are neglected. The only inputs of the developed model are the control parameters of the pilot plant (HTFs temperatures and mass flow rates, rich solution mass flow rate and temperature glide in the evaporator).
Experimental effectiveness were calculated comparing the actual performance of exchangers with that of ideal components. Three dimensionless numbers were used in the modelling of the effectiveness as suggested recently in [29]: the energetic ratio $R_{en}$, the number of transfer units $NTU$ and the Jakob number $Ja$. $R_{en}$ is defined as the ratio of the maximum power transferable to the non-limiting (having the higher transferable power) fluid over the maximum power transferable to the limiting fluid (having the lower transferable power) in the exchange:

$$R_{en} = \frac{\max(\dot{Q}_{HTF,max}, \dot{Q}_{sol,})}{\min(\dot{Q}_{HTF,max}, \dot{Q}_{sol,max})} \tag{4.2}$$

The number of transfer units NTU is a dimensionless parameter characterizing the rate of heat transfer in heat exchangers. It is defined as the ratio of the product of the heat transfer coefficient K and the exchange S surface to the smallest heat capacity rate between the two fluids [188]:

$$\mathrm{NTU} = \frac{\mathrm{K \cdot S}}{(\dot{m} \cdot \mathrm{Cp})_{min}} \tag{4.3}$$

Since the HTF mass flow rate is always much higher than the solution mass flow rate, the solution is always characterised by the smallest heat capacity rate. Hence this value is indicated in the following for the calculation of the NTU. The overall heat transfer coefficient K considers both convective transfers between falling film and plate and between the HTF and plate and conduction across the absorber plate. For the external heat exchangers, the HTF side heat transfer coefficient is calculated with a correlation developed for corrugated plates with a Reynolds number value between 50 and 14,600 [175], while the convective heat transfer coefficient between the falling film and the plates is calculated with the Wilke's correlation [175]. For the solution heat exchanger correlations developed by the GREThe are used on both sides. More details on the calculation of the NTU are given in *Section 7.3*.

The Jakob number $(Ja)$ is a dimensionless number defined as the ratio of the solution sensible heat to the latent heat released during the liquid vapour phase change:

$$\mathrm{Ja} = \frac{\rho_{\mathrm{sol}} \cdot \mathrm{cp}_{\mathrm{sol}} \cdot (\mathrm{T}_{\mathrm{HTF,i}} - \mathrm{T}_{\mathrm{liq,sat}})}{\rho_{\mathrm{vap}} \cdot \mathrm{L}} \tag{4.4}$$

Where $\rho_{\mathrm{sol}}$, $\mathrm{cp}_{\mathrm{sol}}$ and $L$ are the density, specific heat and latent heat of vaporization of the entering solution, $\mathrm{T}_{\mathrm{HTF,i}}$ is the temperature of the HTF at inlet and $\mathrm{T}_{liq,sat}$ is the temperature of the saturated liquid solution at the inlet at the given pressure and concentration. The following sections show the definition of the effectiveness for each component and the semi-empirical correlations proposed for modelling them.

## *Desorber model*

The performance of the desorber considered in the present study can be characterized using three effectiveness: thermal, mass and species [29]. These effectiveness relate the functioning of the desorber to that of an ideal one. In an ideal desorber, the vapour at the outlet reaches the temperature $\mathrm{T}_3$ of the entering rich solution with which it exchanges heat, increasing its ammonia concentrations to that of saturated vapour at $\mathrm{T}_3$ (**Eq.(4.5)**). For fixed mass flow rate and thermodynamic conditions at the inlet, the minimum mass flow rate of poor solution $\dot{m}_{4,min}$, the maximum mass flow rate of vapour $\dot{m}_{7,max}$ and the maximum power exchanged by the ideal desorber $\dot{\mathrm{Q}}_{\mathrm{d,max}}$ are deduced from mass, species and energy balances and assuming the poor solution at the outlet to be saturated:

$$x_{7,id} = x_{vap,sat}(T_3, \mathrm{P}_7) \tag{4.5}$$

$$x_{4,id} = x_{liq,sat}(T_4, \mathrm{P}_4) \tag{4.6}$$

$$\dot{\mathrm{m}}_3 = \dot{\mathrm{m}}_{4,\mathrm{min}} + \dot{\mathrm{m}}_{7,\mathrm{max}} \tag{4.7}$$

$$\dot{\mathrm{m}}_3 \,.\, \mathrm{x}_3 = \dot{\mathrm{m}}_{4,\mathrm{min}} \cdot \mathrm{x}_{4,\mathrm{id}} + \dot{\mathrm{m}}_{7,\mathrm{max}} \cdot \mathrm{x}_{7,\mathrm{id}} \tag{4.8}$$

$$\dot{\mathrm{Q}}_{\mathrm{d,max}} = \dot{\mathrm{m}}_{4,\mathrm{min}} \cdot \mathrm{h}\left(\mathrm{T}_4, \mathrm{P}_4, \mathrm{x}_{4,\mathrm{id}}\right) + \dot{\mathrm{m}}_{7,\mathrm{max}} \cdot \mathrm{h}\left(\mathrm{T}_3, \mathrm{P}_7, \mathrm{x}_{7,\mathrm{id}}\right) - \dot{\mathrm{m}}_3 \cdot \mathrm{h}(\mathrm{T}_3, \mathrm{P}_3, \mathrm{x}_3) \tag{4.9}$$

If the solution is the limiting fluid ($\dot{\mathrm{Q}}_{\mathrm{d,max}} = \dot{\mathrm{Q}}_{\mathrm{sol,d,max}}$), the HTF imposes the temperature as the poor solution at the exit and:

$$T_4 = T_{d,i} \tag{4.10}$$

If instead the HTF is the limiting fluid ($\dot{\mathrm{Q}}_{\mathrm{d,max}} = \dot{\mathrm{Q}}_{HTF,d,\mathrm{max}}$) the HTF reaches the same temperature of the solution at the inlet ($T_{d,o} = T_3$ ), and the first term of **Eq.(4.9)** is equal to:

$$\dot{\mathrm{Q}}_{\mathrm{d,max}} = \dot{\mathrm{m}}_{HTF,\mathrm{d}} \cdot \mathrm{cp}_{\mathrm{HTF,d}} \cdot \left(\mathrm{T}_{\mathrm{d,i}} - \mathrm{T}_3\right) \tag{4.11}$$

The desorber thermal effectiveness is defined as the ratio between the power transferred from the HTF fluid to the solution and the maximum transferable power [29]:

$$\varepsilon_{th,d} = \frac{\dot{\mathrm{Q}}_{\mathrm{d}}}{\dot{\mathrm{Q}}_{\mathrm{d,max}}} \tag{4.12}$$

The desorber mass effectiveness is defined as the ratio of the vapour mass flow rate generated in the desorber to the maximum vapour mass flow rate that could be generated [29] :

$$\varepsilon_{\text{mass,d}} = \frac{\dot{m}_7}{\dot{m}_{7,\text{max}}} \tag{4.13}$$

The desorber species effectiveness is defined as the ratio of the difference between actual ammonia and minimum ammonia concentration reachable at the outlet of the desorber, to the difference between the maximum and the minimum ammonia concentrations reachable [29]:

$$\varepsilon_{\text{species,d}} = \left( \frac{x_7 - x_{7,\text{min}}}{x_{7,\text{id}} - x_{7,\text{min}}} \right) \tag{4.14}$$

When the solution is the limiting fluid, the minimum ammonia concentration corresponds to the case in which the saturated vapour exits the desorber at the HTF inlet temperature and is calculated as:

$$x_{7,min} = x_{vap,sat}\,(T_{d,i}, P_3) \tag{4.15}$$

The energetic ratio $R_{en}$, number of transfer units $NTU$ and Jakob number $Ja$ are defined for the desorber as:

$$\text{R}_{\text{en,d}} = \frac{\max(\dot{\text{Q}}_{\text{sol,d,max}},\ \dot{\text{Q}}_{HTF,d,\text{max}})}{\min(\dot{\text{Q}}_{\text{sol,d,max}},\ \dot{\text{Q}}_{HTF,d,\text{max}})} \tag{4.16}$$

$$\text{NTU}_{\text{d}} = \frac{\text{K}\cdot\text{S}}{(\dot{m}_3.\text{Cp}_3)} \tag{4.17}$$

$$\text{Ja}_{\text{d}} = \frac{\rho_3 \cdot \text{Cp}_3 \cdot (\text{T}_{\text{d,i}} - \text{T}_{3,\text{sat}})}{\rho_{\text{vap}} \cdot \text{L}} \tag{4.18}$$

The desorber effectiveness are calculated for each experimental point and a correlation was found based on these three parameters using an exponential correlation similar to the ones typically used in modelling heat exchanger effectiveness [189] with the addition of the Jakob number $Ja$. The calculated effectiveness can vary between zero and one, asymptotically approaching this value when the magnitude of the parameters inside the exponential increases. The four coefficients of correlations are obtained by minimizing the mean square error with respect to experimental effectiveness. The correlations found show that mass and thermal effectiveness have similar functions and depend mainly on the $NTU$ and $Ja$. On the other hand, the species effectiveness is negatively affected by the $NTU$ and depends mainly on the Jakob number $Ja$.

$$\varepsilon_{th,d} = 1 - exp\,(-6.0 \cdot 10^{-3} \cdot Ja_{\text{d}}{}^{1} \cdot NTU_{\text{d}}{}^{1.5} \cdot R_{en,\text{d}}{}^{0.5}) \tag{4.19}$$

$$\varepsilon_{mass,d} = 1 - exp(-2.7 \cdot 10^{-3} \cdot Ja_{\text{d}}{}^{1.45} \cdot NTU_{\text{d}}{}^{1.5} \cdot R_{en,\text{d}}{}^{0.5}) \tag{4.20}$$

$$\varepsilon_{\text{species,d}} = 1 - exp(-2.3 \cdot 10^{-1} \cdot Ja_{\text{d}}{}^{1.3} \cdot NTU_{\text{d}}{}^{-0.5} \cdot R_{en,\text{d}}{}^{0.3}) \tag{4.21}$$

As shown in **Fig. 4.3** the effectiveness recalculated with the correlations approximate the experimental ones well, with errors below 15% and an average error of 5.6% for the thermal effectiveness, 7.5% for the mass effectiveness and 2.63% for the species effectiveness. Desorber mass effectiveness is however not used in the modelling of the cycle, since it was found that imposing the state of the poor solution at outlet to be saturated liquid yielded better results.

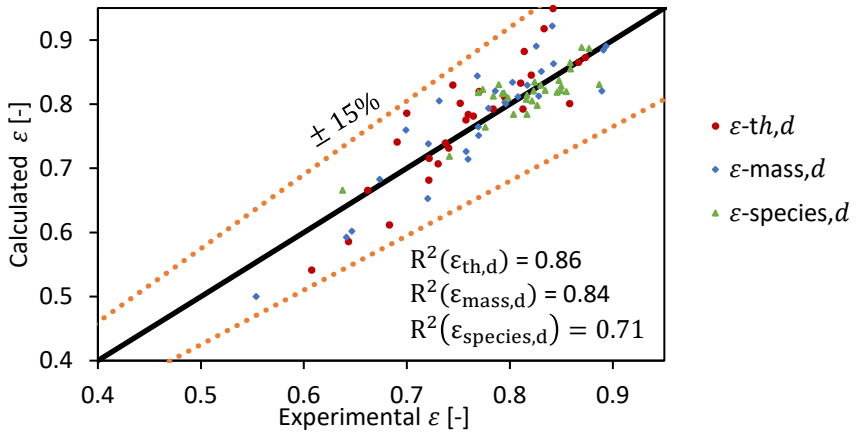


**Fig. 4.3 -** Calculated desorber effectiveness vs. experimental effectiveness.

## *Absorber model*

The performance of the absorber can be characterized using two effectiveness [190]: thermal effectiveness and mass effectiveness. In an ideal infinitely long absorber, after the vapour reabsorption, the solution exits from the component as saturated liquid and balance equations can therefore be written as:

$$x_{1,id} = x_{liq,sat}(T_1, P_1) \tag{4.22}$$

$$\dot{m}_1 = \dot{m}_{6,min} + \dot{m}_{13,max} \tag{4.23}$$

$$\dot{m}_1 \cdot x_{1,id} = \dot{m}_{6,min} \cdot x_6 + \dot{m}_{13,max} \cdot x_{13} \tag{4.24}$$

$$\dot{Q}_{a,max} = \dot{m}_{6,min} \cdot h(T_6, P_6, x_6) + \dot{m}_{13,max} \cdot h(T_{13}, P_{13}, x_{13}) - \dot{m}_1 \cdot h(T_1, P_1, x_{1,id}) \tag{4.25}$$

If the solution is the limiting fluid ($\dot{Q}_{a,max} = \dot{Q}_{sol,a,max}$), the solution exits at the absorber HTF inlet temperature:

$$T_1 = T_{a,i} \tag{4.26}$$

If instead the HTF is the limiting fluid ($\dot{Q}_{a,max} = \dot{Q}_{HTF,a,max}$), the latter will reach the temperature of the poor solution entering the absorber ($T_{a,o} = T_6$) and therefore the first side of **Eq. (4.25)** will be equal to:

$$\dot{Q}_{a,max} = \dot{m}_{HTF,a} \cdot Cp_{HTF,a} \cdot (T_6 - T_{a,i}) \tag{4.27}$$

The absorber thermal effectiveness is defined as the ratio between the actual power transferred from the solution to the HTF fluid and the maximum transferable power in an ideal absorber.

$$\varepsilon_{th,a} = \frac{\dot{Q}_a}{\dot{Q}_{a,max}} \tag{4.28}$$

The absorber mass effectiveness is defined as the ratio of the absorbed vapour mass flow rate and the maximum vapour mass flow rate that could be absorbed in an ideal component [175]:

$$\varepsilon_{mass,a} = \frac{\dot{m}_{13}}{\dot{m}_{13,max}} \tag{4.29}$$

The energetic ratio $R_{en}$, number of transfer units *NTU* and Jakob number $Ja$ are defined for the absorber as:

$$R_{en,a} = \frac{\max(\dot{Q}_{sol,a,max}, \dot{Q}_{HTF,a,max})}{\min(\dot{Q}_{sol,a,max}, \dot{Q}_{HTF,a,max})} \tag{4.30}$$

$$NTU_a = \frac{K \cdot S}{(\dot{m}_1 \cdot Cp_1)} \tag{4.31}$$

$$Ja_a = \frac{\rho_6 \cdot Cp_6 \cdot (T_{6,sat} - T_6)}{\rho_{vap} \cdot L} \tag{4.32}$$

The two effectiveness are modelled based on these three parameters (**Fig. 4.4**).

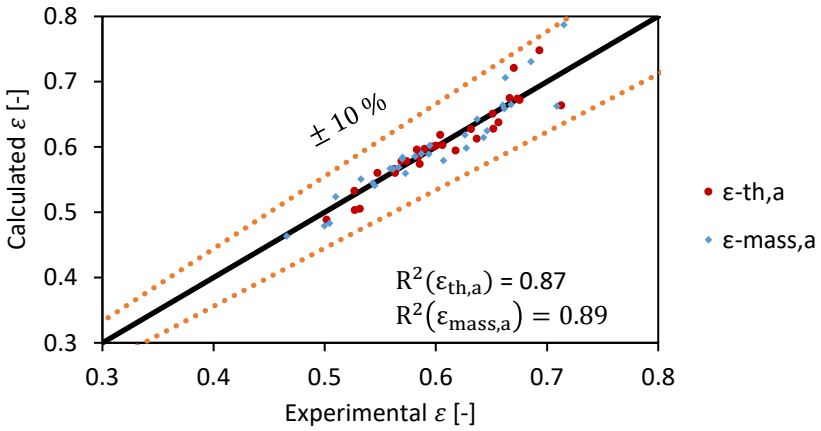


**Fig. 4.4 -** Calculated absorber effectiveness vs. experimental effectiveness.

The correlations found exhibit a similar dependence on the NTU as in the case of the desorber, but the $R_{en}$ is raised to a negative power:

$$\varepsilon_{th,a} = 1 - exp\,(-9.2 \cdot 10^{-3} \cdot {Ja_a}^{0.4} \cdot {NTU_a}^{1.5} \cdot {R_{en,a}}^{-0.72}) \quad (4.33)$$

$$\varepsilon_{mass,a} = 1 - exp\,(-9.1 \cdot 10^{-4} \cdot {Ja_a}^{0.4} \cdot {NTU_a}^{1.5} \cdot {R_{en,a}}^{-0.92}) \quad (4.34)$$

The maximum error of the correlations is below 10% for both effectiveness (**Fig. 4.4),** while the average error is 1.91% for the absorber thermal effectiveness and 2.1% for the mass effectiveness.

### *Other exchangers*

The evaporator being a component in which no concentration variation takes place, its functioning can be described simply using a thermal effectiveness. The maximum power that can be exchanged at the evaporator is:

$$\dot{Q}_{e,max} = \dot{m}_{12} \cdot [h(T_{12}, P_{12}, x_{12}) - h(T_{11}, P_{11}, x_{11})] \quad (4.35)$$

If the solution is the limiting fluid ($\dot{Q}_{e,max} = \dot{Q}_{sol,e,max}$): $T_{12} = T_{e,i}$, while if the HTF is the limiting fluid $(\dot{Q}_{e,max} = \dot{Q}_{HTF,e,max})$:

$$\dot{Q}_{e,max} = \dot{m}_{HTF,e} \cdot [h_{HTF}(T_{e,i}, P_{HTF}) - h_{HTF}(T_{12}, P_{HTF})] \quad (4.36)$$

The evaporator thermal effectiveness is defined as the ratio between the actual power transferred from the HTF fluid to the solution to the maximum transferable power.

$$\varepsilon_{th,e} = \frac{\dot{Q}_e}{\dot{Q}_{e,max}} \quad (4.37)$$

The evaporator effectiveness is modelled well using $R_{en}$ and $NTU$ defined as:

$$R_{en,e} = \frac{\max(\dot{Q}_{sol,e,max},\ \dot{Q}_{HTF,e,max})}{\min(\dot{Q}_{sol,e,max},\ \dot{Q}_{HTF,e,max})} \quad (4.38)$$

$$NTU_e = \frac{K \cdot S}{(\dot{m}_{13} \cdot Cp_{13})} \quad (4.39)$$

The correlation found for the thermal effectiveness of the evaporator depends mainly on the $R_{en}$ while the $NTU$ is raised to a relatively smaller power.

$$\varepsilon_{th,e} = 1 - exp\,(-1.23 \cdot {NTU_e}^{0.25} \cdot {R_{en,e}}^{0.8}) \quad (4.40)$$

As for the case of the evaporator, the condenser is also described well using just a thermal effectiveness function of $R_{en}$ and $NTU$. Therefore, an identical method can be applied in the case of the condenser, leading to the following correlation:

$$\varepsilon_{th,c} = 1 - exp\,(-1.93 \cdot {NTU_c}^{0.1} \cdot {R_{en,c}}^{0.2}) \quad (4.41)$$

The correlation found for the thermal effectiveness of the condenser reveals the small value of the powers to which both $NTU$ and $R_{en}$ are raised in accordance with the small variance of this effectiveness. The maximum error of the correlations is below 1% for both the evaporator and condenser thermal effectiveness while the average error is 0.2% and 0.25% respectively as shown in **Fig. 4.5**.

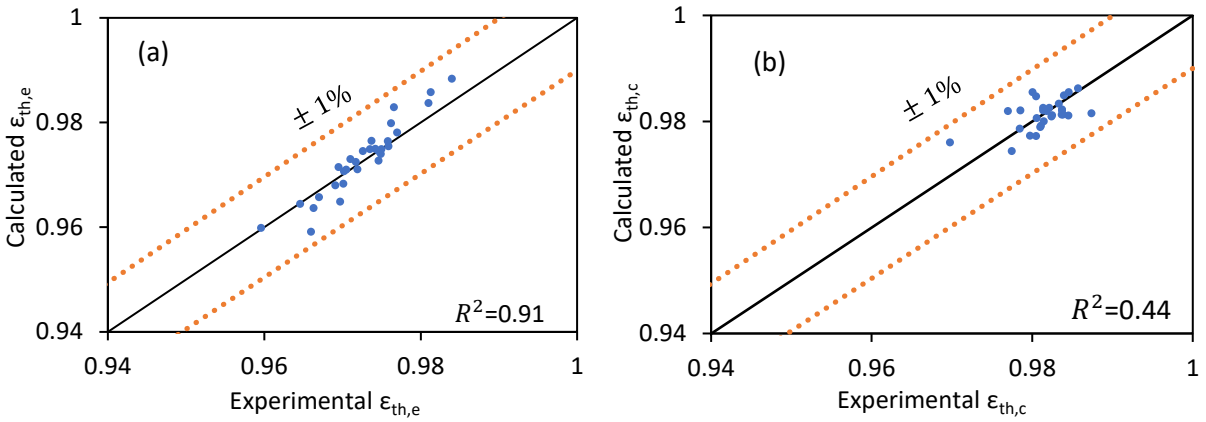


**Fig. 4.5 -** Calculated evaporator (a) and condenser (b) effectiveness vs. experimental effectiveness.

Equivalent thermal effectiveness can also be defined for the two internal heat exchangers, the solution heat exchanger and the subcooler.

$$\varepsilon_{th,shx} = 1 - exp\,(-6.3\ \cdot 10^{-1} \cdot {NTU_{\mathrm{shx}}}^{0.88} \cdot {R_{en,\mathrm{shx}}}^{0.5}) \quad (4.42)$$

$$\varepsilon_{th,sub} = 1 - exp\,(-5.4 \cdot 10^{-2} \cdot {NTU_{sub}}^{1.8} \cdot {R_{en,\mathrm{sub}}}^{2.2}) \quad (4.43)$$

The maximum error of the correlation with respect to the experimentally calculated effectiveness is below 5% for the solution heat exchanger and below 3% for the subcooler, with an average error below 1.2% and 0.9% respectively as shown in **Fig. 4.6**.

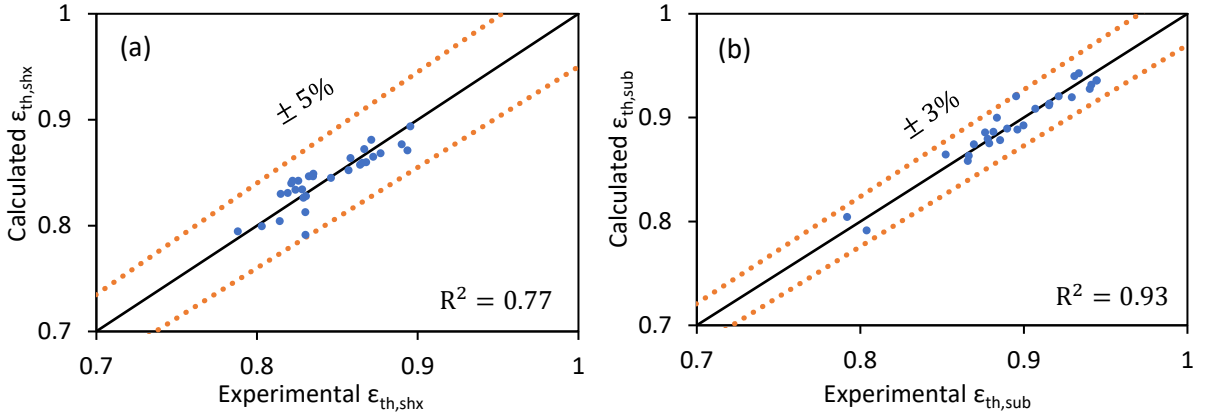


**Fig. 4.6 –** Calculated solution heat exchanger (a) and subcooler (b) effectiveness vs. experimental effectiveness.

## *Alternative thermal effectiveness modelling*

An alternative to the use of the thermal effectiveness presented in the previous sections is to model for each exchanger the ΔT between the HTF and the working fluid. This can be especially useful in cases where, due to the limited variability of experimental conditions, the range of variation of the thermal effectiveness is very small. In particular, this is the case for the condenser where the range of variation of the thermal effectiveness is smaller than 1.7% (**Fig. 4.5**). In addition, the temperature pinch between the solution and the HTF on the condenser and on the evaporator is a very important parameter defining the high and low pressure of the cycle respectively. Therefore, in the case of the condenser and evaporator this second type of modelling for the thermal effectiveness was preferred.

The correlation found for the condenser pinch of temperature $\Delta T_c = \mathrm{T_9} - \mathrm{T_{c,i}}$ as a function of $\Delta T_{c,max} = \mathrm{T_8} - \mathrm{T_{c,i}}$, $R_{en,c}$ and $NTU_c$ is :

$$\Delta T_c = (T_8 - T_{ci}) \cdot exp\,(-6.2 \cdot 10^{-1}\ \cdot {NTU_c}^{0.2} \cdot {R_{en,e}}^{0.3}) \quad (4.44)$$

The functional form of the correlation for $\Delta T_c$ was developed, using a similar form with respect to the one used to model exchangers effectiveness, in order to comply with boundary conditions imposing that $(\Delta T_c)_{min} \geq 0$ and $(\Delta T_c)_{max} = (T_8 - T_{ci})$. Knowing $\Delta T_c$, $\varepsilon_{th,c}$ can be calculated as follows:

$$\varepsilon_{th,c} = \frac{\dot{m}_{ref.}\,[h(T_8, P_8, x_{ref}) - h(T_9, P_9, x_{ref})]}{\dot{Q}_{c,max}} \tag{4.45}$$

Where $T_9 = T_{ci} + \Delta T_c$. The average and maximum error for the $\Delta T_c$ are 2.2% and 5% (**Fig. 4.7**), while the average error for the $\varepsilon_{th,e}$ calculated through the use of $\Delta T_c$ is 0.27%.

The correlation found for the evaporator pinch of temperature $\Delta T_e = T_{ei} - T_{12}$ is:

$$\Delta T_e = (T_{ei} - T_{11}) \cdot exp\,(-7.2 \cdot 10^{-2} \cdot {NTU_e}^{0.7} \cdot {R_{en,e}}^{1}) \tag{4.46}$$

The average and maximum error for $\Delta T_e$ are 3.1% and 11% respectively.

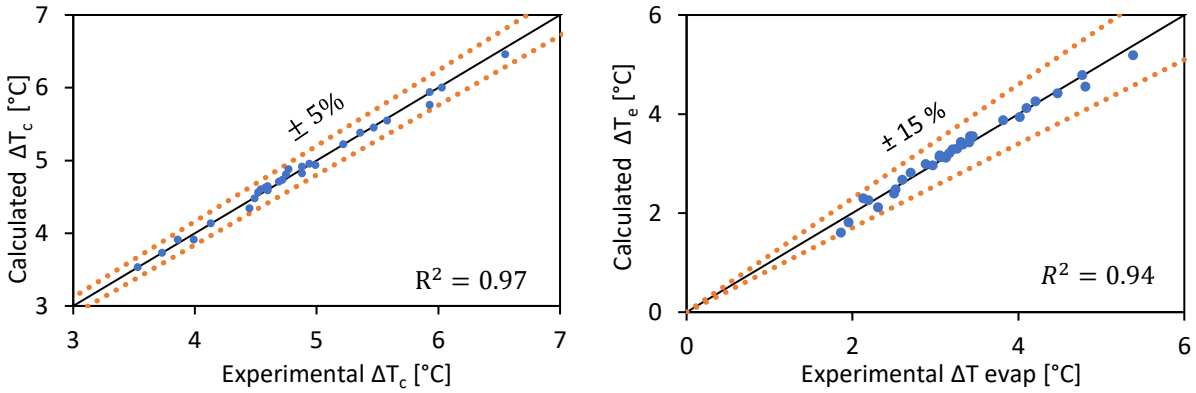


**Fig. 4.7** - Calculated vs. experimental $\Delta T_c$ and $\Delta T_e$.

### 4.2.3 Comparison of the simplified and effectiveness models

The correlations for the component effectiveness modelled in the previous sections are implemented in the numerical model of the cycle. In particular, for the desorber, the assumption of saturated liquid at outlet (for the poor solution) and thermal (**Eq. (4.19))** and species effectiveness (**Eq. (4.21)**) are used. Thermal and mass effectiveness (**Eq.(4.33)-(4.34)**) are used for the absorber, while thermal effectiveness (**Eq. (4.42)-(4.43)**) are used for the solution heat exchanger and subcooler. Finally the correlation for the calculation of temperature pinches are used for the evaporator and condenser (**Eq. (4.44) and Eq. (4.46)**). The comparison of the ε-model results to the experimental data (**Fig. 4.8**) shows that the model predicts the performance of the machines very well both in terms of COP and cooling power output with errors below 6% for the COP and 15% for the cooling power.

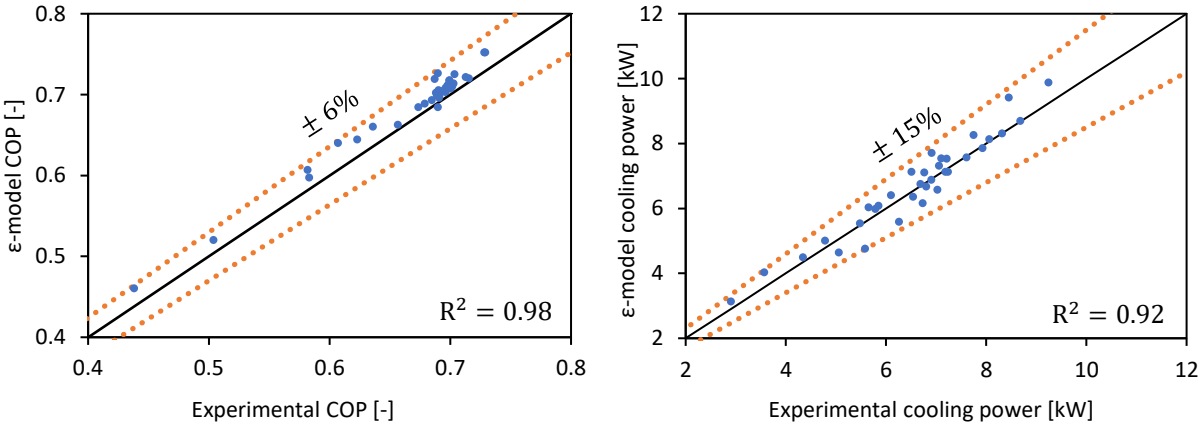


**Fig. 4.8** – Calculated Effectiveness model results compared to experimental results.

**Table 4.1** compares the average and maximum error of the effectiveness model with those of the simplified model presented in *Section 4.2.1*. It is evident that the effectiveness model improves the accuracy of the predicted cycle performance significantly with an average error compared to experimental results of only 2.4% for the COP and 5.4% for the cooling power output, against 6.3% and 12.5% average error respectively in the case of the simplified model. Even more remarkable is the improvement in the maximum error, which was reduced from 50% to 5.5% for the COP and from 65% to 14.8% for the cooling power output.

**Table 4.1** - Simplified model and effectiveness model error compared to experimental data.

| | Simplified model | | Effectiveness model | |
|---|---|---|---|---|
| | COP | Cooling power output | COP | Cooling power output |
| Average Error | 6.3% | 12.5% | 2.4% | 5.4% |
| Maximum Error | 50% | 65% | 5.5% | 14.8% |
| $R^2$ | 0.39 | 0.70 | 0.98 | 0.92 |

**Fig. 4.9** compares the performance calculated by the simplified and the ε-model at the same points tested in the experimental campaign shown in **Table 3.4** where only one parameter at a time is changed while the others are left constant at nominal conditions (**Table 3.2**).

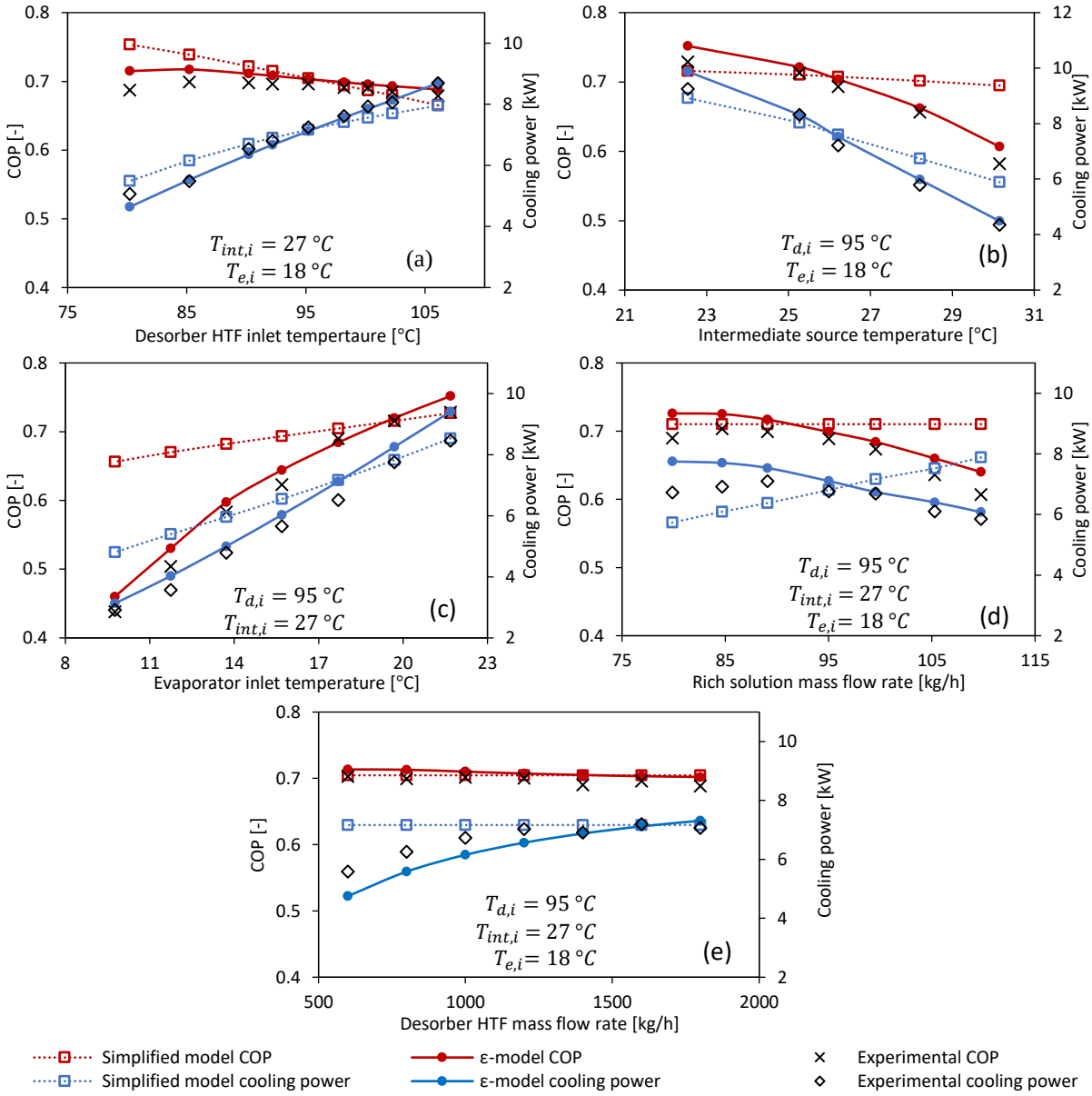


**Fig. 4.9 –** Simplified model and ε-model results compared to experimental results.

**Fig. 4.9(a)** shows that, as expected, the cooling power produced $\dot{Q}_e$ strongly increases when the desorber inlet temperature $T_{d,i}$ increases reaching up to 9 kW at 106°C, while the influence of $T_{d,i}$ on COP appears to be more limited with an optimum of 0.72 around 80°C. Higher desorber inlet temperatures increase the thermal effectiveness of the component and thus the mass flow rate of desorbed vapour, thus increasing the cooling production of the cycle. However, the COP decreases slightly due to the reduced purification capacity of the desorber (i.e., species effectiveness) when the hot source temperature increases. The COP and $\dot{Q}_e$ predicted by the simplified model are accurate near the nominal working conditions where the results are very similar to those of the ε-model. Nevertheless, given that fixed effectiveness and ΔT are used for all operating points, the simplified model fails to predict the variation of performance found with variation of both the intermediate source and the evaporator inlet temperature. In fact, **Fig. 4.9(b)** shows that in the case of the simplified model the COP is only slightly affected by the intermediate source temperature while instead, in accordance with experimental results, the COP decreases noticeably in the case of the ε-model from 0.75 at 23 °C to 0.6 at 30 °C. The difference found when decreasing the evaporator inlet temperature appears to be even more significant (**Fig. 4.9(c)**). This reduces the COP from over 0.7 at 21 °C to 0.45 at 10 °C for the ε-model, but only a much smaller performance decrease is predicted by the simplified model. In addition, the simplified model does not take into account the geometry of the exchangers and therefore, in contrast with the experimental results, the mass flow rate of solution has no effect on COP and linearly increases $\dot{Q}_e$ (**Fig. 4.9(d)**). Results of the adjusted effectiveness model show instead a performance increase when the solution mass flow rate increases with an optimum of around 85 kg/h. Finally, the HTF fluid side is not considered in the simplified model and therefore it has no influence on the behaviour of the machine, as opposed to the effectiveness model which considers it. As an example, **Fig. 4.9(e)** shows that reducing the desorber HTF has little effect on the COP but strongly reduces the cooling power output.

### *Comparison of ε-model results and second experimental campaign measurements*

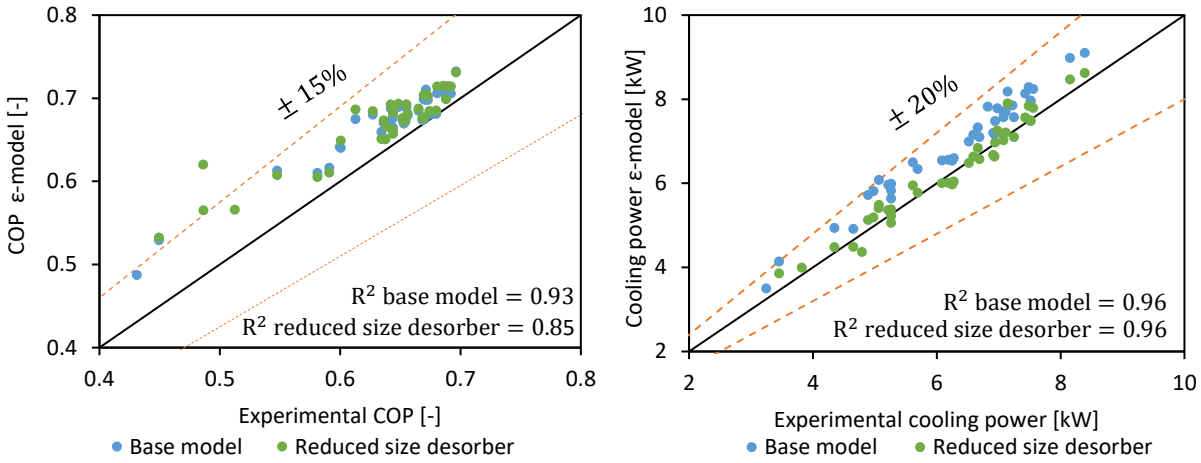


**Fig. 4.10** – Calculated Effectiveness model results compared to experimental results.

Results of the ε-model were compared to experimental measurements relative to the experimental campaign presented in **Table 3.7**. As discussed in *Section 3.5*, most of the test points presented an undesirable partial flooding of the desorber, resulting in lower cooling power output and COP values with respect to the experimental campaign presented in *Section 3.4.1*. Since the model is adjusted on the unflooded desorber configurations, the ε-model results (**Fig. 4.10**) overestimate the performance of the plant. Since the effect of flooding is to reduce the exchange area, it was tested if a matching with experimental results could be achieved by reducing the desorber area used in the model. **Fig. 4.10** shows that acceptable agreement on the experimental data can be obtained for the cooling power produced, indicating that the correlation found for thermal efficiency can also be adapted to a partially flooded desorber mode of operation. The same cannot be said for COP, whose dispersion increases by reducing the desorber area. This is probably due to the fact that partial flooding generates phenomena (e.g. the increase in solution average temperature or the entrainment of liquid droplets in the vapour) that are not taken into account by the current formulation of species efficiency, which is calibrated on non-flooded desorber experimental measures.

### 4.2.4 Parametric study on the size of components

The model developed takes into account the heat exchangers area (**Eq.(4.3)**), making it possible to perform parametric analysis on their size to study its influence on global performance of the cycle. This feature, later used in the scale-up and optimisation of the cycle, is illustrated in this section. **Fig. 4.11** shows the impact on cycle performance of doubling or halving the size of the absorber for different intermediate and evaporator temperatures at the nominal desorber conditions and solution mass flow rate (**Table 3.2**). The absorber is a bottleneck component [45] and reducing its size by half compared to the base case presented in **Table 3.1** generates an average COP and $\dot{Q}_e$ output reduction of 31% and 57% respectively. In addition, significant performance improvements are possible by increasing its size. For example, doubling the size of the absorber leads to an average increase in the COP of 14% and in the cooling power of 41%. Additionally, the impact of the absorber size on COP is higher at evaporator temperatures lower than design conditions, where the component operates at lower pressure and thus less efficiently. On the other hand, in the nominal operating point, increasing the size of the absorber has a smaller impact, since the absorber base size was designed to guarantee good performance in that point.

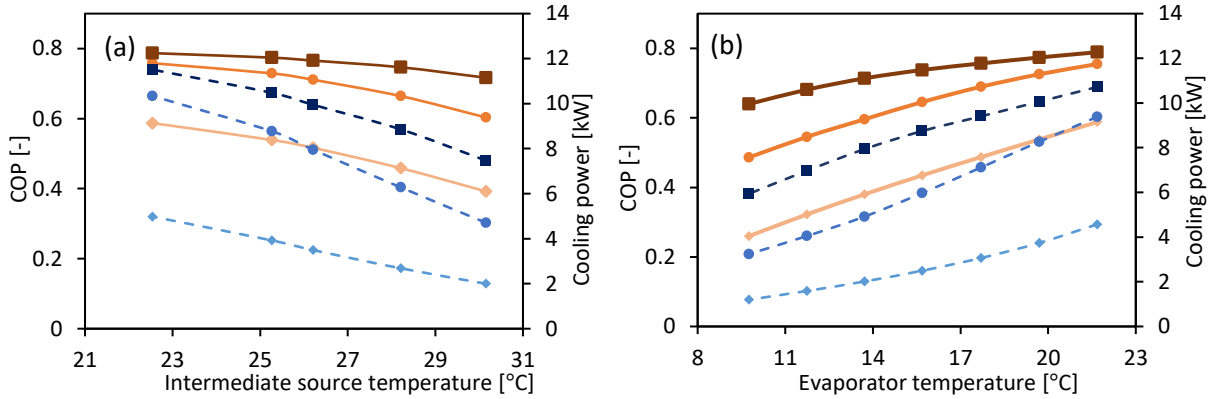


**Fig. 4.11 –** Change of COP [-] (orange symbols, bold line) and cooling power [kW] (blue symbols, dotted line) as a function of the intermediate temperature (a), evaporator temperature (b) and absorber size (● = base size, ■ = double size, ◆ = half size) for nominal desorber conditions and solution mass flow rate.

The results of the analysis carried out for the evaporator are shown in **Fig. 4.12**. In this case a reduction in the size of the evaporator also generates an average reduction of 9% in the COP and 22% in the cooling power output. Doubling the size of the evaporator instead leads on average to a 5.5% increase in the COP and 17% in the cooling output.

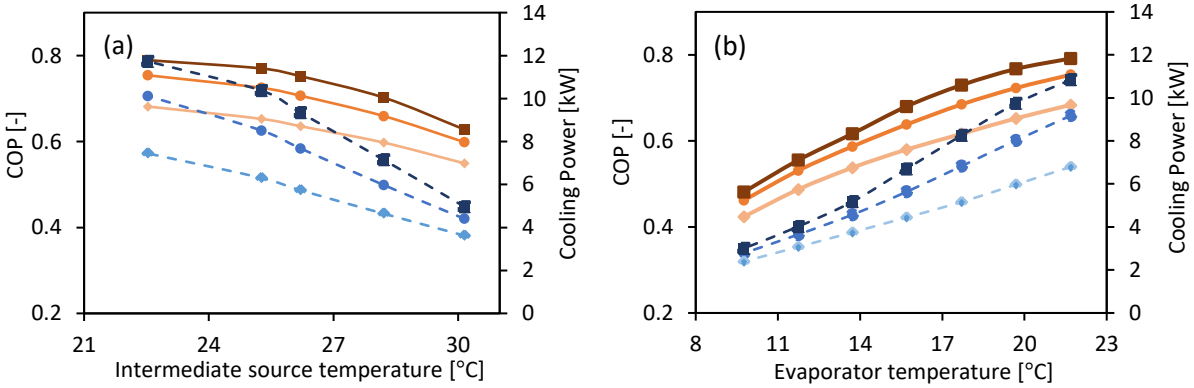


**Fig. 4.12** – Change of COP [-] (orange symbols, bold line) and cooling power [kW] (blue symbols, dotted line) as a function of the intermediate temperature (a), evaporator temperature (b) and evaporator size (● = base size, ■ = double size, ◆ = half size) for nominal desorber conditions and solution mass flow rate.

The effect of the size of the desorber on the cycle performance is different, as shown in **Fig. 4.13**. In fact, an increase in size has a positive effect on cooling power output, with an average $\dot{Q}_e$ increase of 18% for a desorber of double the size and a 44% decrease on average for a desorber of half the size. The same is not true for the COP of the cycle which does not always increase with the size of the desorber. This is because a larger desorber enables

the transfer of more power to the solution and to the desorbed vapour ($\varepsilon_{th,d}$ increases with the $NTU$ in **Eq.(4.19)**) which will be hotter and produced at higher mass flow rates. This influences the internal rectification process in the adiabatic part of the desorber, increasing the ΔT between the exiting vapour and the solution at inlet. The ability to purify the refrigerant vapour is therefore reduced as confirmed by the negative power to which the $NTU$ is raised in the correlation for $\varepsilon_{species,d}$ in **Eq. (4.21)**. Imperfect vapour purification can have a very negative impact on COP, suggesting the need for increasing the solution mass flow rate or adding a rectifier to further purify the vapour when the desorber size is increased.

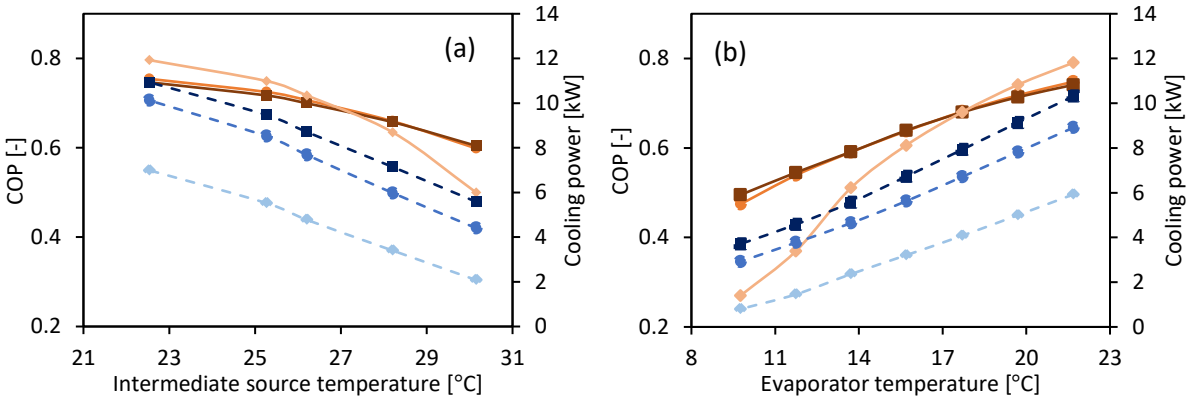


**Fig. 4.13 -** Change of COP [-] (orange symbols, bold line) and cooling power [kW] (blue symbols, dotted line) as a function of the intermediate temperature (a), evaporator temperature (b) and desorber size (● = base size, ■ = double size, ◆ = half size) for nominal desorber conditions and solution mass flow rate.

Finally, the condenser was found to have a smaller impact on the performance of the machine: doubling the condenser size leads to an average improvement of 3% in the COP and 12% in the cooling power while a condenser of half the size reduces the COP by 5% on average and the cooling power output by 16%. **Table 4.2** summarizes the effect on performance of the size of the components in the operating range considered. The results are due to the intrinsic criticality of the components in the cycle. Components where heat and mass transfers take place at the same time (the desorber and even more the absorber), are the most crucial ones in absorption machines and particular attention needs to be paid to their design. It should be highlighted that the results of the parametric analysis also depend on the base (nominal) size of the pilot plant components. The possibility of performing such studies on the size of components can be very useful in the design phase and when performing techno-economic or thermo-economic analysis of the technology.

**Table 4.2** - Influence of the size of components on COP and cooling production for variation of the intermediate source temperature [22-30 °C] and evaporator temperature [10-22 °C] around the nominal point.

| | Double Size | | Half Size | |
|---|---|---|---|---|
| | COP | Cooling Power | COP | Cooling Power |
| Absorber | + 17% | + 51% | - 30% | - 54% |
| Desorber | + 0.14% | + 18% | - 7.6% | - 45% |
| Evaporator | + 5.5% | + 17% | - 9% | - 22% |
| Condenser | + 3% | + 12% | - 5% | - 16% |

## 4.2.5 Synthesis of the absorption chiller modelling

Experimental data gathered during the experimental campaigns presented in *Section 3.4.1* were analysed critically to obtain all the necessary thermo-physical properties, and unreliable points were excluded from further analysis (*Section 3.4.1*). First, a simplified model based on fixed temperature pinches and absorber mass effectiveness estimated from experimental tests was developed. The model provided good results at the nominal operating point but did not sufficiently describe the behaviour of the machine under different conditions.
Therefore, another model was developed based on thermal, mass, and species effectiveness relating the functioning of components to that of ideal ones. Experimental measures were used to characterize the effectiveness of the components in different operating conditions and correlations were found to model them, based on three

dimensionless parameters: the Jakob number *Ja*, the energetic ratio $R_{en}$ and the number of transfer units *NTU*. The model integrating correlations for each component showed very good agreement with experimental results, with a maximum error below 6% for the COP and 15% for the cooling power output.
The tuned model was used to perform a parametric analysis on the dimension of the components, highlighting the absorber, the desorber and the evaporator to be the most critical components of the pilot plant and therefore those with the greatest room for improvement. The use of dimensionless parameters makes this approach well suited for analysis at larger scales and to carry out thermo-economic optimisations. Nevertheless, further experimental studies are necessary to confirm the validity of the model for different plant sizes and architectures.

## 4.3 Turbine model

This section presents the development of a numerical model of turbine integrated into the absorption chiller, presented in *Section 3.3.2*.
Due to the limited experimental data available, a 3D model of the impulse turbine was generated, and its functioning studied with CFD simulations using pure ammonia. A compressible real gas 1D model of the turbine was later developed in EES® for the ammonia-water mixture and compared to CFD simulation (carried out in Ansys-Fluent), adjusting loss term parameters to match CFD results. Hence, CFD simulation are only used as a validation tool. Indeed, although CFD simulations involve some approximations (i.e., some clearances and mechanical losses not considered, limitations related to mesh discretization, boundary layer and turbulence description etc.), they allow a good estimation of the main loss terms due to injector non isentropicity, shock phenomena between stator and rotor, and turbulent flow in the rotor vanes. Since the developed model takes into account the partial admission ratio, a parametric study on this parameter is presented at the end of this section to show the response of the model to its variation.

### 4.3.1 1D real gas model

#### *Injector*

The turbine studied is a supersonic axial turbine, which is of great interest for small scale applications due to the high power it provides, allowing the use of only one stage. This results in a lighter turbine as well as lower manufacturing and operational costs compared with multi-stage turbines. It is helpful to regard the flow in the nozzle (injector) as a one-dimensional flow. This assumption is justified when the following conditions are verified [191]:

(*a*) changes in flow area and curvature of the axis are gradual,
(*b*) all properties are uniform across sections normal to the axis,
(*c*) any heat transfer per unit mass across the surface area of the duct changes the properties uniformly over the cross-section, and
(*d*) the effect of friction can be represented by a shear stress τ at the wall.

The flow is steady if there is no change in the mass flowing per unit time at successive sections along the duct, and if the properties of the gas at any section do not change with time. Under these conditions the conservation of mass equation can be written as:

$$\frac{\mathrm{d}\rho}{\rho} + \frac{\mathrm{dC}}{\mathrm{C}} + \frac{\mathrm{dA}}{\mathrm{A}} = 0 \tag{4.47}$$

Introducing the Mach number $M = C/a$, where the sound speed $a = \sqrt{\left(\frac{\partial \mathrm{P}}{\partial \rho}\right)_{\mathrm{s=k}}}$, **Eq. (4.47)** can be expressed as:

$$\frac{\mathrm{dC}}{C} = \frac{1}{(1 - \mathrm{M}^2)} \cdot \frac{\mathrm{dA}}{\mathrm{A}} \tag{4.48}$$

**Eq. (4.48)** allows identification of the different behaviour of a subsonic and supersonic flow as the section of the duct varies. In the case of subsonic flow (M <1), as the section increases (dA / A> 0) the speed C decreases, while when it decreases (dA / A <0) the speed C increases. Therefore, there is an upper limit to the speed of discharge reachable by means of a converging nozzle, corresponding to M=1. The Swedish engineer de Laval, showed that it is possible to further accelerate the flow up to supersonic outlet conditions, following an isentropic

transformation, adding a suitably designed divergent section to the converging duct. **Fig. 4.14** shows the typical pressure distribution along a nozzle when the outlet pressure is varied. Only two isentropic solutions exist after the sonic conditions are reached in the sonic section: a supersonic and a subsonic solution represented by lines with constant entropy, as shown in **Fig. 4.14**. The subsonic solution is reached when the outlet pressure is equal to $P_L$, which is the minimum pressure necessary to reach sonic conditions in the throat. The supersonic solution is reached when the pressure is equal to $P_{ad}$ which is the design pressure of the nozzle allowing it to avoid shock waves. In fact, when the outlet pressure is appreciably above the value which would give the right amount of expansion to suit the outlet area of the nozzle, the gas is over-expanded so that before the gas can discharge into the surroundings, some recompression and deceleration of the gas must occur. This recompression can only be brought about by a non-isentropic shock wave, because a convergent duct would be necessary for the isentropic diffusion of a supersonic stream. A shock wave generates a rise in static pressure and temperature, but a drop in stagnation pressure as some of the kinetic energy is dissipated with an increase in entropy. As the outlet pressure is reduced, the plane normal shock wave moves towards the exit and for an outlet pressure equal to $P_{se}$ ( $P_L > P_{se} > P_{ad}$) the shock waves occur in the exit section. Further reducing the pressure towards the design outlet pressure $P_{ad}$ is accompanied by more complex oblique shock waves outside the nozzle. Finally, for pressures lower than $P_{ad}$, the flow is under-expanded and a further expansion takes place outside the nozzle. It is worth noting that oblique shock waves and expansion fans occurring outside the nozzle have an inherently multidimensional nature.

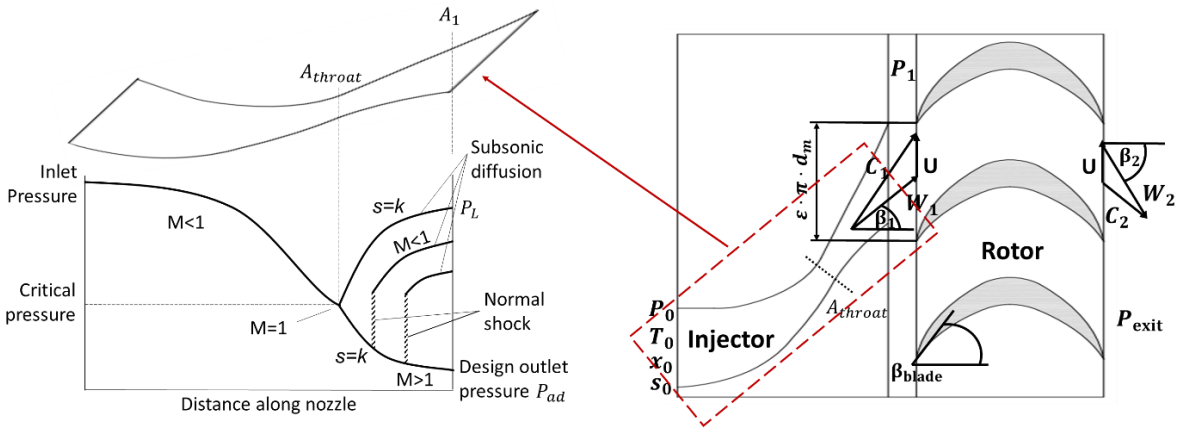


**Fig. 4.14 -** Nozzle (injector) flow pressure diagram [191] and turbine schematic diagram.

A compressible 1D model of the turbo-expander was created in EES [192]. The routine developed takes into account the different aforementioned expansion processes that the fluid can undergo depending on the injector exit pressure. Since the turbine model has been developed to be integrated into the combined cooling and power cycle, the working fluid is an ammonia-water mixture. The ammonia concentration is set to 0.999 when comparing results of the 1D model with the CFD simulations, which in turn are run using pure ammonia. The behaviour as a real gas and a two-phase mixture of the fluid is taken into account using EES internal library correlations developed by Ibrahim and Klein [179] describing the thermodynamic states of the water-ammonia mixture.

The first step of the routine is the calculation of three characteristic expansion ratios $r = P/P_0$ corresponding to $P_L$, $P_{se}$ and $P_{ad}$ in order to identify the operating condition of the injector determined by the outlet pressure $P = P_1$. The fluid entering the turbine accelerates until it reaches the throat section $A_{throat}$ due to the pressure gradient and the converging section of the injector. The total inlet conditions ($P_0$, $T_0$, $x_0$) correspond to the uniquely determined sonic conditions (*) reached in the throat section for $P_1 \leq P_L$, which can be calculated by supposing a guess value of $P^*$ and iterating on **Eq.(4.49)-(4.54)** until a maximum value for the mass flow $\dot{m}^*$ rate is found:

$$\mathrm{h}_{is}^* = h\,(P^*, s_0, x_0) \tag{4.49}$$
$$h^* = h_0 - \eta_n \cdot (h_0 - \mathrm{h}_{is}^*) \tag{4.50}$$
$$\rho^* = \rho(\,P^*, h^*, x_0) \tag{4.51}$$
$$s^* = s(\,P^*, h^*, x_0) \tag{4.52}$$
$$c^* = \sqrt{2(h_0 - h^*)} \tag{4.53}$$
$$\dot{m}^* = \rho^* c^* A_{throat} \tag{4.54}$$

The calculation of choking conditions is usually performed by setting the Mach number equal to one at the throat section [25]. However, another approach consists in maximizing the treated mass flow rate [193] though iteration on $P^*$. This approach was used in the present model as it yields more precise results in the case of non-isentropic expansion and does not require the computation of the sound speed. Partial condensation or flashing can take place during the expansion. When this is the case, the homogeneous equilibrium hypothesis is used in the present model. As explained in [194], this assumption allows treating the flow within the ejector as steady-state and one-dimensional even when the fluid becomes a liquid-vapour two-phase mixture. Finally, in order to take into account friction, an isentropic efficiency of the nozzle $\eta_n$ is introduced in **Eq. (4.50)** and further discussed in *Section 4.3.3*. **Eq. (4.49)-(4.54)** enable calculation of the maximum mass flow rate $\dot{m}^*$ treatable by the injector and the state of the fluid in the throat section for given total inlet conditions.
Starting with the choking conditions $(*)$, one can compute $P_L$ and $P_{ad}$ writing the equations for an expansion (or recompression) in the divergent part of the nozzle from the choking pressure $P^*$ to the exit pressure $P_1$:

$$h_{1,is} = h\,(P_1, s^*, x_0) \tag{4.55}$$
$$h_1 = h^* + \max((h_{1,is} - h^*)/\eta_n\,, 0) - \max\,(\eta_n \cdot (h^* - h_{1,is})\,, 0) \tag{4.56}$$
$$\rho_1 = \rho(P_1, h_1, x_0) \tag{4.57}$$
$$s_1 = \mathrm{s}(P_1, h_1, x_0) \tag{4.58}$$
$$c_1 = \sqrt{2(h_0 - h_1)} \tag{4.59}$$
$$\dot{m}_1 = \rho_1 c_1 A_1 = \dot{m}^* \tag{4.60}$$

The set of equations **Eq. (4.55)-(4.60)** has two possible solutions, one subsonic for $P_1$ corresponding to $P_L$ in which a recompression takes place in the divergent, and one supersonic when $P_1 = P_{ad}$ in which the flow continues to expand up to the exit section.

For exit pressures slightly lower than $P_L$ a normal shock takes place in the divergent immediately downstream from the throat section. Defining as *a* and *b* the conditions before and after the normal shock wave, the equations describing the shock can be written as:

$$\rho_a c_a = \rho_b c_b \tag{4.61}$$
$$P_a + \rho_a c_a^2 = P_b + \rho_b c_b^2 \tag{4.62}$$
$$h_a + \frac{1}{2} c_a^2 = h_b + \frac{1}{2} c_b^2 \tag{4.63}$$
$$\rho_b = \rho(P_b, h_b, x_0) \tag{4.64}$$

Apart from the trivial solution in which all quantities remain equal, the set of equations **Eq. (4.61)-(4.64)** has another solution describing the presence of a shock, which can be found by setting appropriately different guess values.

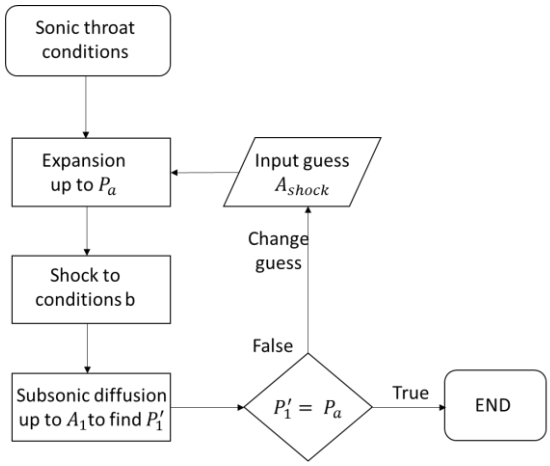


**Fig. 4.15 -** Shock section calculation algorithm.

The section where the normal shock takes place is unknown and therefore it must be found through the iterative process illustrated in **Fig. 4.15**. An input value for the shock section is guessed and **Eq. (4.55)-(4.60)** are used replacing state *1* with state *a*, to find the thermodynamic conditions of the fluid upstream of the shock. **Eq. (4.61)-(4.64)** are then used to find the state of the flow downstream of the shock and finally **Eq. (4.55)-(4.60)** are used

again, replacing state * with state $b$, to describe the subsonic diffusion of the fluid up to the exit section. The procedure is repeated changing the shock section until the pressure calculated after the subsonic diffusion corresponds to the exit pressure.

As stated before, as the outlet pressure is reduced, the plane normal shock wave moves towards the exit and for a pressure $P = P_{se}$ this will take place at the exit section of the injector. The pressure $P_{se}$ can be found by imposing $A_{shock} = A_1$ in the algorithm of **Fig. 4.15**. For outlet pressures between $P_{se}$ and $P_{ad}$ there is no shock in the divergent, the flow coming out of the injector at $P_{ad}$, meaning that an oblique shock will have to take place outside the injector to recompress the fluid up to the exit pressure. This is modelled in the present work as a recompression efficiency $\eta_{rec}$ to be used instead of $\eta_n$ solving **Eq. (4.55)-(4.60)** from $P_{ad}$ to $P_1$. Finally, when $P_1 < P_{ad}$ the fluid is said to be under-expanded and undergoes a further expansion outside the nozzle. As this happens for a very low exit pressure, outside the range of operation of the machine, this last case is not considered in this study. **Fig. 4.16** summarises the different expansion processes that the fluid can undergo in the injector depending on the injector outlet pressure.

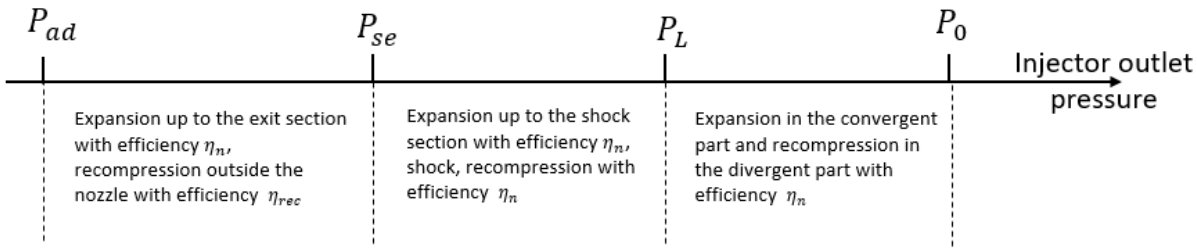


**Fig. 4.16 -** Expansion process as a function of the injector outlet pressure.

In the operating conditions of the prototype, the injector outlet pressure is usually between $P_{se}$ and $P_{ad}$, the case in which both $\eta_n$ and $\eta_{rec}$ are needed. In order to find an expression for the injector isentropic efficiency $\eta_n$, the mass flow characteristic of the 1D model and of the CFD model were compared and $\eta_n$ was tuned on CFD results (see *Section 4.3.2*). **Fig. 4.17** shows the injector mass flow rate characteristics calculated by the 1D model as a function of the total outlet pressure, setting the total inlet pressure (**Fig. 4.17(a)**) and vice versa (**Fig. 4.17(b)**) for different isentropic efficiencies of the injector in the case of pure ammonia.

A slight pressure difference between $P_0$ and $P_1$ is sufficient to reach choking condition and maximum flow rate through the throat section of the injector. In the case where the isentropic efficiency of the injector is equal to one, the outlet to inlet pressure ratio sufficient to achieve sonic conditions in the throat section, $r_L = P_L/P_0$, is equal to 0.912. As the isentropic efficiency of the injector decreases, the $r_L$ required to achieve sonic conditions decreases and the same happens for the maximum flow rate treated. Indeed, lower injector efficiencies correspond to larger total pressure losses leading to increased pressure drops needed to reach sonic state. These conditions will be reached at lower pressures resulting in a decreased fluid density at higher velocity, resulting in a lower mass flow rate in the sonic section. **Fig. 4.17(b)** shows the same mass flow characteristics, setting the injector downstream pressure and varying it upstream.

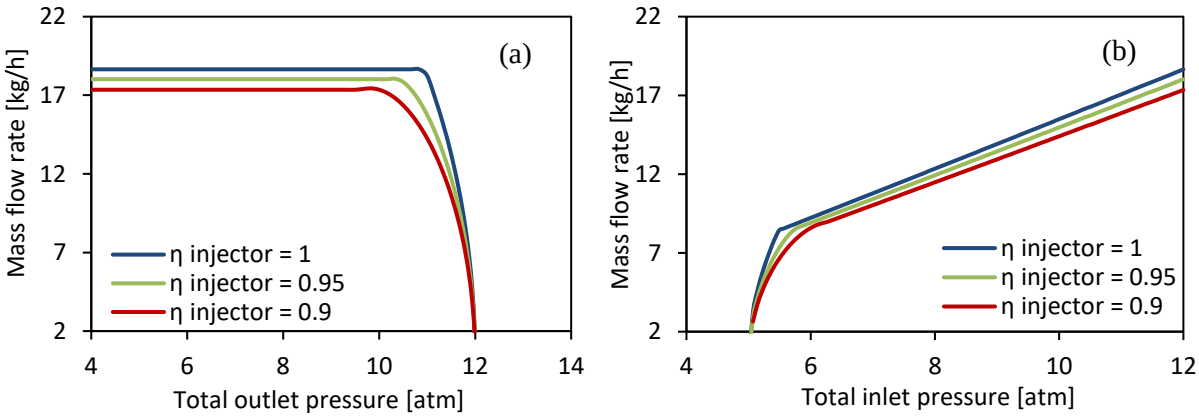


**Fig. 4.17 -** Turbine mass flow rate characteristic fixing the total inlet pressure to 12 atm (a), and the total outlet pressure to 5 atm (b).

The efficiencies $\eta_n$ and $\eta_{rec}$ have a strong influence on the entry velocity in the rotor and are therefore a determining factor for the overall efficiency of the turbine. Therefore, the mass flow rate and inlet rotor speed calculated by the CFD simulation were used as a term of comparison for appropriate tuning, as shown in *Section 4.3.3*.

### *Rotor*

The injector routine described in the previous section enables characterisation of the flow entering the rotor in section *1* (**Fig. 4.14**) in terms of thermodynamic properties, mass flow rate and velocity. The flow is assumed to enter the rotor inlet section with a direction given by the geometric injector angle ($\beta_1 = \alpha_{\text{injector}}$). Given $\beta_1$, $C_1$ and U = ωR the velocity triangle at rotor inlet is fully defined:

$$C_{1,u} = C_1 \sin(\beta_1) \tag{4.65}$$
$$C_{1,ax} = C_1 \cos(\beta_1) \tag{4.66}$$
$$W_{1,u} = C_{1,u} - U \tag{4.67}$$
$$W_{1,ax} = C_{1,ax} \tag{4.68}$$
$$W_1 = \sqrt{W_{1,u}^2 + W_{1,ax}^2} \tag{4.69}$$
$$\beta_1 = \tan^{-1}(W_{1,u}/W_{1,ax}) \tag{4.70}$$

Assuming that $W_2 = W_1$ and that the relative velocity angle at the rotor exit is equal to the blade angle ($\beta_2 = \beta_{\text{blade}}$), the velocity triangle at the rotor exit is characterised:

$$W_{2,u} = W_2 \sin(\beta_2) \tag{4.71}$$
$$W_{2,ax} = W_2 \cos(\beta_2) \tag{4.72}$$
$$C_{2,u} = W_{2,u} + U \tag{4.73}$$
$$C_{2,ax} = W_{2,ax} \tag{4.74}$$
$$C_2 = \sqrt{C_{2,u}^2 + C_{2,ax}^2} \tag{4.75}$$

Given the velocity triangles, Euler's equation [69] enables calculation of the ideal work $Work_{id} = U \cdot (C_{1,u} - C_{2,u})$ exchangeable by the fluid with the moving blades. $Work_{id}$ is the maximum theoretical work that can be produced from the rotor inlet kinetic energy and includes the losses reducing the rotor inlet speed represented by $\eta_n$and $\eta_{rec}$. In the present study, loss terms are subtracted from $Work_{id}$ to take into account the loss phenomena within the rotor. For this purpose, the loss terms are written in the form of an enthalpy increase. Here the following are considered [195]:

- passage loss $\Delta h_p$, due to fluid dynamic friction in mobile blades and non-optimal incidence angle of the jet incoming to the rotor blades
- friction loss $\Delta h_f$, due to the resistance to motion encountered by the vaneless surfaces of the rotor
- leaking loss $\Delta h_l$, due to leaking of the working fluid outside the active blade channels not performing work
- partial admission loss $\Delta h_{pa}$ (see below for details).

Full admission turbines generally have higher efficiencies than partial admission turbines, but in circumstances that do not permit full admission such as for very low mass flow rates, partial admission turbines are used. They incur performance penalties that can be significant and are generally divided into pumping and sector losses. Pumping losses refer to inactive blades rotating in a fluid-filled casing [196] as well as flow from active blades re-entering inactive blade passages [197]. The sector losses refer to the stagnant fluid in inactive blades having to be accelerated by the fluid from stator nozzles as the inactive blade enters the active arc [198]. When a turbine has a high degree of partial admission, pumping and sector losses can become the major source of loss [199,200].

Passage loss due to friction in the blade channels is taken into account as [195]:

$$\Delta h_p = k_p \frac{1}{2} \cdot (1 - \Psi^2) \cdot W_1^2 \tag{4.76}$$

Where $\Psi = 0.99 - \left(\frac{2.28 \cdot \Delta\beta}{10^4}\right) - \left(\frac{4.97}{180 - \Delta\beta}\right)$ and $\Delta\beta = \beta_1 - \beta_2$ measured in degrees.

The friction loss of the non-bladed surfaces of the rotor moving in the stagnant fluid filling the casing can be quantified according to [201]:

$$\Delta h_f = \frac{k_f \, d_m^2 \, \rho_2 U^3}{\dot{m}} \tag{4.77}$$

Leaking losses are expressed as a fraction of maximum ideal work that can be produced:

$$\Delta h_l = (1 - k_l) \cdot Work_{id} \tag{4.78}$$

Finally, the partial admission loss is instead related to the fluid density, the mean diameter of the rotor $d_m$, the tangential velocity, the blade height and the partial admission ratio $\varepsilon$ (i.e., the ratio of active to total blades) as [201]:

$$\Delta h_{pa} = \frac{k_w \, d_m b_1 \, \rho_2 \, U^2 (1 - \varepsilon)}{\dot{m}} \tag{4.79}$$

In **Eq. (4.79)**, the velocity power is set to 2 instead of 3 (as in [195]), which can be justified by the prevalence of laminar regime conditions with respect to full turbulent regime conditions, which are typical of larger scale turbines of several megawatts. Clearly, the coefficient $k_w$ in **Eq. (4.79)** is not dimensionless.

The isentropic efficiency of the expander is then calculated as follows:

$$\eta_{is,tur} = \frac{W_{id} - \Delta h_p - \Delta h_f - \Delta h_{pa} - \Delta h_l}{\Delta h_{is}} \tag{4.80}$$

### 4.3.2 CFD model

With the goal of tuning the 1D model coefficients, CFD simulation of the turbine was carried-out in the framework of a collaboration with ENEA Portici. A 3D model of the turbine was developed in SolidWorks® (**Fig. 4.18**) and CFD simulation were carried out by ENEA serving as a validation tool for the 1D model. For the CFD simulations, the finite volume Ansys-Fluent® software was used and the implicit density-based solver was adopted. The governing continuity, momentum, energy and species transport equations are solved simultaneously as a set of equations: the continuity equation is used to obtain the density field, while the pressure field is determined from the equation of state. The governing equations for other additional scalars are instead solved sequentially. The density-based approach is more suitable and it provides an accuracy (i.e., shock waves) advantage for high-speed compressible flows over the pressure-based solver. Since the problem involves moving parts, it is unsteady when viewed from a stationary frame. To obtain a first solution the multiple reference frame approach was used for each rotational speed. The equation set is solved in a stationary (or inertial) reference frame for the non-rotating parts and in a rotating frame for the rotor. In this way the problem can be modelled as a steady-state problem with respect to the moving frame, but the relative motion of a moving zone with respect to adjacent zones is not accounted for, because the mesh remains fixed. After a first solution is obtained, the sliding mesh approach is employed to calculate the time dependent flow field. As in the moving reference frame approach, the stationary and the rotating parts are connected to each other through non-conformal interfaces which, as the mesh motion is updated in time, are likewise updated to reflect the new positions of each zone.
Turbulence was modelled using the popular two-equation k-ε realisable turbulence model [202]. It is widely used for engineering applications due to its robustness, economy and reasonable accuracy. The model equations are based on phenomenological considerations and empiricism and on the hypothesis that the flow is fully turbulent and the effects of molecular viscosity are negligible. With respect to the standard k-ε model, the realisable version demonstrated substantial improvements when for example the flow presents strong streamline curvature, vortices and rotation. Near wall turbulence was treated by scalable wall functions, since the resolution of the boundary layer requires very fine meshes at walls (y+=1). With this approach, the inner region affected by the viscosity (viscous sublayer and buffer layer) is modelled by semi-empirical formulas termed *wall functions* which bridge the viscosity-affected region between the wall and the fully-turbulent region. Moreover *scalable wall functions* avoid the problems caused by standard wall functions under excessive grid refinement, producing consistent results for arbitrary grid refinements. The generated mesh (**Fig. 4.18**) is made of about six million computational cells and was refined around the blades of the rotor. The time step adopted is $10^{-7}$ s for the unsteady simulations.

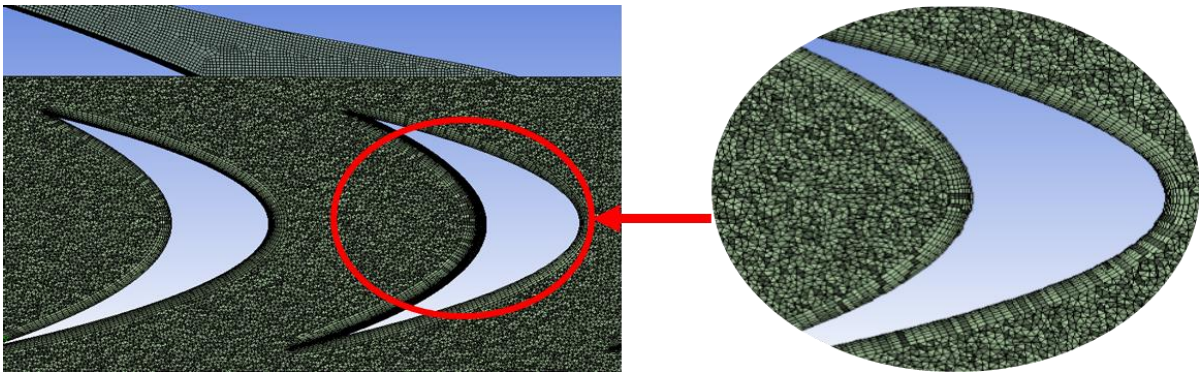

**Fig. 4.18 -** Generated mesh of the 3D model.

### 4.3.3 CFD results and 1D turbine model tuning

The CFD model developed was used to simulate the functioning of the turbine in different operating conditions which can occur in the cycle. First, the injector was simulated separately, to tune the injector model and then the complete turbine was simulated. Injector simulations made it possible to validate the calculation of the mass flow rate treated by the turbine and of the rotor inlet speed. The nozzle back pressure was fixed to 5 atm and three different inlet pressures were considered: 6, 9 and 12 atm.

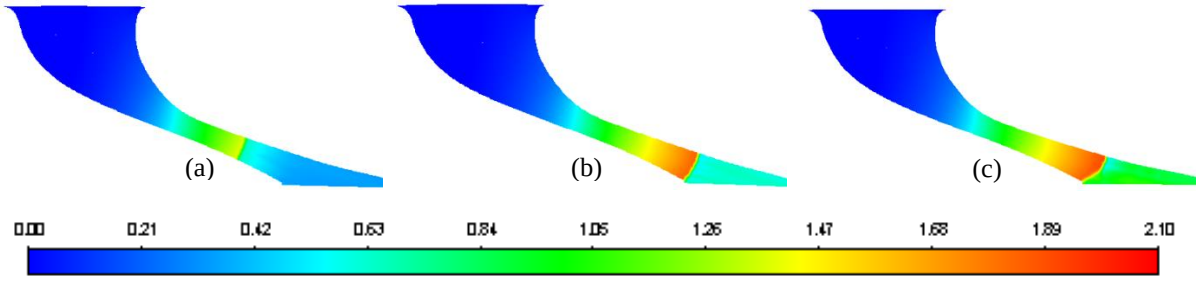


**Fig. 4.19 –** Injector Mach number distribution for an outlet pressure of 5 atm and different total inlet pressure of 6 atm (a), 9 atm (b) and 12 atm (c).

As shown in **Fig. 4.19 (a)**, for an inlet pressure of 6 atm the flow already reaches sonic conditions in the throat section and continues accelerating in the divergent part of the nozzle, where a shock takes place after reaching a Mach of 1.5. For an inlet pressure of 9 and 12 atm, **Fig. 4.19 (b)-(c)**, the shock takes place outside the divergent section, from which the jet exits with almost the same Mach number of around 2, with a recompression of different magnitude taking place outside the nozzle.
As stated before, the isentropic efficiency of the injector is an important parameter determining the mass flow rate treated by the injector and the rotor inlet speed. **Table 4.3** shows the isentropic efficiency needed to obtain agreement of the two models. Results show that the nozzle isentropic efficiency slightly decreases when the ΔP increases, but this value is very close to 0.96 which was hence fixed in the model.

**Table 4.3** - Isentropic efficiency allowing agreement between the 1D and CFD mass flow rate output.

| Inlet pressure [atm] | ΔP [atm] | $r_{exp}$ [-] | Mass flow rate [kg/h] | $\eta_n$ [-] |
|---|---|---|---|---|
| 14 | 9 | 0.36 | 21.17 | 0.954 |
| 12 | 7 | 0.42 | 18.15 | 0.959 |
| 10 | 5 | 0.50 | 15.11 | 0.963 |

After setting the injector efficiency, the other injector-related parameter affecting the turbine power output is the recompression efficiency $\eta_{rec}$. This parameter was set equal to 0.85 to have agreement with the velocity after the recompression calculated by the CFD and 1D models.

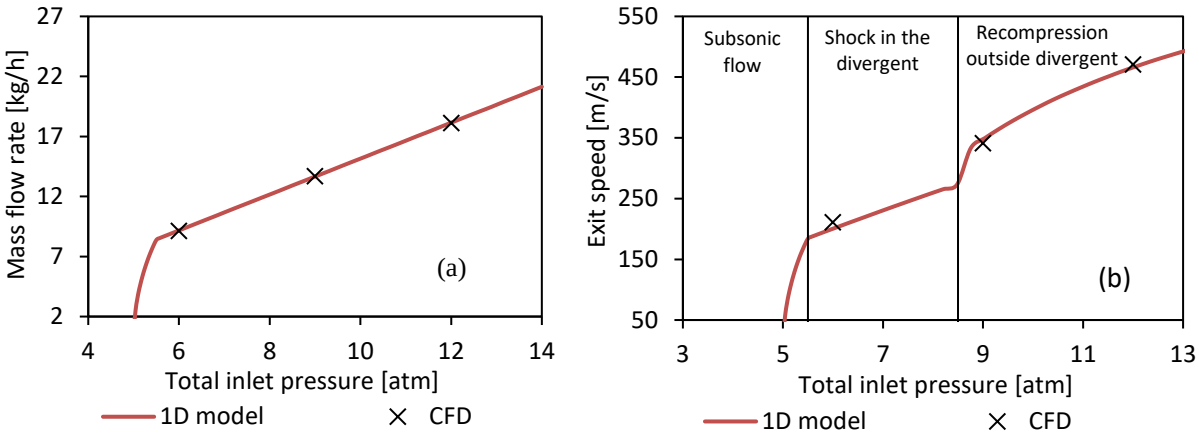


**Fig. 4.20** – Injector mass flow rate (a) and exit speed (b) for an outlet pressure of 5 atm and changing the total inlet pressure calculated by the 1D and CFD model

The mass flow rate treated by the injector shown in **Fig. 4.20 (a)** highlights the perfect agreement between the mass flow rate calculated by the 1D and CFD models. A total inlet pressure of 5.5 atm is already sufficient to reach choking conditions in the nozzle for an outlet pressure of 5 atm, and further increasing the inlet pressure leads to a linear increase in the mass flow rate treated as predicted by the ideal gas theory (**Eq. (3.10)**). Very good agreement between the 1D and CFD models is also found in terms of the rotor inlet speed (**Fig. 4.20 (b)**) which rapidly increases for increasing total inlet pressures until reaching sonic conditions in the throat section. For higher inlet pressures, a shock takes place in the divergent section and the exit speed increases less with an increase in the total inlet pressure due to the loss involved with the normal shock. For a total inlet pressure higher than 8.5 atm, an oblique shock takes place outside the injector and the slope of the exit speed curve with respect to the inlet pressure increases due to the smaller magnitude of the loss linked to oblique shocks compared with normal shocks.

Subsequently, simulation of the entire turbine was undertaken. Inlet temperature was fixed at 120 °C and outlet pressure was fixed at 5 atm while three inlet pressures (14 atm, 12 atm and 10 atm) were analysed for different rotational speeds **(Table 4.4**).

**Table 4.4** - CFD simulation points.

| Inlet pressure [atm] | Inlet temperature [°C] | Outlet pressure [atm] | Rotational speed [rpm] | $\dot{W}_t$ [W] |
|---|---|---|---|---|
| 10 | 120 | 5 | 10,000 | 61 |
| | | | 25,000 | 125 |
| | | | 50,000 | 137 |
| | | | 75,000 | 39 |
| 12 | 120 | 5 | 10,000 | 87 |
| | | | 25,000 | 182 |
| | | | 50,000 | 221 |
| | | | 75,000 | 166 |
| 14 | 120 | 5 | 10,000 | 117 |
| | | | 25,000 | 254 |
| | | | 50,000 | 357 |
| | | | 75,000 | 298 |
| | | | 100,000 | 131 |

**Fig. 4.21 (a)** shows Mach number distribution for total inlet conditions of 12 atm, 120 °C, total outlet pressure of 5 atm and rotating speed of 50,000 rpm. As shown in the injector simulations (**Fig. 4.19**), Mach number distribution also remains the same in the case of inlet at 10 and 14 atm up to the injector outlet, where a recompression takes place, decelerating the flow, which then enters the rotor blades with a Mach number close to one. Enthalpy drop due to the exchange of work with moving blades further slows the flow, which exits from the rotor at a low Mach. **Fig. 4.21 (b)** shows the pressure distribution for the same base case as **Fig. 4.21 (a)**. Pressure and density distribution follow the same pattern, decreasing until the injector exit section where a sudden recompression takes place.

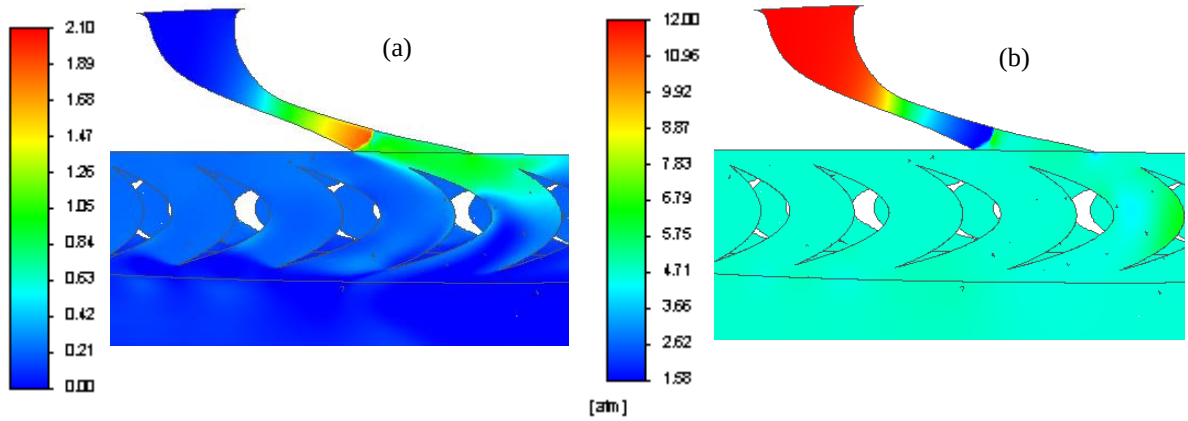


**Fig. 4.21** – Mach number (a) and absolute pressure (b) distribution for total inlet temperature of 120 °C, total outlet pressure of 5 atm, rotating speed of 50,000 rpm and total inlet pressure of 12 atm.

Since the problem involves moving parts, it is unsteady and the power produced exchanged by the fluid with the moving blades changes over time depending on the relative position of the active blades with respect to the incoming jet from the rotor. Therefore, when calculating the power produced by the turbine at each simulation point, results were averaged over five oscillation periods.

CFD simulations were used for the tuning of the 1D model presented in *Section 4.3.1*. The results presented in **Fig. 4.22** show very good agreement between the results of the 1D model and of the CFD model with mean average errors below 7% for all inlet pressure values. As expected, the power produced by the turbine increases when the inlet pressure increases, reaching a maximum around 360 W ($\eta_{is,tur}$=37%) around 55,000 rpm for an inlet pressure of 14 atm. For lower total inlet pressure the optimal rotating speed decreases to 45,000 rpm for a total inlet pressure of 10 atm where the maximum power production is around 140 W.

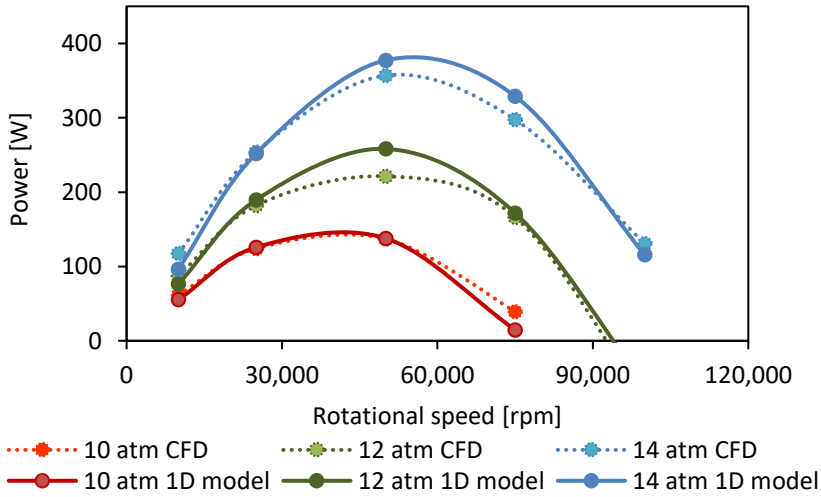


**Fig. 4.22 –** CFD and 1D model turbine power output characteristics for an outlet pressure of 5 atm and inlet pressure of 14 atm (blue lines), 12 atm (green lines) and 10 atm (red lines).

**Table 4.5** details the value of the coefficients used in the loss term models after tuning of the 1D model on CFD simulations.

**Table 4.5 -** Coefficients of the loss model

| $\eta_n$ | $\eta_{rec}$ | $k_p$ | $k_f$ | $k_w$ | $k_l$ |
|---|---|---|---|---|---|
| 0.96 | 0.85 | 0.15 | 0.00066 | 7.15 | 0.8 |

**Fig. 4.23** shows the dependence of loss terms from the rotation speed of the turbine. Passage loss plays an appreciable role only at low rotational speed, while it decreases for higher speeds. Friction and partial admission losses dramatically increase at high rotational speed and partial admission loss represents the main performance limiting factor. Leaking loss increases up to a maximum corresponding to the rotational speed where the theoretical Euler's work $Work_{id}$ is maximum. The light blue line corresponding to $W_{id}$ in **Fig. 4.23** refers to the maximum work that can be obtained from the inlet kinetic energy and therefore already takes into account the loss due to the non-isentropicity of the nozzle and the loss due to the recompression shock taking place (in this case) outside the nozzle.

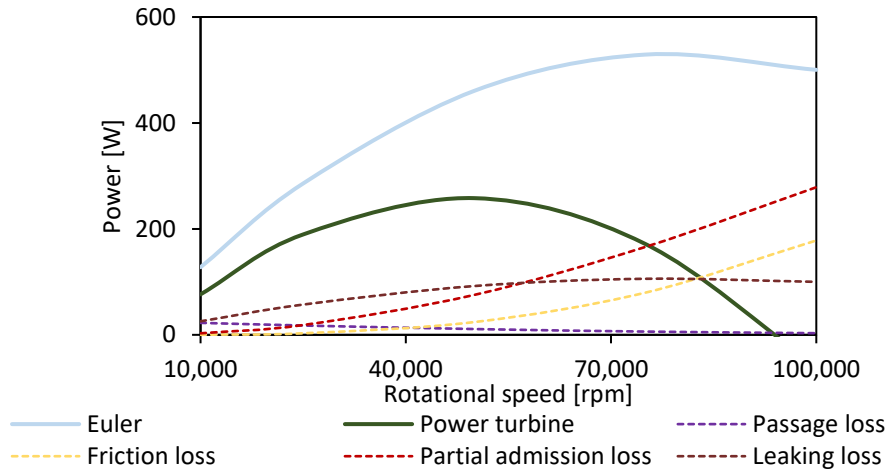


**Fig. 4.23 –** Loss term variation changing the turbine rotational speed in the case of total inlet pressure and temperature of 12 atm and 120 °C and total outlet pressure of 5 atm for pure ammonia.

## *Impact of the ammonia concentration and inlet temperature*

CFD simulations were performed using pure ammonia, since the ammonia-water mixture was available. Hence, a parametric analysis was performed using the 1D model to assess the impact on the turbine mass flow rate and power output of the presence of a small percentage of water in the mixture.

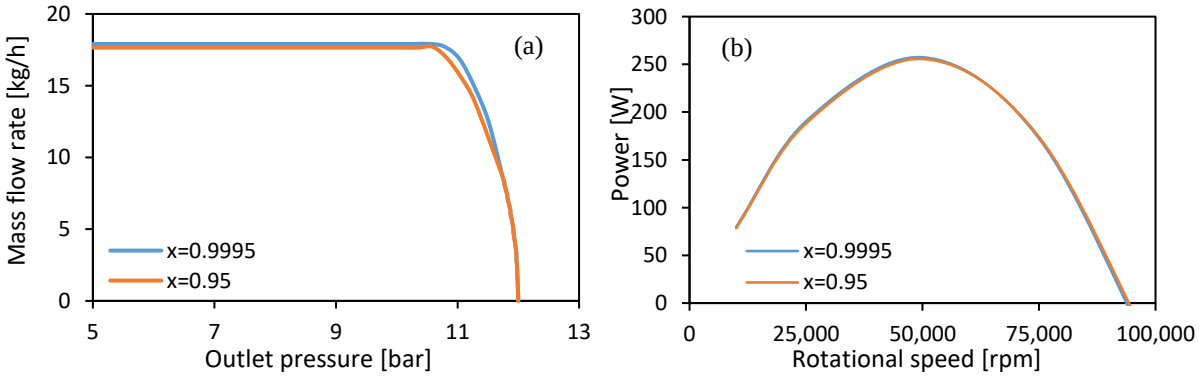


**Fig. 4.24 –** Influence of the ammonia concentration on the model output turbine mass flow rate (a) and power production (b). Turbine inlet conditions of 12 bar and 120 °C, and outlet pressure of 5 bar (b).

The range of ammonia concentrations in the refrigerant vapour that can be found in the cycle (rarely less than 96%) has little influence on the flow rate treated by the injector (as shown in **Fig. 4.24**). For example, for inlet conditions of 12 bar and 120°C, there is a 1.5% mass flow rate reduction in the case of a mixture with an ammonia content of 95% compared to the case of pure ammonia.

The influence of the turbine inlet temperature is shown in **Fig. 4.25**. As confirmed by experimental tests on the turbine (**Fig. 3.17**), increasing the turbine inlet temperature slightly reduces the mass flow rate passing through the expander. The effect on power production is negligible at low rotational speeds, while it becomes slightly more important at high rotational speeds, with an increase of the maximum power output of 10% passing from 100 °C to 150 °C.

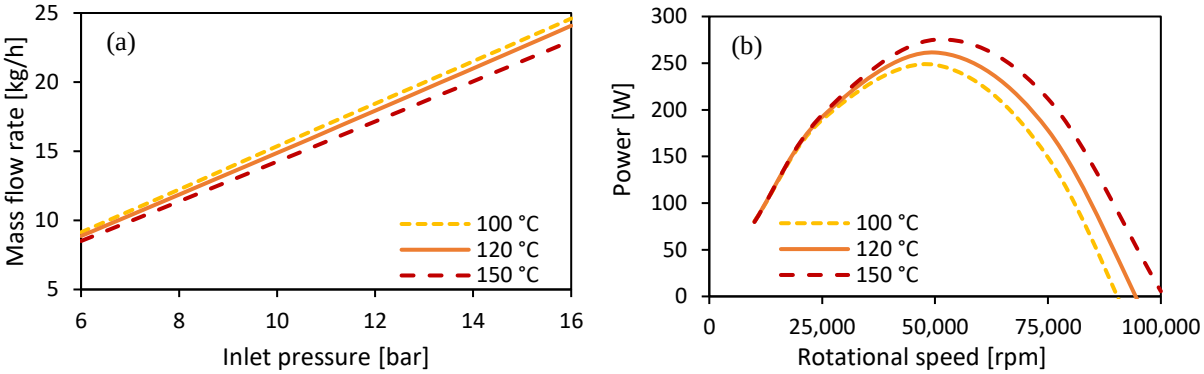


**Fig. 4.25 –** Influence of the ammonia concentration on the model output turbine mass flow rate treated (a) and power production (b). Turbine inlet conditions of 12 bar and 120 °C, and outlet pressure of 5 bar (b).

### 4.3.4 1D model mass flow rate calculation validation on experimental results

Results of the 1D real-gas model were compared to experimental results also for the use of fluids other than the ammonia-water mixtures. As shown in **Fig. 4.26**, a very good matching was obtained regarding the mass flow rate treated by the turbine. The same injector throat section of 3 mm$^2$ (*Section 3.4.2*) was used for the simulation with all the fluids, obtaining an average error of 1.8% and a maximum error with respect to experimental results of 5.8%. Compared to results shown in **Fig. 3.11**, a very good agreement is found also in the case of ammonia, showing that discrepancies were due to the real-gas behaviour of the working fluid and not to condensation of the mixture during the expansion.

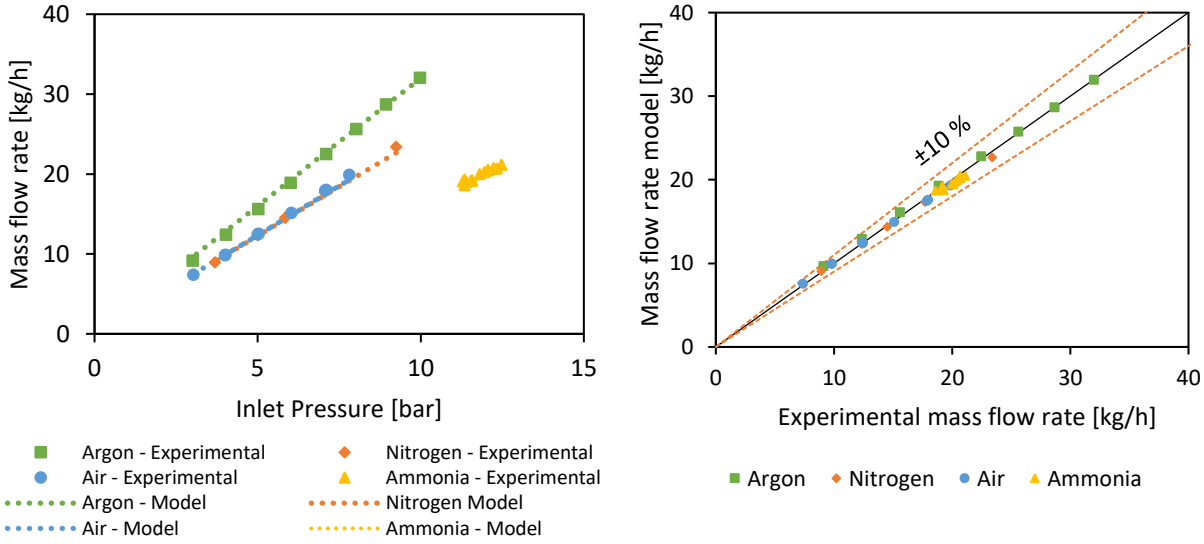


**Fig. 4.26 –** Turbine model output and experimental mass flow rate comparisons.

Validation of the model with regards to electrical production was not possible due to the lack of knowledge of the efficiency of the experimental electrical generator, which is likely to depend also on the rotational speed. More details on this aspect are given in *Section 7.4*, where evidence of the very low electromechanical efficiency of the turbine (estimated between 0.1 and 0.3) is presented.
A complementary validation effort has been performed through the cross-comparisons between a supersonic ORC turbine experimental results and the present model. Such comparison has given encouraging results without the need of great modifications of the model. These results are not presently published.

### 4.3.5 Scale-up evaluation

The turbine model presented in Section 4.3.1 contains loss terms taking into account penalties due to partial admission. Since one of the objectives of the study is the evaluation of the scale-up of the cycle, it is interesting to analyse the behaviour of the model when the partial admission ratio is varied with respect to the experimental value of 0.037. **Fig. 4.27**, referring to the use of ammonia with inlet conditions of 12 bar and 100 °C and outlet pressure of 5 bar, was obtained by finding the rotational efficiency maximising the isentropic efficiency for each point (passing from 48,000 rpm for ε=0.04 to 79,000 rpm for ε=1). Increasing the partial admission ratio, the efficiency of the turbine increases significantly, from 34% to 56%, with stronger variation particularly for ε < 0.2 (corresponding in this case to the presence of 4 injectors). It is important to highlight however, that results presented in **Fig. 4.27** only give an indication of what could occur when reducing ε, but they need validation. Indeed, very few experimental studies are available in literature on partial admission turbines. Lee et al. [178] reported an almost linear increase the efficiency with the partial admission ratio, but focused however only on partial admission ratio ε > 0.17 for which also results of the present model are almost linear.

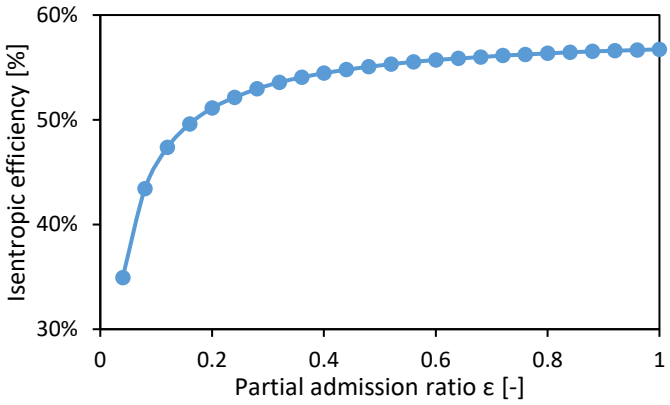


**Fig. 4.27 –** Effect of partial admission ratio on the turbine maximum efficiency.

Finally, since the turbine design inlet-outlet pressure of 16-4 bar (*Section 3.3.2*) are quite different from the actual cycle working pressures, shock phenomena take place, strongly affecting the isentropic efficiency of the expander. An appropriate design of the injector could reduce these losses and improve performance. In particular it is desirable that the injector outlet pressure (determined by $A_1$) is equal to the turbine back pressure. Hence, the effect of an injector re-design was evaluated for the same conditions of **Fig. 4.27 (**ammonia vapour inlet conditions of 12 bar and 100 °C and outlet pressure of 5 bar). **Fig. 4.28** shows redesigning the injector (varying $A_1$) so that $P_{ad} = P_1$ allows a further increase of the isentropic efficiency of the turbine passing from 56% to 73%. Also in this case it should be highlighted that these results need further validation, but they appear to be reasonable considering the small size of the turbine.

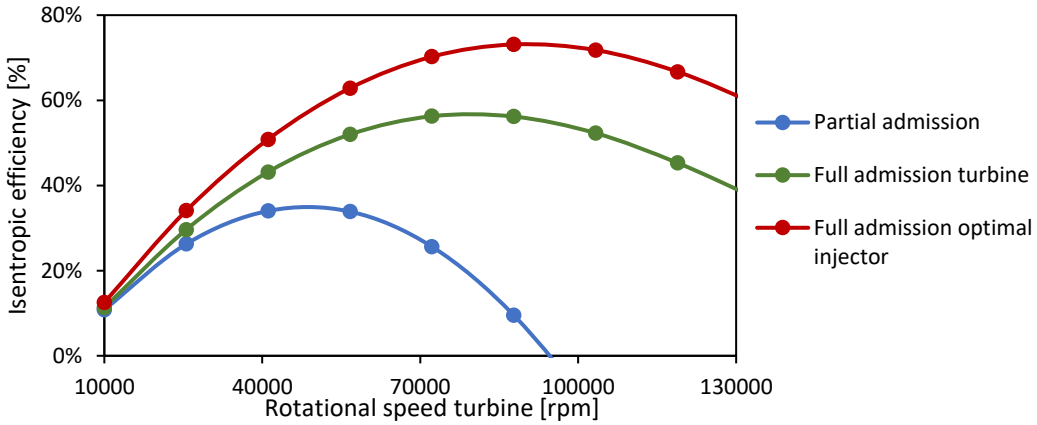


**Fig. 4.28 –** Turbine isentropic efficiency as a function of its rotational speed for a single injector (blue line) and full admission (green line) using a the existing injector, and for a full admission turbine using an optimized injector (red line). Inlet conditions of 12 bar and 100°C and outlet pressure of 5 bar.

### 4.3.6 Synthesis of the turbine model

Given the insufficiency of experimental data, a 3D model of the impulse axial turbine presented in *Section 3.3.2* was developed and its functioning studied with CFD simulations using pure ammonia. A compressible real gas 1D model of the turbine was developed in EES® for the ammonia-water mixture. The proposed model includes a description of the expansion occurring in the supersonic injector and contains the most relevant loss terms to take into account partial admission and the small scale of the turbine. The 1D model was compared to CFD simulation and loss term parameters adjusted to match CFD results. The results show that the 1D model is able to accurately predict the expansion process through the turbine injector and in particular the treated mass flow rate. The model shows the strong influence of the nozzle on the turbine performance due to the relationship between inlet pressure and the treated flow rate and the presence of non-isentropic recompression phenomena (i.e., shocks) in the divergent section or at the outlet of the nozzle. An average discrepancy below 7% was obtained between the 1D model and the CFD power output demonstrating that the selected loss terms are well suited for the application. Loss terms are highly dependent on the rotational speed of the turbine and partial admission and leaking losses appear to be the most influential on turbine performance. The optimum rotational speed depends on operating conditions and increases for increasing inlet pressure up to around 55,000 rpm for an inlet at 14 atm where simulated power production is 360 W.
Validation on experimental results was only possible for the treated mass flow rate since the experimental electrical generator efficiency was not known. Finally, the possibility to use the model to predict the performance of the turbine when reducing the partial admission ratio has been shown.

## 4.4 Synthesis of the numerical models development

To finish the development of the combined cycle, the turbine model is integrated into the absorption chiller model. The coupling is performed by imposing that the mass flow rate passing through the cooling production line is equal to the desorbed vapour mass flow rate minus the turbine mass flow rate ($\dot{m}_8 = \dot{m}_7 - \dot{m}_{14}$) with reference to **Fig. 3.1**.
To complete the cycle model, a simplified representation of the superheater is included. In fact, the superheater integrated in the pilot plant is an electric resistance heater. This choice guarantees a better control of the plant during the experimental campaign but would not be a suitable option for a real machine, particularly for larger plant sizes. Hence, the superheater is also modelled as a plate heat exchanger, but a fixed overall heat transfer coefficient $K$ of $300\ W/(m^2K)$ [167] is considered. The calculation of the superheater area, needed for cost estimation, is performed using the LMTD (logarithmic mean temperature difference) method [203]:

$$S_{sh} = \frac{\dot{Q}_{sh}}{\mathrm{K}_{sh} \cdot \Delta\mathrm{T}_{lm}} \tag{4.81}$$

where $\Delta\mathrm{T}_{lm}$ represents the mean temperature difference between the HTF and the working fluid. The hot temperature HTF is assumed to first feed the superheater and then enter the desorber. Hence the superheater HTF mass flow rate is equal to the desorber HTF mass flow rate, $\mathrm{T}_{sh,i}$ is equal to the available hot source temperature and $\mathrm{T}_{d,i} = \mathrm{T}_{sh,o}$.

For the purpose of evaluating the efficiency of cooling production of the cycle, the thermal COP of the cooling production is defined as follows:

$$COP_c = \frac{\dot{Q}_e}{\dot{Q}_d \cdot r_s} \tag{4.82}$$

Where, to account for the fact that not all the vapour produced is used for cooling production, the power supplied to the desorber is multiplied by the split ratio $r_s$ between the mass flow rate passing through the evaporator to the vapour mass flow rate produced at the desorber which as a reminder is defined as (see state points in **Fig. 3.1**):

$$r_s = \frac{\dot{m}_{11}}{\dot{m}_7} \tag{4.83}$$

On the other hand, the efficiency of the power cycle is calculated as follows:

$$\eta_{power} = \frac{\dot{W}_T}{\dot{Q}_d \cdot (1 - r_s) + \dot{Q}_{sh}} \tag{4.84}$$

Finally, the possibility of performing a throttling before the turbine was introduced. Indeed, the fact that the mass flow rate treated by the turbine is fixed for a given inlet pressure imposes strict limits on the cycle in terms of cycle operability range and flexibility of distribution of the refrigerant mass flow rate between the cold and mechanical power production lines. Therefore, even though throttling would decrease the performance of the cycle, the introduction of a throttling valve could add an additional degree of freedom to the system since the mass flow rate treated by the injector can be reduced by reducing the pressure upstream of the turbine, thus increasing the split ratio $r_s$. Hence, the possibility of performing an adjustable isenthalpic throttling process before the superheater was added into the model. A throttling ratio $R_{th}$ was defined as the ratio of downstream over upstream pressure to the valve (**Fig. 3.1**):

$$R_{th} = \frac{P_{14}}{P_7} \tag{4.85}$$

The combined cycle model was developed from the integration of the adjusted absorption chiller and turbine models, therefore it also has the limitations of the two models on which it is based. In particular, it should be noted that results have been adjusted for a hot source temperature in the range of 85-115°C, an intermediate source temperature of 22-30°C and a cold source temperature of 8-20 °C. Additionally, the model refers to the use of plate exchangers and, in particular to the use of a very specific desorber technology.
Concerning the turbine, limitations include the fact that pure ammonia was used in CFD simulations (while some water traces are present in the vapour entering the turbine). Additionally, CFD simulations involve other approximations such as the fact that some clearances and some mechanical losses are not represented and limitations related to mesh discretization, boundary layer and turbulence description, etc. Possible condensation of the working fluid during expansion also needs further investigation.
The models are adjusted on the pilot plant and although their use to evaluate its scale-up is possible a thorough validation is needed. Finally, the model can be used to simulate the functioning of the plant only in simple absorption and combined functioning mode, but not the pure power production functioning. In this case the cycle operates like a Kalina cycle, and modifications to the model need to be included. Indeed, in that case the pressure of the cycles would not be imposed by the evaporator and condenser (cut off the cycle), but rather by the desorber and absorber. The combined production cycle model presented in this chapter is used in the following to perform energy, exergy and exergoeconomic analyses, investigate alternative architecture and carry-out a preliminary assessment of the economic interest of using this cycle in a real industrial application.

# Chapter 5

# Energy, exergy and exergoeconomic analysis

*This chapter presents a thermodynamic and economic investigation of the combined cooling and power production cycle. Energy and exergy analysis at the pilot plant scale are presented first, to evaluate the effect on performance of changing operating conditions. Subsequently the evaluation of a plant scale-up, up to reaching full-admission conditions for the turbine, is evaluated. In particular, the exergoeconomic method is applied to allocate costs to products based on their exergetic value. Finally, an optimisation is performed on heat exchangers area to minimise the cost of products. Given the strong limitations imposed by turbine, a new architecture integrating an ejector is proposed to increase the flexibility of the cycle.*
*Finally, a preliminary techno-economic assessment of the use of the technology in a real-life industrial application is performed in the last part of the chapter.*

## 5.1 Introduction

The review on absorption based cooling and power cycles presented in *Section 2.5* highlights the interest of combining cooling and power generation systems. However, it should be noted that the performance of these systems still needs to be improved as they often remain bulky, heavy and more costly than conventional systems [204]. Exergoeconomics has emerged in this respect, as one of the best scrutinizing tools, since it mixes thermodynamic analysis with economic analysis [205]. Several contributions to exergoeconomics have been made by Bejan et al. [205], Tsatsaronis et al.[206], Lozano et al. [207], Valero et. al [208], Frangopoulos et al. [209], each bringing valuable insights on different directions of development [204].

While several exergoeconomic analyses have been performed on combined power and cooling cycles, most of them are generally limited to high heat source temperatures [8–10] or complex architectures [10]. Here instead, the object is a low-temperature heat driven absorption cooling and power (APC) production system with a focus on space cooling (around 10 °C), of which, for simplicity, a schematic diagram is shown again in **Fig. 5.1**.
The energy and exergy performance of the pilot plant is analysed through parametric studies and exergoeconomic parameters are evaluated based on the methodology detailed in [205]. An exergoeconomic analysis of the combined plant is then performed with the objective of understanding the cost formation process within the plant and how costs can be divided between the two products: cooling and power output. An evaluation of the scale-up of the plant is carried out for a base case working point, representative of a space cooling application, to assess economic attractiveness of the application and thermodynamic and exergoeconomic performance change with plant size. Subsequently, fixing the size of the turbine and the solution mass flow rate, an optimisation of the heat exchangers area is carried out for the scaled-up plant working in the base case conditions to minimise the unit cost of exergy of the products.

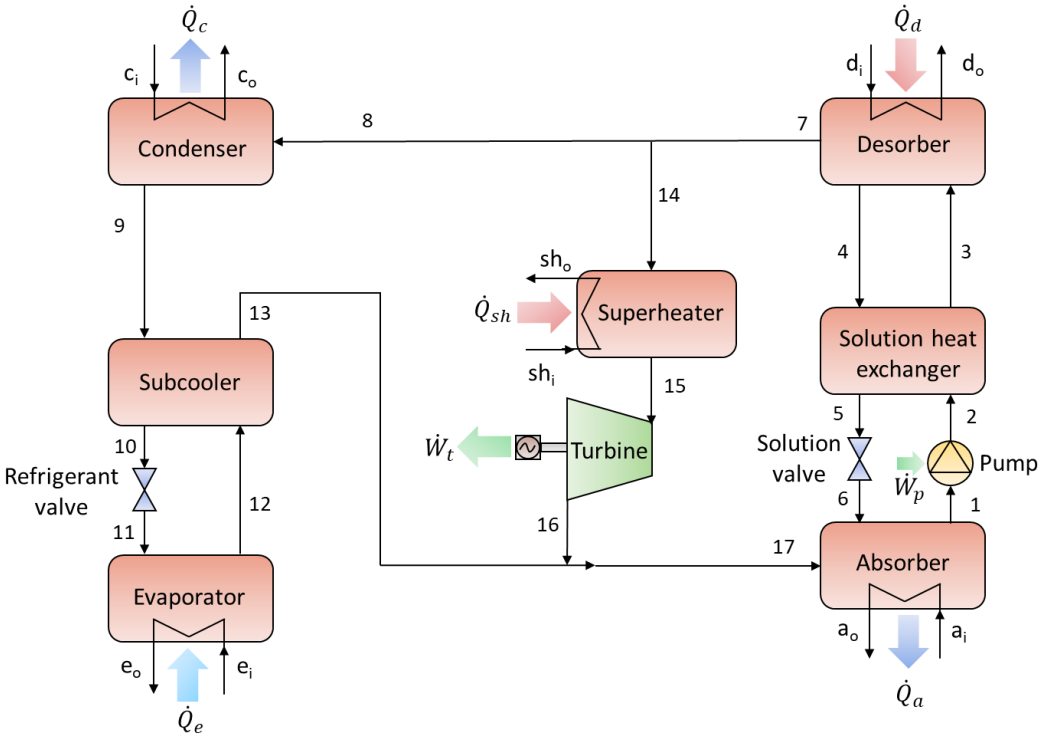


**Fig. 5.1 -** Schematic of the combined cooling and power (APC) cycle.

Subsequently, in order to improve the flexibility, limited by the constraints imposed by the turbine, an alternative architecture including an ejector is proposed and its performance assessed.
Furthermore, assuming that the ratio of cooling and power production can be varied, the economic interest of the cycle is evaluated in a case study representing a real industrial application.

## 5.2 Exergy analysis methodology

The method of exergy analysis provides insights that may elude a purely first principle analysis, enabling the identification of the irreversibility occurring in a system as well as the evaluation of their magnitude [205].

Exergy is the maximum theoretical useful work obtainable from a system of interest interacting to equilibrium with an idealized system called environment [210] (here $T_0 = 25°C$ and $P_0 = 1.013\ bar$). Unlike energy, exergy is not generally conserved and can be destroyed by thermodynamic irreversibility. Considering a steady state control volume, the exergy balance states that the rate at which exergy is transferred into the control volume must exceed the rate at which exergy is transferred out, the difference being the destroyed exergy $\dot{E}x_D$:

$$\sum_j (\dot{E}x_{i,j} + \dot{E}x_{Q,i,j}) = \sum_j (\dot{E}x_{o,j} + \dot{E}x_{Q,o,j}) + \dot{W}_{cv} + \dot{E}x_D \tag{5.1}$$

$\dot{E}x_{Q,j}$ is the thermal exergy, associated to heat transfer out or into the control volume and defined as:

$$\dot{E}x_{Q,j} = \left(1 - \frac{T_0}{T_j}\right) \cdot \dot{Q}_j \tag{5.2}$$

$\dot{W}_{cv}$ represents the rate of energy transfer of work other than flow work and $\dot{E}x_i$ and $\dot{E}x_o$ are exergy transfer rates at inlet and outlet. In the absence of nuclear, magnetic, electrical and surface tension effects, they can be divided into four components [205]: physical exergy $Ex^{PH}$, chemical exergy $Ex^{CH}$, kinetic exergy $Ex^{KN}$ and potential exergy $Ex^{PT}$. Kinetic and potential exergy are usually neglected [211] and therefore the total exergy rate of a stream becomes the sum of physical and chemical exergy [204]:

$$\dot{E}x = \dot{m} \cdot ex = \dot{E}x^{PH} + \dot{E}x^{CH} \tag{5.3}$$

The physical exergy is associated to the temperature and pressure of a stream of matter and is given by the following expression:

$$\dot{E}x^{PH} = \dot{m} \cdot ex^{PH} = \dot{m} \cdot [(h - h_0) - T_0 \cdot (s - s_0)] \tag{5.4}$$

Physical exergy does not take into account the exergy component associated to the departure of the chemical composition of a system from that of the environment, which can be evaluated through chemical exergy. The calculation of chemical exergy based on standard (referred to $T_0 = 25°C$ and $P_0 = 1.013\ bar$) chemical exergy values of respective species is detailed, among others, by Bejan et al. [205] and Szargut et al. [210]. For the ammonia-water APC cycle considered, the chemical exergy of the flows is calculated using the following relation:

$$\dot{E}x^{CH} = \dot{m} \cdot ex^{CH} = \dot{m} \cdot \left[\left(\frac{x}{M_{NH_3}}\right) \cdot ex^0_{NH_{3,CH}} + \left(\frac{1-x}{M_{H_2O}}\right) \cdot ex^0_{H_2O,CH}\right] \tag{5.5}$$

where $x$ is the ammonia mass fraction, while $ex^0_{NH_{3,Ch}}$ and $ex^0_{H_2O,Ch}$ are the standard chemical exergy of ammonia and water respectively, and their values are taken from Szargut et al. [210]. In **Eq. (5.5)**, the mixing effect (i.e., $RT_0 \sum_i [x_i \cdot ln\ (x_i)]$ ) is neglected given its small magnitude with respect to other terms [212].
As exergy gives information about the quality of energy, the exergetic efficiency provides a true measure of the performance of a system. In order to define this parameter, it is necessary to identify both a product and a fuel of the system studied. The product is the desired useful effect, while the fuel represents the resources spent to generate the product. An exergy rate balance for the system can be then written as:

$$\dot{E}x_F = \dot{E}x_P + \dot{E}x_L + \dot{E}x_D \tag{5.6}$$

where $\dot{E}x_F$ is the fuel exergy, $\dot{E}x_P$ is the product exergy, $\dot{E}x_L$ is the exergy loss (the exergy associated with the heat rejected to the environment) and $\dot{E}x_D$ is the exergy destroyed. The exergetic efficiency is the ratio between the product and fuel exergy:

$$\eta_{ex} = \frac{\dot{E}x_P}{\dot{E}x_F} \tag{5.7}$$

The definition of a product and the calculation of an exergetic efficiency is not immediate for all components when considering them individually (**Table 5.1**). For example, this is the case of throttling valves, exchangers crossing $T_0$ (usually the case of the subcooler in this cycle) or cooling heat exchangers, like the condenser, that serve other components. In addition, a comparison of exergetic efficiencies of dissimilar devices is generally not meaningful [205].

However, applying **Eq.(5.6)** and using the definitions of **Table 5.1**, it is possible to calculate the values of the rates of exergy destroyed ($\dot{E}x_{D,k}$) and exergy loss ($\dot{E}x_{L,k}$) in each component and in the overall system ($\dot{E}x_D$ and $\dot{E}x_L$). It is then interesting to calculate the ratio of exergy destruction and exergy loss ratios, expressed as follows:

$$Y_{D,k} = \frac{\dot{E}x_{D,k}}{\dot{E}x_F} \tag{5.8}$$

$$Y^*_{D,k} = \frac{\dot{E}x_{D,k}}{\dot{E}x_D} \tag{5.9}$$

$$Y_{L,k} = \frac{\dot{E}x_{L,k}}{\dot{E}x_F} \tag{5.10}$$

While the rates of $\dot{E}x_{D,k}$ and $\dot{E}x_{L,k}$ give a thermodynamic measure of the system inefficiencies, $Y_{D,k}$, $Y^*_{D,k}$ and $Y_{L,k}$ are useful to compare different components of the same system.

**Table 5.1** - Fuel, product and loss definition for the system. Absolute vales of exergy flow rates considered.

| Component | Fuel | Product | Loss |
|---|---|---|---|
| Absorber | $\dot{E}x_{F,a} = \dot{E}x_{17} + \dot{E}x_6 - \dot{E}x_1$ | − | $\dot{E}x_{L,a} = \dot{E}x_{a,o} - \dot{E}x_{a,i}$ |
| Condenser | $\dot{E}x_{F,c} = \dot{E}x_8 - \dot{E}x_9$ | − | $\dot{E}x_{L,c} = \dot{E}x_{c,o} - \dot{E}x_{c,i}$ |
| Desorber | $\dot{E}x_{F,d} = \dot{E}x_{d,i} - \dot{E}x_{d,o}$ | $\dot{E}x_{P,d} = \dot{E}x_7 + \dot{E}x_4 - \dot{E}x_3$ | − |
| Electric generator | $\dot{E}x_{F,ele} = \dot{W}_t$ | $\dot{E}x_{P,ele} = \dot{W}_{t,ele}$ | − |
| Evaporator | $\dot{E}x_{F,e} = \dot{E}x_{11} - \dot{E}x_{12}$ | $\dot{E}x_{P,e} = \dot{E}x_{e,o} - \dot{E}x_{e,i}$ | − |
| Mix cooling and power | $\dot{E}x_{F,mix} = \dot{E}x_{17} - \dot{E}x_{16} - \dot{E}x_{13}$ | − | − |
| Pump | $\dot{E}x_{F,p} = \dot{W}_p$ | $\dot{E}x_{P,p} = \dot{E}x_2 - \dot{E}x_1$ | − |
| Refrigerant expansion valve | $\dot{E}x_{F,refvalv} = \dot{E}x_{10} - \dot{E}x_{11}$ | − | − |
| Solution expansion valve | $\dot{E}x_{F,solvalv} = \dot{E}x_5 - \dot{E}x_6$ | − | − |
| Solution heat exchanger | $\dot{E}x_{F,shx} = \dot{E}x_4 - \dot{E}x_5$ | $\dot{E}x_{P,shx} = \dot{E}x_3 - \dot{E}x_2$ | − |
| Subcooler | $\dot{E}x_{F,sub} = \dot{E}x_9 - \dot{E}x_{10}$ | $\dot{E}x_{P,sub} = \dot{E}x_{13} - \dot{E}x_{12}$ | − |
| Superheater | $\dot{E}x_{F,sh} = \dot{E}x_{sh,i} - \dot{E}x_{sh,o}$ | $\dot{E}x_{P,sh} = \dot{E}x_{15} - \dot{E}x_{14}$ | − |
| Turbine | $\dot{E}x_{F,t} = \dot{E}x_{15} - \dot{E}x_{16}$ | $\dot{E}x_{P,t} = \dot{W}_t$ | − |
| Overall system | $\dot{E}x_F = \dot{E}x_{d,i} - \dot{E}x_{d,o} + \dot{E}x_{sh,i} - \dot{E}x_{sh,o}$ | $\dot{E}x_P = \dot{W}_{ele,net} + \dot{E}x_{e,i} - \dot{E}x_{e,o}$ | $\dot{E}x_L = \dot{E}x_{c,o} - \dot{E}x_{c,i} + \dot{E}x_{a,o} - \dot{E}x_{a,i}$ |

In addition to the cooling and electrical power outputs, both first and second law based performance criteria are used here to evaluate the combined cycle performance. In particular, definitions presented in **Eq.(2.19)-(2.21)** are used to assess the energy and exergy performance of the cycle.

# 5.3 Exergoeconomic analysis methodology

Exergoeconomics is the branch of engineering that combines exergy analysis and economic principles [205]. It is based on the idea that exergy is the only true thermodynamic measure to value the interactions that a system experiences with its surroundings, and therefore the only meaningful way to assign a monetary cost to them. An exergoeconomic (or thermoeconomic) analysis is particularly useful when dealing with complex systems with more than one useful product, like the combined system under investigation. Indeed, a thermoeconomic analysis allows calculating separately the cost of each product generated by the system, understanding the cost formation process and optimising specific variables in a single component or in the overall system. This approach, referred to as exergy costing, consists in associating a cost rate $\dot{C}$ to each exergy stream entering the system:

$$\dot{C}_i = c_i \cdot \dot{E}x_i; \quad \dot{C}_o = c_o \cdot \dot{E}x_o\,; \quad \dot{C}_w = c_w \cdot \dot{W}\,; \quad \dot{C}_Q = c_Q \cdot \dot{E}x_Q \tag{5.11}$$

In **Eq. (5.11)**, $c_i$, $c_o$, $c_w$ and $c_Q$ denote the average cost per unit of exergy in dollars per joule (\$/J). Exergy costing involves applying a cost balance, usually formulated for each component $k$ of the system, stating that the total cost of the streams exiting are equal to the expenditure to obtain them:

$$\sum_{i} \dot{C}_{i,k} + \dot{C}_{Q,k} + \dot{Z}_k = \sum_{o} \dot{C}_{o,k} + \dot{C}_{w,k} \tag{5.12}$$

Here, the right term represents the total cost rate of the energy streams exiting the system, while the left term of the equation represents the cost rate necessary to generate them. $\dot{Z}_k$ (\$/s) is the total cost rate associated with capital investment (CI) and operating and maintenance costs (O&M) needed to own and operate component k:

$$\dot{Z}_k = \dot{Z}_{CI,k} + \dot{Z}_{OM,k} \tag{5.13}$$

Since costs vary from year to year, levelized cost are considered when evaluating cost of a thermal system. Consequently, costs in **Eq. (5.13)** are to be intended as levelized costs and in particular $\dot{Z}_{CI,k}$ represents the total capital investment, while $\dot{Z}_{OM,k}$ represent O&M expenditures. The hourly levelized capital investment can be calculated for component $k$ as:

$$\dot{Z}_{CI,k} = \left(\frac{\mathrm{CRF}}{\tau}\right) \cdot Z_k \tag{5.14}$$

where $\tau$ is the number of annual operating hours, $Z_k$ is the capital investment cost of the component and CRF is the capital recovery factor calculated as:

$$\mathrm{CRF} = \frac{i_r \cdot (1 + i_r)^n}{(1 + i_r)^n - 1} \tag{5.15}$$

In **Eq. (5.15)**, $i_r$ indicates the interest rate and the n the number of useful years. The annual levelized O&M costs for component k is given by [205]:

$$\dot{Z}_{OM,k} = \frac{\gamma_k \cdot Z_k}{\tau} + \omega_k \cdot \dot{E}x_{p,k} + \dot{R}_k \tag{5.16}$$

where $\gamma_k$ and $\omega_k$ are associated with fixed and variable O&M costs respectively. $\dot{R}_k$ comprises all other operation and maintenance costs independent of investment cost and product exergy. Since $\omega_k \cdot \dot{E}x_{p,k}$ and $\dot{R}_k$ are significantly smaller than $\frac{\gamma_k \cdot Z_k}{\tau}$, they are most often neglected [205]. Therefore, the annual levelized cost for component k can finally be written as:

$$\dot{Z}_k = \left(\frac{\mathrm{CRF}}{\tau}\right) \cdot Z_k + \left(\frac{\gamma_k}{\tau}\right) \cdot Z_k \tag{5.17}$$

In this study, the investment lifetime n is assumed to be 20 years [35], the interest rate $i_r$ 10% [167], the number of operating hours is 8,000 [35,156,213] and the maintenance factor $\gamma_k$ taken is 0.06 [169,214] for all components. Capital cost functions used for each component, expressed in US dollars, are shown in **Table 5.2**. These data are brought to a reference year (2021) using the chemical engineering plant cost index (CEPCI) [215]:

$$Z_{year2} = Z_{year1} \cdot \left(\frac{\mathrm{CEPCI}_{year2}}{\mathrm{CEPCI}_{year1}}\right) \tag{5.18}$$

Cost correlation for plate heat exchangers is based on French cost in 2021 and obtained using data from 8 different heat exchangers. Indeed, vendor's price quote or data from previously bought similar equipment are the best way to estimate cost [216]. Heat exchangers cost correlations are often formulated as [217]:

$$Z = k_1 + k_2 \cdot S^m \tag{5.19}$$

in which the exponent $m$ to which the exchanger area S is raised is usually smaller than one. The exponent used here, 0.67, is in agreement with the six-tenths rule [218], stating that when costs of a component are known, but its area ($S_b$) differs from that of the to be estimated component ($S_a$), costs can be roughly estimated using the correlation:

$$\frac{Z_a}{Z_b} = \left(\frac{S_a}{S_b}\right)^n \tag{5.20}$$

The exponent $n$ differs per type of equipment, but s is often comprised between 0.5-0.7 for thermal systems [205].

In the base case of heat exchanger area of 1 $m^2$, using the correlation in **Table 5.2** results in slightly higher cost than the widely used [219] linear correlation proposed by Quoilin [55] for plate heat exchangers, also reported in the table as a term of comparison. Cost correlations of the ammonia turbine is complicated by the fact that this technology has not yet reached market diffusion and very often the reported costs refer to FOAK (first of a kind) costs. Here a correlation frequently used in literature is used [167,220,221]. The correlation was originally proposed by Rodriguez et al.[222], but without giving a detailed explanation on how it was derived.

**Table 5.2** - Cost functions for the economic modelling of the system ($\dot{W}_t$, $\dot{W}_{t,ele}$, $\dot{W}_{pump}$ in kW and S in $m^2$).

| Component | Capital investment cost function | Reference | Year | CEPCI |
|---|---|---|---|---|
| Ammonia turbine | $4405 \cdot \dot{W}_t^{0.7}$ | [167,220,221] | 2005 | 468 |
| Generator and electrical auxiliaries | $10^7 \cdot \left(\frac{\dot{W}_{t,ele}}{1.6 \cdot 10^5}\right)^{0.7}$ | [169] | 1998 | 389 |
| Heat exchangers | $130 + 564 \cdot S^{0.67}$ | - | 2021 | 700 |
| Heat exchangers (alternative correlation) | $130 + 310 \cdot S$ | [55,169,219] | 2010 | 551 |
| Pump | $1120 \cdot \dot{W}_p^{0.8}$ | [167,169,220] | 2005 | 468 |

As done in the case of the fuel and product exergy (**Table 5.1**), also in the case of exergy costing all the components of the system are considered as individual units, as also assumed for example in [169,223]. **Table 5.3** lists all cost rate balance and auxiliary equations for each system component. Since only the costs of the streams entering the system are known (left term in **Eq. (5.12)**), when the product definition for a component involves $m$ exiting streams, $m-1$ auxiliary equations must be formulated.

**Table 5.3** - Exergetic cost rate balance and auxiliary equations for the system.

| Component | Cost rate balance equation | Auxiliary equations |
|---|---|---|
| Absorber | $\dot{C}_{a,i} + \dot{C}_{17} + \dot{C}_6 + \dot{Z}_{abs} = \dot{C}_{a,o} + \dot{C}_1$ | $c_{a,i} = c_{a,o} = 0$ |
| Condenser | $\dot{C}_{c,i} + \dot{C}_8 + \dot{Z}_{cond} = \dot{C}_{a,o} + \dot{C}_9$ | $c_{c,i} = c_{c,o} = 0$ |
| Desorber | $\dot{C}_{d,i} + \dot{C}_3 + \dot{Z}_{des} = \dot{C}_{d,o} + \dot{C}_7 + \dot{C}_4$ | $\frac{\dot{C}_7 - \dot{C}_3}{\dot{E}x_7 - \dot{E}x_3} = \frac{\dot{C}_4 - \dot{C}_3}{\dot{E}x_e - \dot{E}x_3}$; $c_{d,i} = c_{d,o} = c_{fuel}$ |
| Electric generator | $\dot{C}_{ele} = \dot{Z}_{gen} + \dot{C}_t$ | − |
| Evaporator | $\dot{C}_{e,i} + \dot{C}_{11} + \dot{Z}_{evap} = \dot{C}_{e,o} + \dot{C}_{12}$ | $c_{11} = c_{12}$ |
| Mix cooling and power lines | $\dot{C}_{13} + \dot{C}_{16} = \dot{C}_{17}$ | − |
| Pump | $\dot{C}_1 + \dot{C}_{pump} + \dot{Z}_{pump} = \dot{C}_2$ | $c_{pump} = c_t$ |
| Refrigerant expansion valve | $\dot{C}_{10} + \dot{Z}_{refvalv} = \dot{C}_{11}$ | − |
| Solution expansion valve | $\dot{C}_5 + \dot{Z}_{solvalv} = \dot{C}_6$ | − |
| Solution heat exchanger | $\dot{C}_4 + \dot{C}_2 + \dot{Z}_{shx} = \dot{C}_3 + \dot{C}_4$ | $c_4 = c_5$ |
| Subcooler | $\dot{C}_9 + \dot{C}_{12} + \dot{Z}_{sub} = \dot{C}_{10} + \dot{C}_{13}$ | $c_{12} = c_{13}$ |
| Superheater | $\dot{C}_{sh,i} + \dot{C}_{14} + \dot{Z}_{sh} = \dot{C}_{sh,o} + \dot{C}_{15}$ | $c_{sh,i} = c_{sh,o} = c_{fuel}$ |
| Turbine | $\dot{C}_{15} + \dot{Z}_t = \dot{C}_t + \dot{C}_{16}$ | $c_{15} = c_{16}$ |

The cooling water used in the condenser and in the absorber is considered as a free resource [169] and hence its cost per unit of exergy is neglected [203] ($c_{a,i} = 0$ and $c_{c,i} = 0$). In the same way, the cost of the exergy of the cooling HTF fluid at the evaporator inlet is assumed to be null [169]. The auxiliary equation most often encountered in literature [35,169,204] in the case of a condenser consists in assuming that the cost per unit of exergy of the working mixture remains constant between condenser inlet and outlet ($c_8 = c_9$). However, in this way the cost rate of the component, $\dot{Z}_{cond}$, is charged to the outlet water used to cool down the condenser. Additionally, since the working mixture undergoes an exergy reduction in the condenser, but the specific exergy cost is assumed to be constant, the cost of the exergy stream at the condenser outlet, $\dot{C}_9 = c_9 \cdot \dot{E}x_9$, is smaller than the cost at inlet $\dot{C}_8$ (as evident from Table 7 in reference [169]). This cost difference also being charged to the cooling water, the overall result is that of a reduction of the cost of the products, which would be smaller than the sum of the total CI and O&M costs of components ($\sum \dot{Z}_k$) and fuel costs.

Indeed, all the costs associated to owning and operating a component should be charged to the product of that component [205]. In the case of the condenser in this study, the useful effect of the component is not the heating of the cooling water, but the condensation of the working fluid. Consequently, the auxiliary equation used for the condenser in this study is $c_{c,i} = c_{c,o} = 0$. Considering that $\dot{E}x_{co} - \dot{E}x_{ci}$ is an exergy loss, this is coherent with what suggested by Bejan et al. [205] with respect to costing of exergy losses. The authors [205] state that the approach

to follow when dealing with exergy losses finally discharged to the environment should be to impose $\dot{C}_{L,k} = 0$, so that the product bears the full burden of the costs associated to component $k$. This is also coherent with the approach proposed by the same authors [205] for cooling heat exchangers.
The same approach was followed in the case of the absorber, where the auxiliary equation $c_{a,i} = c_{a,o} = 0$ was used.

## *Exergoeconomic parameters*

Exergoeconomic parameters play an important role in the evaluation and in the optimization of thermal systems. The most used ones are the average unit cost of fuel $c_{F,k}$, the average unit cost of products $c_{P,k}$, the cost rate of exergy destruction $\dot{C}_{D,k}$, the cost rate of exergy loss $\dot{C}_{L,k}$, and the exergoeconomic factor $f_k$ [205], defined as:

$$c_{F,k} = \frac{\dot{C}_{F,k}}{\dot{E}x_{F,k}} \tag{5.21}$$

$$c_{P,k} = \frac{\dot{C}_{P,k}}{\dot{E}x_{P,k}} \tag{5.22}$$

$$\dot{C}_{D,k} = c_{F,k} \cdot \dot{E}x_{D,k} \tag{5.23}$$

$$\dot{C}_{L,k} = c_{F,k} \cdot \dot{E}x_{L,k} \tag{5.24}$$

$$f_k = \frac{\dot{Z}_k}{\dot{Z}_k + \dot{C}_{D,k} + \dot{C}_{L,k}} \tag{5.25}$$

The cost of exergy destruction and loss calculated with **Eq. (5.23)** and **Eq. (5.24)** can be interpreted as the cost rate of the additional fluid that must be supplied to component $k$ to cover the rate of exergy destruction and loss. Another definition for the two quantities is possible by using the specific cost of the product $c_{P,k}$ instead of $c_{F,k}$ in **Eq. (5.23)** and **Eq. (5.24)**. This formulation is equivalent to considering $\dot{C}_{D,k}$ and $\dot{C}_{L,k}$ as the monetary loss associated with the loss of product [205]. In reality, neither expression is strictly correct, with the actual cost being in the middle between the two resulting values. Using **Eq. (5.23)** and **Eq. (5.24)** is however a more conservative approach with respect to capital investment, and therefore these expressions are more commonly used [8,169].
The exergoeconomic factor $f_k$ can be very useful in the identification of design changes that could improve the cost-effectiveness of a thermal system. The exergoeconomic factor measures the relative importance of two types of cost sources: exergy related costs (exergy destroyed and loss) and non-exergy related costs (CI and O&M costs). When $f_k$ is very high for a component $k$, costs savings for the entire system could be achieved by reducing the investment cost of the component, at the price of lowering its exergetic performance. On the other hand, low values of $f_k$ indicate the possibility of increasing the exergoeconomic performance of the system by increasing the capital investment for the component and increasing its exergetic efficiency.

After solving the system equations listed in **Table 5.3**, the specific cost of electricity ($c_{ele} = \dot{C}_{ele}/\dot{W}_{t,ele}$) and the specific cost of cooling ($c_{cooling} = \dot{C}_{e,o}/(\dot{E}x_{e,o} - \dot{E}x_{e,i})$ ) can be calculated using **Eq. (5.22)**. The overall unit cost of product for the system is obtained through the following equation [8]:

$$c_{prod} = c_{cooling} + c_{ele} \tag{5.26}$$

The unit cost of produced exergy ($UCOPE$) is another useful parameter to analyse the system from an economic point of view. For systems with more than one product UCOPE can be defined as [8,224]:

$$UCOPE = \frac{\sum \dot{Z}_k + \sum (c_{F,k} \cdot \dot{E}x_{F,k})}{\sum \dot{E}x_P} \tag{5.27}$$

For the system considered, in light of the discussion above and of equations in **Table 5.3**, the $UCOPE$ can be written for this system as:

$$UCOPE = \frac{\dot{C}_{e,o} + \dot{C}_{ele} + c_{fuel} \cdot \left(\dot{E}x_{F,d} + \dot{E}x_{F,sh}\right)}{\dot{E}x_{P,e} + \dot{W}_{t,ele}} = \frac{c_{cooling} \cdot \left(\dot{\mathrm{E}}\mathrm{x}_{\mathrm{e,o}} - \dot{\mathrm{E}}\mathrm{x}_{\mathrm{e,i}}\right) + c_{ele} \cdot \dot{W}_{t,ele}}{\left(\dot{\mathrm{E}}\mathrm{x}_{\mathrm{e,o}} - \dot{\mathrm{E}}\mathrm{x}_{\mathrm{e,i}}\right) + \dot{W}_{t,ele}} \tag{5.28}$$

showing that the UCOPE is a weighted average on the useful exergy of each product of their relative specific cost. Finally, one last important parameter for the evaluation of the exergoeconomic performance of the system is the sum of the capital investment cost rate and of the total exergy destruction for each component ($\sum \dot{Z}_k + \sum \dot{C}_{D,k}$).

# 5.4 Results and discussion

Simulations of the cycle were conducted using the model presented in *Chapter 4*. In the following, the energy and exergy performance of the pilot plant is evaluated through parametric studies around the nominal operating point. Subsequently, the system thermodynamic and exergoeconomic performance is analysed for the pilot plant design operating conditions and for a base case operating point, representing a space cooling application. For the base case conditions, the performance achievable by increasing of 25 times the size of the plant (so that a full admission turbine can be used) is evaluated.
A parametric study on the temperature of the sources is then performed to assess the impact of the hot and cold source temperatures, all other conditions being fixed. The impact of heat exchangers area is also evaluated. Finally, an optimization is performed for the scaled-up plant in order to find the optimal exchangers area minimizing the unit cost of produced exergy ($UCOPE$) of the system.

## 5.4.1 Pilot plant energy and exergy analysis

**Table 5.4** shows the effect of integrating the turbine model into the absorption cycle model at the nominal operating point characterised by a pump flow rate of 100 kg/h, a hot source temperature of 95 °C, an intermediate source temperature of 27 °C and a cold source temperature of 18 °C.

When the turbine is added to the cycle, the desorbed vapour is divided between the mechanical power production and the cooling production lines. The mass flow rate passing through the power production line is fixed by the pressure upstream of the turbine (as explained in *Section 3.4.2*), while the remaining vapour mass flow rate passes through the cooling production line. As confirmed by experimental results (**Table 3.6**), the presence of the turbine in the cycle increases the amount of vapour desorbed because of the higher efficiency of heat exchangers working with a reduced refrigerant vapour mass flow rate. Cooling power production is reduced to around 2.85 kW, while the turbine isentropic efficiency is only 25%, producing 100 W of mechanical power, corresponding to a power cycle efficiency of 1.9%, due to the performance penalty resulting from partial admission. The turbine inlet and outlet pressure ($P_{15}$= 10.9 bar, $P_{16}$=6.2 bar) at nominal operating pressures imply the presence of an oblique shock at the injector outlet, indicating that there is room for optimisation of its design.

**Table 5.4** - Effect of the turbine on the cycle at nominal operating conditions.

| | $\dot{\mathrm{Q}}_e$ [kW] | $\dot{\mathrm{W}}_T$ [kW] | $\dot{m}_8$ [kg/h] | $\dot{m}_{14}$ [kg/h] | $\dot{\mathrm{Q}}_d$ [kW] | $\dot{\mathrm{Q}}_{sh}$ [kW] | $\mathrm{COP_c}$ [-] | $\eta_{\mathrm{power}}$ [-] | $\eta_{\mathrm{is,tur}}$ [-] |
|---|---|---|---|---|---|---|---|---|---|
| Turbine line closed | 7.01 | - | 22.62 | - | 10.18 | - | 0.69 | - | - |
| Turbine line open | 2.85 | 0.10 | 8.94 | 17.0 | 11.57 | 0.25 | 0.71 | 0.013 | 0.255 |

**Fig. 5.2** shows the impact of increasing the desorber inlet temperature on the performance of the cycle. The losses linked to the small size and to the partial admission of the turbine highly penalize the power production of the cycle. Thus, as an upper performance limit, it is interesting to look also at the power that could be produced by an ideal turbine having a unitary isentropic efficiency (dotted line in **Fig. 5.2 (a)**). A higher hot source temperature increases the power exchanged at the desorber for a fixed solution mass flow rate, and thus the refrigerant vapour mass flow rate produced (**Fig. 5.2 (b)**). This increases considerably the cooling power output (**Fig. 5.2 (a)**), but moderately increases the mechanical power output. In fact, the mass flow rate treated by the turbine only slightly increases, passing from 16.6 kg/h at 85 °C to 17.2 kg/h at 125 °C, because of the slight high pressure increase. The latter is due to the higher pinch on the condenser caused by the higher vapour mass flow rate and temperature on the component.

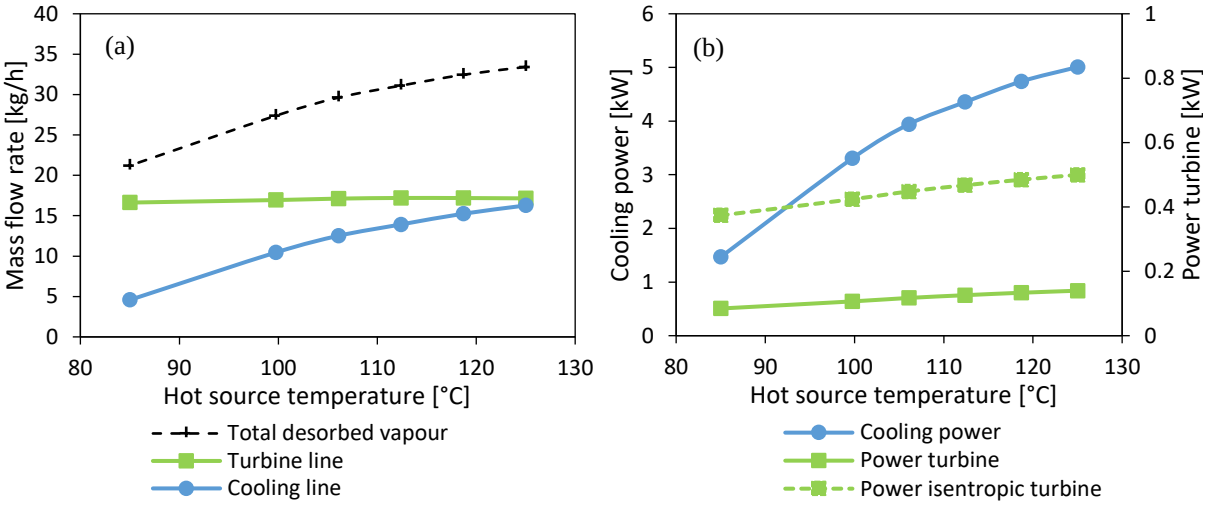


**Fig. 5.2** - Impact of the hot source temperature on (a) the refrigerant vapour mass flow rate and (b) output of the system (all other conditions fixed to nominal point).

In accordance with experimental results, similar considerations apply also for variation of the intermediate and cold source temperatures. Increasing the intermediate source temperature (**Fig. 5.3**) leads to an increase of the high pressure of the cycle. Therefore, a larger pressure drop is available to the turbine, increasing its power output and the efficiency. On the other hand, increasing the high pressure of the cycle reduces the circulating mass flow rate of refrigerant vapour, while increasing the mass flow rate treated by the turbine. This reduces the mass flow rate passing through the cooling production line, approaching zero for an intermediate source temperature of 31 °C, thus limiting the operation range of the combined cycle.

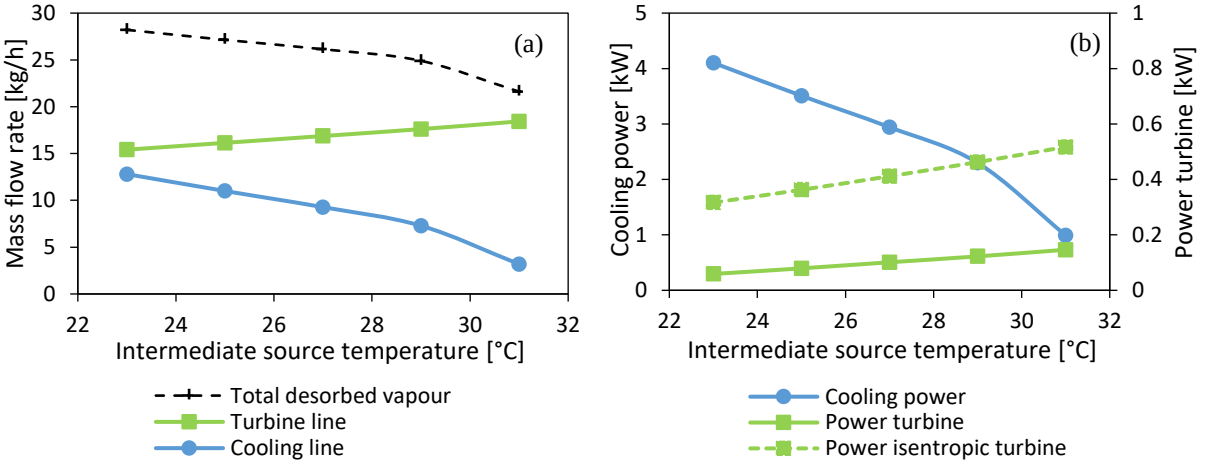


**Fig. 5.3** - Impact of the intermediate source temperature on (a) the refrigerant vapour mass flow rate and (b) power output of the system (all other conditions fixed to nominal point).

On the other hand, lowering the cold source temperature (**Fig. 5.4**) decreases the low pressure of the cycle (and therefore the efficiency of the absorption process), thus reducing the circulating vapour mass flow rate. The lower mass flow rate passing through the cooling production line increases the efficiency of the condenser, reducing the temperature pinch on the component. Even though this slightly reduces the turbine mass flow rate, the cooling line mass flow rate approaches zero for a cold source temperature around 8°C (for other conditions fixed at nominal point). While reducing the evaporator temperature has a negative impact on the cooling production of the cycle, it improves the performance of the power production thanks to the higher pressure drop available to the turbine.

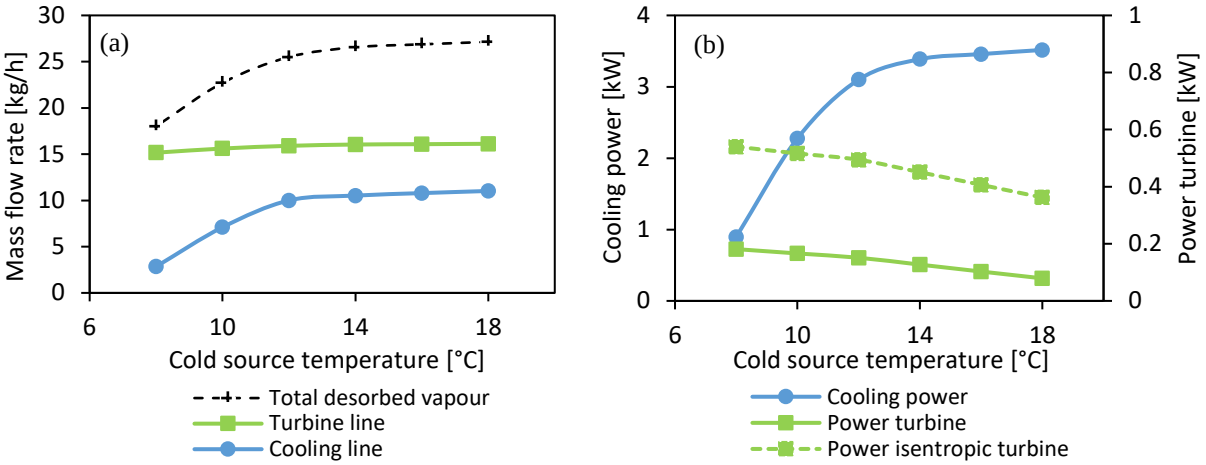


**Fig. 5.4** - Impact of the cold source temperature on (a) the refrigerant vapour mass flow rate and (b) output of the system (all other conditions fixed to nominal point).

All of the above highlights the strict limits that this type of expander imposes to the cycle, both in terms of the vapour inlet conditions needed to avoid condensation during the expansion, which requires the presence of a superheater, and in terms of mass flow rate treated. Particularly, the latter constraint restrains the flexibility of the cycle, making it impossible to regulate the ratio of cooling and power production according to the actual needs for fixed sources temperatures.

Subsequently, the exergetic performance of the system was evaluated at the nominal operating point. **Fig. 5.5** shows that the absorber and the desorber are the components where most of the exergy destruction takes place (42% and 24% respectively). The turbine is responsible for 14%, while the solution heat exchanger accounts for 10% of the exergy destruction within the cycle. Other components play a smaller role.

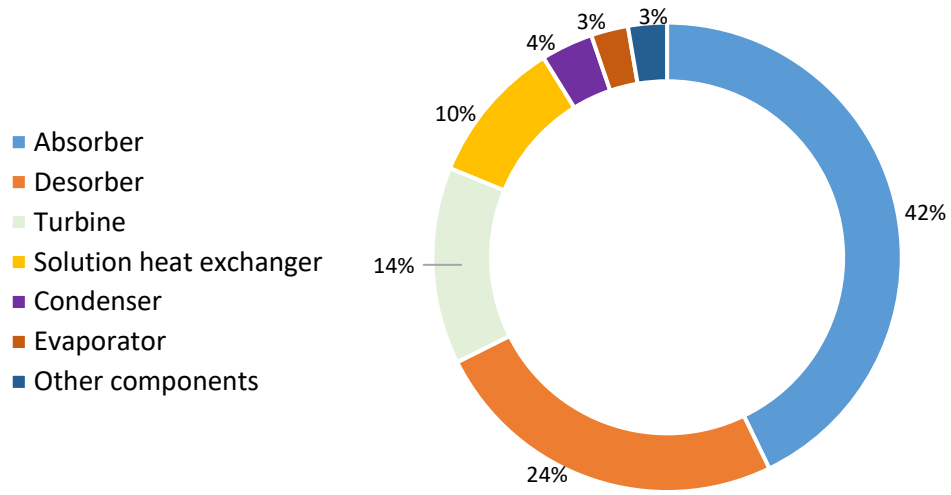


**Fig. 5.5** – Exergy destruction ratio $Y^*_{D,k}$ of the systems components for the nominal operating point.

A parametric study on the effect of the temperature of the sources is presented in **Fig. 5.6**. The intermediate source temperature has a relatively small impact on exergetic efficiency compared to the cold source temperature. On the other hand, reducing the cold source temperature from 18 °C to 12 °C significantly improves the exergetic efficiency of the cycle. However, lower cold source temperatures and higher intermediate source temperatures require higher temperatures of the driving thermal power and limit the operation range of the cycle.

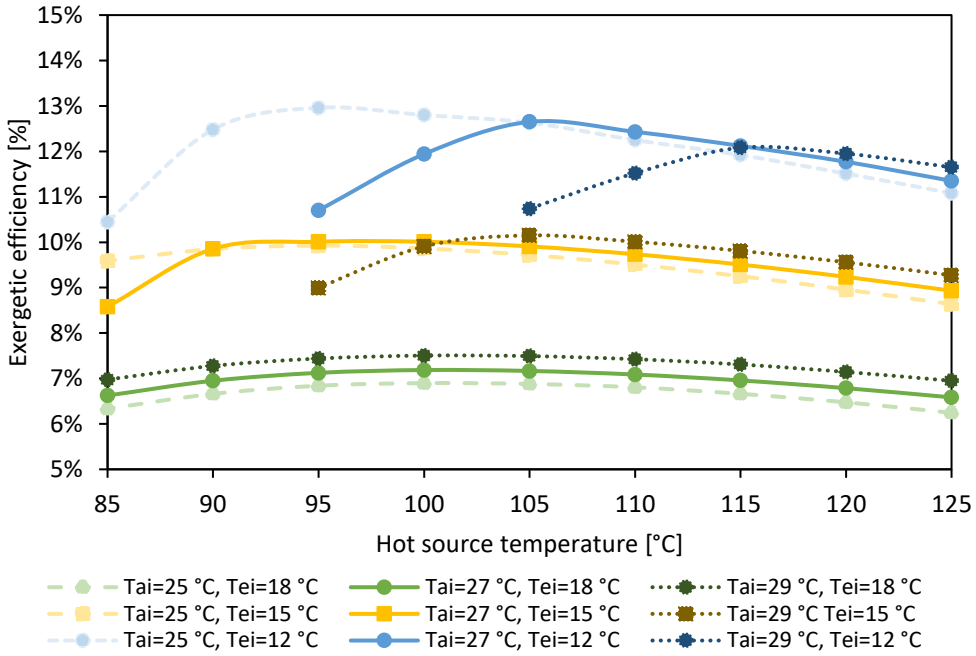


**Fig. 5.6 –** Parametric analysis on the temperature of the sources (all other conditions fixed to nominal point).

## *Throttling before the turbine*

The strict limits imposed by the turbine on the flexibility of the cycle have been highlighted in the previous section. Referring to the nominal operating point, **Fig. 5.7** shows that reducing the turbine inlet pressure through a throttling process (i.e., decreasing $R_{th}$ defined in **Eq. (4.85)**) allows increasing the cooling power output because of the increased mass flow rate passing through the cold production line. On the other hand, the turbine mechanical power output tends to zero, due both to the reduced enthalpy drop available and to the reduction of the turbine efficiency. The latter passes from 25% to 8% for R_th=0.8 if the rotational speed is optimised for the working conditions. In fact, the smaller enthalpy drop available reduces the injector outlet speed, meaning that the optimal efficiency will be at a lower rotational speed, decreasing from 38,000 rpm to 18,000 rpm. Nevertheless, for this pressure, the power production of the turbine goes to zero and the turbine line should be closed. Furthermore, the throttling process before the turbine reduces the exergetic efficiency of the cycle. The above demonstrates that throttling offers only a partial solution to the cycle's lack of flexibility, as the additional flexibility is very limited and is obtained at the detriment of the cycle's (and turbine) exergetic performance. An alternative solution, explored in *Section 5.5*, is represented by the development of adapted architectures, allowing higher flexibility.

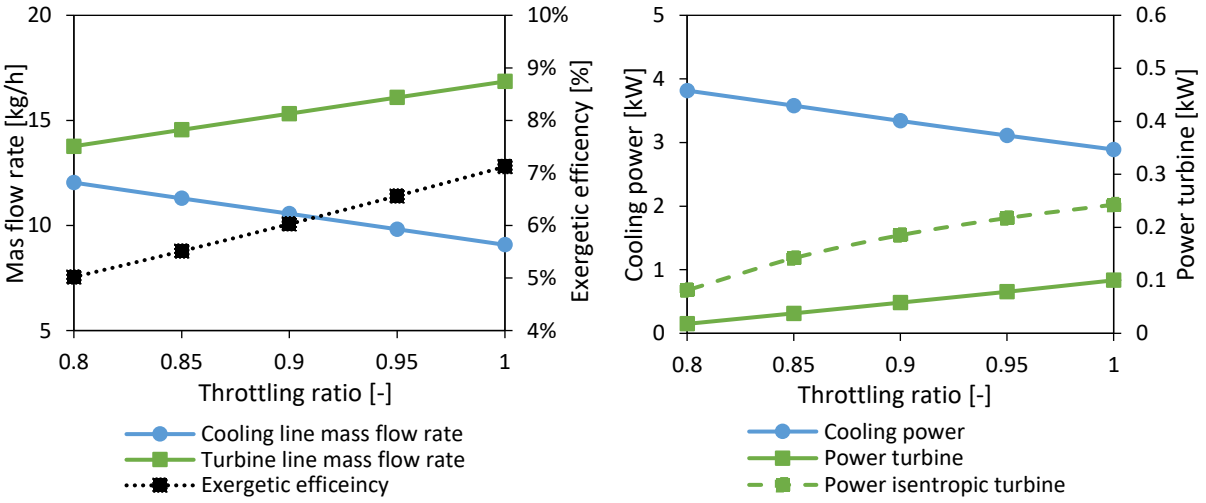


**Fig. 5.7 –** Impact of the throttling process on the performance of the cycle

### 5.4.2 Exergo-economic analysis and scale-up evaluation

Two operating points are evaluated (**Table 5.5**), the design point of the pilot plant (considering a hot source temperature of 100°C) and a base case representative of a typical refrigeration application, for which also the effect of scaling-up the plant is studied. The temperature of the hot source HTF considered is $100\ °C$, while the temperature of the cold source HTF considered are $18\ °C$ and $10\ °C$ respectively (corresponding to an outlet cooled HTF temperature $T_{e,o}$ of 15.4°C and 7.3 °C respectively). The hot temperature HTF is used first to supply thermal power to the superheater and then to the desorber (hence $T_{sh,o} = T_{d,i}$).

**Table 5.5** - Input parameters and predicted performance of the pilot plant at nominal and base case operating points.

| Parameters | Nominal point | Base case | Scale-up x25 |
|---|---|---|---|
| **Input parameters** | | | |
| Hot source temperature, $T_{sh,i}$ [°C] | 100 | 100 | 100 |
| Intermediate source temperature, $T_{a,i}$ and $T_{c,i}$ [°C] | 25 | 25 | 25 |
| Cold source temperature, $T_{e,i}$ [°C] | 18 | 10 | 10 |
| Rich solution mass flow rate, $\dot{m}_1$ [kg/h] | 100 | 100 | 2,500 |
| **Thermal power exchangers** | | | |
| Absorber, $\dot{Q}_a$ [kW] | 12.76 | 11.73 | 297 |
| Condenser, $\dot{Q}_c$ [kW] | 4.45 | 3.75 | 101 |
| Desorber, $\dot{Q}_d$ [kW] | 13.10 | 12.09 | 310 |
| Evaporator - Cooling power, $\dot{Q}_e$ [kW] | 3.93 | 3.31 | 90 |
| Superheater, $\dot{Q}_{sh}$ [kW] | 0.31 | 0.28 | 7 |
| **Turbine** | | | |
| Turbine isentropic efficiency, $\eta_{is,tur}$ [%] | 40.6 | 44.1 | 73.2 |
| Rotational speed turbine, ω [rpm] | 39,200 | 49,500 | 80,000 |
| Mechanical power turbine, $\dot{W}_t$ [kW] | 0.16 | 0.24 | 10 |
| Electrical power turbine, $\dot{W}_{ele,turb}$ [kW] | 0.15 | 0.22 | 9.5 |
| Net electrical power cycle, $\dot{W}_{ele,net}$ [kW] | 0.13 | 0.20 | 8.9 |
| **Overall performance indicators** | | | |
| Cooled water temperature, $T_{e,o}$ [°C] | 14.9 | 7.3 | 7.2 |
| Desorbed vapour mass flow rate, $\dot{m}_8$ [kg/h] | 28.78 | 26.21 | 679 |
| Split Ratio, $r_s$ [-] | 0.43 | 0.39 | 0.41 |
| First law efficiency, $\eta_I$ [%] | 30.27 | 28.41 | 31. 17 |
| Effective first law efficiency, $\eta_{I,eff}$ [%] | 1.81 | 3.18 | 4.44 |
| Exergetic efficiency, $\eta_{ex}$ [%] | 9.37 | 16.45 | 22.96 |
| **Exergoeconomic performance for $c_{fuel} = 0$ \$/GJ** | | | |
| Exergoeconomic factor, $f$ [-] | 1 | 1 | 1 |
| Unit cost of produced cooling, $c_{cooling}$ [$/GJ] | 175 (0.63 $/kWh) | 96 (0.35 $/kWh) | 14.8 (0.05$/kWh) |
| Unit cost of produced electricity, $c_{ele}$ [$/GJ] | 1,681 (6.05 $/kWh) | 1,073 (3.86 $/kWh) | 45 (0.16 $/kWh) |
| Unit cost of products, $c_{prod}$ [$/GJ] | 1,856 (6.68 $/kWh) | 1,169 (4.21 $/kWh) | 59.8 (0.21 $/kWh) |
| Unit cost of produced exergy, $UCOPE$ [$/GJ] | 1,012 (3.64 $/kWh) | 626 (2.25 $/kWh) | 34.2 (0.12 $/kWh) |
| **Exergoeconomic performance for $c_{fuel} = 15$ \$/GJ** | | | |
| Exergoeconomic factor, $f$ [-] | 0.87 | 0.88 | 0.39 |
| Unit cost of produced cooling, $c_{cooling}$ [$/GJ] | 292 (1.05 $/kWh) | 160 (0.58 $/kWh) | 75 (0.27 $/kWh) |
| Unit cost of produced electricity, $c_{ele}$ [$/GJ] | 1,879 (6.76 $/kWh) | 1,190 (4.28 $/kWh) | 113 (0.41 $/kWh) |
| Unit cost of products, $c_{prod}$ [$/GJ] | 2,171 (7.81 $/kWh) | 1,350 (4.86 $/kWh) | 188 (0.68 $/kWh) |
| Unit cost of produced exergy, $UCOPE$ [$/GJ] | 1,174 (4.22 $/kWh) | 718 (2.58 $/kWh) | 99 (0.35 $/kWh) |

The scale-up of the heat exchangers is performed so as not to affect their effectiveness with respect to operation in the pilot plant (i.e., leaving dimensionless parameters constant). In this study, this is done simply by increasing the number of plates of the heat exchangers. Although this is not the way heat exchangers would be scaled in reality, the assumption is that the same exchangers effectiveness could be achieved with well designed heat exchangers also at larger sizes. Since heat exchangers area would increase less than linearly with exchanged power in real life applications, linearly increasing the number of plates as done here gives an upper cost estimation.
When scaling-up the desorber the hypothesis is made that the ratio between adiabatic and heated plates surface is equal to the one of the pilot plant (35%) to guarantee the same vapour purity.
Since the design point of the turbine (inlet pressure of 16 bar and outlet pressure of 4 bar) is quite different from the actual conditions in the cycle (**Table 7.5-Table 7.7** in *Section 7.5*), the flow at the injector outlet is over-expanded and shock phenomena take place, affecting the turbine's performance (*Section 4.3.1*). Performance

analysis using the turbine model shows that a converging-only injector is optimal for the conditions under investigation. Hence, this configuration is retained for the study. For each case considered in **Table 5.5** and in **Fig. 5.8**, the optimal rotational speed maximizing the turbine efficiency is found. Additionally, it is assumed that the reduced number of injectors linked to a partial admission turbine does not entail a significant cost reduction. Thus, the cost of the turbine is considered equal to the cost of a full-admission turbine (mechanical power estimated from simulations in **Table 5.5** of around 10 kW) also in the case of partial admission configurations. It is worth mentioning that the cost calculated for $\dot{W}_t = 10$ kW using the correlation of **Table 5.2** brought to the reference year of 2021, is higher than the actual cost of turbine integrated in the pilot plant, which was however designed for a higher pressure ratio.
The specific cost of the thermal input, $c_{fuel}$, is an important parameter determining the cost of the products. Different values of this parameter can be found in literature: [169] and [225] assumed it to be waste heat with negligible cost, [162,226,227] considered it to be vapour with cost of 15.24 $/GJ while [8] considered a cost of 17.85 $/GJ. Two different scenarios are analysed in the present study: the use of waste heat with negligible cost and the use of a fuel with a cost of 15 $/GJ, to assess how the exergoeconomic performance of the plant is affected by the cost of the fuel.

At the nominal point, the system absorbs 13.10 kW from the hot source (considering both $\dot{Q}_d$ and $\dot{Q}_{sh}$), producing 3.93 kW of cooling at 14.9 °C and 130 W of net electrical output. The high pressure of the cycle determines the mass flow rate treated by the turbine, corresponding in the design point to approximately 57% of the desorbed vapour ($r_s$ = 0.43). The first law efficiency of the cycle is 30.27%, while the exergetic efficiency 9.37%.
For the base case, the lower cooling output temperature increases the exergetic efficiency of the system, as shown in **Table 5.5**. This is due to the fact that the cooling power output remains almost constant but its exergetic value is higher as a consequence of the lower temperature. Additionally, the low pressure of the cycle being determined by the evaporating temperature ($T_{11}$), the pressure drop available to the turbine increases, increasing the power production of the expander. Consequently, the an UCOPE passing from 1,012 $/GJ to 654 $/GJ in the case of $c_{fuel} = 0$ and from 1,174 $/GJ to 762 $/GJ in the case of $c_{fuel} = 15$ $/GJ.

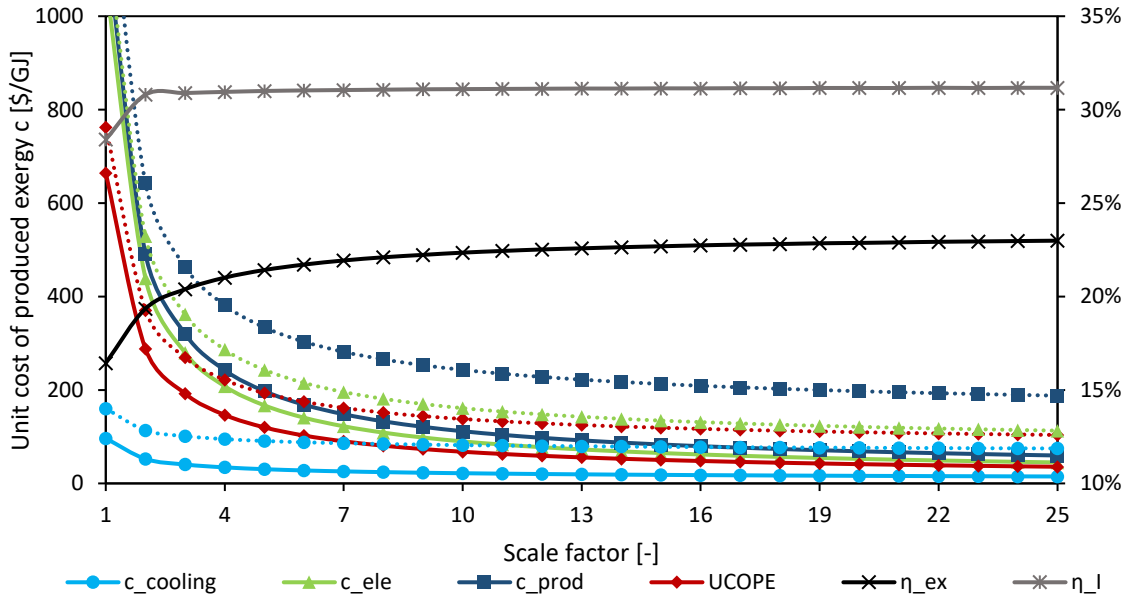


**Fig. 5.8** - Change of energy efficiency, exergetic efficiency and unit cost of produced exergy (bold lines for the case of $c_{fuel} = 0$ $/GJ, dotted lines for the case of $c_{fuel} = 15$ $/GJ) increasing the plant size with respect to the pilot plant size.

**Fig. 5.8** shows for the base case operating point the effect of increasing the plant size, measured by the scale factor (i.e., the relative area of heat exchangers, working fluid and HTF mass flow rate values with respect to the pilot plant area). It can be seen how the specific cost of products decreases significantly when increasing the plant size. This is due to the fact that components cost increases less than linearly with their size, and to the fact that the turbine cost, the main cost item (**Table 5.6**), remains constant. Moreover, reducing the partial admission ratio improves the isentropic efficiency of the turbine $\eta_{is,tur}$, reaching 73.2% in the case of a full admission turbine (*Section 4.3.5)*. This leads to an increase in the exergetic efficiency of the system, passing from 16.45% to 22.96% which is not reflected however in an equal increase in the first law efficiency. As a result, the cost $c_{cooling}$ is 14.8

(75) \$/GJ, $c_{ele}$ is 45 (113) \$/GJ, $c_{prod}$ is 60 (188) \$/GJ and the UCOPE 34.2 (99) \$/GJ for a plant 25 times bigger than the pilot plant for $c_{fuel} = 0$ ($c_{fuel} = 15$ \$/GJ respectively). **Table 7.4** (*Section 7.5*) shows the outputs of the exergoeconomic analysis when using alternative heat exchangers cost correlations proposed by [55]. Predicted cost of products in this case are very similar for the pilot plant size and slightly higher for the scaled-up plant.
The values of exergy destroyed and lost in each component, and the ratios of exergy destroyed relative to the net fuel exergy supplied ($Y_{D,k}$) and relative to the total exergy destruction in the system ($Y^*_{D,k}$) are shown in **Table 5.6**. The absorber and the desorber are the primary contributors to the total exergy destruction ($Y^*_{D,k}$ of 42.5% and 26.8% respectively), followed by the solution heat exchanger and turbine. **Table 5.6** also shows exergoeconomic analysis results in the case of $c_{fuel} = 15$ \$/GJ (for $c_{fuel} = 0$ \$/GJ, $\dot{C}_{D,k}$ and $\dot{C}_{L,k}$ would always be equal to 0). The turbine and the electric generator present the highest values of $\dot{Z}_{,k}$ (0.73 \$/h and 0.42 \$/h respectively), but have a relatively low cost of exergy destruction compared to the absorber, desorber and solution heat exchanger. The low values of the exergoeconomic factor for these components indicates that cost savings could possibly be achieved by increasing their size and efficiency (and hence their cost). In contrast, the pump, turbine and electric generator have high exergoeconomic factors indicating that capital cost rates could be decreased at the expense of a reduced component efficiency. The overall exergoeconomic factor for the system is 0.4 and 53.7% of total costs for the system (2.31\$/h) come from exergy destruction.
Stream thermodynamic properties and cost data corresponding to the three cases shown in **Table 5.5** are presented in *Section 7.5*.

**Table 5.6** - Exergy and exergoeconomic indicators for the system components and overall system for the case of the scaled up plant (scale factor 25) and $c_{fuel} = 15$\$/GJ.

| Component | $\dot{E}x_{Dk}$ $[kW]$ | $\dot{E}x_{Lk}$ $[kW]$ | $Y_{D,k}$ $[-]$ | $Y^*_{D,k}$ $[-]$ | $Y_{L,k}$ $[-]$ | $\dot{Z}_{,k}$ $[\$/h]$ | $\dot{C}_{D,k}$ $[\$/h]$ | $\dot{C}_{L,k}$ $[\$/h]$ | $f_k$ $[-]$ |
|---|---|---|---|---|---|---|---|---|---|
| Absorber | 18.18 | - | 0.295 | 0.425 | 0.073 | 0.10 | 0.98 | 0.23 | 0.10 |
| Condenser | 1.80 | 0.49 | 0.029 | 0.042 | 0.009 | 0.13 | 0.10 | 0.03 | 0.52 |
| Desorber | 11.45 | 4.17 | 0.186 | 0.268 | - | 0.12 | 0.62 | - | 0.16 |
| Electric generator | 0.60 | - | 0.010 | 0.014 | - | 0.42 | 0.03 | - | 0.93 |
| Evaporator | 1.32 | - | 0.021 | 0.031 | - | 0.09 | 0.07 | - | 0.57 |
| Mix cooling and power | 0.23 | - | 0.004 | 0.005 | - | 0.00 | 0.01 | - | 0.00 |
| Pump | 0.12 | - | 0.002 | 0.003 | - | 0.02 | 0.01 | - | 0.94 |
| Refrigerant expansion valve | 0.09 | - | 0.001 | 0.002 | - | 0.00 | 0.00 | - | 0.00 |
| Solution expansion valve | 0.32 | - | 0.005 | 0.007 | - | 0.00 | 0.02 | - | 0.00 |
| Solution heat exchanger | 4.92 | - | 0.080 | 0.115 | - | 0.05 | 0.27 | - | 0.16 |
| Subcooler | 0.06 | - | 0.001 | 0.001 | - | 0.04 | 0.00 | - | 0.93 |
| Superheater | 0.26 | - | 0.004 | 0.006 | - | 0.02 | 0.01 | - | 0.59 |
| Turbine | 3.42 | - | 0.056 | 0.080 | - | 0.73 | 0.18 | - | 0.80 |
| Overall system | 42.76 | 4.66 | 0.695 | 1.000 | 0.082 | 1.75 | 2.31 | 0.25 | 0.40 |

### 5.4.3 Parametric analysis

The influence of the temperature of the hot and cold sources on the thermodynamic and exergoeconomic performance of the cycle is evaluated in **Fig. 5.9**. Reducing the evaporator temperature increases the exergetic efficiency of the cycle, up to a maximum depending on the hot and medium source temperatures. The maximum reachable value of the exergetic efficiency changes little in the temperature range studied, but the hot source temperature maximising the exergetic efficiency increases when reducing the cold source temperature. On the other hand, the first principle efficiency of the cycle is substantially reduced at lower evaporator temperature because the cooling power production decreases. This is due to the fact that the mass flow rate of circulating refrigerant vapour decreases at lower evaporator temperatures (determining the low pressure of the cycle) mainly because the absorption process becomes less efficient at lower pressure. Since the mass flow rate treated by the turbine remains constant (*Section 4.3*), the mass flow rate passing through the cooling line of the cycle is reduced, as shown by the split ratio tending to zero for temperatures below 4 °C in the case of a hot source temperature of 100 °C (**Fig. 5.9**).
The exergoeconomic performance of the cycle is also strongly affected by the temperature of the sources. In particular, the higher the temperature of the hot source the more convenient it is to produce cooling at lower temperature. However, also in this case, there exists a cold source temperature minimising the $UCOPE$. In the case of ambient temperature of 25 °C and hot source temperature of 100 °C, this temperature is slightly below 10 °C, corresponding to the base case under investigation.

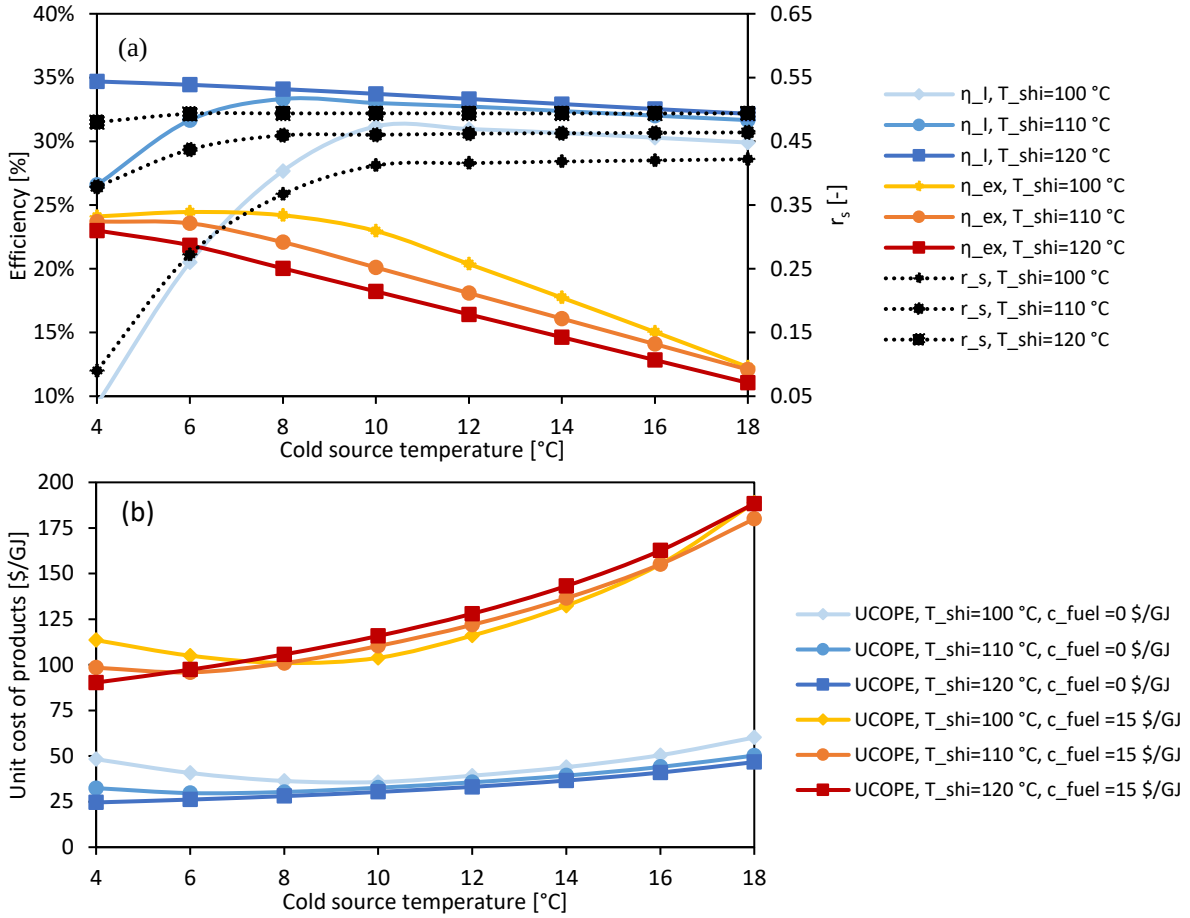


**Fig. 5.9** - Impact of the temperature of the cold and hot source on the thermodynamic (a) and exergoeconomic performance of the cycle (b) for an ambient temperature of 25 °C.

Subsequently, the influence of the size of components on the performance of the cycle was analysed. **Fig. 5.10** presents results concerting the size of the absorber, the component presenting the highest value of the sum of the capital cost of the component and exergy destroyed in the component ( $\dot{Z}_k + \dot{C}_{D,k}$ in **Table 5.6**), and hence the first to address in an optimization procedure. Increasing the size of the absorber initially reduces the $UCOPE$, because the thermodynamic efficiency of the cycle increases. However, further increasing the absorber size increases the capital costs more than the cost savings linked to reduced exergy destruction. Following this method, an optimization of all heat exchangers area in order to minimize the $UCOPE$ is presented in the next section.

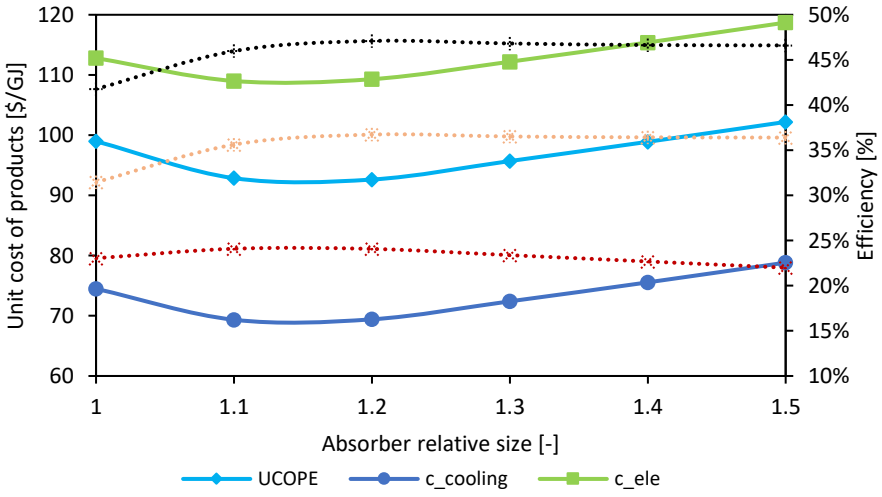


**Fig. 5.10** - Impact of the absorber area with respect to the scaled up plant in the base case operating point for $c_{fuel} = 15\$/GJ$.

### 5.4.4 Optimization

Exergoeconomic optimization aims at maximizing thermal and exergy efficiencies and minimizing the cost of products simultaneously. Objective functions can vary widely, depending on the desired decision variable, and optimization criteria can be based on maximizing first principle or exergetic efficiency or at minimizing the cost per unity of exergy of the products (i.e., $UCOPE$, $c_{prod}$, $c_{ele}$, $c_{cooling}$). In this work, the $UCOPE$ (**Eq. (5.27)**) is considered as the most significant variable representing the exergoeconomic performance of the cycle. An optimisation is carried out aiming at minimizing its value in the base case working point (hot source temperature 100°, intermediate source temperature 25 °C and cold source temperature 10 °C), by varying the area of the system heat exchangers. More specifically, the size of the turbine and the solution mass flow rate are kept constant, while heat exchangers area is varied looking for the optimal trade-off between their cost and performance in the system under investigation.
Several optimization methods are available in the EES software [228]. The EES internal genetic algorithm, used in several studies [155,162,227], has the advantage of being the most robust and not being affected by the guess values of the independent variables as is the case for direct search and variable metric methods. However, the genetic method is the slowest of the available methods and Zare et al. [162] concluded that by assigning appropriate guess values for the parameters, the genetic and direct search methods yield the same optimization results.
Since reliable guess values for the optimal area of components are available from parametric studies on exchangers area (like the one presented for the absorber in *Section 5.4.3*), the direct search method was used in this study. This method, also commonly used in literature [212], is based on an iterative search intended to find an optimum by directly comparing function values at a sequence of trial points without involving derivatives
**Fig. 5.11** outlines the results of the optimization process both in the case of $c_{fuel}$ equal to 0 and 15 \$/GJ. In the first case the U$COPE$ is reduced of 17.2% with respect to the base case in **Table 5.5**, down to reaching 28 \$/GJ, while in the second case the $UCOPE$ is reduced of 8.8% down to reaching 90.8 \$/GJ. The relatively small $UCOPE$ reduction indicates that the pilot plant is well designed. **Table 5.7** also presents the relative area of heat exchangers resulting from the optimization, with respect to the linear scale up of the plant presented in **Table 5.5**.

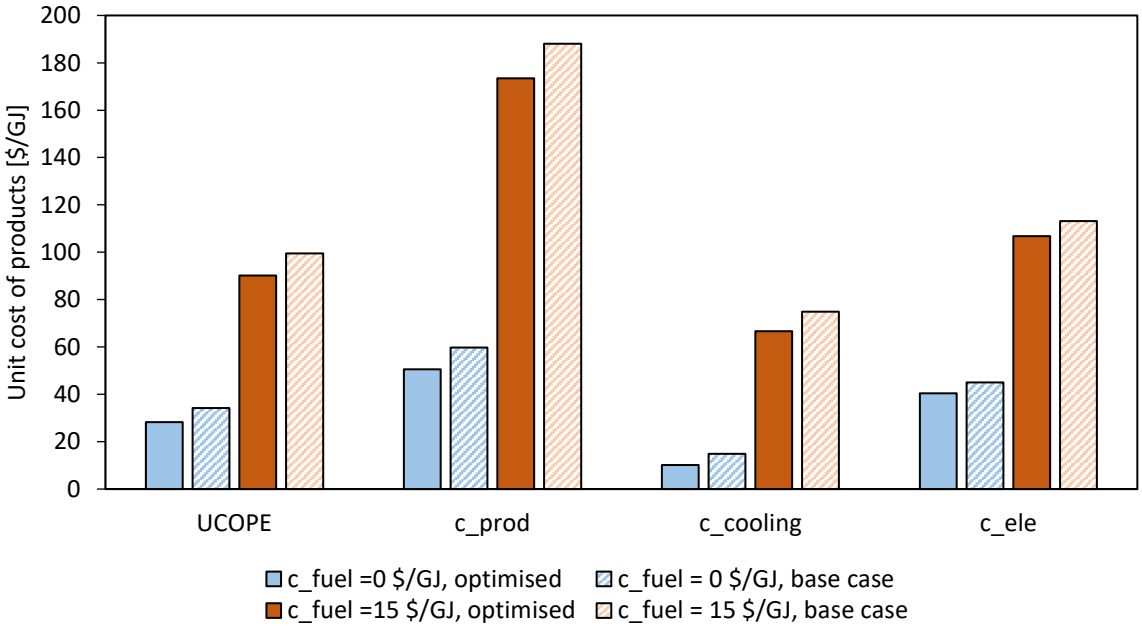


**Fig. 5.11** - Heat exchangers size optimization results.

It can be noticed that overall the total capital cost do not change much compared to results in **Table 5.6** ($\sum \dot{Z}_k = 1.75\,\$/h$), with a small reduction in the case of $c_{fuel} = 0$ \$/GJ, where, since the cost of the fuel is neglected, higher exergetic losses are acceptable. This is due to two main reasons. The first is that the major cost item, the cost of the turbine (accounting together with the electrical generator for a capital cost of 1.15 \$/h in the base case) is kept constant. The second reason is that the resulting optimal area increases for some exchangers while it decreases for others. The optimal area of the absorber, for example, is found to be around 14% bigger than in the base case. This is not surprising since the absorber of the pilot plant has been designed for a nominal cold source temperature of 18 °C, and hence benefiting from a higher working pressure. On the other hand, the optimal area of heat exchangers of the cooling production line is found to be significantly smaller than in the base case. Also this is not surprising, since in the pilot plant was designed to treat all the desorbed mass flow rate, but the

addition of the turbine deviates a considerable part of it (around 60%) to the power production line. Finally, for the optimal configuration, the split ratio increases with respect to the base case, reaching 0.47.

**Table 5.7 -** Exergy and exergoeconomic indicators for the optimised configurations.

| **Thermodynamic and exergoeconomic performance parameters** | $c_{fuel} = 0$ **\$/GJ** | $c_{fuel} = 15$ **\$/GJ** |
|---|---|---|
| Unit cost of produced exergy, $UCOPE$ [\$/GJ] | 28.31 (0.101 \$/kWh) | 90.24 (0.324 \$/kWh) |
| Unit cost of products, $c_{prod}$ [\$/GJ] | 50.58 (0.182 \$/kWh) | 173.5 (0.624 \$/kWh) |
| Unit cost of produced electricity, $c_{ele}$ [\$/GJ] | 40.45 (0.146 \$/kWh) | 106.8 (0.384 \$/kWh) |
| cost of produced cooling, $c_{cooling}$ [\$/GJ] | 10.14 (0.036 \$/kWh) | 66.7 (0.240 \$/kWh) |
| Exergetic efficiency, $\eta_{ex}$ [%] | 23.8 | 24.2 |
| First law efficiency, $\eta_I$ [%] | 35.7 | 36.5 |
| Split Ratio, $r_s$ [-] | 0.46 | 0.47 |
| Evaporator - Cooling power, $\dot{Q}_e$ [kW] | 116.1 | 119.6 |
| Net electrical power cycle, $\dot{W}_{ele,net}$ [kW] | 9.8 | 9.5 |
| | | |
| **Heat exchangers relative area with respect to base case** | | |
| Relative area absorber [-] | 1.14 | 1.14 |
| Relative area condenser [-] | 0.48 | 0.79 |
| Relative area desorber [-] | 1.2 | 1.01 |
| Relative area evaporator [-] | 0.49 | 0.72 |
| Relative area solution heat exchanger [-] | 1.09 | 1.04 |
| Relative area subcooler [-] | 0.51 | 0.86 |
| Relative area superheater [-] | 1.25 | 1.43 |
| Total Capital cost, $\sum \dot{Z}_k$ [\$/h] | 1.71 | 1.75 |

### 5.4.5 Synthesis of the energy, exergy and exergoeconomic analysis

The performance of the combined production cycle is investigated using the numerical models presented in *Chapter 4*. Parametric studies around the nominal operating point highlighted the often opposite effect that a variation of the temperature of the source has on the two outputs of the cycle.
The supersonic turbine appears to impose strict limits on the cycle in terms of treated mass flow rate, not allowing the possibility of choosing the vapour split ratio between the cooling and electricity production line. On the other hand, this is imposed by the relative size of turbine and heat exchangers. Carrying out a throttling process before the turbine is studied in order to add a degree of freedom to the system. However, the additional freedom granted to the system by this solution is very limited and has a negative impact on the exergetic performance of the cycle.

Subsequently, the exergoeconomic performance of the cycle is analysed. Fixing the hot source temperature to 100 °C, the performance of the prototype is studied in the design working point and in a base case characterised respectively by a cold source temperature of 18 °C and 10 °C respectively.
The small size of the pilot plant (thermal power input of 12-13 kW) proves to be very penalizing for the $UCOPE$, in particular because of the very high cost of the partial-admission turbine. For this reason, the effect of increasing the plant size of 25 times (up to reach full admission conditions for the turbine) is evaluated for the base case working point. In this case, the cycle produces around 90 kW of cooling at around 7 °C and about 9 kW of electricity reaching and exergetic efficiency of 23%.
A parametric study performed on the temperature of the sources highlights their strong influence on the performance of the cycle and showing that for given conditions of the hot and intermediate source temperature, there is a cooling production temperature maximizing exergetic efficiency or minimizing the $UCOPE$.
Finally, fixing the size of the turbine and the solution mass flow rate, an optimisation of the area of heat exchangers is performed to minimise the UCOPE for two different costs of the fuel: the use of waste heat having negligible cost and the use of a thermal input with a cost of 15 \$/GJ.
When the fuel cost is neglected, the optimisation process leads to an UCOPE of 28.31 \$/GJ, a unit cost of cooling $c_{cooling}$ of 10.14 \$/GJ and a cost of electricity $c_{ele}$ of 40.45 \$/GJ. When the cost of fuel is 15 \$/GJ instead, the optimal UCOPE is 90.24 \$/GJ, $c_{cooling}$ is 66.7 \$/GJ and $c_{ele}$ is 106.8 \$/GJ. In both cases, the optimisation leads to an increased absorber and desorber area, increasing the circulating mass flow rate (and hence the cooling production). Indeed, the higher cost per unity of exergy of electricity production compared to cooling suggests favouring the production of cooling.

## 5.5 Novel cycle architecture

Results presented in *Section 5.4.1* highlighted the strict limits imposed by the supersonic turbine to the cycle, preventing from varying the flow rates between the cold production line and the power production line for fixed temperatures of the sources.
For larger turbines, it is usually possible to vary the partial admission ratio of the turbine through adjustable moving stators or the closing of individual injectors or sectors of the turbine. However, for small-scale turbines this can often prove to be complex and very costly. A solution often practised at industrial level in power plants is to perform a throttling process before the turbine. However, as shown in *Section 5.4.1*, in the case of the cycle under investigation, this reduces significantly the exergetic efficiency of the cycle and the additional flexibility obtained is very limited.
A more efficient solution may be to integrate an ejector within the combined absorption cycle. As discussed in Section 2.4.1, the integration of ejectors into absorption cycles has been envisaged by several authors. Here a novel cycle architecture (**Fig. 5.12**) integrating an ejector, is proposed to limit some of the flexibility limitations imposed by the turbine. The cycle architecture is object of a patent [180].

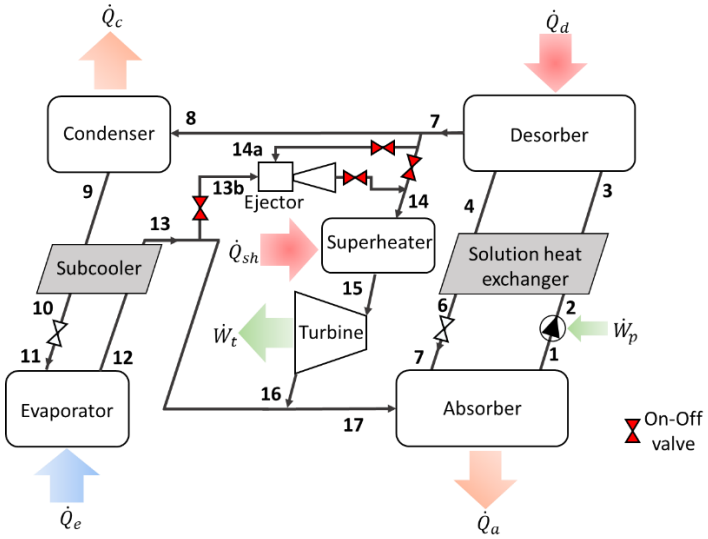


**Fig. 5.12 –** Novel cycle architecture.

The introduction of the ejector into the cycle adds an intermediate efficient operating point to the cycle, in addition to operation as a simple absorption machine and operation in combined mode without throttling. Indeed, with respect to performing a throttling process (**Fig. 5.13(b)**), the use of the ejector ((**Fig. 5.13(a)**), allows increasing the mass flow rate passing through the cooling production line by reducing less the mass flow rate passing through the turbine ($\dot{m}_{14}$). This is possible because a part of it comes from the evaporator outlet (point 13b) after having been used to obtain the cooling effect. Since the mass flow rate treated by the turbine ($\dot{m}_{14}$) depends on the turbine inlet pressure ($P_{15}$), the power production is favoured by both a higher mass flow rate and pressure drop available.

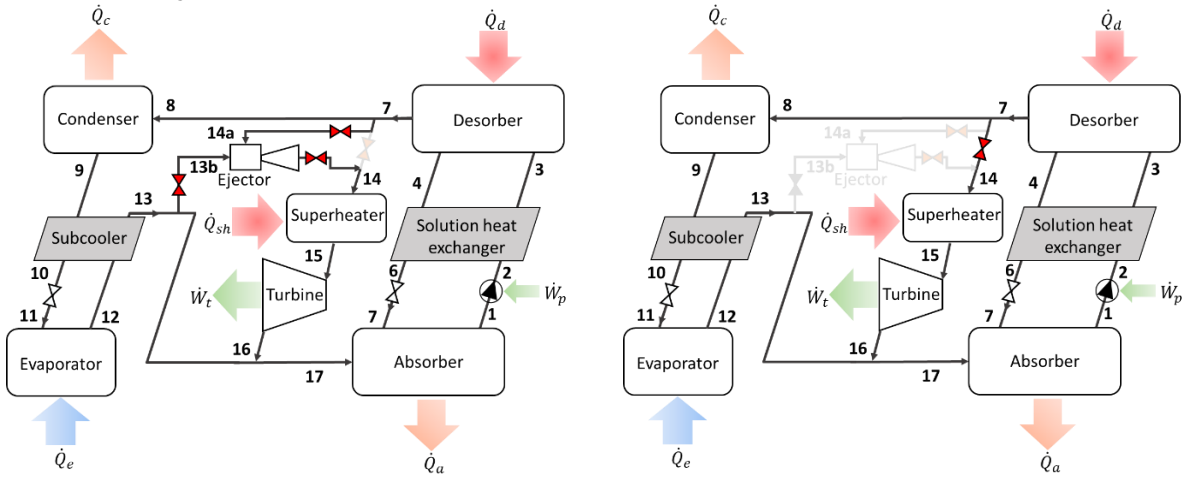


(a) (b)

**Fig. 5.13 –** Novel cycle architecture with ejector line open (a) and closed (b).

The architecture presented was investigated through the integration of an ejector model into the combined cycle model. The ejector model used for this preliminary analysis is the model proposed by Chen et al. [229] adapted to the use of real-gas equations (as shown in *Section 7.2*). This model is capable of predicting the optimum performance of the ejector working at its design point as well as the design area ratio, but not off-design performance. Despite the simplified calculation procedure with respect to the model presented in *Section 7.1*, the model developed by Chen et al. [229] shows very good agreement with experimental data from ejectors working at optimum operating conditions, where, with an appropriate tuning of coefficients, it yields the same results as mass flow rate maximization model presented in *Section 7.1*. The integration of the ejector in the model is performed by imposing that the mass flow rate passing through the cooling production line ($\dot{m}_8$) is equal to the desorbed vapour mass flow rate minus ($\dot{m}_7$) the mass flow rate treated by the ejector primary nozzle ($\dot{m}_8 = \dot{m}_7 - \dot{m}_{14a}$). The primary fluid inlet conditions and the geometry of the ejector determine its entrainment ratio ($\dot{m}_{13b}/\dot{m}_{14a}$) and hence the secondary fluid mass flow rate ($\dot{m}_{13b}$). Finally, the mass flow rate treated by the turbine is equal to the total ejector mass flow rate ($\dot{m}_{14} = \dot{m}_{13b} + \dot{m}_{14a}$), while the vapour mass flow rate entering the absorber is equal to the sum of the turbine mass flow rate and the remaining refrigerant mass flow rate coming from the evaporator ($\dot{m}_{17} = \dot{m}_{16} + \dot{m}_{13} - \dot{m}_{13b}$). The values of the efficiencies (*Section 7.2)* used for the ejector model are: 0.95 for the primary nozzle efficiency ($\eta_p$), 0.95 for the secondary nozzle efficiency ($\eta_s$), 0.8 for the mixing efficiency ($\eta_m$) and 0.9 for the diffuser efficiency ($\eta_d$).

Considering the scaled-up plant working in the base case operating point presented in **Table 5.5**, the simplest way to increase the production of cooling is to perform a throttling process before the turbine (**Fig. 5.13(b)**). Here it is assumed that the cooling production needs to be increased up to 130 kW. Doing so requires a 35% reduction of the pressure upstream the turbine ($R_{th}$=0.65), thus reducing the mass flow rate passing though the expander. However, this reduces the power production of the turbine, passing from 10 kW to 2.88 kW because of the reduced pressure drop and mass flow rate available in addition to a reduction of the isentropic efficiency of the turbine. The overall effect of the throttling is a considerable reduction of the exergetic efficiency of the cycle, passing from 22.9% to 16.4%, as shown in **Table 5.8**.

**Table 5.8** - Effect of the including the ejector in the cycle with respect to performing a throttling process to increase the cooling production.

| | $\dot{Q}_e$ [kW] | $\dot{W}_T$ [kW] | $\dot{Q}_d$ [kW] | $\dot{Q}_{sh}$ [kW] | $\dot{m}_8$ [kg/h] | $\dot{m}_{14}$ [kg/h] | $\dot{m}_{13b}$ [kg/h] | $\eta_{is,tur}$ [-] | $\eta_{ex}$ [-] | $P_{14}$ [bar] |
|---|---|---|---|---|---|---|---|---|---|---|
| Base case | 90.2 | 10.0 | 310.8 | 7.2 | 279.8 | 399.4 | 679.2 | 0.73 | 0.229 | 10.39 |
| Throttling ($R_{th}$=0.65) | 130.0 | 2.88 | 306.2 | 5.61 | 403.3 | 269.7 | 673.0 | 0.61 | 0.164 | 7.00 |
| Ejector use | 130.0 | 8.07 | 306.8 | 10.55 | 398.9 | 364.7 | 672.6 | 0.71 | 0.239 | 8.55 |

As an alternative, the ejector line can be opened as shown in **Fig. 5.13(a)**. Cross sectional areas of the ejector integrated in the combined cycle are presented in **Table 5.9**. As shown in **Table 5.8**, in this case the power production of the turbine is significantly higher (8 kW). This is due to the fact that the inlet pressure of the turbine is higher ($\boldsymbol{P_{14}}$=8.55 bar) than in the case of a throttling before the turbine (7 bar). This allows to have a smaller reduction of the available enthalpy drop, a higher isentropic efficiency of the turbine and a higher treated mass flow rate (364.7 kg/h instead of 267.7 kg/h). As a result, cooling production can be increased without reducing the exergetic efficiency of the cycle, which on the other hand increases in this case, reaching 23.9%, compared to 22.9% in the base case.

**Table 5.9** – Cross sectional areas of the ejector integrated in the combined cycle.

| Primary nozzle throat [mm$^2$] | Primary nozzle exit section [mm$^2$] | Mixing section [mm$^2$] |
|---|---|---|
| 44.87 | 47.87 | 95.68 |

This example shows the interest of integrating one or several ejectors in the combined cycle to be able to reach different ratios of cooling and power production, hence increasing the flexibility of the cycle. Indeed, ejectors are very simple components, with no moving parts and with a low cost. However, further studies are needed to assess the off-design behaviour of the cycle presented in **Fig. 5.12**. The integration of the more detailed ejector model presented in *Section 7.1* could allow the prediction of the ejector performance in off-design working points and an evaluation of when the use of the ejector is more efficient than the throttling process.

## 5.6 Case study

To illustrate the potential applications of the presented combined cycle, it is interesting to evaluate its use in a real case study, assuming that the split ratio can be varied either by variation of the partial admission ratio or by the use of the architecture integrating, an ejector presented above. Here, a simplified assessment is presented in which correlations based on the numerical models developed in *Section 4* are used for the calculation of the thermodynamic performance of the cycle.
The case study considered here is that of a small agricultural enterprise ('AziendaAgricola Pezzaviva') based in the southern Italy region of Apulia. The company has been operating for many years in the agricultural and livestock sector, both in the production of dairy and wine products, and needs cooling throughout the year to keep wine silos at a constant temperature. The cooling demand is currently provided by a conventional vapour compression chiller with nominal power of 40 $kW_{el}$. The company has a connection to the external power grid with a committed power capacity of 102 $kW_{el}$ and has installed a photovoltaic system of approximately 90 kW peak with on-site exchange. Additionally, the company owns an anaerobic digestion plant coupled to a biogas internal combustion engine, connected to the grid, with a nominal power of 100 $kW_{el}$. The system benefits from feed-in tariff incentives of 0.28 €/kWh. However, the electricity produced must be sold to the grid and cannot be used directly. Object of the case study is the evaluation of the interest of recovering the internal combustion engine exhaust gases to feed the combined cooling and power cycle under investigation. The analysis is conducted over the period going from July 2021 to June 2022.

### *Relevancy of the case study*

According to the EBA (European Biogas Association), Europe is today the largest biogas producer in the world, with a current biogas production of 18.2 billion cubic metres, of which 64% are exploited for power production (31%) or cogeneration (33%) [230]. Germany is by far the largest market and hosts two-thirds of Europe's biogas plant capacity, followed by Italy, the UK and France.
Looking at the Italian situation only, 2010 anaerobic digestion plants are listed on the GSE (Italian national energy services manager) website. According to the GSE Statistical Report [231] these plants produced 8.2 TWh of electricity, equal to 7% of the total electricity production from renewables (116.9 TWh). The capacity factor on a national scale is about 6118 hours/year. Looking at the distribution by power classes, 38% of the installed plants have a nominal power between 100 and 300 $kW_{el}$, 13% between 300 and 600 $kW_{el}$, 43% between 600 and 1,000 $kW_{el}$ and 6% higher than 1,000 $kW_{el}$.
Because of existing incentives, most of such plants are aimed at the production of electricity, and cogeneration plants are mostly aimed at optimising the process for maintaining biodigesters in thermophilic conditions (35-40 °C). More specifically, of the approximately 13.8 TWh of available waste heat, only 3.6 TWh, were recovered i.e., only 25% of potential. Focusing only on small power plants (600 kW), corresponding to an electric power output of about 282 $MW_{el}$ and a thermal output of about 475 MW, recoverable heat is about of about 2.9 TWh. The use of just 30% of this heat for electricity production could lead to an additional electricity production of 52.3 GWh (assuming a 6% electrical efficiency), equal to the demand of 20,000 households (average consumption of about 2,700 kWh/year).

### 5.6.1 Energy demand of the company

The agricultural enterprise object of the present case study owns a digester for the production of biogas. The produced biogas is used in an internal combustion engine that produces electricity (100 $kW_{el}$) fed to the grid. The internal combustion engine is equipped with an internal heat exchanger for waste heat recovery, currently not exploited. For safety reasons, a flare is installed to be used in case of emergency, in the event of a breakdown or maintenance of the engine. The plant configuration allows the production of electricity through the use of a *Doosan* internal combustion engine, with 6 cylinders, for a total displacement volume of 11051 $cm^3$, having a recoverable heat rejection between cooling water and fumes, of 170 kW at a temperature of 100 °C.
The electrical energy produced by the engine and transferred to the power grid is constantly measured and recorded at 15 minutes intervals. The electricity produced in the considered period (of one year) is approximately 748.7 MWh corresponding to 7480 equivalent hours, thus an annual availability at rated power of approximately 87%. This value can be considered as high in view of the size of the plant, small compared to a typical biogas engine, usually characterised by electrical power in the order of the $MW_{el}$.

The company also owns a photovoltaic power plant with on-site exchange, with a capacity of 88.20 kW peak made of 360 monocrystalline silicon photovoltaic modules of 245 W peak.

The photovoltaic plant was built in the framework of a national incentive programme providing an incentive of 0.23 €/kWh produced, and unlike the case of the biogas engine allows the direct use of the energy produced. Production data at 15-minute intervals are available also for the photovoltaic plant. Daily site meteorological data (irradiance, air temperature, wind speed, etc.), measured every 10 seconds, are available from national databases [232]. Production data was analysed for a one-year period, revealing a total production of 121 MWh.

The company's energy consumption was analysed in detail on an hourly basis. The annual electrical consumption is about 420.3 MWh. Because of self-produced electricity, the electricity consumed from the grid is about 306.8 MWh, while the energy transferred to the grid is only 7.6 MWh. Therefore, it can be concluded that except for a few days, usually holidays and very sunny days, all the energy produced by the photovoltaic system is self-consumed. It should also be noted that the biogas plant benefits from incentives that do not allow the self-consumption of the energy produced. Hence, although the plant could largely satisfy the electricity demand, due to the stipulated contracts, the company is obliged to sell to the grid the electricity produced by the biogas engine at a price of 0.28 €/kWh. The average monthly electricity cost has experienced great variability during the period considered in the analysis as shown in **Table 5.10**, but the average price paid by the company in the reference period (excluding taxes and levies) was around 0.26 €/kWh.

**Table 5.10** – Wholesale reference price and effective electricity price paid by the company in the considered period.

| | Average | Jun 21 | Jul 21 | Aug 21 | Sep 21 | Oct 21 | Nov 21 | Dec 21 | Jan 22 | Feb 22 | Mar 22 | Apr 22 | May 22 | Jun 22 |
|---|---|---|---|---|---|---|---|---|---|---|---|---|---|---|
| Wholesale reference price [€/kWh] | **0.216** | 0.102 | 0.112 | 0.158 | 0.217 | 0.226 | 0.281 | 0.224 | 0.211 | 0.308 | 0.246 | 0.230 | 0.271 | 0.102 |
| Price paid by the company [€/kWh] | **0.257** | 0.122 | 0.134 | 0.189 | 0.258 | 0.270 | 0.330 | 0.276 | 0.262 | 0.366 | 0.292 | 0.269 | 0.323 | 0.122 |

On the other hand, it is possible to recover the thermal energy of the engine's exhaust, which is currently rejected to the ambient and could be used to drive the cooling and power combined production ammonia-water cycle investigated in this PhD thesis.

## *Cooling demand estimation*

The period from the 1st July 2021 until 30th of June 2022 is considered in the present study. For the period considered, the thermal power rejected by the biogas engine (calculated from the electrical power output and efficiency of the engine) is available at 15 minutes intervals. The power production of the photovoltaic plant, and the electrical power absorbed by the grid is also available at 15 minutes intervals, allowing the calculations of the electricity consumption of the company. However, the power consumption of the vapour compression chiller, necessary for a techno-economic evaluation of the case study is not known and an estimation was needed.

With this goal, a measurement apparatus was installed to measure the electricity consumed by the vapour compression chiller during the months of August and September 2022. Subsequently, a correlations was searched to correlate the chiller electricity consumption to ambient temperature and solar radiation. Indeed, studies have demonstrated the correlation between cooling demand and ambient temperature and solar radiation [233].
The correlation used to model the electricity demand of the vapour compression chiller is:

$$\dot{W}_{VCC} = 0.5 + 0.57 \cdot (T_{amb} - 8) + 0.015 \cdot I_{rad} \quad (5.29)$$

where $\dot{W}_{VCC}$ is expressed in kW, $T_{amb}$ is the ambient temperature in °C and $I_{rad}$ is the solar radiance in W/m$^2$. No cooling need ($\dot{W}_{VCC}$=0) is considered when ambient temperature is below 8 °C.
Coefficients of **Eq.(5.29)** were tuned on data from the 3rd to the 10th of September 2022. The correlation used appears to be in acceptable agreement with experimental measures (**Fig. 5.14**). Indeed, the overall measured electricity consumption of the chiller was of 2461 kWh, while the value predicted by the correlation is of 2531, corresponding to a 3% error. Experimental measures and predictions of the correlations were compared on an additional dataset of measures from the 14th to the 22nd of October 2022. Although the resulting maximum discrepancy is very high, the average hourly error found was of 8%, while the error on the overall electricity consumption was of 2.6% (1,944 kWh measured with respect to 1,891 kWh predicted using **Eq.(5.29)**). Thus,

**Eq.(5.29)** has been used to estimated electricity consumption of the vapour compression chiller throughout the whole reference period.
Once the electricity consumption is known, the cooling demand can be calculated from the COP of the machine as $\dot{Q}_{Cooling} = \dot{W}_{VCC} \cdot \mathrm{COP}_{VCC}$. $\mathrm{COP}_{VCC}$values given by the manufacturer as a function of the ambient temperature for cooling at 10 °C are given in **Table 5.11**.

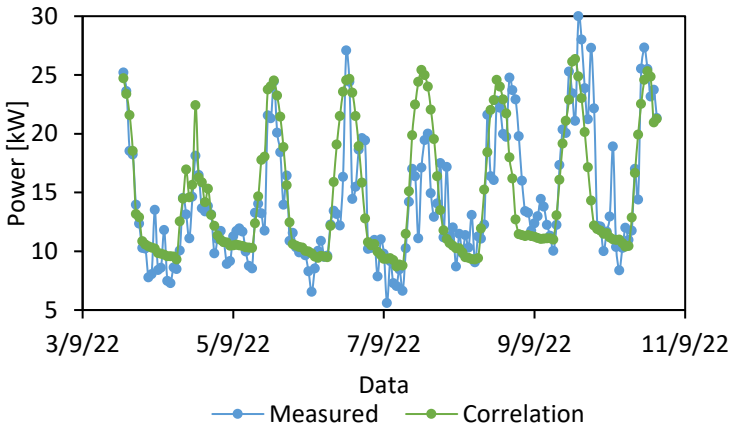


**Fig. 5.14 –** Measures and recalculated electrical power consumption of the vapour compression chiller.

**Table 5.11** – Vapour compression chiller COP values as a function of the ambient temperature for cooling at 8°C (Rhoss model TCAEBY [234]).

| Ambient temperature [°C] | $\mathrm{COP}_{VCC}$ [-] |
|---|---|
| 35 | 2.8 |
| 30 | 3.32 |
| 25 | 4.97 |
| 20 | 5.67 |
| 15 | 5.95 |
| 10 | 6 |

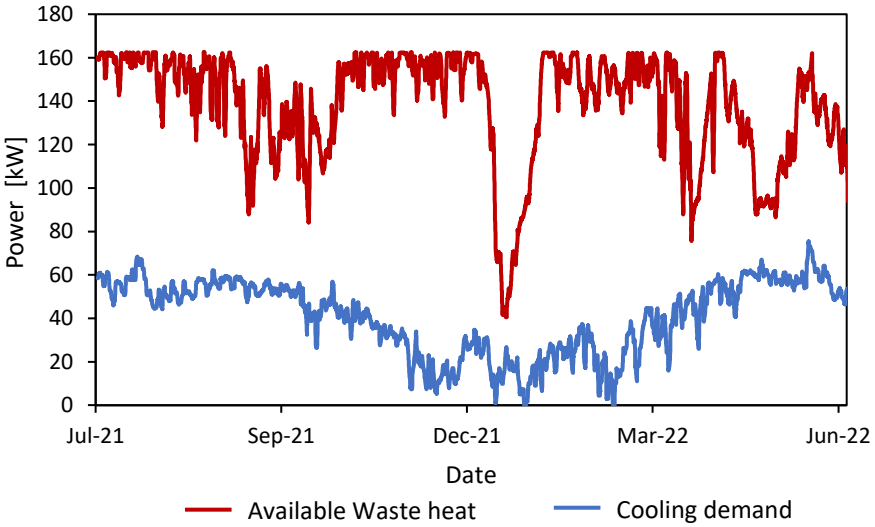


**Fig. 5.15** – Waste heat availability and estimated cooling needs of the company.

A third order polynomial expression was used to interpolate values from **Table 5.11**:

$$\mathrm{COP}_{VCC} = 0.0004 \cdot {T_{amb}}^3 - 0.0334 \cdot {T_{amb}}^2 + 0.6854 \cdot T_{amb} + 2.0138 \quad (5.30)$$

The moving average of the hourly data on 24 hours periods of the available waste heat and the estimated cooling demand is shown in **Fig. 5.15**.

### 5.6.2 Energy savings calculation

Although an optimal sizing study would be required, a preliminary sizing of the combined cooling and power absorption cycle was performed using the simplified cycle model presented in Section 4.4.
Sizing of the heat exchangers was performed by setting as a design point the one of maximum available thermal power (160 kW) and maximum cooling need (70 kW), hot source temperature of 100 °C, cold source temperature of 10 °C and intermediate source temperatures of 30 °C.
However, since simulation of the performance of the cycle for each hour of the year proved to very difficult using the developed EES model, a simplified evaluation procedure was used.
The combined cycle model was used to study the variation of the $COP_c$ (**Eq. (4.82)**) of the system as a function of the ambient temperature, in the simplified hypothesis that this is independent from the split ratio $r_s$ (**Fig. 5.16**). An expression relating the $COP_{Carnot}$ to the $COP_C$, was then developed:

$$COP_C = 0.722 - \exp\left(-0.02 \cdot COP_{Carnot}^{4.167} - 0.778\right) \tag{5.31}$$

Concerning the power production cycle, the efficiency is obtained using the following expression:

$$\eta_{power} = \eta_{power,nom} \cdot \frac{\eta_{is,tur}}{\eta_{is,tur,nom}} \tag{5.32}$$

Where $\eta_{power,nom}$ is the power cycle efficiency (**Eq. (4.84)**) efficiency in the design point, equal to 5.75%, $\eta_{is,tur,nom}$ is the isentropic efficiency at design point of the turbine (working in full-admission conditions) and $\eta_{turb}$ is calculated using an expression obtained from the numerical model:

$$\eta_{is,tur} = 0.743 - \exp\left(-1.937 \cdot \dot{W}_t^{0.35}\right) \tag{5.33}$$

The use of **Eq. (5.32)** is equivalent to making the simplified assumption that the power cycle efficiency is independent from the turbine inlet conditions (however fairly constant given the fixed hot and cold source temperature), and only function of the turbine partial admission ratio (used to regulated the split ratio of the cycle).
The correlation presented in **Eq. (5.33)** is obtained based on the turbine 1D model with adapted injector exist section used in *Section 5.4.2*. In particular, the number of injectors is increased up to reaching full admission, where, in the working conditions investigated, the turbine produces 10.5 kW. The maximum producible power given the available waste heat is very close to this value (around 9.5 kW), Hence, since a very similar turbine can be used, it is assumed that **Eq. (5.32)** can be used to estimate the isentropic efficiency of the expander.

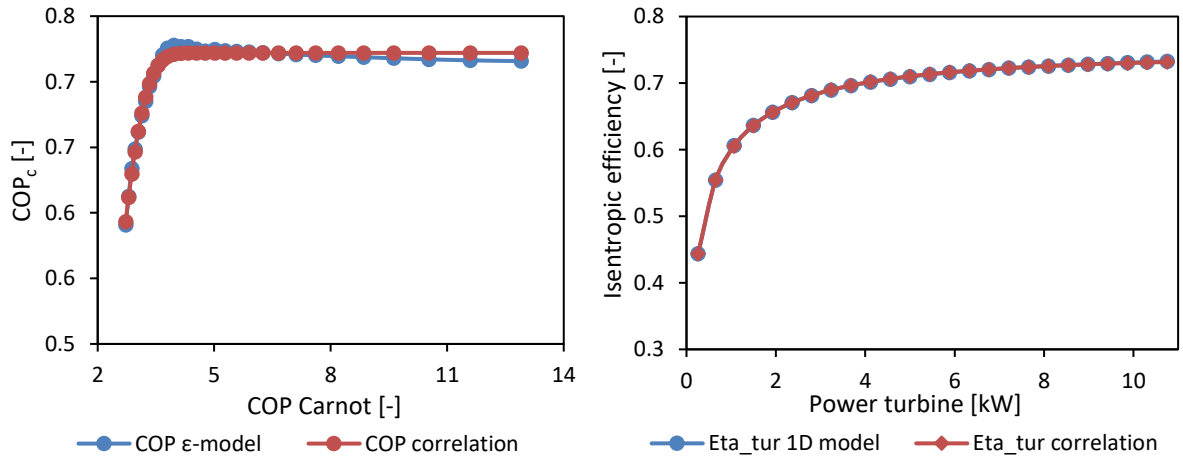


**Fig. 5.16** – Comparison of results of the numerical model and correlations used for the calculation of the $COP_C$ and $\eta_{is,tur}$.

Hence, for each hour, the thermal power needed by the absorption combined cycle to satisfy the cooling demand ($\dot{Q}_{H,cooling}$) is calculated as the cooling demand divided by $COP_C$:

$$\dot{Q}_{H,cooling} = \dot{Q}_{Cooling}/COP_C \tag{5.34}$$

The effective cooling produced $\dot{Q}_{Cooling,eff}$ corresponds to the cooling demand $\dot{Q}_{Cooling}$ only if $\dot{Q}_{H,cooling}$ is smaller than the available thermal power $\dot{Q}_H$:

$$\dot{Q}_{Cooling,eff} = \left[\min\left(\dot{Q}_H, \dot{Q}_{H,cooling}\right)\right] \cdot COP_C \tag{5.35}$$

Additionally, it was supposed that the cooling production was only possible for ambient temperatures below 35 °C. The remaining thermal power that can be used for the production of electricity ($\dot{Q}_{H,power}$) is calculated as:

$$\dot{Q}_{H,power} = \dot{Q}_H - \frac{\dot{Q}_{Cooling,eff}}{COP_C} \tag{5.36}$$

Finally, the electrical power produced is calculated as:

$$\dot{W}_t = \dot{Q}_{H,power} \cdot \eta_{power} \tag{5.37}$$

Additionally, a minimum power production of 2 $kW_{el}$, below which the turbine cannot work, is set so that if the calculated value of $\dot{W}_t$ is smaller than 2 kWel in a given hour, this value is set to zero.
Finally, the power consumption of the pump as well as power consumption of the auxiliaries and presences of intermediate HTF circuits are not considered.

### 5.6.3 Techno-economic evaluation

The techno-economic assessment of the application is based on the estimation of the equipment cost of components. The same correlations presented in **Table 5.2** are used for the estimation of components cost. Sizing of heat exchangers is performed as described in the previous chapter, while a nominal power of 9.5 kW is considered for the turbine. Resulting costs of components are presented in **Table 5.12**, where it can be noticed that the main cost items are represented by the turbine and electrical generator.

**Table 5.12** – Cost of components of the system.

| Component | Cost [€] |
|---|---|
| Absorber | 2,496 |
| Condenser | 3,523 |
| Desorber | 4,854 |
| Electric generator | 19,629 |
| Evaporator | 3,158 |
| Pump | 3,311 |
| Solution heat exchanger | 1,550 |
| Subcooler | 1,151 |
| Superheater | 305 |
| Turbine | 31,581 |

The cost of piping and circuits, including all valves and necessary tanks ($Z_{p\&t}$), is expressed as a function of the heat exchangers (HEX), turbine, electric generator and pump cost. This cost is given by [235]:

$$Z_{p\&t} = 0.1 \cdot (Z_{HEX} + Z_t + Z_{elec,gen} + Z_{p\&t}) \tag{5.38}$$

The cost of electrical equipment $Z_{elec}$, including the cost of electric/control panel, pressure switches and electronic expansion valves is also given as a function of the main components cost [235,236]:

$$Z_{ele} = 0.1 \cdot (Z_{HEX} + Z_t + Z_{elec,gen} + Z_{p\&t}) \tag{5.39}$$

Total equipment cost is calculated as the sum of all previous costs:

$$Z_{equip} = Z_{HEX} + Z_t + Z_{elec,gen} + Z_{p\&t} + Z_{p\&t} + Z_{ele} \tag{5.40}$$

The equipment cost calculated using **Eq.(5.40)** represents simply the cost of purchasing the different components. However, additional costs need to be considered, such as labour costs, engineering costs, overhead costs, installation costs etc. Commonly, a multiplication factor of 4.16 of equipment costs is used to take into account all of these costs [205,235], so that the cost of the project can be calculated as:

$$Cost_{proj} = 4.16 \cdot Z_{equip} \tag{5.41}$$

Finally, annual savings can be calculated as the electricity consumption reduction (due to the non-use of the vapour compression chiller), plus the value of the electricity produced by the turbine, minus operating and management costs:

$$E_s = Sv_{cooling} + Sv_t - Cost_{OM} \tag{5.42}$$

where $E_s$ are the net annual savings in €/year, operating and management costs are assumed equal to 2% of the total project cost and savings are calculated by multiplying the amount of electricity saved or produced by the electricity price. The electricity price considered is 0.216 €/kWh, i.e., the average wholesale reference price over the period considered. This is a conservative estimate, as both the actual price paid by the company (0.257 €/kWh) and the price at which self-produced, non-consumed electricity could be sold to the grid (0.23 €/kWh) are higher.

### *Techno-economic parameters*

Two parameters are used in this work to evaluate the economic interest of the proposed case study. The first is the discounted payback period (PBP), indicating the time required to earn the initial investment back. It is calculated using the following expression and a discount rate of 5% [235,237], typical for waste heat recovery projects:

$$PBP = \frac{ln\left(\frac{1}{1 - \frac{Cost_{proj}}{E_s}}\right)}{ln(1+r)} \tag{5.43}$$

The other evaluation parameter used is the net present value (NPV), reflecting the value created by investing in the project. All future cash flows are discounted using the same discount rate of 5% and the NPV is calculated as:

$$NPV = -Cost_{proj} + \sum_{t=0}^{n} \frac{E_s}{(1+r)^t} \tag{5.44}$$

Where n is the economic lifetime of the project (in years), here considered as 20 years, and t is the point in time. The simplified assumption of considering annual net savings constant through time is adopted here for the calculation of PBP and NPV.
Finally, it is interesting to also look at the LCOE (levelized cost of energy), representing the minimum electricity price needed for the system to achieve break even and calculated as:

$$LCOE = \frac{NPV\ (total\ costs\ over\ time)}{NPV\ (Energy\ savings)} = \frac{\sum_{t=0}^{n} \frac{Cost_{proj,t} + Cost_{OM,t}}{(1+r)^t}}{\sum_{t=0}^{n} \frac{E_{s,t}}{(1+r)^t}} \tag{5.45}$$

## 5.6.4 Techno-economic analysis results

The use of the combined absorption plant allows to save 72.5 MWh of electricity (corresponding to 89.4% of the electricity currently used to satisfy the cooling demand), with an additional 36.4 MWh of electricity produced by the turbine. Indeed, of the 1211 MWh of waste heat at 100 °C available, 43% (515 MWh) is used for the production of cooling, 54% (667 MWh) for the production of electricity and only 3% is then wasted (since it assumed that the turbine could not generate power below 2 $kW_{el}$).
Hence, it can be seen that the presence of the turbine more than doubles the heat recovery efficiency of the system with respect to the use of a simple absorption chiller, allowing recovering almost all the available waste heat.

However, given the high cost of the turbine, the investment cost is not recovered and the final NPV is negative and equal to -147 k€ (**Fig. 5.17**). The project can hence be divided into 2 subprojects, the first relative to the installation of the simple absorption chiller, and the second to the integration of a power production line (turbine, electrical generator, superheater and the relative piping and electrical components).
Calculation of the PBP for the simple absorption chiller reveals a payback time of 8.7 years and a positive NPV of 76 k€. On the other hand, the final NPV of the power production line is of -223 k€. Correspondingly, the LCOE of the simple absorption chiller process is 0.131 €/kWh, while for the power production line it is of 0.702 €/kWh.

Therefore, although interesting from a thermodynamic point of view, the project appears not economically feasible in current conditions, because of the extremely high cost of the turbine considered (resulting in a total cost of the power production line components of 62 k€). Concerning the cost of the turbine however, it should be noted that the correlation presented in **Table 5.2**, and used by several authors [167,220,221] for the estimation of ammonia turbines cost, was originally proposed by Rodriguez et al. [222] without a detailed explanation on how it was derived. Experience gained during the combined cycle development suggests that the cost calculated through such correlation is closer to the cost of an experimental prototype than to the possible cost of mass production.

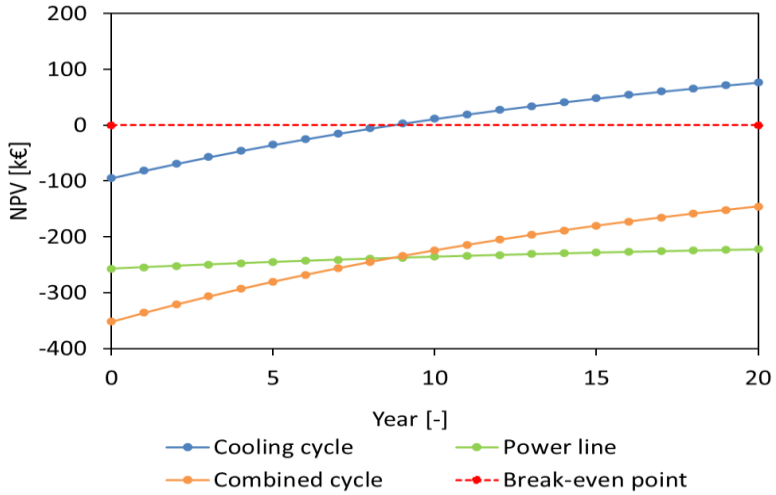


**Fig. 5.17** – NPV calculation using ammonia turbines cost correlation.

Other authors [8] used correlations relative to classical steam turbines also in the evaluation of ammonia turbines. In particular, a correlation often found in literature for the estimation of steam turbines cost is [238]:

$$\log(Z_t) = 2.6259 + 1.43981 \cdot \log(\dot{W}_t) - 0.1776 \cdot \left(\log(\dot{W}_t)\right)^2 \tag{5.46}$$

Usually, when this correlation is used, the cost of the electrical generator is considered included in the turbine cost. If this correlation is used, the resulting 9.5 kW turbine cost brought to the reference year (2021) using the chemical engineering plant cost index is of 8.9 k€, for a total cost of the power production line of 11 k€. Hence, this can be regarded as a reasonable long-term cost which could be reached if a diffusion of the technology would take place. It should be noted that this cost and cost calculated using the ammonia turbine correlation presented in **Table 5.2** (62 kW), simply account for the cost of the power line components. However, these costs result in much higher project cost increase (through **Eq. (5.41)**) and in increased O&M costs.
In the case of turbine costs similar to those of classical steam turbines, the economic interest of the project is greatly increased. Indeed, the PBP of the absorption chiller subproject remains of 8.7 years, while the one of the power production line is of 8.2 years, bringing the overall PBP of the project down to 8.5 years. Additionally, the final NPV of the power production line is of 40.5 k€, which summed to the 76.5 k€ of the absorption chiller subproject brings the overall NPV of the project up to 117 k€ (+52%). Indeed, the LCOE of the power production line in this case is of 0.125 €/kWh.

A parametric analysis of the NPV of the overall project as function of the electricity price and the cost of the power line cost is presented in **Fig. 5.18**. In general, for electricity prices below 0.15 €/kWh the project is not interesting from a purely economic point of view even in when using steam turbines correlation costs (total power production line cost of 11 k€). On the other hand, when considering ammonia turbines cost correlations (total power production line cost of 62 k€), an electricity price of 0.45€/kWh is needed for the project to be profitable.

Finally, a comparison of the simple absorption chiller subproject and combined cycle project is also shown in **Fig. 5.18**. In the considered conditions, the recovery of heat for cooling production through the ammonia-water absorption chiller is profitable for electricity prices above 0.15 €/kWh. Additionally the simple absorption chiller subproject is more interesting than the combined cycle project for high costs of the power production line and low electricity prices.

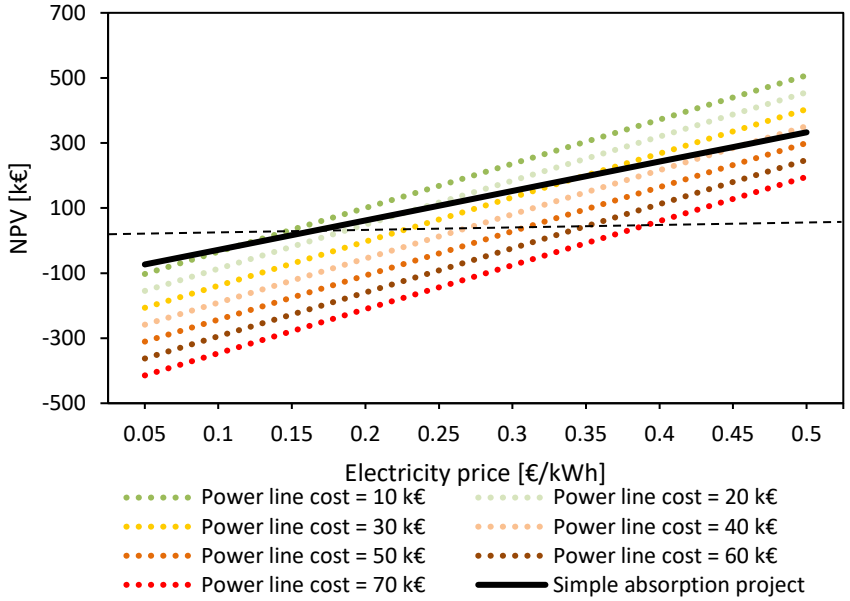


**Fig. 5.18 –** NPV of the overall project for different power line costs (dotted lines) and of the simple absorption project (bold line).

### 5.6.5 Case study synthesis

The economic evaluation of the use of the absorption combined cooling and power cycle was carried out in this section. The case study chosen is that of an agricultural company, which needs cooling all year round and owns a biogas engine whose waste heat is not recovered. The available waste heat temperature is 100 °C and cooling is needed at 10 °C. The available thermal power was measured in 15-minutes steps, but since cooling demand was not explicitly known, it was deduced using correlations developed as a function of ambient temperature and solar irradiation.
The dimensioning of the system for the calculation of component costs was done using the numerical models developed, in the hypothesis of using all the available waste heat and meeting peak cooling demand. On the other hand, for the calculation of energy savings, it was pursued a simplified approach based on the use of performance correlations deduced from numerical models.

The use of the combined cycle allows to save 72.5 MWh of electricity each year (corresponding to 89% of the current electricity consumption to satisfy cooling needs) as well as to obtain and additional electricity production of 36.4 MWh. However, the use of ammonia turbine cost correlations from literature leads to very high costs of the power production line of the cycle, making the project unprofitable for electricity prices below 0.45 €/kWh.
On the other hand, if the cost of ammonia turbines approaches the cost of standard steam turbines, the project can be profitable already for electricity prices above 0.15 €/kWh.

## 5.7 Synthesis of the cycle performance simulation

To properly evaluate the combined cooling and electrical power production efficiency, an exergy and exergoeconomic approach was pursued, leading to the definition of an overall exergetic efficiency along with cost per unity of exergy of the products. First, simulation of the pilot plant functioning was carried out, to study the effect of a variation of the temperature of the sources.

Subsequently, a baseline condition, representing a typical industrial refrigeration application, was defined to assess the interest of such cycle. For the turbine, the optimisation of the injector exit section was considered to avoid shock phenomena between stator and rotor, and scale-up up to full admission was carried out. For the heat exchangers, the corresponding scale-up was performed by increasing exchange areas, and then an optimisation allowed minimizing the unit cost of exergy of the products.
Increasing the plant size 25 times lead to the possibility to use a full admission turbine, producing around 90 kW of cooling at around 7 °C and about 9 kW of electricity reaching, and exergetic efficiency of 23%.
Limitations to the flexibility of the cycle imposed by the supersonic turbine lead to the proposal of an alternative cycle architecture. This layout uses an ejector between the cooling and power production lines, increasing the flexibility of the system.
The modelling approach developed based on the use of effectiveness for heat exchangers and 1D loss models for the turbines allowed an in-depth investigation of the cycle, proving the possibility of producing both outputs within the same cycle and of switching between different production modes.
Finally, a preliminary techno-economic analysis on a real-life case showed the interest of the cycle to optimise heat recovery efficiency, but highlighted that the effective economic interest needs to be evaluated based on the cost of the turbine and comparing the cost of the products with their market value.

# Chapter 6
# Conclusions and perspectives

*This chapter is dedicated to a summary of the main achievements of the present work. The most relevant conclusions, coming both from experimental and numerical studies are presented and detailed. Finally, proposals for the pursuit of the work are put forward and perspectives concerning the diffusion and development of the absorption combined cooling and power production technology are discussed.*

# 6.1 Conclusions

Absorption-based combined cooling and power production cycles are a very interesting solution to respond to the increasing cooling demand and overcome the issues related to the strong fluctuations characterising it and limiting the diffusion of absorption cycles due to their possibly low utilization rate. In addition to a more effective use of the heat source, these systems can lead to increased conversion efficiency (avoiding the use of multiple energy vectors and cascade transformations), as well as the mutualisation of components for vapour generation, condensation, pumping, etc, within the cycle.
In this context, the focus of this thesis is the development and investigation of an absorption-based cooling and power cycle using low-temperature heat.
The novelty of the work lies in the fact that an impulse micro-axial turbine was integrated into an ammonia-water absorption chiller plant. Feedback and experimental data from the pilot plant, as well as detailed analysis of the components, allowed access to accurate data concerning components performance and cost, serving as a base for the development of detailed numerical models. In particular, a 0D model of the absorption chiller based on experimental data, and a 1D model based on CFD simulations results were developed. These models were then used to perform an energy, exergy and economic assessment of the cycle.

Regarding the absorption chiller, data from previous experimental campaigns were considered and critically analysed along with new data gathered during this work in similar operating conditions. This allowed characterising and understanding of the functioning of the pilot plant and its components, leading to the following main considerations:

- Particular attention must be paid to reach steady operation of the pilot plant, all variables of interest must be constant (below a certain variation threshold).
- Crucial for plant stabilization are the reservoir level regulation and actuated valve opening (i.e., throttling valves upstream the absorber and evaporator).
- Experimental data analysis requires checking of energy balances on each component. In the present work, operating conditions characterised by errors higher than 5% were discarded.
- The combined desorber integrated in the pilot plant, in addition to avoiding the use of a separated rectifier, simplifies the plant management compared to the use of a classical boiling heat exchanger architecture. Indeed, steady state conditions are reached more quickly and the higher component efficiency leads to increased COP of the cycle.
- Partial flooding of the desorber can occur leading to reduced efficiency of the component affecting the overall cycle performance.
- Experimental results on the pilot plant are in accordance with theoretical analysis on single stage absorption chillers.
- Despite the small scale, a thermal COP higher than 0.7 was reached in the investigated operating conditions.

The development of the axial turbine prototype was undertaken out together with the turbine manufacturer facing several problems related to the small size of the application, ammonia related corrosion and mechanical resistance for which workable solutions were found. Testing of the single-injector impulse axial micro-turbine was carried out both inside the experimental loop (using ammonia) and outside the loop, using air, nitrogen and argon.

- Due to the ratio between the injector exit and throat section, the turbine was in choking conditions in all the points tested. Therefore, the linear dependency reported between the turbine inlet pressure and treated mass flow rate is in accordance with theory.
- The consideration of the real-gas behaviour is relevant for the turbine mass flow rate calculation for ammonia, while it is negligible for the other tested gases.
- The overall electrical efficiency and power production are strongly correlated to the pressure drop through the turbine and its rotational speed for all fluids tested.
- Because of the small scale of the turbine, and significant losses of the electricity generation components, the maximum electrical efficiency achieved was of 7% and the corresponding optimal rotational speed, 20,000 rpm significantly lower than the expected theoretical value of 50-75,000 rpm.
- Limited influence of the turbine inlet temperature on the overall electrical efficiency was found for the conditions tested.

The integration of the micro-turbine into the single-stage absorption chiller was analysed through an experimental campaign. Tests were conducted only around the nominal operating point of the absorption chiller. Dynamic switching between the three possible operating modes (i.e., cooling, combined cooling and power and only power production in a Kalina cycle configuration) was tested.

- The lack of possibility to regulate the mass flow rate treated by the turbine imposes strict limits on the cooling production of the bench.
- The reduced mass flow rate passing through the cooling line heat exchangers (condenser and evaporator) increases their efficiency, affecting the pressure equilibrium established within the cycle and the circulating vapour mass flow rate.
- Operating mode switching proved to be stable and quick to reach steady state, provided that the starting point was already stable.

Numerical models were developed for the absorption chiller cycle alone and for the single injector micro-turbine and finally the two models were integrated to simulate the combined cycle.
Concerning the absorption chiller modelling, a zero-dimensional steady-state representation of the components was used, considering a fix isentropic efficiency of the pump, isenthalpic throttling in the valves and neglecting thermal and pressure losses outside the main components. For the heat exchangers (i.e., absorber, desorber, condenser, evaporator, solution heat exchanger and subcooler), first a simplified approach based on fix temperature pinches was implemented and tested. Subsequently, a second approach was pursued based on the characterisation of heat exchangers through semi-empirical effectiveness, modelled using three dimensionless parameters (*NTU*, *Ja* and $R_{en}$). The main results of this stage of the work are summarized in the following:

- The approach based on fix temperature pinches is not able to predict the performance of the cycle in operating conditions different from those used for the tuning of the model parameters.
- In particular, the fix temperature pinches model is incapable of predicting the dependency of the chiller performance on the rich solution mass flow rate and misrepresents the correlation between the COP and intermediate and cold source temperatures.
- The model based on semi-empirical correlations describing exchangers effectiveness allows representing all the variations in all operating conditions considered, although it needed to be tuned on the same extended set of experimental data.
- The effectiveness model showed a maximum error below 6% for the COP and 15% for the cooling power output.
- The effectiveness model gives insights on the influence of the exchangers' area on the overall performance variations with reliable quantitative estimations.

A 1D loss model was developed for the turbine accounting for non-ideal behaviour of the working fluid by means of fluids state properties libraries. The proposed model includes a description of the expansion occurring in the supersonic injector and contains the most relevant loss terms to take into account partial admission and the small scale of the turbine. Due to unavailability of detailed data regarding the turbine power production, unsteady CFD simulation of the entire turbine was undertaken to characterise the expander and tune 1D loss model parameters. Operating conditions tested reproduce working pressures and temperatures in the range encountered in the combined cycle. Thus, the expansion ratio varies between 0.36-0.5, inlet temperature is fixed to 120 °C. Additionally, rotational speed of the turbine was varied between 10-100,000 rpm.

- The supersonic injector strongly influences the performance of the turbine due to the relationship between inlet pressure and mass flow rate and the presence of non-isentropic recompression phenomena (i.e., shocks) in the divergent section or at the outlet of the nozzle.
- Comparison to CFD results lead to the inclusion of a minimum number of loss terms necessaries for the 1D model to predict the performance of the turbine, namely passage, friction, partial admission and leaking.
- Loss terms are highly dependent on the rotational speed of the turbine and partial admission and leaking losses appear to be the most influential on the turbine performance.
- An average discrepancy below 7% was obtained between the 1D and the CFD models power output, demonstrating that the selected loss terms are well tuned for the application.
- The optimal rotational speed depends on operating conditions and increases for increasing inlet pressure up to around 55,000 rpm for an inlet at 14 atm where power production is 360 W.
- Extremely low partial admission ratios, like the case of a single injector, are highly penalising for the turbine efficiency, which in a reference case passes from 34% to 56% in the case of full admission. However, turbine efficiency appears acceptable (50%) already for ε higher than 0.2, corresponding to 5 injectors.
- Experimental tests on the turbine allowed the validation of the injector modelling with different fluids, with discrepancies between measured and modelled mass flow rates below 6%.

The developed turbine 1D model was integrated in the absorption chiller model, thus allowing the study of the absorption-based combined cycle in variable operation conditions and for different heat exchangers areas. To properly evaluate the combined cooling and electrical power production efficiency, an exergy and exergoeconomic approach was pursued, leading to the definition of an overall exergetic efficiency, along with cost per unity of exergy of the products. First, simulation of the pilot plant functioning was carried out. Subsequently, a baseline condition, representing a typical industrial refrigeration application, was defined to assess the interest of such cycle. For the turbine, the optimisation of the injector exit section was considered to avoid shock phenomena between the stator and the rotor, and scale-up up to full admission was carried out. For the heat exchangers, the corresponding scale-up was performed by increasing exchange areas, and then, an optimisation changing heat exchangers area allowed minimizing the unit cost of exergy of the products.

- Parametric studies highlighted that a variation of the temperature of the source is likely to have opposite effect on cooling and mechanical power production, demonstrating the necessity to use second principle performance parameters.
- The supersonic turbine does not allow varying the vapour split ratio between the cooling and electricity production lines, representing a strict limitation for flexibility of the base cycle architecture.
- A throttling process upstream the turbine, is effective on reducing the turbine mass flow rate, but a dramatic drop of the mechanical power production makes this type of regulation limitedly suitable for this application.
- The small size of the pilot plant proves to be very penalizing for the UCOPE, in particular because of the very high cost of the partial-admission turbine.
- Increasing the plant size 25 times leads to a full admission turbine and a scale of industrial interest. For the base case this corresponds to the production of 90 kW of cooling at around 7 °C and about 9 kW of electricity reaching an exergetic efficiency of 23%.
- For negligible cost of the fuel (i.e., thermal input) the heat exchangers area optimisation leads to an UCOPE of 28.31 \$/GJ, a unit cost of cooling $c_{cooling}$ of 10.14 \$/GJ and a cost of electricity $c_{ele}$ of 40.45 \$/GJ.
- When the cost of fuel is 15 \$/GJ instead, the optimal UCOPE is 90.24 \$/GJ, $c_{cooling}$ 66.7 \$/GJ and $c_{ele}$ is 106.8 \$/GJ.
- In both cases, the optimisation leads to an increased absorber and desorber area, increasing the circulating mass flow rate (and hence the cooling production).
- The higher cost per unit of electricity production compared to exergy of cooling seems to favour the production of cooling.
- A preliminary techno-economic assessment of the use of the technology in a waste-heat recovery case study showed that a minimum cost of electricity of 0.15 €/kWh and important reductions of the cost of the turbine are needed.

The limited regulations possibility experienced on the combined cycle during tests and confirmed by numerical simulations, is recognised a limitation to the applicability of the technology. Thus, an alternative architecture with an ejector connecting the cooling and power production lines was proposed to widen the operability of the plant and was proven to represent a promising solution. In principle, the choice of a parallel architecture was intended at separating cooling and power production, guaranteeing the independence of the two sub-cycles. However, the study made apparent that two production lines exert a strong influence on each other since the turbine by-pass has effects on all the heat exchangers. The proposed use of the ejector is a very interesting solution in this respect, as it is found that an increase in flexibility can be achieved with a more intimate connection of the two production lines through the use of a device such as the ejector, which allows the mass flow rate treated by the turbine to be more effectively regulated.

In conclusion, the modelling approach developed based on the use of effectiveness for heat exchangers and 1D loss models for the turbines proved to be effective for the in-depth investigation of this type of cycles.
Overall, the use of an axial turbine appears to be a suitable choice for this kind of application, provided that reasonable (above 0.2) and adjustable partial admission ratios are used.
Finally, the possibility of producing both outputs within the same cycle has been proved, with the possibility of switching between cooling and power productions by alternative architectures, but the effective economic interest needs to be evaluated comparing the cost of the products with their market value.
Indeed, the assessment of the use of the combined cycle in a real industrial application highlighted that this technology can greatly increase heat recovery efficiency of absorption cycles, but economic profitability strongly depends on the cost of electricity and on the cost of components. Nevertheless, the cycle proved to have a strong potential and to represent an interesting solution, particularly in the current context of the energy crisis and climate change.

## 6.2 Perspectives

Concerning the **experimental study**, a more in-depth discussion is required regarding the investigation of the combined cycle at the pilot plant scale, particularly with respect to the expander. In fact, it was shown that information gathered on the absorption chiller prototype are not substantially altered by a scale-up of the technology. On the contrary, conclusions drawn from this work suggest that the same extrapolation procedure is hardly feasible and, moreover, less meaningful in the case of the expander. As proof of this, the chiller COPs are in line with that of the ammonia-water absorption technology even at bigger scales, while turbine efficiencies are not compatible with the very small size, having achieved efficiencies of up to 7%, against expected values of at least 30%-35%.
With regards to operational difficulties, tests carried out on the axial micro-turbine and subsequent analyses highlighted that such a small scale turbine suffers from severe limitations. These arise already from the expander architecture needed to make it feasible: in this specific case the single injector, leading to extreme partial admission ratio is required not by the cycle itself, but by the need to limit the turbine's rotational speed. Furthermore, at this scale, phenomena which are of secondary importance at scales of industrial interest, become prevalent and make it extremely difficult to quantitatively assess the most important loss terms and reliably estimate performance. This aspect was also shown in a previous study with reference to the use of a Scroll expander [33], considered for use on the same experimental rig, and discarded since numerical models showed that the effect of volumetric efficiency alone was sufficient to cancel out the mechanical power production.
These considerations explain how testing at this scale is complex and requires **detailed measurements** allowing the separate evaluation of all the different effects, including mechanical and electricity generation losses. This was clearly highlighted when testing the micro turbine for which an overall mechanical and electrical efficiency comprised between 0.1-0.25 was estimated. This may be partly due also to the titanium casing added as a to protect the electrical generator from corrosion caused by ammonia, and which is thought to have degraded the performance of the component. However, this low efficiency is also explainable by the fact that electric generators capable of operating at these rotational speeds with reasonable efficiencies have not benefited from the development resulting from existing applications on this scale (e.g. small turbines for ORC in automotive application).
In addition to these operational difficulties, it should be noted that an appropriate choice of the expander technology is intimately related to the scale of the application, as explained in the expander selection process description.
A suitable alternative to overcome these difficulties is to use a throttling valve along with a heat exchanger simulating the expander, and separately test the expander of interest for the application on a minimum scale significant for the technology, and not limited by the constraint of the pilot plant size.
A last note regarding the expander testing is related to the necessity to solve issues experienced when using ammonia as a working fluid, **ranging from condensation to corrosion and mechanical failures**.

Furthermore, although this work did not focus on the combined desorber design and operation, it was possible to evaluate its characteristics and potential through experimental tests and comparison with previous campaigns. Though it proved to represent a significant improvement with respect to the previous architecture, it is worth mentioning the challenges linked to its use, and in particular its tendency to partial flooding, which causes a degradation in performance, and deserves further investigation. With respect to this aspect, a redesign of the component is currently ongoing, in order to make the component more easily manageable and eliminate these issues. Finally, to be able to extend and deepen the experimental analysis on the combined cycle, a required change on the pilot plant would be to increase the capacity of the external HTF circuits to match the higher thermal powers exchanged with the sources (compared to a simple absorption chiller) brought into play by the presence of the turbine in the cycle. Indeed, only tests around the nominal working point could be conducted due to limitations in the maximum exchangeable power of current HTF external circuits.

Regarding the **numerical investigation**, the specificity of the application and the peculiar characteristics of some components, which needed the development of tailored models, would require the validation of the numerical models with respect to their extrapolation to different scales to make them suitable for accurate quantitative analyses. For example, in the case of the turbine, the effect of passing from extremely low to full admission ratios requires in-depth analysis of individual loss phenomena as well as comparison to experimental tests. This is even more important if the variation of the partial admission ratio is considered as a means of regulation between cooling and electricity production. From the point of view of physical phenomena, it was not possible to carry out a detailed investigation of the **possible condensation** taking place during the expansion, which is likely to be relevant with the ammonia-water mixture. This phenomenon is difficult to detect and the test rig used was not equipped with adequate measurement instrumentation for this purpose.

In light of all of the above, and given the inherent difficulties even at larger scales due to the complexity of measurements and high costs of test campaigns, a useful tool to be implemented as a bridge between semi-empirical 0D and 1D models and experiments can be computational thermo-fluid dynamics modelling and simulation. This tool was already used in this work to overcome the described difficulties coming from the micro turbine testing. Moreover, CFD represents an extremely powerful instrument to get insights into highly complex 3D phenomena, like those related to shock/expansion waves interactions and secondary flows.
Additionally, in cases where an optimisation of the geometry and simulation under very different operating conditions is needed, CFD can be very useful. In the case of the combined cycle, in addition to the study of the turbine (where CFD analysis can be used more extensively and at different scales), it would also be useful to use **CFD for other components** (in particular for heat exchangers such as the desorber and absorber), and to study the functioning and design of ejectors, components that are particularly sensitive to variations of operating conditions.
Another approach to be pursued is the development of detailed physical models of components (particularly of the absorber and desorber), which could be very useful for the tuning of the developed effectiveness model moving to larger scales or different exchanger technologies. This approach is currently under investigation.

Concerning the **positioning of the technology**, the results of the exergetic, exergoeconomic and techno-economic analysis, although preliminary and based on the small-scale pilot plant, showed that an absorption-based combined cooling and power production cycle can be useful for exploiting low-temperature sources at a cost competitive with other technologies.
The same study also highlighted technical difficulties in the handling of some equipment, and in particular of the turbine design, as discussed earlier. Here, however, it is useful to emphasise that it is necessary to **obtain accurate cost estimates associated to this technology, and in particular with the use of the ammonia-water mixture**.
In fact, the technical difficulties and uncertainties pointed out already entail a potential increase in operating costs, which must be managed through specific long-term tests or at least through an increase in the incidence of contingencies. Among the issues yet to be resolved, those considered most critical and therefore worthy of further study are the costs related to the management of the turbine in a wide operating range, necessary to give flexibility to the cycle, and the management of the most innovative components like the desorber, and the most critical like the absorber.
An impact in terms of costs must also be expected because of the management of ammonia, a working fluid requiring particular attention and having a very specific regulations, and whose compatibility with components designed for other fluids can lead to a reduced lifetime.
Once these issues are resolved, it will be possible to better define possible applications, on which the design and control of the system has to be optimised in order to estimate in a more meaningful way the advantages (economic, emissions reduction, etc.) compared to other more established technologies.

# Chapter 7
# Appendixes

*This last part of this thesis provides additional details and further information concerning some parts of the study. In particular, the first appendix is dedicated to a novel mass-flow rate maximisation ejector model, validated on experimental data from literature and capable of predicted on-design and off-design ejector performance. The second appendix presents a simplified ejector model only capable of predicting on-design performance of the ejector, which was integrated in the combined absorption cooling and power production cycle for the evaluation of the novel architecture. The third appendix gives more details on the calculation of the NTU and Jakob numbers. Comparison between experimental measurements and 1D model results concerning the turbine power production is presented in shown in the fourth appendix. Finally, the last appendix includes state properties and cost tables relative to the exergoeconomic study.*

# 7.1 Mass flow rate maximisation overall modes ejector model

The analysis of the combined carried out in *Section 5.4* highlighted the strict limits imposed to the cycle by the turbine. For this reason, a novel architecture integrating an ejector was proposed in *Section 5.5*. In order to better evaluation of this solution, an in-depth analysis of the functioning of ejectors was undertaken.
Hence, the thermodynamic model and simulation of supersonic real-gas ejectors used in refrigeration systems is presented in this section. Ejector refrigeration cycles offer an alternative to traditional systems for the production of cooling using low temperature heat. The model presented is based on mass flow rate maximisation. Hence, it has the advantage of simplifying the calculation algorithm and avoiding a complex description of the double choking mechanism taking place within the ejector. First, the model hypothesis and calculation algorithm are presented. The impact of each efficiency is evaluated and a tuning procedure is developed to calibrate the model on experimental data. Validation is performed on multiple datasets relative to two different fluids: R600a and R134a. The ejector model is then used to simulate a SERS (single ejector refrigeration system) cycle, to validate its robustness and capability to be used in the prediction of thermodynamic cycles performance. A comparative analysis of different fluids is carried out on the SERS, highlighting the important role played by the choice of the superheating. Finally, the model is used to predict performance in the case of a two-phase primary flow pointing out the limits of the model and the need of further experimental studies for the inclusion of appropriate semi-empirical corrections.

## 7.1.1 Introduction

Among the most studied low-grade heat driven refrigeration cycles, i.e. absorption cycles [118], adsorption cycles [131] and ejector cycles [126] presented in *Section 2*, ejector cycles are getting increasing attention.

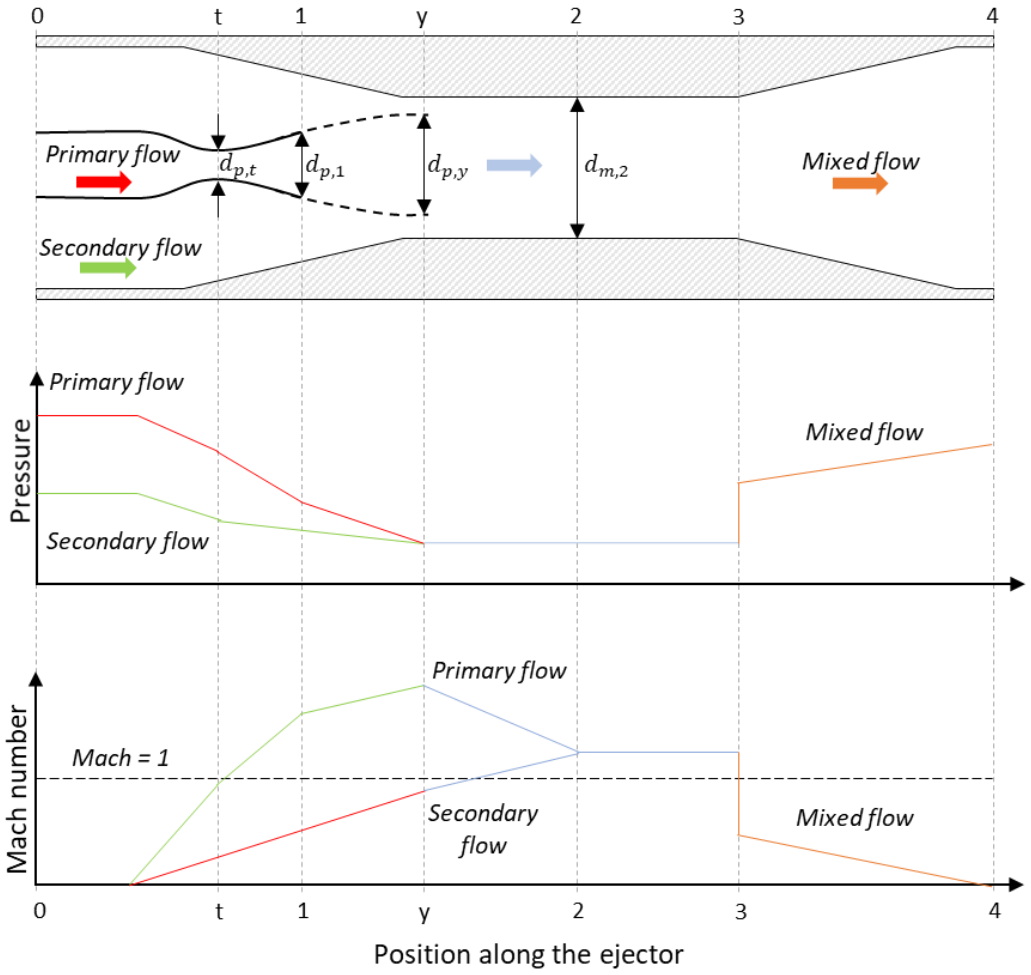


**Fig. 7.1** - Schematic diagram of the ejector geometry and corresponding pressure and velocity profiles.

The fundamental working principle of an ejector is to use a high-pressure flow (referred to as primary flow) to entrain and compress a low-pressure flow (referred to as secondary flow). The high-pressure primary flow enters a usually converging-diverging (though sometimes converging-only) primary nozzle inside of which it undergoes an expansion to high velocity and low pressure. The now low-pressure and high velocity primary flow is used to entrain the secondary flow from the suction chamber into the mixing chamber. In the mixing chamber, the two flows mix, and the high-speed mixed flow is decelerated in a diffuser, where it recovers pressure before leaving the ejector. The pressure of the mixed flow leaving the ejector is usually referred to as the ejector backpressure $P_c$. A more detailed description of the ejector working principle is presented in the following. In particular, **Fig. 7.1** shows a typical ejector geometry and the velocity and pressure profiles along the ejector, giving a visual representation of the thermodynamic transformations undergone by the flow during its passage in the component.

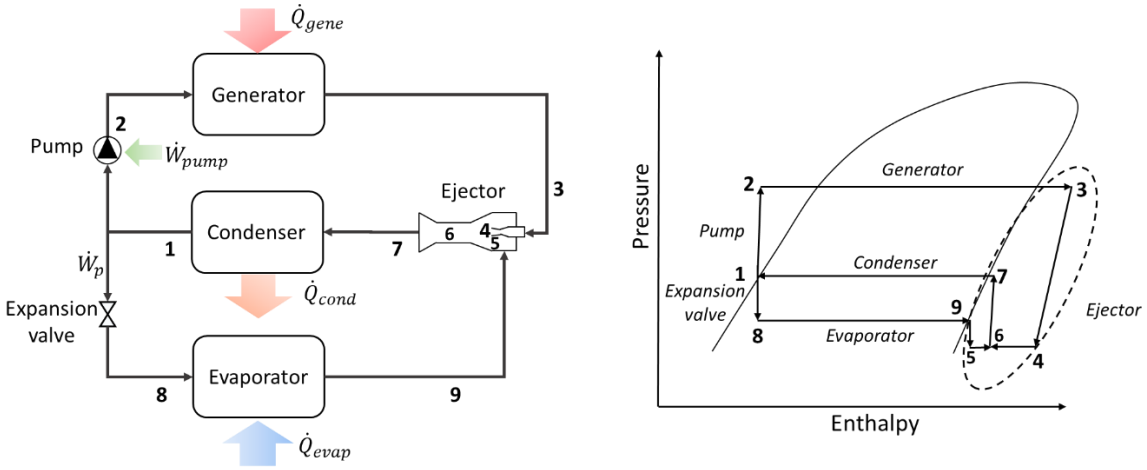


**Fig. 7.2 -** Standard ejector refrigeration cycle (SERS) schematic diagram and corresponding pressure-enthalpy diagram.

Ejectors can be used in various low-grade heat refrigeration cycles [124]. The most basic design of such cycle is the standard SERS (single ejector refrigeration system) previously presented in *Section 2.4.1* and shown on **Fig. 7.2**. In this cycle, the ejector is combined with three heat exchangers (condenser, evaporator and generator), a pump and an expansion valve. Low-grade heat allows the production of high-pressure primary vapour in the generator used to entrain the low-pressure secondary vapour leaving the evaporator. This cycle is the most commonly described and studied ejector cycle in literature because of its simplicity [124].Indeed, a large number of experimental and theoretical studies have been performed on this cycle [124,126], and their results used to improve ejector design and validate numerical models. In light of the above, the SERS is considered in this study for the validation of the developed ejector model and as a base for performance evaluation.

Since they have no moving parts, ejectors are very robust, reliable and are characterized by a very simple geometry involving low-maintenance and low costs. However, one of the main barriers to a widespread usage of ejector in refrigeration cycles resides precisely in their relatively narrow range of use due to the absence of control moving parts. When operating outside of their design conditions, ejectors suffer significant performance reductions and might even stop working. Thus, being able to predict ejectors performance in both on-design and off-design conditions is of paramount importance to develop thermodynamic cycles and devise appropriate control strategies. This is confirmed by the increasing number of studies that are currently being carried out with focus on the improvement of ejector models [239,240].

Different types of model are used to describe ejectors operation such as CFD models ([240,241]) zero-dimensional [242] and one-dimensional [243] empirical or semi-empirical models ([244,245]). As highlighted by He et al. [246] and Elbel et al. [126], steady-state zero-dimensional and one-dimensional models are the most studied and used type of ejector models. Indeed, the nature of flows inside ejectors being very complex (turbulent mixing, presence of shocks, condensation, two-phase flow phenomena, etc.), even more detailed models fail to precisely capture the flow patterns inside ejectors. There are two major types of steady state ejector models: single-phase (vapour) or two-phase ejector models. Single-phase ejector models are the most commonly used for refrigeration cycles, as single-phase ejectors are used in many ejector cycles, including the SERS cycle. Two-phase ejectors are used in other ejector refrigeration cycles such as transcritical ejector cycles or recirculation cycles [126]. The present model focuses on steady-state single-phase ejector thermodynamic model.

This type of model is based on the calculation of the thermodynamic state of the fluid in different sections of the ejector using mass, momentum and energy conservation equations. The first single-phase model was introduced by Keenan et al. [247] and later improved by the same authors [248]. Two types of ejectors were analysed and modelled: constant-area mixing and constant-pressure mixing ejectors. Although models for constant-area ejectors appeared to be more accurate, it was shown that constant-pressure mixing ejectors had better performance than constant-area mixing ejectors. Thus, starting from 1950, several studies focused on constant-pressure mixing ejector modelling [249,250]. Based on Keenan et al. constant-pressure mixing model [248], Munday et al. introduced the idea that primary and secondary fluid do not mix directly at the exit of the primary nozzle, but rather only start mixing at a section located further in the ejector (section y in **Fig. 7.1**). This model first postulated the idea of a hypothetical throat, formed by the primary flow and the ejector wall, where the secondary flow reaches chocking conditions. This theory was related to previous experimental results [251] showing chocked secondary flow patterns. This double-choking regime, also referred to as Fabri-choking, constitutes the foundation of the majority of most recent ejector models. Eames et al. [252] introduced isentropic efficiency coefficients to take into account the irreversibilities due to friction losses. Huang et al. [253] included the idea of efficiency coefficients proposed by Eames et al. [252] inside the double-choking model developed by Munday et al. [254], supposing that the hypothetical throat is located inside the constant area duct. Experimental studies [255] and [256] have shown that ejectors have different working modes, depending on the inlet and outlet conditions. The most important indication of ejector performance is the entrainment ratio ω defined as the ratio of the motor primary flow to the entrained secondary flow:

$$\omega = \frac{\dot{m}_p}{\dot{m}_s} \tag{7.1}$$

Results varying the ejector backpressure for fixed inlet conditions show that the entrainment ratio remains constant when increasing the backpressure until a critical backpressure $P_{cri}$is reached. The working mode with a constant entrainment ratio (i.e., for $P_c < P_{cri}$) is known as the on-design or critical working mode. This working mode corresponds to the presence of a double-choking as described by [253]. For $P_c > P_{cri}$ the ejector enters a working mode in which the entrainment ratio rapidly decreases when increasing the ejector backpressure. This working mode, known as the off-design or subcritical working mode, corresponds to the case in which only the primary flow is choked (also known as single-choking). Finally, if the backpressure of the ejector is further increased, the ejector starts malfunctioning and reverse flow phenomena can be observed. **Fig. 7.3** shows a typical characteristic curve of an ejector entrainment ratio as a function of the backpressure.

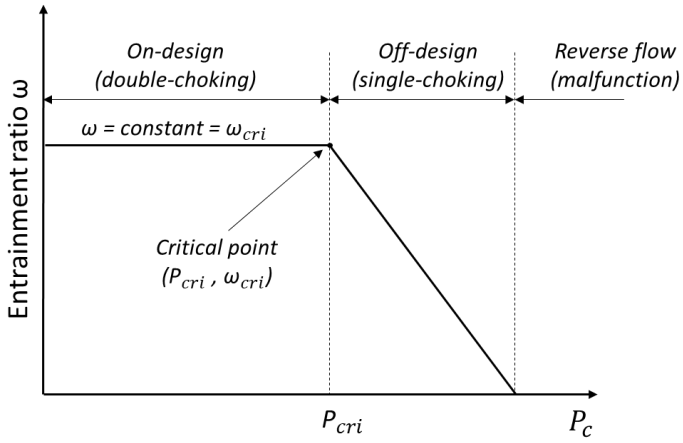


**Fig. 7.3 -** Schematic view of ejector operational modes.

The model proposed by Huang et al. [253] was able to describe the performance of the ejector in on-design working mode, but did not describe the off-design behaviour. Based on [253], Chen et al. developed the first model that could predict the performance of the ejector in both on- and off-designs working mode formulating the mixing efficiency in off-design working mode as a linear function of the back pressure. This model, based on the ideal gas assumption, was later adapted by the same authors to take into account real-gas behaviour [257]. More recently, Metsue et al. [258] developed a real gas thermodynamic model, modifying the model of Chen et al. [257] to integrate the compound-choking theory, proposed by Bernstein et al. [259] and by Lamberts et al. [260] for perfect-gas ejectors. While in the Fabri-choking theory the secondary flow is assumed to reach sonic conditions in a

hypothetical throat, the compound-choking theory postulates that a nozzle flow with two streams characterised by two different total pressures, can be in choking conditions with one of the streams being subsonic, if the other one is supersonic. Hence, since the combinations of two streams may behave as a sonic stream, while the Fabri-choking theory only takes into account the secondary stream, both streams are considered when analysing the choking process in the compound-choking theory [261]. This is supported by experimental [261] and numerical [262,263] studies, showing that the choking mechanism taking place does not necessarily coincides with the Fabri-choking theory since the secondary stream can remain subsonic. Metsue et al. [258] also performed an analytical study on the compound-choking criteria applied to non-isentropic perfect gas ejector showing that the use of this criterion is equivalent to maximizing the total mass flow rate within the ejector. The model presented by Metsue et al. [258] is arguably one of the most detailed steady-state thermodynamic single-phase ejector model developed to date. The compound-choking theory appears to yield more accurate results than the Fabri-chocking theory but has however some limitations that will be further discussed in Section 2. The present model is based on the works Chen et al. [257] and Metsue et al [258], with the difference that mass flow-rate maximization is directly applied instead of using a specific double-choking criterion (Fabri-choking or compound choking). This avoids the use of a more complex description of the on-design double-choking phenomena and simplifies considerably the calculation algorithm. Finally, using the mass flow rate maximization eliminates the spurious overshoot around $P_{cri}$, described in *Section 7.1.2*, present in most other models.

### 7.1.2 Ejector model

This study presents an updated thermodynamic real-gas model for supersonic ejectors capable of predicting performance in both the critical and sub-critical regimes.
Metsue et al. [258] observed that both the Fabri and the compound-chocking criterion (as defined by Croquer et al. [264]) do not maximise the entrainment ratio (and thus the total mass flow rate) in the case of non isentropic flows. As explained by Croquer et al. [264], since these criteria are obtained with the hypothesis of isentropic flow, when losses are introduced through isentropic efficiencies, they are not rigorously correct and accurate anymore. Therefore, characteristic curves obtained with these models are spoiled by the presence of spurious overshoots in the near-critical off-design part of the curve, where the entrainment ratio is higher than in the on-design working mode. This behaviour, not present in experimental tests, is in contradiction with the double-choking theory, starting point of such models. Indeed, the primary definition of a choked flow is constituted by the mass flow rate maximization and therefore, entrainment ratio and total mass flow rate cannot be higher than in the critical chocked point. It is worth mentioning that, when using such models for ejector design, the accurate prediction of the maximum mass flow rate and pressure is of paramount importance to guarantee good performance. Hence, Metsue et al. [258] proposed a corrected expression for the compound choking criteria generalised to the case of non-isentropic perfect gas flow. The authors showed that the application of this criterion is equivalent to mass flow rate maximization of the flow within the ejector, thus proving the choking mechanism at play in supersonic ejectors is indeed the compound-choking. Since the two criteria lead to the same results it is possible to use mass flow rate maximization when dealing with non-isentropic flows. Metsue et al. [258] solved the primary flow by maximizing the mass flow rate instead of imposing Mach equal to unity, but did not present a calculation procedure for the maximization of the total mass flow rate. Instead, the algorithm presented used the compound choking theory [258]. In the present work, both the primary flow and the total ejector mass flow rate are found by imposing the maximization of mass flow rate. To do so, the off-design mass flow rate characteristic of the ejector is calculated and its maximum taken as the critical mass flow rate. The aim of this approach is to simplify the calculation algorithm and to avoid a complex description of the double-choking mechanism at play. The validation of this model on experimental results available in literature, shows its capability to predict very accurately the critical conditions of the ejector ($P_{cri}, \omega_{cri}$). This makes the model a very valuable tool, not only for simulation of thermodynamic cycles, but also for ejector preliminary design.

#### *Model hypothesis*

The ejector geometry used in this study is presented on **Fig. 7.1**. It is the constant pressure geometry considered by Munday et al. [254] and Huang et al. [253]. The presented schematization of the flows within the ejector is the one based on the double-choking theory. The primary flow enters the converging part of the primary nozzle at section 0 and is expanded and accelerated up to the primary nozzle exit. The secondary flow enters the suction chamber at section 0 and is entrained by the primary flow inside the mixing section. The primary flow continues its expansion outside the primary nozzle, forming a converging duct for the secondary flow. Consequently, the secondary flow is also separately accelerated and expanded up to section y. As supposed by Munday et al. [254], the assumption is also made that the two flows do not start mixing until section y, located in the constant area

mixing section. The flows mix at constant pressure and are assumed to be fully mixed at section 2. The mixed fluid usually undergoes a normal shock at section 3 up to reaching subsonic velocities. A subsonic diffusion takes place in the diffuser where the flow is slowed down and pressure is recovered. The velocity and pressure profiles resulting from these hypotheses are shown in **Fig. 7.1**. The model is based on mass, momentum and energy balance equations between the different sections. Additionally, the following assumptions are made:

- The flows are steady and one-dimensional
- Adiabatic flow
- Kinetic energy at primary nozzle inlet, suction chamber inlet and diffuser outlet is negligible
- Non-isentropic phenomena are taken into account through isentropic and mixing efficiencies $\eta_p$, $\eta_{py}$, $\eta_s$, $\eta_m$ and $\eta_d$ (setting of these efficiencies will be further discussed in *Section 7.1.3*)

Partial condensation or flashing can take place inside the ejector [265]. When this is the case, the homogeneous equilibrium hypothesis is used in the present model. As explained in [194], this assumption allows treating the flow within the ejector as steady-state and one-dimensional even when the fluid becomes a liquid-vapour two-phase mixture.

The model was developed in EES (Engineering Equation Solver) [192]using EES internal thermodynamic libraries for the different fluids. The model can be used both to simulate ejector performance and for the preliminary design of the ejectors characteristics sections, as explained in *Section 7.1.4*.

## *Computational procedure*

**Fig. 7.4** shows the calculation algorithm developed for the present model. The inputs are:

- The ejector geometry and in particular the primary nozzle throat diameter $d_{p,t}$, primary nozzle exit diameter $d_{p,1}$, and mixing chamber diameter $d_{m,2}$
- The isentropic efficiencies $\eta_p$, $\eta_{py}$, $\eta_s$ and $\eta_d$ as well as the two coefficients $\varphi_m$ and $\alpha_m$ that define the mixing efficiency $\eta_m$ as detailed in the following
- The inlet and outlet conditions of the ejector: pressure and enthalpy at the primary nozzle entrance ($P_{p,0}$ and $h_{p,0}$), at the suction chamber entrance ($P_{s,0}$ and $h_{s,0}$), and the ejector backpressure $P_c$.

Clearly, the thermodynamic state of the flows entering the ejector is then fully determined and in particular the entropies $s_{s,0}$ and $s_{p,0}$ are also known:

$$s_{p,0} = s(P_{p,0}, h_{p,0}) \tag{7.2}$$

$$s_{s,0} = s(P_{s,0}, h_{s,0}) \tag{7.3}$$

The outputs are the primary and secondary mass flow rates $\dot{m}_p$, $\dot{m}_s$ (and consequently the entrainment ratio of the ejector ω) and the thermodynamic state of the flow exiting the ejector.

The first step of the algorithm consists in applying the maximization of mass flow rate to determine the primary mass flow rate and the properties of the fluid leaving the primary. The second step of the algorithm consists in maximizing the ejector total mass flow rate and entrainment ratio to determine the critical point of the ejector ($P_{cri}, \omega_{cri}$ ). Finally, once the critical point is determined, performance simulation can be carried out. To this end, equations describing the on-design or off-design working mode are used, depending on whether the actual ejector backpressure $P_c$ is higher or lower than the critical backpressure $P_{cri}$.

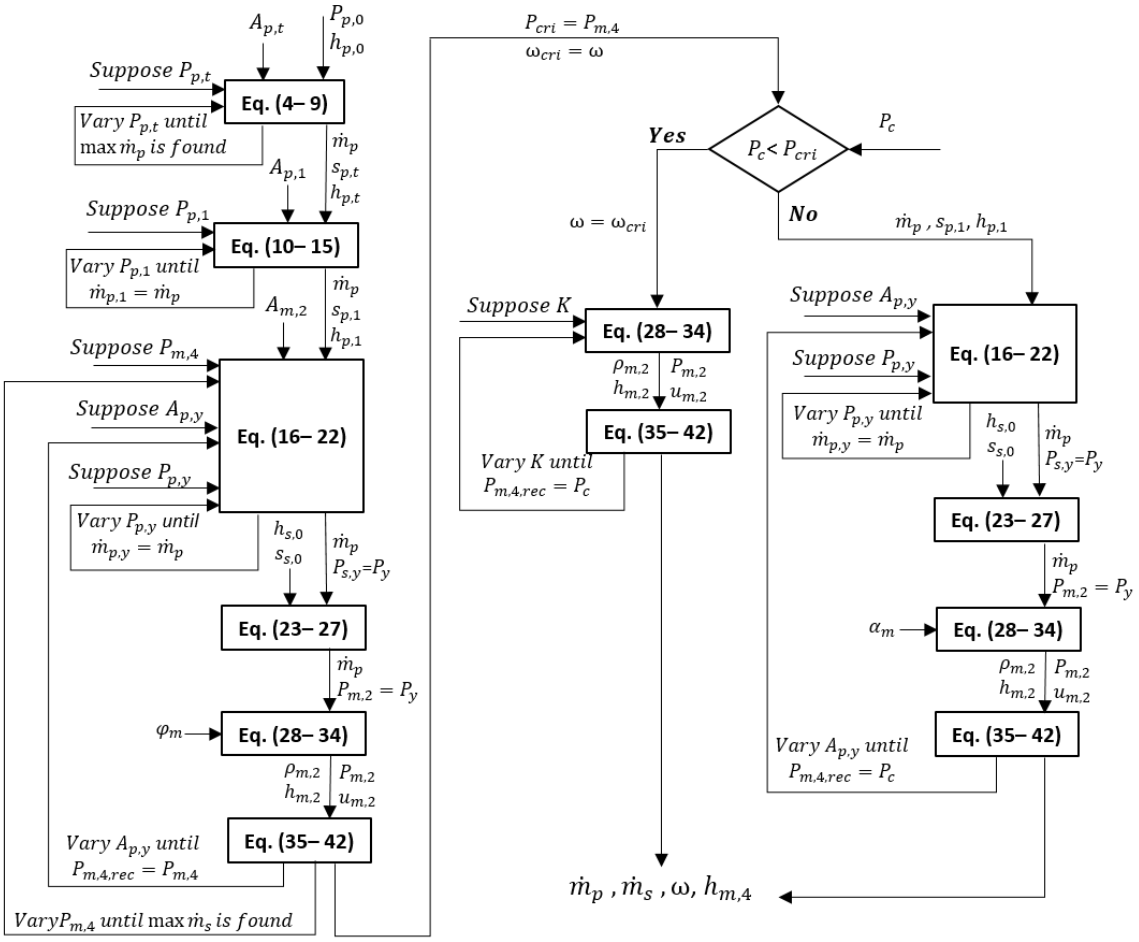


**Fig. 7.4 -** Flowchart of the performance simulation calculation procedure.

## *Primary nozzle*

Choking of the primary fluid is assumed to solve the primary flow. As shown in [43], even a very small pressure difference between inlet and outlet of a converging-diverging nozzle is sufficient to achieve sonic conditions in the throat. Since pressure ratios normally encountered in ejector refrigeration cycles are generally higher, the primary nozzle nearly always works in choking conditions. This is usually imposed by setting the Mach number equal to one at the throat section [257]. However, another approach consists in maximizing the treated mass flow rate [258]. This approach was used in the present model as it yields more precise results in the case of non-isentropic expansion and does not require the computation of the sound speed.

A guess value for the pressure at the primary nozzle throat $P_{p,t}$ is supposed and updated iterating on **Eq. (7.4)-(7.8)** until a maximum for the primary flow mass flow rate $\dot{m}_p$ is found:

$$h_{p,t,is} = h(P_{p,t}, s_{p,0}) \tag{7.4}$$

$$h_{p,t} = h_{p,0} - \eta_p \cdot (h_{p,0} - h_{p,t,is}) \tag{7.5}$$

$$\rho_{p,t} = \rho(P_{p,t}, h_{p,t}) \tag{7.6}$$

$$u_{p,t} = \sqrt{2 \cdot (h_{p,0} - h_{p,t})} \tag{7.7}$$

$$\dot{m}_p = \rho_{p,t} \cdot u_{p,t} \cdot A_{p,t} \tag{7.8}$$

The entropy of the fluid at the primary nozzle throat is then also determined:

$$s_{p,t} = s(P_{p,t}, h_{p,t}) \tag{7.9}$$

Similarly, also for the diverging part of the nozzle an exit pressure value $P_{p,1}$ is supposed and **Eq. (7.10)-(7.14)** are solved iteratively, changing $P_{p,1}$ until the exit mass flow rate equals the one calculated for the nozzle throat:

$$h_{p,1,is} = h(P_{p,1}, s_{p,t}) \tag{7.10}$$
$$h_{p,1} = h_{p,t} - \eta_p \cdot (h_{p,t} - h_{p,1,is}) \tag{7.11}$$
$$\rho_{p,1} = \rho(P_{p,1}, h_{p,1}) \tag{7.12}$$
$$u_{p,1} = \sqrt{2 \cdot (h_{p,t} - h_{p,1}) + {u_{p,t}}^2} \tag{7.13}$$
$$\dot{m}_p = \rho_{p,1} \cdot u_{p,1} \cdot A_{p,1} \tag{7.14}$$

The state of the fluid leaving the primary nozzle is then fully determined and, in particular, the value of the entropy is:

$$s_{p,1} = s(P_{p,1}, h_{p,1}) \tag{7.15}$$

## *Critical point determination through entrainment ration maximization*

Once the flow in the primary injector is solved, the critical point determination can be performed though the entrainment ratio maximization (i.e., the maximization of the secondary flow mass flow rate, since the primary flow mass flow rate was already determined in the previous step), necessary before performance simulation.
For a given ejector backpressure $P_{m,4}$, **Eq. (7.16)-(7.42)** are used to compute the secondary mass flow rate $\dot{m}_s$ and therefore the value of the entrainment ratio corresponding to the backpressure $P_{m,4}$. The indication $P_{m,4}$ is used here for a generic backpressure on which an iterative process is performed for the critical point determination. This is done to distinguish $P_{m,4}$ from the actual ejector backpressure $P_c$ used for performance simulation.
As previously explained, it is assumed that the primary and secondary flow start a constant pressure mixing process at section $y$ in the constant area section of the ejector. Therefore, by initially taking a guess value for $A_{p,y}$, it is possible to write:

$$A_{s,y} = A_{m,2} - A_{p,y} \tag{7.16}$$
$$P_{s,y} = P_{p,y} \tag{7.17}$$

The same equations used before are applied between the primary nozzle exit and section $y$ to find the pressure $P_{p,y}$ allowing the conservation of the primary fluid mass flow rate. The only difference with respect to before is that in this case **Eq. (7.19)** also takes into account the possibility of a recompression taking place from section 1 to section $y$ [43]:

$$h_{p,y,is} = h(P_{p,y}, s_{p,1}) \tag{7.18}$$
$$h_{p,y} = h_{p,1} - \max\left[\eta_{py} \cdot \left(h_{p,1} - h_{p,y,is}\right), 0\right] + \max\left[\frac{(h_{p,y,is} - h_{p,1})}{\eta_{py}}, 0\right] \tag{7.19}$$
$$u_{p,y} = \sqrt{2 \cdot (h_{p,1} - h_{p,y}) + {u_{p,1}}^2} \tag{7.20}$$
$$\rho_{p,y} = \rho(P_{p,y}, h_{p,y}) \tag{7.21}$$
$$\dot{m}_p = \rho_{p,y} \cdot u_{p,y} \cdot A_{p,y} \tag{7.22}$$

Similarly, **Eq. (7.23)-(7.27)** describe the expansion of the secondary fluid between the suction chamber inlet and the beginning of mixing sections:

$$h_{s,y,is} = h(P_{s,y}, s_{s,0}) \tag{7.23}$$
$$h_{s,y} = h_{s,0} - \eta_s \cdot (h_{s,0} - h_{s,y,is}) \tag{7.24}$$
$$u_{s,y} = \sqrt{2 \cdot (h_{s,0} - h_{s,y})} \tag{7.25}$$
$$\rho_{s,y} = \rho(P_{s,y}, h_{s,y}) \tag{7.26}$$
$$\dot{m}_s = \rho_{s,y} \cdot u_{s,y} \cdot A_{s,y} \tag{7.27}$$

**Eq. (7.28)-(7.34)** describe the mixing process that occurs between sections $y$ and 2. The mixing efficiency $\eta_m$ is used to take into account the irreversibilities of the mixing process and is initially considered equal to the input parameter $\varphi_m$ :

$$\dot{m}_m = \dot{m}_p + \dot{m}_s \tag{7.28}$$

$$P_{m,2} = P_{p,y} \tag{7.29}$$

$$u_{m,2,is} = \frac{\dot{m}_p \cdot u_{p,y} + \dot{m}_s \cdot u_{s,y}}{\dot{m}_m} \tag{7.30}$$

$$\eta_m = \varphi_m \tag{7.31}$$

$$u_{m,2} = \sqrt{\eta_m} \cdot u_{m,2,is} \tag{7.32}$$

$$h_{m,2} = \frac{\dot{m}_p}{\dot{m}_m} \cdot \left( h_{p,y} + \frac{{u_{p,y}}^2}{2} \right) + \frac{\dot{m}_s}{\dot{m}_m} \cdot \left( h_{s,y} + \frac{{u_{s,y}}^2}{2} \right) - \frac{{u_{m,2}}^2}{2} \tag{7.33}$$

$$\rho_{m,2} = \rho(P_{m,2}, h_{m,2}) \tag{7.34}$$

The mixed fluid at section 2 is usually (although not necessarily [258]) still supersonic, but the fluid leaving the ejector is subsonic therefore a diffusion must take place. This recompression can only be brought about by a shock wave because a convergent duct is necessary for isentropic diffusion of a supersonic stream [266]. For simplicity, it is assumed that a normal shock occurs in the constant section area after the end of the mixing process, before entering the diffuser. The Rankine-Hugoniot equations that govern this shock are:

$$\rho_{m,3} = \rho(P_{m,3}, h_{m,3}) \tag{7.35}$$

$$u_{m,3} = \frac{\rho_{m,2} \cdot u_{m,2}}{\rho_{m,3}} \tag{7.36}$$

$$h_{m,3} = h_{m,2} + \frac{{u_{m,2}}^2}{2} - \frac{{u_{m,3}}^2}{2} \tag{7.37}$$

$$P_{m,3} = \rho_{m,2} \cdot {u_{m,2}}^2 + P_{m,2} - \rho_{m,3} \cdot {u_{m,3}}^2 \tag{7.38}$$

When the flow is supersonic, in addition to the trivial solution in which all quantities remain the same, this set of equations has another solution, relative to the presence of a shock, which can be found by setting appropriately different guess values [266,267]. The entropy after the shock is:

$$s_{m,3} = s(P_{m,3}, h_{m,3}) \tag{7.39}$$

Finally, the mixed fluid undergoes a compression in the diffuser before leaving the ejector:

$$h_{m,4} = h_{m,3} + \frac{{u_{m,3}}^2}{2} \tag{7.40}$$

$$h_{m,4,is} = h_{m,3} + \eta_d \cdot (h_{m,4} - h_{m,3}) \tag{7.41}$$

$$P_{m,4,rec} = P(h_{m,4,is}, s_{m,3}) \tag{7.42}$$

For a given value of $A_{p,y}$, mixing, normal shock and diffusion equations allow the unambiguous determination of the exit pressure $P_{m,4,rec}$ which however may not coincide with the input $P_{m,4}$.
Indeed, while $A_{m,2}$ is an input parameter relative to the geometry of the ejector, the hypothetical section $A_{p,y}$ used in **Eq. (7.16)** is not known from the beginning. A guess value is therefore needed and an iterative calculation has to be performed until the recalculated $P_{m,4,rec}$ equals the input generic input pressure $P_{m,4}$. In order to determine the critical working point of the ejector the maximization of the total mass flow rate is used. This is done by changing the value of the backpressure $P_{m,4}$ and updating **Eq. (7.16)-(7.42)** until the value of $P_{cri}$ corresponding to the maximum entrainment ratio $\omega_{cri}$ is found. It is worth mentioning that, since in this study the model is developed in EES, all the iterative process described above do not need to be carried out explicitly. In fact, in view of the fact that EES is an equation solver, it is sufficient to input the right number of equations and constraints and the software will perform the iterative processes internally.

## *Performance simulation*

After the critical point ($P_{cri}$ and $\omega_{cri}$) is determined, simulation of the ejector performance can be carried out. Performance simulations is executed using essentially the same equations needed for the performance critical point

determination. Some differences are however introduced depending on whether the ejector is functioning in the on-design or in the off-design working mode.

If the actual backpressure of the ejector is lower than the critical backpressure (i.e., $P_c < P_{cri}$ ), the ejector is in on-design working mode with a choking of both the primary and secondary flow. The equations describing the transformations undergone by the fluid are the same used for the critical point determination with a few differences:

- $P_{m,4}$ is replaced by the actual backpressure value $P_c$
- The entrainment ratio is imposed to be equal to the critical entrainment ratio ($\omega = \omega_{cri}$ )
- A coefficient K is added to the definition of the mixing efficiency of **Eq. (7.31)**:

$$\eta_m = K \cdot \varphi_m \tag{7.43}$$

Note that this approach is possible because the critical point ($P_{cri}, \omega_{cri}$ ) is determined beforehand. Since the entrainment ration is imposed equal to the previously determined $\omega_{cri}$, the coefficient *K* is used to give one needed degree of freedom to the set of equations. This coefficient considers the adjustment loss phenomena enabling the ejector to reach the imposed backpressure in the on-design working mode.

If the actual backpressure of the ejector is greater than the critical backpressure (i.e., $P_c > P_{cri}$ ), the ejector works in off-design working mode, where only the primary flow is choked. Also, in this case the necessary equations remain largely unchanged from those described for the critical point determination with the only differences that:

- $P_{m,4}$ is replaced by the actual backpressure value $P_c$.
- The expression for the mixing efficiency becomes:

$$\eta_m = \varphi_m \cdot \left[1 - \alpha_m \cdot \left(\frac{P_c - P_{cri}}{P_c}\right)\right] \tag{7.44}$$

**Eq. (7.44)** describes the off-design efficiency of the mixing process. $\varphi_m$ and $\alpha_m$ are input parameters that are tuned on experimental data (see *Section 7.1.3*). The linear dependency of the mixing efficiency from the back-pressure in off-design mode, first implemented by Chen et al. [152], results in a better fit with experimental data.

### 7.1.3 Model validation and coefficients calibration

#### *Parameters tuning*

Experimental datasets are used to validate the model and its ability to accurately describe ejectors performance. As explained in *Section 7.1.2*, irreversibilities occurring inside the ejector are considered in the model through efficiency coefficients. The typical approach when comparing thermodynamic models and experimental results consists in tuning efficiency coefficients for each fluid in order to obtain the best possible match with experimental results. However, experimental data are needed for each fluid studied and the tuning process must be repeated. The impact of each of the ejector efficiency coefficient has been investigated in various studies ([258,268–270]). **Fig. 7.5**, in accordance with existing literature, shows the influence of of $\eta_p$, $\eta_s$ , $\varphi_m$ and $\alpha_m$ values on the primary and secondary mass flow rates. **Fig. 7.5** was obtained through the simulation of the SERS cycle of **Fig. 7.2**, using R290 as refrigerant. The primary and secondary mass flow rate are plotted versus the ejector backpressure. Four parameters are considered to evaluate the impact of each efficiency: the value of the primary mass flow rate, the value of the on-design secondary mass flow rate, the value of the critical backpressure and the slope of the off-design secondary mass flow rate curve.

The nozzle efficiency $\eta_p$ (**Fig. 7.5 (a)**) only affects the primary mass flow rate and the value of $P_{cri}$. An increase of $\eta_s$ (**Fig. 7.5 (b)**) leads to a higher on-design secondary mass flow rate with no impact on other quantities. A variation of $\varphi_m$ **Fig. 7.5 (c)** is instead directly linked to a variation of the critical backpressure. Finally, $\alpha_m$ (**Fig. 7.5 (d)**) determines the slope of the off-design curve. The impact of $\eta_{py}$ and $\eta_d$ was also studied, validating the observations of [258]: a variation of $\eta_{py}$ has the same effect as a variation of $\eta_s$, while changing $\eta_d$ is equivalent to changing $\varphi_m$. Therefore, here it was chosen to only tune $\eta_p$, $\eta_s$ , $\varphi_m$ and $\alpha_m$ to fit experimental results while $\eta_{py}$ and $\eta_d$ were fixed to 0.99, assuming surface conditions guaranteeing an almost isentropic flow.

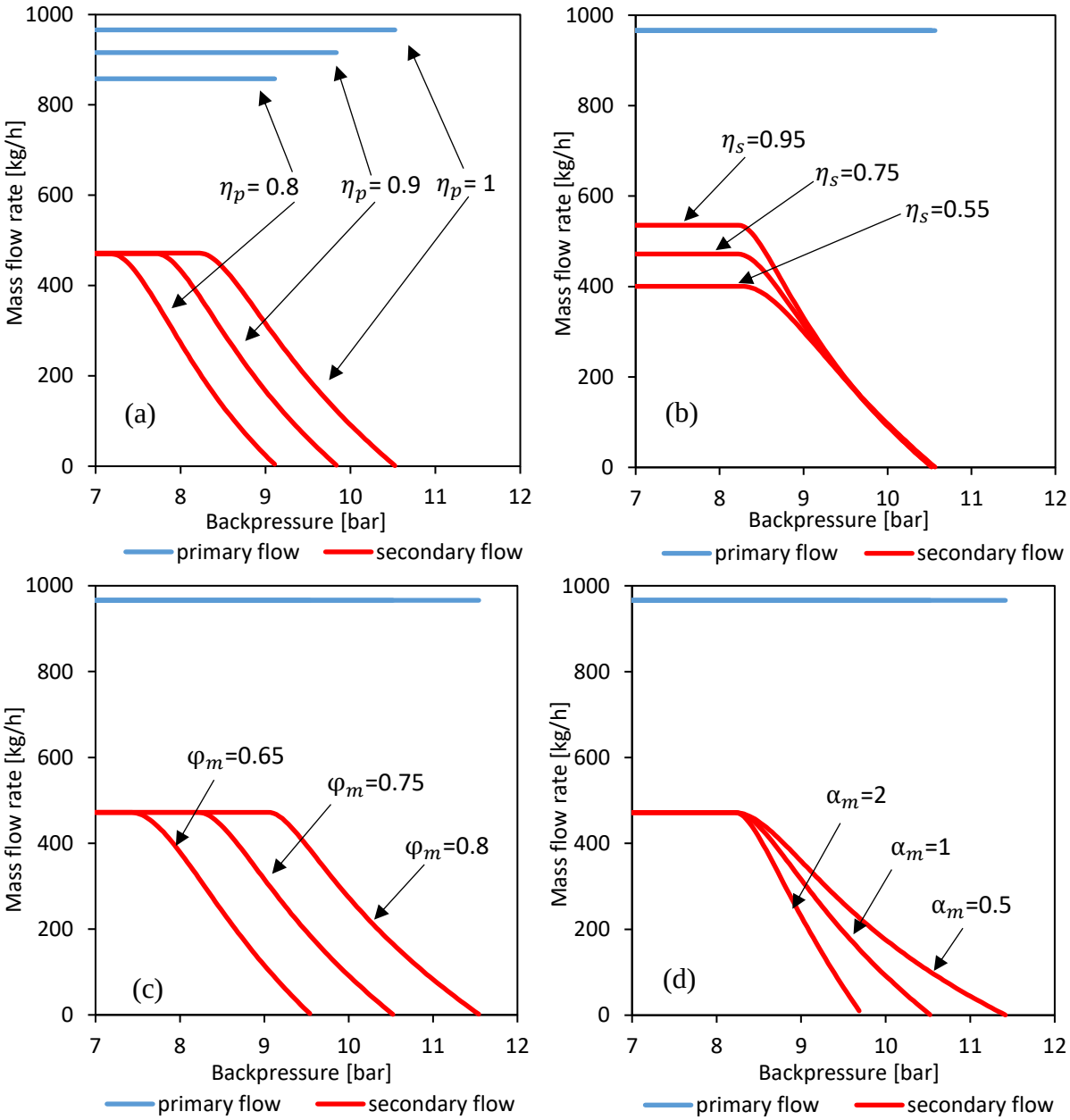


**Fig. 7.5 -** Impact of the efficiency coefficients on the primary and secondary mass flows variations as a function of the ejector backpressure.

Considering that each efficiency has a different impact on the performance of the ejector, the following fitting procedure was applied:

- $\eta_p$ is adjusted to match the experimental and primary fluid mass flow rates. Unfortunately, in most of experimental studies available in the literature the primary mass flow rate is not given. In such cases $\eta_p$ is taken equal to 0.99. This is consistent with most previous studies, where the primary nozzle efficiency is most often fixed at values between 0.95 and 1 ([194,248]).
- $\eta_s$ and $\varphi_m$ are tuned to match respectively $\omega_{cri}$ and $P_{cri}$ thus guaranteeing a good prediction of the critical point.
- $\alpha_m$ is varied to approximate the experimental slope of the ejector characteristic off-design part.

When multiple datasets are available, the procedure presented above for adjusting the four coefficients $\eta_p$, $\eta_s$, $\varphi_m$ and $\alpha_m$ is performed for each dataset and an average value is then taken for the fluid considered.
Two examples of model validation/experimental data fitting through the adjustment of those coefficients are presented the following.

*Calibration of an R600a ejector*

The validation of the model for the case of R600a (isobutane) was performed using data from Butrymowicz et al. [271] referring to a solar-powered SERS using R600a . The dimensions of the ejector studied are: $d_{p,t}$= 3.5mm, $d_{p,1}$= 5mm and $d_{m,2}$= 6mm. Four datasets are present in the study referring to the variation of the condensation temperature for different generator temperature (55-63.5°C) but constant evaporator temperature (7°C), superheating at evaporator outlet (6.5°C), and superheating at generator outlet (8°C).

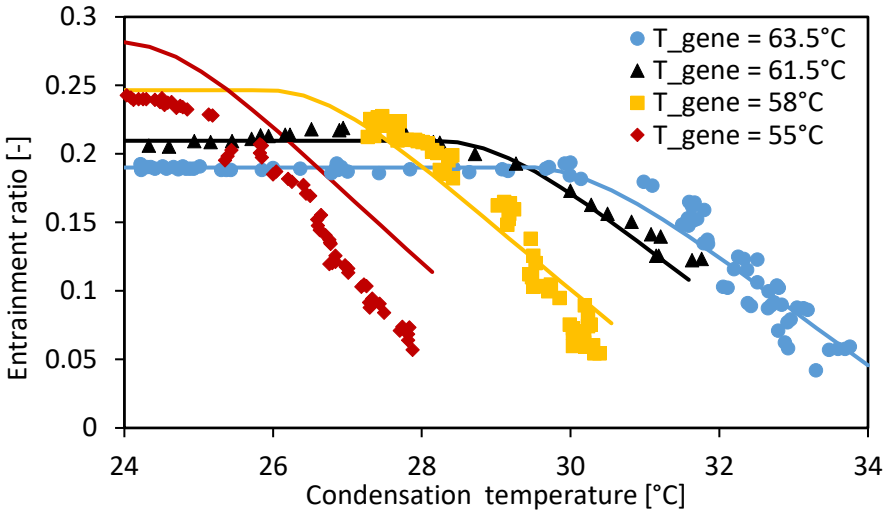


**Fig. 7.6 -** Simulation model results (lines) compared to the experimental results (markers) from [271]: impact of the condensation temperature on the entrainment ratio, for different generator temperatures.

In this study, no precise information on the primary mass flow was available so $\eta_p$ was set to 0.99. The adjusted efficiency coefficients that give the best fitting between experimental theoretical data are found to be $\eta_s$= 0.77, $\varphi_m$= 0.72 and $\alpha_m$= 0.99. **Fig. 7.6** shows the results of the model using the adjusted coefficient (lines) compared to the experimental results (markers). It can be noted that, for the two highest generator temperatures ($T_{gene}$= 61.5°C and $T_{gene}$= 63.5°C) the ejector operates in both on-design and off-design modes, the on-design mode being easily recognizable by the constant entrainment ratio plateau. For the two other experimental datasets ($T_{gene}$= 58°C and $T_{gene}$= 55°C), only off-design conditions are present. The numerical model predicts very well the on-design plateau and the location of the critical point. The model also appears to fit quite well the off-design operation of the ejector, except for the case of $T_{evap}$= 55°C where the model seems to overestimate the entrainment ratio.

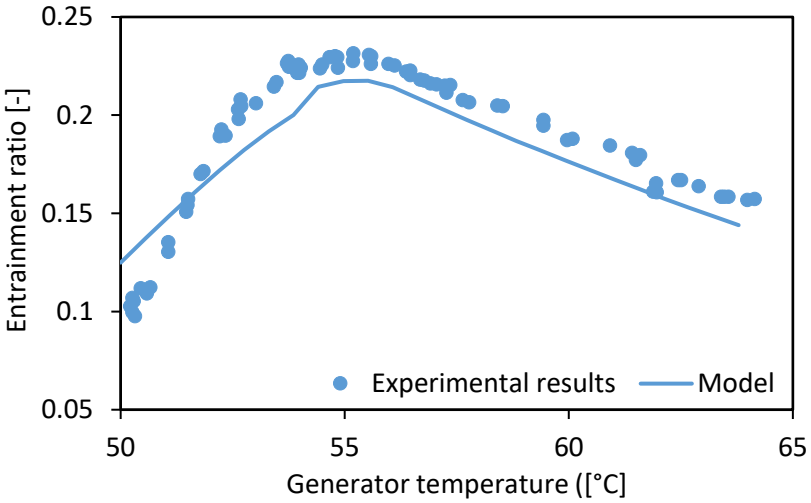


**Fig. 7.7 -** Simulation model results (lines) compared to the experimental results (markers) from [271]: impact of the generator temperature on the entrainment ratio.

**Fig. 7.7** compares the results of the model and experimental results at the variation of the generator temperature while keeping all other parameters constant (condenser temperature 24 °C and evaporator temperature 3.5 °C). Experimental tendencies are respected, especially in the on-design working mode ($T_{gene}$>55°C), and position of the critical point is accurately predicted.

## *Calibration of an R134a ejector*

A second fitting procedure was performed for R134a using experimental data from Hakkaki-Fard et al. [272] where three different ejector geometries are studied (referred to as EJEI, EJEII and EJEIII). Inlet conditions in the study are specifically fixed for each ejector geometry while the backpressure is varied.

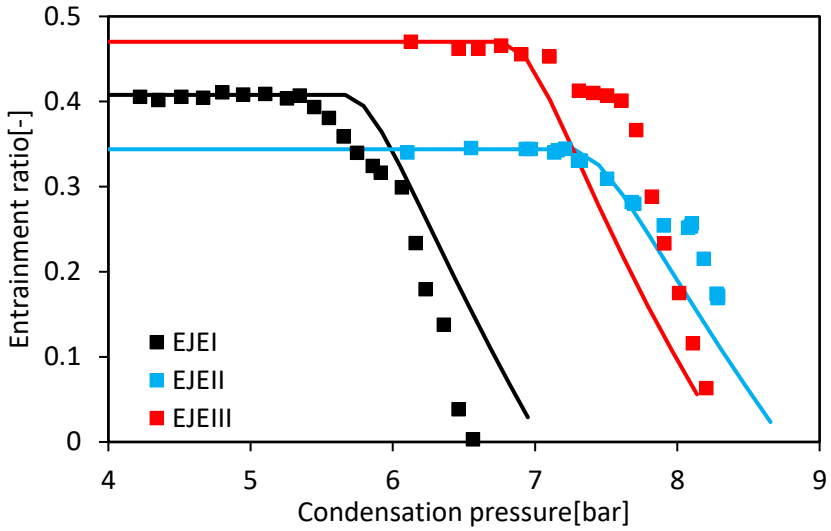


**Fig. 7.8 -** Simulation model results compared to the experimental results from [272] for the effect of the condensation pressure on the entrainment ratio, for different ejector geometries and inlet conditions.

Since also in this case no information is available concerning the primary fluid mass flow rate, $\eta_p$ was fixed at 0.99. The adjusted coefficient guaranteeing the best accordance with experimental results are found to be: $\eta_s$=0.72, $\varphi_m$=0.76 and $\alpha_m$=1.46.
**Fig. 7.8** shows the adjusted model output (lines) compared to experimental results (markers). Each of the three datasets in the picture refers to one particular ejector geometry operating at its specific working conditions. For the three different geometries, the model fits well the experimental data (**Fig. 7.8),** predicting accurately the on-design plateau and the location of the critical point. The off-design part of the ejector characteristic is also well approximated.

The same experimental Hakkaki-Fard et al. [272] results and results from the present model shown in **Fig. 7.8** are divided into 3 subplots (one for each ejector geometry) in **Fig. 7.9** and compared to CFD results from [272] and to 1D thermodynamic model based on the compound choking theory from [258]. Compared to the CFD model, the present model is able to give an equally accurate prediction of the on-design operation and critical point location but appears to be less accurate in the description of the off-design behaviour of the ejectors. Compared to the thermodynamic model based on the compound choking theory from [258], the present model yields more accurate results in the on-design functioning mode, while results in the off-design functioning mode are comparable.

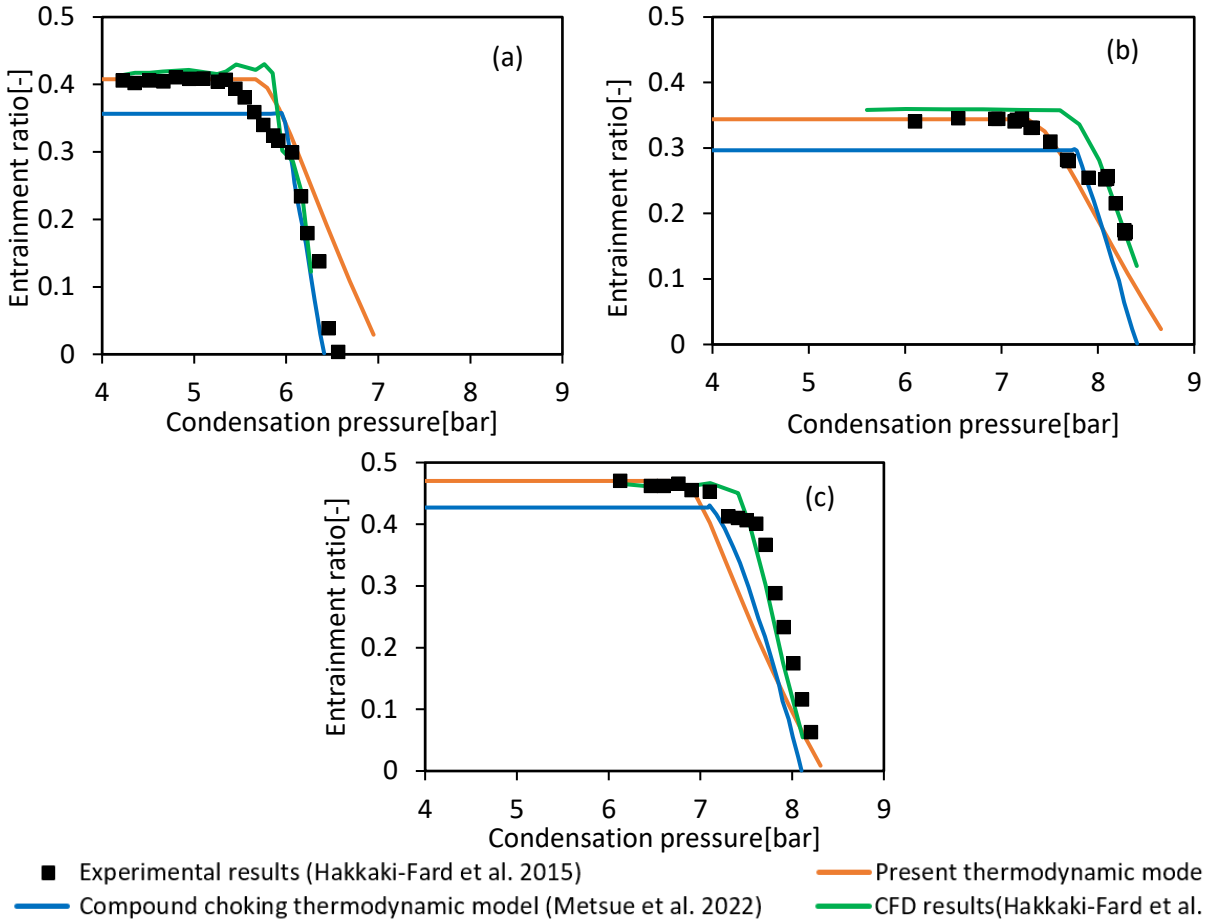


**Fig. 7.9 -** Simulation model results (lines) compared to the experimental results (markers) from [272], CFD results from [272], and results from compound choking 1D model [258], for the effect of the condensation pressure on the entrainment ratio, for three different ejector geometries and inlet conditions ((a): EJEI, (b): EJEII and (c): EJEIII).

### 7.1.4 Case study

The present model was used to simulate a SERS cycle (**Fig. 7.2)** to prove its robustness and ability to be used in the performance evaluation of thermodynamic cycles and for ejector preliminary design. In the application considered, the evaporator temperature is taken constant and equal to 5°C, the condenser temperature is taken equal to 20°C while the generator temperature is varied between 60°C and 150°C. The available thermal power at the generator is supposed equal to 100 kW. Seven different working fluids are tested and their performance compared. For each fluid, the ejector model is used to find the optimal ejector geometry for each working condition considered. Performance of the SERS cycle integrating optimal geometry ejectors is then compared for the different fluids to give some insights on the choice of the most appropriate fluid.

**Table 7.1 -** Main properties of the fluids selected for the study.

| | R134a | R152a | R290 | R600a | R717 | R1234yf | R1234ze(Z) |
|---|---|---|---|---|---|---|---|
| Fluid type | Wet | Wet | Wet | Dry | Wet | Isentropic | Isentropic |
| Fluid class | HFC | HFC | HC | HC | - | HFO | HFO |
| Critical Temperature [°C] | 101.1 | 113.3 | 96.7 | 134.7 | 132.4 | 94.7 | 150.1 |
| Critical Pressure [bar] | 40.6 | 45.2 | 42.5 | 36.3 | 113.6 | 33.8 | 35.3 |
| ODP | 0 | 0 | 0 | 0 | 0 | 0 | 0 |
| GWP | 1430 | 124 | 20 | 20 | <1 | 4 | 7 |
| ASHRAE safety class | A1 | A2 | A3 | A3 | B2L | A2L | A2L |

Seven fluids are considered in the application of the ejector model to the SERS cycle, as shown in **Table 7.1**. In particular they are two HFCs (R134a and R152a), two HFOs (R1234yf and R1234ze(Z)), two hydro-carbons (R290 and R600a) and an inorganic natural refrigerant (R717). R134a is considered as reference for performance comparison. R152a is also used in the study, as it is an HFC with a GWP lower than the 150 actual limit. Finally, the five other fluids represent the most commonly studied environmentally friendly replacements to R134a.

## *Design model*

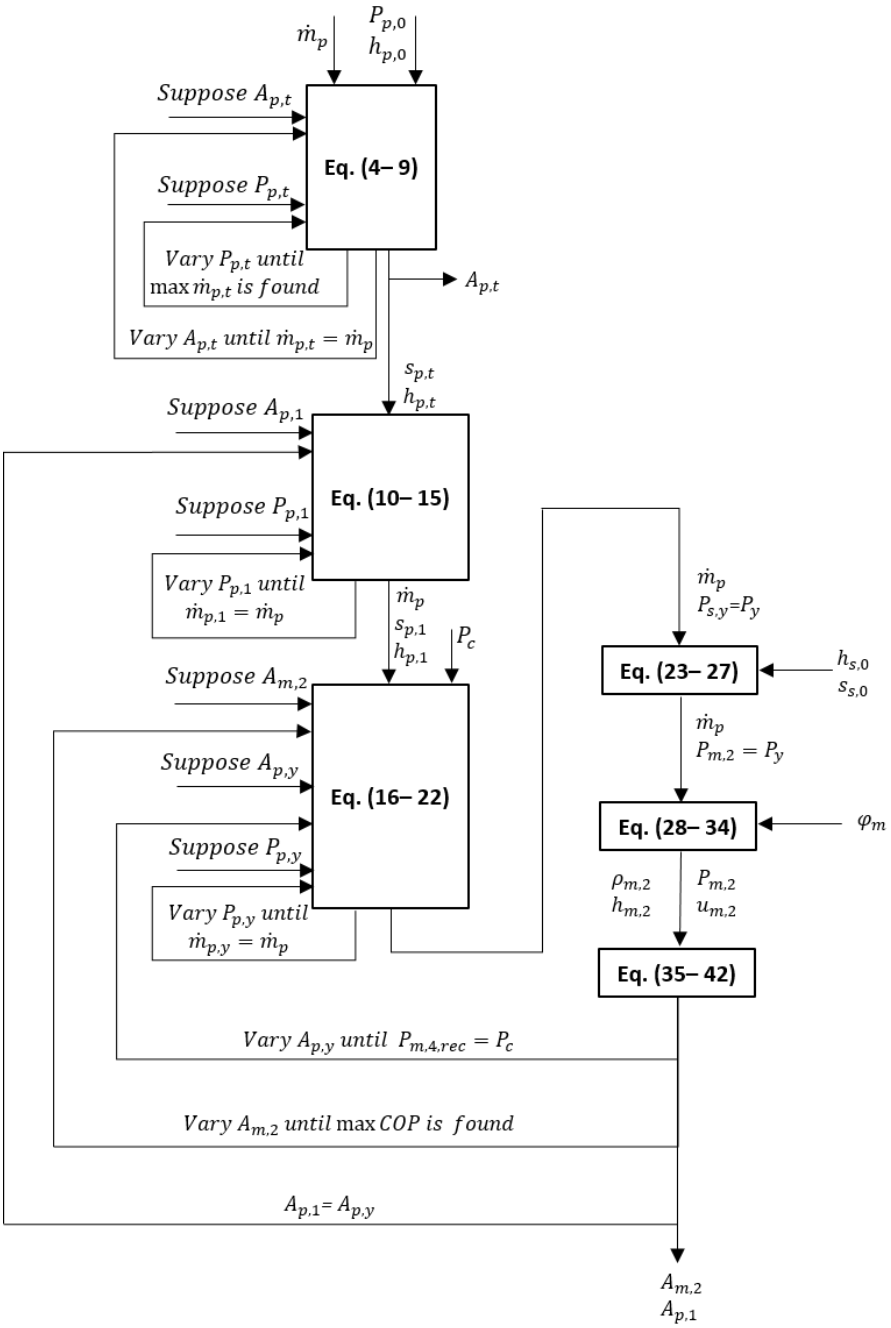


**Fig. 7.10 -** Flowchart of the design procedure.

**Fig. 7.10** shows the calculation algorithm to be used in the case of design. The geometry of the ejector (i.e., primary nozzle throat and exit diameter $d_{p,t}$, and $d_{p,1}$, and mixing chamber diameter $d_{m,2}$) is in this case an output of the model. Mass flow rate and inlet conditions of the fluid being fixed by the available heat source and the chosen

superheating of the vapour, the primary nozzle throat section (i.e., $d_{p,t}$) is easily accessible through **Eq. (7.8)**. The choice of the superheating is a very influential parameter on the performance of the cycle and will be further discussed in the following**.** Furthermore, the diameter of the mixing chamber $d_{m,2}$ is obtained by maximizing the COP of the cycle. Finally, it is worth mentioning that the impact of $d_{p,1}$ on the entrainment ratio of the ejector (and thus on the COP of the cycle) is not very important in this model. This is because the primary nozzle is virtually extended up to the hypothetical throat section whose position has in turn a very important impact on the component performance. In the study, the primary nozzle exit diameter is set through **Eq. (7.45)**, so that the flow leaving the primary nozzle is in adapted conditions, with no compression or further expansion taking place outside the nozzle (thus avoiding further irreversibilities).

$$A_{p,1} = A_{p,y} \tag{7.45}$$

## *Application to the studied fluids*

Even though it was shown clarified that efficiency coefficients should be calibrated for each fluid, experimental data were not available for all of the seven fluids selected for the comparative study so the ejector efficiency coefficients calibration was not possible for all of the seven fluids tested. For this reason, the same ejector efficiencies were considered for all the fluids, and particularly average values with respected to the two calibrations were used: $\eta_p = 0.99$ , $\eta_s = 0.75$ , $\alpha_m$= 1.23 , which are close to the values found during the calibrations of *Section 7.1.3*. Note that since ejectors are designed to work at their critical-point the value of $\varphi_m$ is not very important since it does not intervene in the critical point determination and has only an impact in the off-design functioning. Using the same efficiencies for all the different fluids and geometries studied constitutes a strong hypothesis. Hence, results obtained here represent a proof of concept, but properly calibrated coefficients should be used for rigorous design.

**Fig. 7.11** shows the results obtained when fixing the superheating at the evaporator exit equal to zero (saturated vapour), while adapting the value of the superheating at the generator exit for each fluid to have saturated vapour at the primary nozzle throat. This choice was made so that that condensation does not affect the choking of the primary fluid. Reaching the state of saturated vapour at the primary nozzle throat means that wet fluids should be superheated at the ejector inlet, isentropic fluids should be saturated while dry fluid should can be in the state of saturated mixture (relying on the validity of the homogeneous equilibrium assumption). **Table 7.2** details the quality $x_{p,0}$ (if the fluid is a saturated mixture) or superheat $T_{sh,p,0}$ (if the fluid is superheated) of the primary flow leaving the generator, while **Table 7.3** presents an example of the diameters of the mains sections of the ejectors designed for each fluid studied for three different generator temperatures.

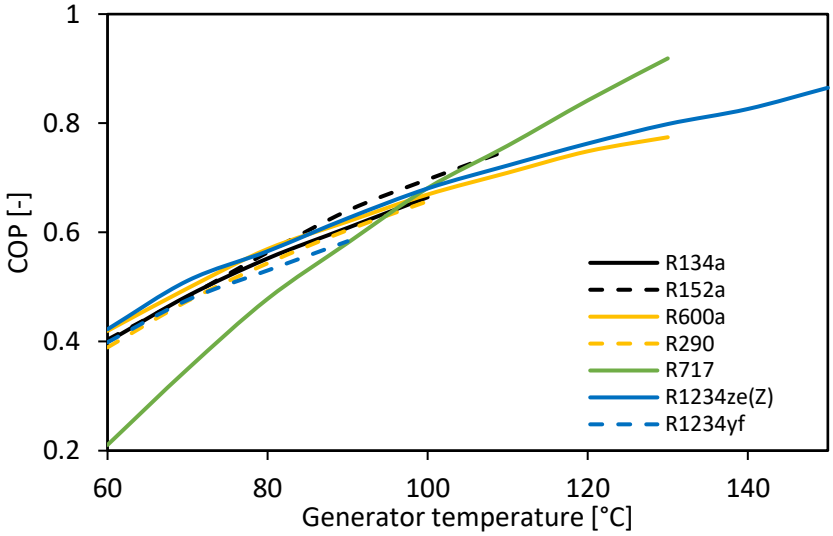


**Fig. 7.11 -** COP of the designed SERS cycle for different generator temperatures, for each study fluids. The generator outlet quality/superheat is chosen so to reach a quality of 1 at the primary nozzle throat.

The generator temperature range considered is between 60-150 °C, but the analysis for each fluid is limited to temperatures below the critical temperature, to avoid modelling of a supercritical SERS cycle. In the temperature range of 60-100 °C, all fluids except R717 yield a similar COP (**Fig. 7.11**). In particular, for the temperature range 60-100 °C, R152a, R600a and R1234ze(Z) seem to be suitable replacements for R134a given their comparable performance. For temperatures higher than 100 °C, R717 appears to be a very promising fluid for SERS cycles yielding significantly better performances than the rest of the fluids.

**Table 7.2 -** Quality $x_{p,0}$ (respectively superheating $T_{sh,p,0}$) of the saturated mixture (respectively superheated fluid) leaving the generator for a primary fluid quality of 1 at the primary nozzle throat.

| | R134a | | R152a | | R290 | | R600a | | R717 | | R1234yf | | R1234ze(Z) | |
|---|---|---|---|---|---|---|---|---|---|---|---|---|---|---|
| $T_{p,0}$ [°C] | $x_{p,0}$ [-] | $T_{sh,p,0}$ [°C] | $x_{p,0}$ [-] | $T_{sh,0}$ [°C] | $x_{p,0}$ [-] | $T_{sh,p,0}$ [°C] | $x_{p,0}$ [-] | $T_{sh,p,0}$ [°C] | $x_{p,0}$ [-] | $T_{sh,p,0}$ [°C] | $x_{p,0}$ [-] | $T_{sh,p,0}$ [°C] | $x_{p,0}$ [-] | $T_{sh,p,0}$ [°C] |
| 60 | - | 1.88 | - | 3.68 | - | 2.10 | 0.97 | - | - | 19.7 | 0.99 | - | 0.99 | - |
| 70 | - | 2.37 | - | 4.47 | - | 2.65 | 0.97 | - | - | 19.8 | - | 0.11 | 0.99 | - |
| 80 | - | 3.02 | - | 4.87 | - | 3.47 | 0.97 | - | - | 19.8 | - | 1.47 | 0.99 | - |
| 90 | - | 3.97 | - | 4.98 | - | 4.33 | 0.95 | - | - | 19.9 | - | 2.62 | 0.99 | - |
| 100 | - | 4.75 | - | 5.40 | - | 5.27 | 0.97 | - | - | 19.9 | | | 0.99 | - |
| 110 | | | - | 6.12 | | | 0.98 | - | - | 19.9 | | | 0.99 | - |
| 120 | | | | | | | - | 0.01 | - | 19.9 | | | - | 0.18 |
| 130 | | | | | | | - | 1.76 | - | 19.9 | | | - | 1.19 |
| 140 | | | | | | | | | | | | | - | 2.23 |
| 150 | | | | | | | | | | | | | - | 3.55 |

**Table 7.3 -** Diameter of the main sections of the ejectors designed for three different generator temperatures for each fluid studied

| Generator Temperature | Diameter | R134a | R152a | R290 | R600a | R717 | R1234yf | R1234ze(Z) |
|---|---|---|---|---|---|---|---|---|
| 60 °C | $d_{p,t}$ [mm] | 9.7 | 9.4 | 7.7 | 11.3 | 6.1 | 10.2 | 15.8 |
| | $d_{p,1}$ [mm] | 13.1 | 12.4 | 9.6 | 15.3 | 7.0 | 13.7 | 23.4 |
| | $d_{m,2}$ [mm] | 20.7 | 19.5 | 14.8 | 25.6 | 9.1 | 12.8 | 38.7 |
| 90 ° | $d_{p,t}$ [mm] | 6.9 | 6.7 | 5.7 | 7.9 | 4.2 | 7.3 | 10.6 |
| | $d_{p,1}$ [mm] | 12.2 | 11.4 | 8.9 | 13.9 | 6.3 | 12.8 | 21.2 |
| | $d_{m,2}$ [mm] | 22.7 | 21.8 | 16.4 | 27 | 11.2 | 23.8 | 42.2 |
| 120 °C | $d_{p,t}$ [mm] | - | - | - | 5.8 | 3.1 | - | 7.6 |
| | $d_{p,1}$ [mm] | - | - | - | 13.2 | 5.9 | - | 19.9 |
| | $d_{m,2}$ [mm] | - | - | - | 28.2 | 12.5 | - | 44.5 |

## *Impact of the superheating definition*

Several other comparative studies have been performed on SERS cycles (Besagni et al. [124], Cizungu et al. [273], Selvaraju et al. [274], Chen et al. [275], etc.). However, results concerning the optimal fluid choice are very different and often contrasting. Chen et al. [275]highlighted that an often overlooked parameter, the choice of the superheating, has in reality a very strong impact on final results. Superheating of the vapour at the ejector inlet is often chosen arbitrarily and the same value is considered for each fluid. In this way, some fluids are clearly favoured while others are instead penalized.

In order to highlight the bias that can be introduced by the choice of the superheating, a second comparative study was carried out in which zero superheating is considered at the generator exit for all of the seven study fluids. Fig. **7.12** shows the results obtained in this case. It appears this time that R152a and especially R717 give better COP when compared to other fluids, even in the 60-100 °C temperature range, in which R717 appeared to give the worst results out of all fluids considered in **Fig. 7.11**. This is because R152a and R717 are two wet fluids, favoured by the choice of a zero superheating compared to the high superheating needed to prevent condensation before the primary nozzle throat. It is apparent that the choice of a constant superheating is not always suitable for a proper comparison of different fluids and that adapting this parameter to each fluid would be preferable. However, there is still no consensus as to how this choice should be made: for example, it can be defined so as to avoid condensation before the primary nozzle sonic section (see **Fig. 7.11**), or to avoid any condensation in the ejector, etc. Further experimental studies focusing on the impact of superheating, condensation and flashing within the

ejector are needed to get a better understanding of these phenomena and help in the determination of the correct superheating depending on the fluid characteristics. Note that for the sake of simplicity the superheating level at the evaporator exit was chosen constant (equal to 0°C) for all the studied fluids. However, the same consideration regarding the choice of the superheating apply also in this case and further experimental data is needed for a correct choice.

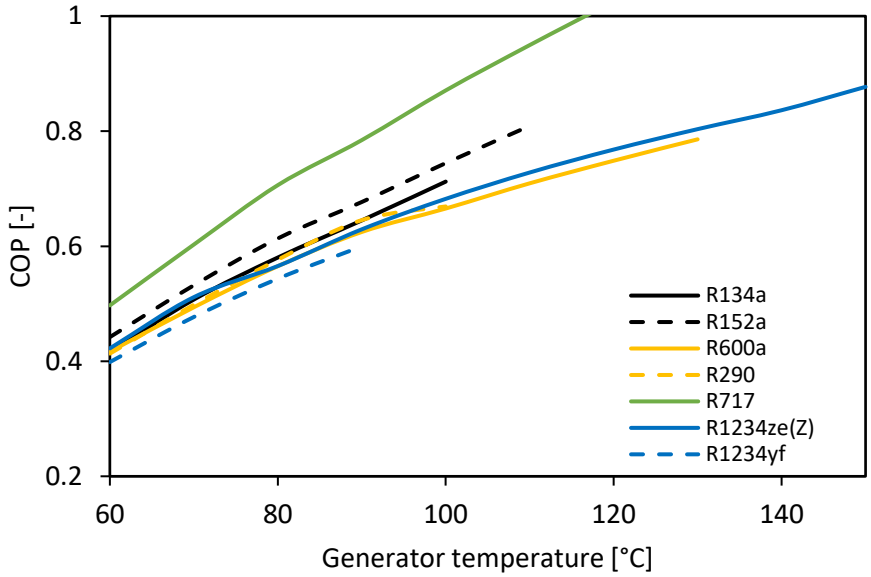


**Fig. 7.12 -** COP of the designed SERS cycle for different generator temperatures, for the seven study fluids. The generator outlet superheat is fixed to 0°C for all cases.

## *Two-phase flow model*

As stated in the previous section, results of this model as well as of previous similar thermodynamic models, in case of two-phase flow, rely on the validity of the homogeneous equilibrium assumption. However, the rapid expansion of a one-component mixture through a converging nozzle is not expected to follow a thermodynamic equilibrium path. In normal nozzle configurations, there is little time for mass transfer to take place, and it is reasonable to assume that the amount of mass transferred in the expansion is negligible [276] and that the quality of the vapour in the throat section is equal to the quality at inlet. This is coherent with experimental works carried out on nuclear steam turbines [277] and on ORC supersonic impulse axial micro turbines [278]. Since the vapour entrains liquid droplets, the homogeneous equilibrium assumption leads to lower calculated mass flow rates than experimentally verified.
Different authors suggested the introduction of a modification in the calculation of an injector mass flow rate, including a dependency from two-phase conditions [278–280]:

$$\dot{m}_{2p} = \frac{\dot{m}_{1p}}{\sqrt{x_0}} \tag{7.46}$$

In **Eq. (7.78)**, $x_0$ is the quality of the fluid entering the ejector, $\dot{m}_{2p}$ is the two-phase mass flow rate and $\dot{m}_{1p}$ is the mass flow rate of a one-phase flow entering the ejector with the same pressure and temperature, but quality equal to one. Recent study carried out at CEA Grenoble on a partial admission axial turbine with a stator made up of a single converging-diverging injector confirm this observation [278] for different pure working fluids (Novec649™, HFE7000 and HFE7100) as well as a zeotropic mixture (Novec649™/HFE7000). Therefore, the introduction of **Eq. (7.78)** was tested in the model.

**Fig. 7.13** shows results of the 1D model assuming homogeneous equilibrium (red curve) and with the introduction of **Eq. (7.78)** (blue curve) for different primary nozzle vapour inlet quality (primary nozzle inlet temperature and pressure of 100°C and 19.8 bar respectively) in the case of R600a.

The modification proposed increases the mass flow rate treated by the primary nozzle with respect to the hypothesis of homogeneous equilibrium but reduces the predicted COP of the SERS cycle. Indeed, results of the present 1D model seem to indicate that using a partially evaporated SERS cycle could lead to an increase in the performance of the cycle. On the other hand, the introduction of the correction on treated mass flow rate in the case of two-phase flows shows a decreasing COP when the vapour quality at inlet decreases. It should be highlighted that no additional loss linked to the flashing of the working fluid was considered here, but taking two phase-related irreversibilities into account is necessary for a correct prediction of ejector performance. Further experimental studies are therefore necessary to properly assess the impact of two-phase conditions on treated mass flow rate and ejector performance. Variations of the heat source conditions being frequent in ejector refrigeration cycles, an appropriate modelling of two-phase functioning is important for accurate performance prediction. Finally, a reliable model could be used to evaluate the interest of partially evaporated cycles and to establish if an optimum exists between performance of the cycle and cost of components, due to the smaller size and thermal power necessary in partially evaporated cycles.

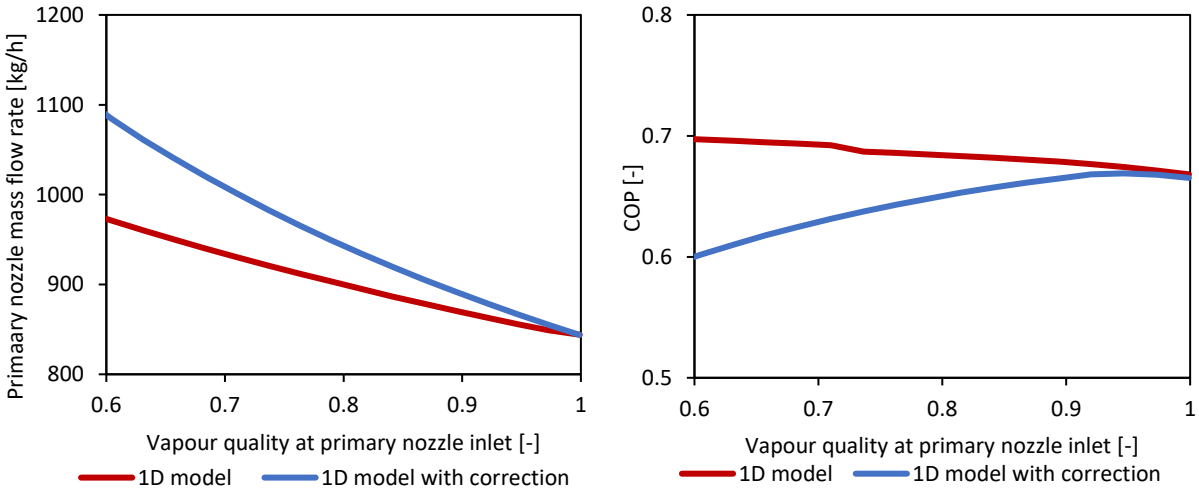


**Fig. 7.13** - Primary mass flow rate and COP of a R600a SERS cycle computed with and without the correction that takes into account two-phase flow impact on the mass flow rate

### 7.1.5 Ejector model synthesis

A real gas thermodynamic model based on mass flow rate maximization has been developed. The model is based on the works of Chen et al. [152], and Metsue et al. [258], but unlike previous models, the procedure proposed simplifies the calculation algorithm and avoids a complex description of the double-choking mechanism at play. Here the novel approach is rather to find both the primary flow and the total ejector mass flow rate by imposing the maximization of mass flow rate. Non-isentropic phenomena are considered through isentropic and mixing efficiencies, which can be used to calibrate the model. Validation in the case of single-phase ejectors was performed with R600a (isobutane) and R134a, and for different ejector geometries, showing that the model is as or more accurate than existing models.

The validated model was used to perform a comparative analysis of the use of different fluids in a SERS cycle for different hot temperature sources. For each operating condition, an optimal ejector geometry was designed. The analysis highlighted that the choice of the superheating, which is often an overlooked parameter, has indeed a strong impact on the cycle performance. The definition of two different criteria for the choice of the superheating in the study lead to different observations with respect to the impact of the refrigerant choice on the performance of the cycle. Since there is still no consensus regarding this choice, further experimental studies are needed to get a better understanding of these phenomena and help in the determination of the correct superheating depending on the fluid characteristics.

Finally, the use of the model in the case of two-phase ejector inlet was tested. Although the model was only validated in the single-phase case, several authors [258] have foreseen the use of such models also for two-phase ejector. Comparison with experimental data on two-phase injectors suggest that correction in the calculated mass flow rate must be included, as well as additional loss terms considering two-phase related irreversibilities. Also, in these cases, additional experimental data is needed to properly assess the impact of the two-phase conditions (such as condensation, flashing, etc.) on ejector performance.

# 7.2 Optimum performance evaluation ejector model

The analysis of the combined carried out in *Section 5.4* highlighted the strict limits imposed to the cycle by the turbine. For this reason, a novel architecture integrating an ejector was proposed in *Section 5.5*. To evaluate the interest of the solution, a detailed ejector model was developed and presented in *Section 7.1*. However, in order to perform a preliminary assessment of the performance of the cycle integrating the ejector a simplified ejector model was also developed and integrated into the combined cycle.
The model is based on the work of Chen et al. [229] who presented a model capable of predicting the optimum performance as well as obtaining the design area ratio ejectors for refrigeration systems. The model presented by Chen assumes ideal gas behaviour. However real-gas equations are used here.
The working principles of ejectors have already been explained in the previous section. Here the simplified representation detailed in the following (with reference to **Fig. 7.14**) is adopted, which works well to estimate on-design performance, but is incapable of predicting off-design performance. The primary flow is supposed to accelerate through the nozzle up to reaching choking sonic conditions in section *t*. The flow then fans out of the primary nozzle at a very low pressure ($P_1$). As a result, the secondary flow is entrained in the suction chamber and its velocity increased during the expansion from inlet conditions (0) to $P_1$. Because of the high velocity difference, the two flows are assumed to only begin mixing in the mixing chamber (2). In the mixing process the primary flow is slowed down, while the secondary flow is accelerated until the two flows are completely mixed (3). A normal compression is assumed to be induced at the beginning of the constant area section (4), after which the flow in subsonic conditions (5) is further diffused until the exit section (6).

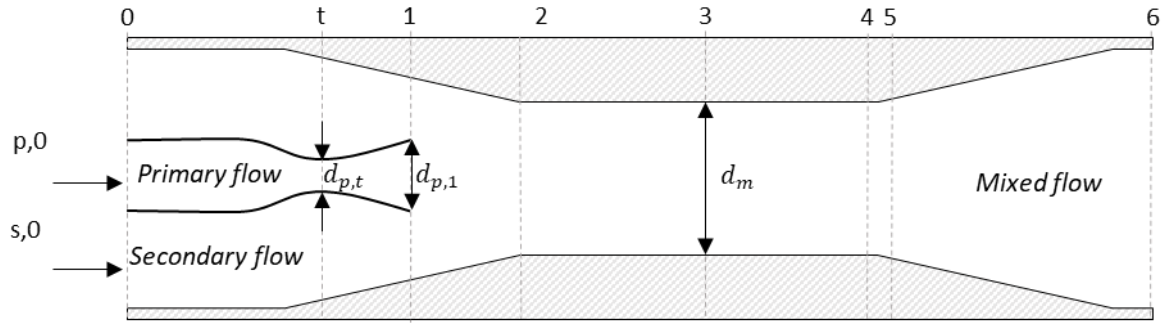


**Fig. 7.14 –** Schematic diagram of the ejector.

Additionally, the flows are considered steady and one dimensional, the inlet velocities are neglected and all losses are taken into account through isentropic efficiency, namely primary nozzle efficiency ($\eta_p$), secondary nozzle efficiency ($\eta_s$), mixing efficiency ($\eta_m$) and diffuser efficiency ($\eta_d$).

## 7.2.1 Governing equations

Based on the above simplified representations of the ejector, the thermodynamic model used to describe the phenomena taking place within the component is presented in the following.

### *Primary flow from inlet to throat section (p,0 → p,t)*

To solve the primary nozzle flow up to the primary nozzle throat section (t), the set of **Eq.(7.47)-(7.54)** must be solved iteratively, updating the value of $P_{p,t}$ until the maximum of the primary flow mass flow rate ($\dot{m}_p$) is found, as discussed in *Section 7.1.2*.

$$h_{p,0} = h(P_{p,0}, T_{p,0}) \quad (7.47)$$
$$s_{p,0} = s(h_{p,0}, T_{p,0}) \quad (7.48)$$
$$h_{p,t,is} = h(P_{p,t}, s_{p,0}) \quad (7.49)$$
$$h_{p,t} = h_{p,0} - \eta_p \cdot (h_{p,0} - h_{p,t,is}) \quad (7.50)$$
$$\rho_{p,t} = \rho(P_{p,t}, h_{p,t}) \quad (7.51)$$
$$s_{p,t} = s(P_{p,t}, h_{p,t}) \quad (7.52)$$

$$u_{p,t} = \sqrt{2 \cdot (h_{p,0} - h_{p,t})} \tag{7.53}$$

$$\dot{m}_p = \rho_{p,t} \cdot u_{p,t} \cdot A_{p,t} \tag{7.54}$$

### *Primary flow from throat section to mixing section outlet (p,t → p,2)*

Also in this case, the set of equations needed to solve the primary nozzle from the primary nozzle throat to the primary nozzle exit section are the same presented in *Section 7.1.2*. Hence, also for the divergent part of the nozzle, **Eq. (7.55)-(7.59)** are solved iteratively, changing $P_{p,1}$ until he exit mass flow rate equals the one calculated for the nozzle throat ($\dot{m}_{p,1}$=$\dot{m}_p$):

$$h_{p,2,is} = h(P_{p,2}, s_{p,t}) \tag{7.55}$$

$$h_{p,2} = h_{p,t} - \eta_p \cdot (h_{p,t} - h_{p,2,is}) \tag{7.56}$$

$$\rho_{p,2} = \rho(P_{p,2}, h_{p,2}) \tag{7.57}$$

$$u_{p,2} = \sqrt{2 \cdot (h_{p,t} - h_{p,1}) + {u_{p,t}}^2} \tag{7.58}$$

$$\dot{m}_{p,2} = \rho_{p,2} \cdot u_{p,2} \cdot A_{p,2} \tag{7.59}$$

### *Secondary flow from inlet to mixing section inlet (s,0 → s,2)*

The mixing is supposed to take place at constant pressure equal to $P_{p,2}$. The secondary flow undergoes an expansion from its inlet conditions ($P_{s,0}$ and $T_{s,0}$) to $P_{p,1}$ described by the following equations:

$$h_{s,0} = h(P_{s,0}, T_{s,0}) \tag{7.60}$$

$$s_{s,0} = s(P_{s,0}, T_{s,0}) \tag{7.61}$$

$$P_{s,2} = P_{p,2} = P_2 \tag{7.62}$$

$$h_{s,2,is} = h(P_{s,2}, s_{s,0}) \tag{7.63}$$

$$h_{s,2} = h_{s,0} - \eta_s \cdot (h_{s,0} - h_{s,2,is}) \tag{7.64}$$

$$u_{s,2} = \sqrt{2 \cdot (h_{s,0} - h_{s,2})} \tag{7.65}$$

$$\rho_{s,2} = \rho(P_{s,2}, h_{s,2}) \tag{7.66}$$

$$\dot{m}_s = \rho_{s,2} \cdot u_{s,2} \cdot A_{s,2} \tag{7.67}$$

where $A_{s,2} = A_{mix} - A_{p,2}$.

### *Mixing process before shock (2 → 4)*

**Eq. (7.68)-(7.74)** describe the mixing process that occurs between sections 2 and 4. The mixing efficiency $\eta_m$ is used to take into account the irreversibilities of the mixing process:

$$\dot{m}_m = \dot{m}_p + \dot{m}_s \tag{7.68}$$

$$P_4 = P_2 \tag{7.69}$$

$$u_{4,is} = \frac{\dot{m}_p \cdot u_{p,1} + \dot{m}_s \cdot u_{s,2}}{\dot{m}_m} \tag{7.70}$$

$$u_4 = \sqrt{\eta_m} \cdot u_{4,is} \tag{7.71}$$

$$h_4 = \frac{\dot{m}_p}{\dot{m}_m} \cdot \left(h_{p,1} + \frac{{u_{p,1}}^2}{2}\right) + \frac{\dot{m}_s}{\dot{m}_m} \cdot \left(h_{s,2} + \frac{{u_{s,2}}^2}{2}\right) - \frac{{u_4}^2}{2} \tag{7.72}$$

$$\rho_4 = \rho(P_4, h_4) \tag{7.73}$$

$$s_4 = s(P_4, h_4) \tag{7.74}$$

### *Mixed flow through the diffuser (2 → 4)*

Finally recompression in the diffuser is described by **Eq.(7.75)-(7.77)**, in which the velocity of the flow leaving the ejector is neglected, and energy conservation can hence be used to calculate the enthalpy at the ejector outlet

$$h_6 = h_4 + \frac{{u_4}^2}{2} \tag{7.75}$$

$$h_{6,is} = h_4 + \eta_d \cdot (h_6 - h_4) \tag{7.76}$$

$$P_6 = P(h_{6,is}, s_4) \tag{7.77}$$

It should be noted here that the recompression in the diffuser includes a shock, followed by a further diffusion. Here the losses involved with the shock are simply included in the diffuser efficiency ($\eta_d$), as described by Chen et al. Chen et al. [229].

### *Calculation procedure*

With the presented ejector model, optimal entrainment ratio (ω) and corresponding areas can be calculated simultaneously. In particular, the computation procedure requires to input inlet conditions ($P_{p,0}$, $T_{p,0}$, $P_{s,0}$ and $T_{s,0}$) and ejector efficiencies ($\eta_p, \eta_s, \eta_m$ and $\eta_d$). In the case of mixtures (like the ammonia-water mixture used in the combined cooling and power production cycle investigated in the present work), mass fractions ($x_{p,0}$ and$x_{s,0}$) must be specified for the calculations of state properties.
If the available primary flow mass flow rate ($\dot{m}_p$) is given as an input, **Eq.(7.47)-(7.54)** allow the direct calculation of $A_{p,t}$. Subsequently, for a given value of $A_{p,2}$ **Eq. (7.60)-(7.77)** need to be solved iteratively updating the value of $A_{s,2}$ until the calculated ejector backpressure is equal to imposed backpressure. Finally,the maximization of the secondary flow mass flow rate (i.e., the maximization of the entrainment ratio) can be performed by updating $A_{p,2}$(determining the mixing pressure $P_2$) and solving iteratively **Eq.(7.47)-(7.77)**. Hence, the optimal ejector mixing section and entrainment ratio can be found at the same time.

## 7.3 NTU and Jakob calculation

The calculation procedure of NTU and Jakob is detailed here, while all the details regarding the calculation of the $R_{en}$ where already given in Section *4.2.2*.

### *NTU calculation*

For the external heat exchangers, the HTF side heat transfer coefficient is calculated with a correlation developed by the Heat Exchangers Research Group (GREThh) for corrugated plates with a Reynolds number value between 50 and 14,600 [175]. The coefficient proposed (0.289) is reduced by a 1.5 factor according to Triché et. al experimental results [45] (**Eq. (7.87)**). The convective heat transfer coefficient between the falling film and the plates is calculated with the Wilke's correlation [45] (**Eq. (7.91)**). For the solution heat exchanger correlations developed by the GREThh was used on both sides.

If *Len* represents the plate length, *Width* the plate width, *N* is the number of plates, $dist_{plates}$ is the distance between the plates, *e* is the plate thickness and $e_{corru}$ is the corrugations height, the heat exchangers area, number of channels and hydraulic diameter $D_h$ can be expressed as:

$$S = Width \cdot Len \tag{7.78}$$

$$N_{channels,HTF} = N/2 \tag{7.79}$$

$$N_{channels,sol} = N/2 - 1 \tag{7.80}$$

$$D_h = 2 \cdot \frac{Width \cdot dist_{plates}}{Width + dist_{plates}} \approx 2 \cdot e_{corru} \tag{7.81}$$

Thermal conductivity of stainless steel $\lambda_{inox}$ was considered equal to 16.3 W/m$^2$. Hence, for a generic internal heat exchanger the NTU calculation procedure is detailed in the following.

$$v_{HTF} = viscosity\ (\mathrm{T_{HTF,in}}, \mathrm{P_{HTF}}) \tag{7.82}$$

$$cp_{HTF} = cp\ (\mathrm{T_{HTF,in}}, \mathrm{P_{HTF}}) \tag{7.83}$$

$$\lambda_{HTF} = conductivity\ (\mathrm{T_{HTF,in}}, \mathrm{P_{HTF}}) \tag{7.84}$$

$$Re_{HTF} = 2 \cdot \frac{\dot{m}_{HTF}}{v_{HTF} \cdot Width \cdot N_{channels,HTF}} \tag{7.85}$$

$$Pr_{HTF} = \frac{v_{HTF} \cdot cp_{HTF}}{\lambda_{HTF}} \tag{7.86}$$

$$h_{HTF} = \frac{0.289}{1.5} \cdot Pr_{HTF}^{1/3} \cdot Re_{HTF}^{0.64} \cdot \frac{\lambda_{HTF}}{D_h} \tag{7.87}$$

$$\lambda_{sol} = conductivity\ (\frac{\mathrm{T_{in,sol}} + \mathrm{T_{out,sol}}}{2}, \mathrm{P_{in,sol}}, Q = 0) \tag{7.88}$$

$$v_{sol} = viscosity\ (\frac{\mathrm{T_{in,sol}} + \mathrm{T_{out,sol}}}{2}, \mathrm{P_{in,sol}}, Q = 0) \tag{7.89}$$

$$\rho_{sol} = density\ (\frac{\mathrm{T_{in,sol}} + \mathrm{T_{out,sol}}}{2}, \mathrm{P_{in,sol}}, Q = 0) \tag{7.90}$$

$$cp_{sol} =$$

$$\delta_{sol} = 3 \cdot \frac{v_{sol} \cdot (\dot{m}_{sol}/N_{channels,sol})}{(\rho_{sol}^2 \cdot 9.807)^{1/3}} \tag{7.91}$$

$$h_{sol} = 1.88 \cdot \frac{\lambda_{sol}}{\delta_{sol}} \tag{7.92}$$

$$K = \left(\frac{1}{h_{HTF}} + \frac{1}{h_{sol}} + \frac{e}{\lambda_{inox}}\right)^{-1} \tag{7.93}$$

$$cp_{sol} = \frac{h(\mathrm{T_{in,sol}} + \mathrm{dT},\ \mathrm{P_{in,sol}}, \mathrm{x_{liq,sat}}) - \mathrm{h}(\mathrm{T_{in,sol}},\ \mathrm{P_{in,sol}}, \mathrm{x_{liq,sat}})}{\mathrm{dT}} \tag{7.94}$$

$$NTU = \frac{K \cdot S}{cp_{sol} \cdot \dot{m}_{sol}} \tag{7.95}$$

### *Jakob number*

A modified version of the Jakob number was used in the present work, calculated as follows:

$$x_m = 0.5 \cdot \left[\mathrm{x_{in}} + x(\mathrm{T_{HTF,in}}, \mathrm{P_{in}}, Q = 0)\right] \tag{7.96}$$

$$L = h(x_m, \mathrm{P_{in,sol}}, \mathrm{Q} = 1) - h(x_m, \mathrm{P_{in,sol}}, \mathrm{Q} = 0) \tag{7.97}$$

$$\rho_{vap} = density\ (\mathrm{T_{in,sol}}, \mathrm{P_{in,sol}}, Q = 1) \tag{7.98}$$

$$Ja = \frac{\rho_{sol} \cdot cp_{sol} \cdot (\mathrm{T_{HTF,in}} - \mathrm{T_{in,sat}})}{\rho_{vap} \cdot L} \tag{7.99}$$

## 7.4 Turbine model power production validation

The experimental measurement from the turbine testing obtained with various gases presented in *Section 3.4.2*, are here compared with results of the 1D model adjusted on CFD results.
Absolute values of power produced by the turbine are much lower than those expected and predicted in the design phase, and much lower values than those predicted by CFD simulations, which, on the other hand, gave results compatible with the size and partial admission ratio of the turbine.
**Fig. 7.15** compares the mechanical power calculated using the 1D model with the electrical power measured for the same fluid and under the same operating conditions presented in **Fig. 3.12**.
Thus, the upstream pressure and temperature and the downstream pressure used in the 1D simulation correspond to the experimental ones. Furthermore, in the 1D model, the rotational speed of the turbine is set equal to the one measured during the tests. Concerning the mass flow rate treated by the turbine, the value calculated by the model 1D has discrepancies of less than 5% with respect to measured values, as shown in **Fig. 4.26**.

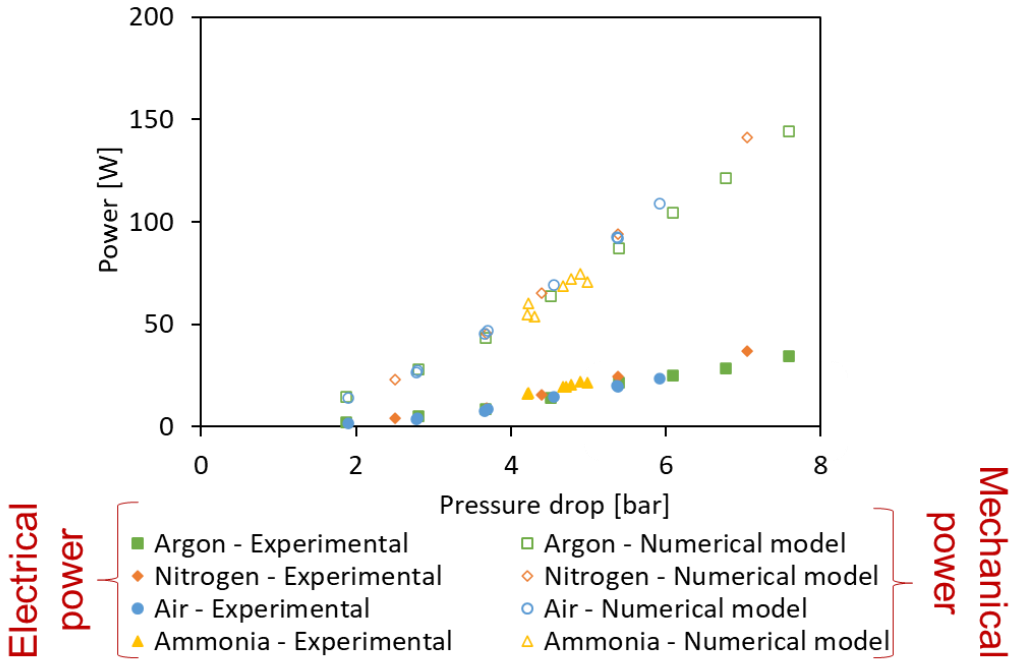


**Fig. 7.15 –** Comparison of mechanical power calculated using the 1D model and experimental results.

A first difference between the two curves stems from the fact that the 1D model was applied for the simple calculation of fluid-dynamic losses (for which it was calibrated on CFD results), without considering mechanical and electrical generation losses.
The hypothesis that the differences are also due to a different magnitude of fluid-dynamic losses seems unlikely, since CFD models are widely used and validated with high accuracy. As evidence supporting this consideration, attempts to re-adjust the 1D model by changing the constants of the loss terms and considering an additional constant electrical and mechanical efficiency did not lead to satisfactory results.
Likewise, the presence of significant losses upstream or downstream of the turbine that have not been taken into account can also be ruled out, since these losses would also significantly alter the turbine mass flow rate, at least in some operating conditions.

Therefore, the most plausible explanation is that this deviation is essentially due to a combination of mechanical and electrical generation losses. While this aspect requires and deserves specific investigation, it is possible to quantify its overall effect by calculating the ratio between the corresponding power produced. These ratio values can be usefully represented with respect to various parameters in order to better understand their trends. **Fig. 7.16** for example, shows the variation of this overall mechanical/electrical efficiency with respect to the power produced and the turbine's rotational speed, two parameters that are likely to influence electrical and mechanical efficiency.

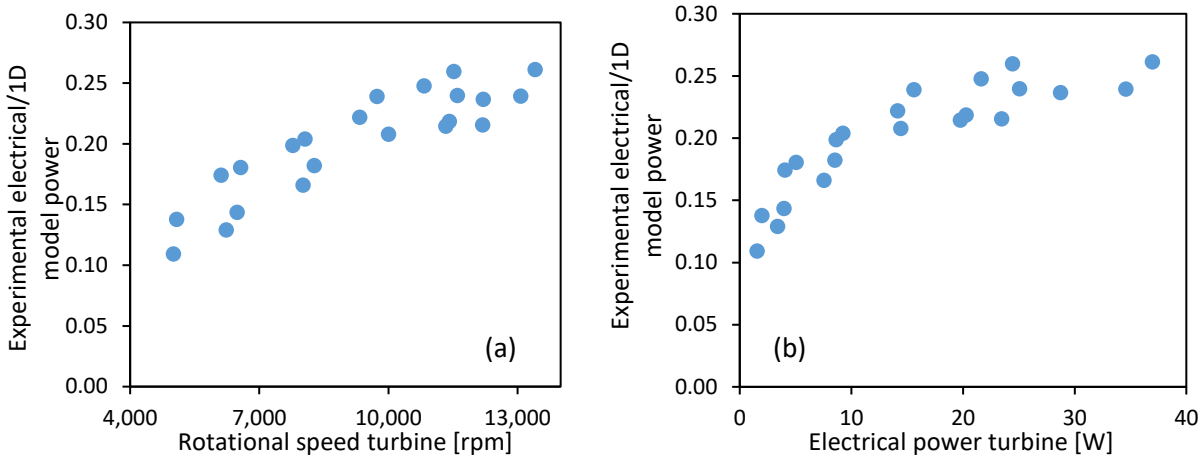


**Fig. 7.16 –** Ratio between experimental electrical power and 1D model mechanical power versus rotational speed (a) and electrical power of the turbine (b)

Finally, **Fig. 7.17** compares experimental turbine power output with the results of the 1D model using a fix electromechanical efficiency of 0.23 **Fig. 7.17(a)** and supposing a linear dependency of this efficiency from the rotational speed of the turbine (**Fig. 7.17(b)** in which $\eta_{elec,mech} = 0.065 + 1.5 \cdot 10^{-5} \cdot \omega_{rpm}$). It can be noticed that the use of a fix efficiency is already sufficient to achieve good agreement between experimental and numerical model results. However, the use of a variable efficiency gives better results for lower power productions (i.e., for lower turbine rotational speeds).

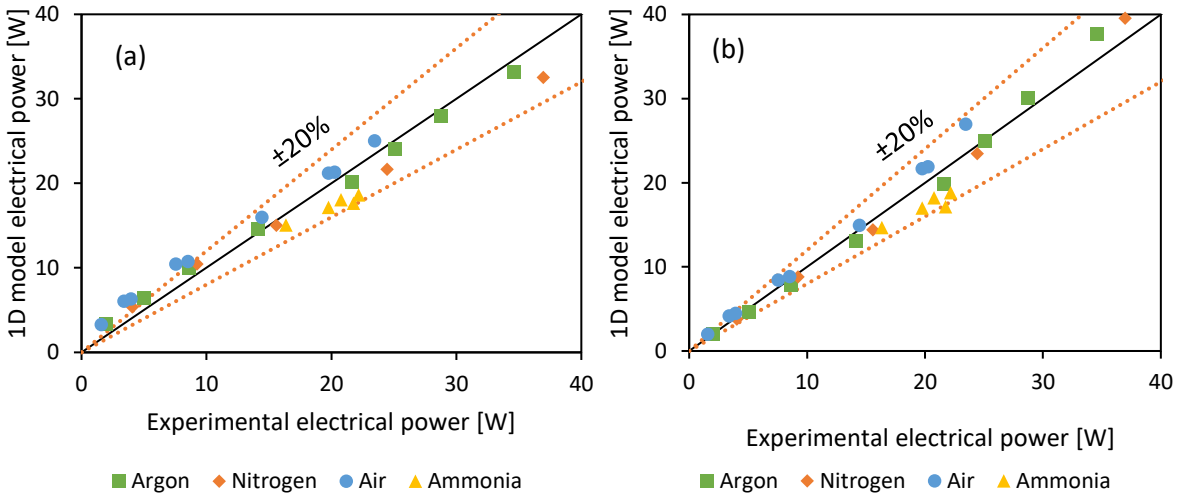


**Fig. 7.17 –** Experimental turbine electrical power output versus numerical model using a fix electromechanical efficiency (a) and a variable electrical efficiency function of the rotational speed (b).

# 7.5 State properties and cost tables

**Table 7.4 -** Exergoeconomic parameters results for the cases in **Table 5.5** using heat exchangers cost correlations from [55].

| Parameters | Nominal point | Base case | Scale-up x25 |
|---|---|---|---|
| **Exergoeconomic performance for $c_{fuel} = 0$ \$/GJ** | | | |
| Exergoeconomic factor, $f$ [-] | 1 | 1 | 1 |
| Unit cost of produced cooling, $c_{cooling}$ [\$/GJ] | 165 (0.60 \$/kWh) | 93 (0.33 \$/kWh) | 26 (0.09 \$/kWh) |
| Unit cost of produced electricity, $c_{ele}$ [\$/GJ] | 1,394 (5.02 \$/kWh) | 1,070 (3.85 \$/kWh) | 52 (0.19 \$/kW) |
| Unit cost of products, $c_p$ [\$/GJ] | 1,559 (5.62\$/kWh) | 1,163 (4.18 \$/kWh) | 78 (0.28 \$/kWh) |
| Unit cost of produced exergy, $UCOPE$ [\$/GJ] | 1,036 (3.73 \$/kWh) | 660 (2.38 \$/kWh) | 43 (0.15 \$/kWh) |
| **Exergoeconomic performance for $c_{fuel} = 15$ \$/GJ** | | | |
| Exergoeconomic factor, $f$ [-] | 0.87 | 0.88 | 0.41 |
| Unit cost of produced cooling, $c_{cooling}$ [\$/GJ] | 275 (0.99 \$/kWh) | 156 (0.56 \$/kWh) | 86 (0.31 \$/kWh) |
| Unit cost of produced electricity, $c_{ele}$ [\$/GJ] | 1,563 (5.62 \$/kWh) | 1,186 (4.27 \$/kWh) | 121 (0.43 \$/kW) |
| Unit cost of products, $c_p$ [\$/GJ] | 1,838 (6.61 \$/kWh) | 1,342 (4.83 \$/kWh) | 207 (0.74 \$/kWh) |
| Unit cost of produced exergy, $UCOPE$ [\$/GJ] | 1,197 (4.31 \$/kWh) | 758 (2.73 \$/kWh) | 108 (0.40 \$/kWh) |

**Table 7.5 -** State properties and costs of the system in the nominal point of the pilot plant.

| *Stream* | $T_i$ $[°C]$ | $P_i$ $[bar]$ | $h_i$ $[kJ/kg]$ | $s_i$ $[kJ/kgK]$ | $\dot{m}_i$ $[kg/h]$ | $x_i$ $[-]$ | $\dot{E}x_i^{PH}$ $[kW]$ | $\dot{E}x_i^{CH}$ $[kW]$ | $c_{fuel} = 0$ \$/GJ | | $c_{fuel} = 15$ \$/GJ | |
|---|---|---|---|---|---|---|---|---|---|---|---|---|
| | | | | | | | | | $c_i$ $[\$/GJ]$ | $\dot{C}_i$ $[\$/h]$ | $c_i$ $[\$/GJ]$ | $\dot{C}_i$ $[\$/h]$ |
| 1 | 28.60 | 6.27 | -109.8 | 0.270 | 100 | 0.535 | 0.9 | 295.3 | 98.57 | 105.1 | 179.80 | 191.7 |
| 2 | 28.66 | 10.54 | -109.1 | 0.270 | 100 | 0.535 | 0.9 | 295.3 | 98.67 | 105.2 | 179.90 | 191.8 |
| 3 | 62.52 | 10.54 | 81.6 | 0.862 | 100 | 0.535 | 1.3 | 295.3 | 98.74 | 105.4 | 180.00 | 192.2 |
| 4 | 94.50 | 10.54 | 204.9 | 1.191 | 71 | 0.351 | 0.6 | 138.4 | 98.00 | 49.1 | 178.80 | 89.5 |
| 5 | 33.92 | 10.54 | -62.8 | 0.396 | 71 | 0.351 | 0.0 | 138.4 | 98.03 | 48.9 | 178.80 | 89.1 |
| 6 | 34.01 | 6.27 | -62.8 | 0.397 | 71 | 0.351 | 0.0 | 138.4 | 98.03 | 48.9 | 178.80 | 89.1 |
| 7 | 67.84 | 10.54 | 1415.0 | 4.707 | 29 | 0.989 | 2.7 | 156.9 | 98.18 | 56.4 | 179.10 | 102.9 |
| 8 | 67.84 | 10.54 | 1415.0 | 4.708 | 12 | 0.989 | 1.1 | 67.5 | 98.18 | 24.3 | 179.10 | 44.3 |
| 9 | 26.95 | 10.54 | 119.3 | 0.459 | 12 | 0.989 | 1.0 | 67.5 | 98.40 | 24.3 | 179.40 | 44.3 |
| 10 | 16.41 | 10.54 | 69.1 | 0.288 | 12 | 0.989 | 1.0 | 67.5 | 98.43 | 24.3 | 179.50 | 44.3 |
| 11 | 10.86 | 6.27 | 69.1 | 0.291 | 12 | 0.989 | 1.0 | 67.5 | 98.43 | 24.3 | 179.50 | 44.3 |
| 12 | 15.86 | 6.27 | 1213.0 | 4.293 | 12 | 0.989 | 0.9 | 67.5 | 98.43 | 24.2 | 179.50 | 44.2 |
| 13 | 22.80 | 6.27 | 1263.0 | 4.464 | 12 | 0.989 | 0.9 | 67.5 | 98.43 | 24.2 | 179.50 | 44.2 |
| 14 | 67.84 | 10.54 | 1415.0 | 4.707 | 16 | 0.989 | 1.5 | 89.4 | 98.18 | 32.1 | 179.10 | 58.6 |
| 15 | 95.00 | 10.54 | 1485.0 | 4.904 | 16 | 0.989 | 1.6 | 89.4 | 98.14 | 32.1 | 179.00 | 58.6 |
| 16 | 74.58 | 6.27 | 1451.0 | 5.051 | 16 | 0.989 | 1.2 | 89.4 | 98.14 | 32.0 | 179.00 | 58.4 |
| 17 | 48.49 | 6.27 | 1370.0 | 4.808 | 29 | 0.989 | 2.1 | 156.9 | 98.28 | 56.3 | 179.20 | 102.6 |

**Table 7.6 -** State properties and costs of the system in the base case point of the pilot plant.

| *Stream* | $T_i$ $[°C]$ | $P_i$ $[bar]$ | $h_i$ $[kJ/kg]$ | $s_i$ $[kJ/kgK]$ | $\dot{m}_i$ $[kg/h]$ | $x_i$ $[-]$ | $\dot{E}x_i^{PH}$ $[kW]$ | $\dot{E}x_i^{CH}$ $[kW]$ | $c_{fuel} = 0$ \$/GJ | | $c_{fuel} = 15$ \$/GJ | |
|---|---|---|---|---|---|---|---|---|---|---|---|---|
| | | | | | | | | | $c_i$ $[\$/GJ]$ | $\dot{C}_i$ $[\$/h]$ | $c_i$ $[\$/GJ]$ | $\dot{C}_i$ $[\$/h]$ |
| 1 | 32.34 | 4.71 | -94.5 | 0.326 | 100 | 0.514 | 0.7 | 284.1 | 61.31 | 62.9 | 112.10 | 114.9 |
| 2 | 32.43 | 10.35 | -93.6 | 0.326 | 100 | 0.514 | 0.7 | 284.1 | 61.39 | 63.0 | 112.20 | 115.0 |
| 3 | 65.15 | 10.35 | 91.0 | 0.894 | 100 | 0.514 | 1.2 | 284.1 | 61.44 | 63.1 | 112.30 | 115.3 |
| 4 | 94.76 | 10.35 | 207.3 | 1.195 | 74 | 0.346 | 0.7 | 141.5 | 61.04 | 31.2 | 111.70 | 57.1 |
| 5 | 38.15 | 10.35 | -42.9 | 0.457 | 74 | 0.346 | 0.0 | 141.5 | 61.06 | 31.1 | 111.70 | 56.9 |
| 6 | 38.26 | 4.71 | -42.9 | 0.459 | 74 | 0.346 | 0.0 | 141.5 | 61.07 | 31.1 | 111.70 | 56.9 |
| 7 | 70.20 | 10.35 | 1424.0 | 4.743 | 26 | 0.987 | 2.4 | 142.6 | 61.05 | 31.9 | 111.70 | 58.3 |
| 8 | 70.20 | 10.35 | 1424.0 | 4.743 | 10 | 0.987 | 0.9 | 56.0 | 61.05 | 12.5 | 111.70 | 22.9 |
| 9 | 26.44 | 10.35 | 115.2 | 0.451 | 10 | 0.987 | 0.9 | 56.0 | 61.23 | 12.5 | 111.90 | 22.9 |
| 10 | 8.79 | 10.35 | 31.8 | 0.164 | 10 | 0.987 | 0.9 | 56.0 | 61.27 | 12.5 | 112.00 | 22.9 |
| 11 | 2.86 | 4.71 | 31.8 | 0.168 | 10 | 0.987 | 0.9 | 56.0 | 61.28 | 12.5 | 112.00 | 22.9 |
| 12 | 7.86 | 4.71 | 1190.0 | 4.336 | 10 | 0.987 | 0.6 | 56.0 | 61.28 | 12.5 | 112.00 | 22.8 |
| 13 | 21.56 | 4.71 | 1274.0 | 4.626 | 10 | 0.987 | 0.6 | 56.0 | 61.28 | 12.5 | 112.00 | 22.8 |
| 14 | 70.20 | 10.35 | 1424.0 | 4.743 | 16 | 0.987 | 1.5 | 86.6 | 61.05 | 19.4 | 111.70 | 35.4 |
| 15 | 95.00 | 10.35 | 1488.0 | 4.921 | 16 | 0.987 | 1.5 | 86.6 | 61.04 | 19.4 | 111.60 | 35.4 |
| 16 | 63.28 | 4.71 | 1433.0 | 5.133 | 16 | 0.987 | 1.0 | 86.6 | 61.04 | 19.3 | 111.60 | 35.2 |
| 17 | 45.02 | 4.71 | 1371.0 | 4.941 | 26 | 0.987 | 1.6 | 142.6 | 61.14 | 31.7 | 111.80 | 58.0 |

**Table 7.7 -** State properties and costs of the streams in the base case for the scaled-up plant (scale factor 25).

| *Stream* | $T_i$ $[°C]$ | $P_i$ $[bar]$ | $h_i$ $[kJ/kg]$ | $s_i$ $[kJ/kgK]$ | $\dot{m}_i$ $[kg/h]$ | $x_i$ $[-]$ | $\dot{E}x_i^{PH}$ $[kW]$ | $\dot{E}x_i^{CH}$ $[kW]$ | $c_{fuel} = 0$ \$/GJ | | $c_{fuel} = 15$ \$/GJ | |
|---|---|---|---|---|---|---|---|---|---|---|---|---|
| | | | | | | | | | $c_i$ $[\$/GJ]$ | $\dot{C}_i$ $[\$/h]$ | $c_i$ $[\$/GJ]$ | $\dot{C}_i$ $[\$/h]$ |
| 1 | 31.28 | 4.71 | -99.0 | 0.310 | 2500 | 0.519 | 19.10 | 7169 | 7.94 | 205.6 | 56.01 | 1449 |
| 2 | 31.37 | 10.39 | -98.1 | 0.310 | 2500 | 0.519 | 19.59 | 7169 | 7.95 | 205.7 | 56.02 | 1450 |
| 3 | 64.68 | 10.39 | 92.3 | 0.897 | 2500 | 0.519 | 30.35 | 7169 | 7.96 | 206.2 | 56.06 | 1453 |
| 4 | 95.32 | 10.39 | 210.4 | 1.203 | 1821 | 0.344 | 16.66 | 3472 | 7.90 | 99.2 | 55.79 | 700.7 |
| 5 | 36.09 | 10.39 | -51.1 | 0.430 | 1821 | 0.344 | 0.99 | 3472 | 7.90 | 98.8 | 55.79 | 697.5 |
| 6 | 36.20 | 4.71 | -51.1 | 0.432 | 1821 | 0.344 | 0.67 | 3472 | 7.90 | 98.8 | 55.80 | 697.5 |
| 7 | 69.91 | 10.39 | 1423 | 4.738 | 679 | 0.988 | 62.36 | 3697 | 7.91 | 107.0 | 55.83 | 755.5 |
| 8 | 69.91 | 10.39 | 1423 | 4.738 | 280 | 0.988 | 25.69 | 1523 | 7.91 | 44.1 | 55.83 | 311.3 |
| 9 | 26.55 | 10.39 | 116.0 | 0.453 | 280 | 0.988 | 23.40 | 1523 | 7.95 | 44.2 | 55.93 | 311.4 |
| 10 | 8.79 | 10.39 | 32.0 | 0.164 | 280 | 0.988 | 23.57 | 1523 | 7.95 | 44.3 | 55.94 | 311.5 |
| 11 | 2.86 | 4.71 | 32.0 | 0.168 | 280 | 0.988 | 23.48 | 1523 | 7.95 | 44.3 | 55.95 | 311.5 |
| 12 | 7.86 | 4.71 | 1192 | 4.343 | 280 | 0.988 | 16.91 | 1523 | 7.95 | 44.1 | 55.95 | 310.2 |
| 13 | 21.93 | 4.71 | 1276 | 4.635 | 280 | 0.988 | 16.68 | 1523 | 7.95 | 44.1 | 55.95 | 310.1 |
| 14 | 69.91 | 10.39 | 1423 | 4.738 | 399 | 0.988 | 36.67 | 2174 | 7.91 | 62.9 | 55.83 | 444.3 |
| 15 | 95.00 | 10.39 | 1487 | 4.918 | 399 | 0.988 | 37.84 | 2174 | 7.91 | 63.0 | 55.81 | 444.4 |
| 16 | 49.94 | 4.71 | 1396 | 5.021 | 399 | 0.988 | 24.34 | 2174 | 7.91 | 62.6 | 55.81 | 441.6 |
| 17 | 39.65 | 4.71 | 1347 | 4.866 | 679 | 0.988 | 40.78 | 3697 | 7.92 | 106.7 | 55.87 | 751.8 |

# List of publications

## *Journal Articles*

- S. Braccio, H. Trieu Phan, M. Wirtz, N. Tauveron, and N. Le Pierrès, "Simulation of an ammonia-water absorption cycle using exchanger effectiveness," *Appl. Therm. Eng.*, p. 118712, 2022, doi: https://doi.org/10.1016/j.applthermaleng.2022.118712.
- S. Braccio, A. Di Nardo, G. Calchetti, H. T. Phan, N. Le Pierrès, and N. Tauveron, "Performance evaluation of a micro partial admission impulse axial turbine in a combined ammonia-water cooling and electricity absorption cycle," submitted to "Energy" Journal, May 2022.
- S. Braccio, N. Guillou, N. Le Pierrès, N. Tauveron, H. Trieu Phan, Mass-flowrate-maximization thermodynamic model and simulation of supersonic real-gas ejectors used in refrigeration systems, Therm. Sci. Eng. Prog. (2022) 101615. https://doi.org/10.1016/j.tsep.2022.101615.
- S. Braccio, H.T. Phan, N. Tauveron, N. Le Pierrès, A. Arteconi, Energy, exergy and exergoeconomic analysis and optimisation of the scale-up of a combined ammonia-water absorption pilot plant producing electricity and refrigeration, Energy Convers. Manag. 278 (2023) 116686. https://doi.org/10.1016/j.enconman.2023.116686.
- S. Braccio, H. T. Phan, N. Le Pierrès, and N. Tauveron, "Development and experimentation of a combined cooling and electricity production prototype integrating an axial micro-turbine in an absorption chiller", submitted to "Applied Thermal Engineering" Journal, January 2023.

## *Conference papers*

- S. Braccio, H. T. Phan, N. Tauveron, and N. Le Pierrès, "Study of a cold and electric cogeneration machine using a low temperature heat source.", SFT 2021, 2021, doi: https://doi.org/10.25855/SFT2021-036.
- S. Braccio, H. T. Phan, N. Tauveron, and N. Le Pierrès, "Study of the integration of a supersonic impulse turbine in a $NH_3/H_2O$ absorption heat pump for combined cooling and power production from a low temperature heat source," E3S Web Conf., vol. 312, p. 08018, 2021, doi: 10.1051/e3sconf/202131208018.
- S. Braccio, A. Arteconi, H. T. Phan, N. Tauveron, and N. Le Pierrès, "Energy and exergy analysis of a pilot plant for the combined production of cooling and electricity from a low temperature heat source through an absorption process.," Proc. ECOS 2022, pp. 529–540, 2022.
- S. Braccio, H. T. Phan, N. Tauveron, and N. Le Pierrès, "Analyse énergétique et exergétique d'une installation pilote de coproduction de froid et électricité," Proc. SFGP 2022.

## *Technical journals articles*

- S. Braccio, H. T. Phan, N. Tauveron, and N. Le Pierrès, "Cycle à absorption NH3/H2O pour coproduction de froid et électricité. Valorisation de sources de chaleur à basse température [80-200 °C]," Techniques de l'ingénieur Innov. Technol., vol. TIP958WEB, doi: https://doi.org/10.51257/a-v1-in701.

## *Patents*

- S. Braccio, H. T. Phan, N. Tauveron, and N. Le Pierrès, "Système de production de froid et d'électricité à partir d'une source thermique à basse température, permettant un réglage du rapport entre production de froid et production électrique". Reference number: FR2107442.
- S. Braccio, N. Guillou, H. T. Phan, "Dispositif de production de froid comprenant un cycle de réfrigération à éjecteur simple amélioré et procédé de production de froid associé". Reference number: FR2212407.

## *Participation to conferences*

- SFT 2021 – Congrès français de thermique 2021. 1-3 June 2021, Online.
- ATI 2021 – Congresso annuale associazione termotecnica italiana. 15-17 September 2021, Online.
- ASME Turbo Expo 2021 – American society of mechanical engineers turbomachinery technical conference and exposition. 7-11 June 2021, Online.
- ESAT 2021 – European symposium on applied thermodynamics. 5-9 July 2021, Online
- ECOS 2022 – 35$^{th}$ international conference on efficiency, cost optimization, simulation and environmental impact of energy systems. 3-7 July 2022, Copenhagen.
- SFGP 2022 – Congrès societé française de genie de proceeds. 7-10 November 2022, Toulouse.

## *Other achievements*

- Three-months research stay at KU Leuven
- Participation to the "Design your own renewable district heating and cooling system". Delft 2022.
- Virtual mobility at Universidad de Zaragoza in the framework of the UNITA alliance virtual mobility program following the course of "Advanced financial instruments".

# References


[1] Mission Innovation initiative, (n.d.). http://mission-innovation.net/ (accessed December 8, 2022).

[2] European Commission, Clean energy for all Europeans, Euroheat Power (English Ed. (2019). https://doi.org/10.2833/9937.

[3] M. Ragwitz, A. Herbst, S. Hirzel, M. Ragwitz, M. Rehfeldt, M. Reuter, J. Steinbach, EUROPEAN COMMISSION DIRECTORATE-GENERAL FOR ENERGY Directorate C. 2 – New energy technologies, innovation and clean coal, (n.d.).

[4] RTE- Electricy Report 2018 in France, https://bilan-electrique-2018.rte-france.com/wp-content/uploads/2019/02/BE-PDF-2018-1.pdf, 2019.

[5] K.E. Herold, R. Radermacher, S.A. Klein, Absorption Chillers and Heat Pumps, Second, CRC Press, 2016. https://doi.org/10.1201/b19625.

[6] F.B. M. Wirtz, B. Stutz, H.T. Phan, Numerical modeling and integration of a falling film plate generator/rectifier in a NH3/H2O absorption machine prototype, (n.d.).

[7] D.Y. Goswami, F. Xu, Analysis of a New Thermodynamic Cycle for Combined Power and Cooling Using Low and Mid Temperature Solar Collectors, J. Sol. Energy Eng. 121 (1999) 91–97. https://doi.org/https://doi.org/10.1115/1.2888152.

[8] N. Shokati, F. Ranjbar, M. Yari, A comprehensive exergoeconomic analysis of absorption power and cooling cogeneration cycles based on Kalina, part 1: Simulation, Energy Convers. Manag. 158 (2018) 437–459. https://doi.org/10.1016/j.enconman.2017.12.086.

[9] H. Ghaebi, T. Parikhani, H. Rostamzadeh, Energy, exergy and thermoeconomic analysis of a novel combined cooling and power system using low-temperature heat source and LNG cold energy recovery, Energy Convers. Manag. 150 (2017) 678–692. https://doi.org/https://doi.org/10.1016/j.enconman.2017.08.052.

[10] W. Huang, J. Wang, J. Xia, P. Zhao, Y. Dai, Performance analysis and optimization of a combined cooling and power system using low boiling point working fluid driven by engine waste heat, Energy Convers. Manag. 180 (2019) 962–976. https://doi.org/https://doi.org/10.1016/j.enconman.2018.11.041.

[11] J. Dardouch, M. Charia, A. Bernatchou, Study of an absorption refrigeration machine improved with distillation column, J Mater Env. 9 (2018) 772–783. https://doi.org/10.26872/jmes.2018.9.2.85.

[12] Q. Blondel, N. Tauveron, N. Caney, N. Voeltzel, Experimental study and optimization of the Organic Rankine Cycle with pure NovecTM649 and zeotropic mixture NovecTM649/HFE7000 as working fluid, Appl. Sci. (2019). https://doi.org/10.3390/app9091865.

[13] F. Boudéhenn, H. Demasles, J. Wyttenbach, X. Jobard, D. Chèze, P. Papillon, Development of a 5 kW cooling capacity ammonia-water absorption chiller for solar cooling applications, Energy Procedia. 30 (2012) 35–43. https://doi.org/10.1016/j.egypro.2012.11.006.

[14] S. Braccio, H.T. Phan, N. Tauveron, N. Le Pierrès, Study of a cold and electric cogeneration machine using a low temperature heat source., SFT 2021. (2021). https://doi.org/https://doi.org/10.25855/SFT2021-036.

[15] W.P. Prospects, World Population Prospects 2022 : Summary of Results Ten key messages, (2023) 2–3.

[16] R. Gugulothu, N.S. Somanchi, H.B. Banoth, K. Banothu, A Review on Solar Powered Air Conditioning System, Procedia Earth Planet. Sci. 11 (2015) 361–367. https://doi.org/https://doi.org/10.1016/j.proeps.2015.06.073.

[17] REPowerEU, Eur. Comm. - Eur. Comm. (2022). https://ec.europa.eu/commission/presscorner/detail/en/ip_22_3131.

[18] D. 2017 DG Energy, The Strategic Energy Technology (SET) Plan - At the heart of energy research and innovation in Europe- European Commission Directorate-General for Research and Innovation, 2017.

[19] International Renewable Energy Agency (IRENA), Global energy transformation: A roadmap to 2050 (2019 edition), ISBN 978-92-9260-121-8. (2019).

[20] EU Strategy on Heating and cooling, 2016. https://eur-lex.europa.eu/legal-content/EN/TXT/?qid=1575551754568&uri=CELEX:52016DC0051.

[21] F. Birol, The Future of Cooling-Opportunities for energy efficient air conditioning- Opportunities for energy efficient air conditioning, OECD/IEA 2018. (2018).

[22] R. Narayanan, Chapter Seven - Heat-Driven Cooling Technologies, in: Clean Energy Sustain. Dev., Academic Press, 2017: pp. 191–212. https://doi.org/https://doi.org/10.1016/B978-0-12-805423-9.00007-7.

[23] Low-grade waste heat utilization in the European Union, Interreg Cent. Eur. (2022). http://www.interreg-central.eu/Content.Node/CE-HEAT/Low-grade-waste-heat-utilization-in-the-European-Union.html.

[24] A. Marina, S. Spoelstra, H.A. Zondag, A.K. Wemmers, An estimation of the European industrial heat pump market potential, Renew. Sustain. Energy Rev. 139 (2021) 110545. https://doi.org/https://doi.org/10.1016/j.rser.2020.110545.
[25] RHC (Renewable Heating and cooling), 2050- Vision for 100 % Renewable heating and cooling in Europe, Https://Www.Euroheat.Org/Publications/2050-Vision-100-Renewable-Heating-Cooling-Europe/. (2020).
[26] Horizon 2020 - Work Programm 2018-2020 - Secure, clean and efficient energy- Version 25 March 2020, Eur. Comm. Decis. C(2020)1862. (2020).
[27] U. Jakob, 6 - Solar cooling technologies, in: Renew. Heat. Cool., Woodhead Publishing, 2016: pp. 119–136. https://doi.org/https://doi.org/10.1016/B978-1-78242-213-6.00006-0.
[28] IEA (2012), Technology Roadmap - Solar Heating and Cooling, IEA, Paris https://www.iea.org/reports/technology-roadmap-solar-heating-and-cooling, (n.d.).
[29] M. Wirtz, Development of a falling-film desorber combining vapor generation and purification for ammonia–water absorption chiller (Modeling and Experiments), PhD Thesis, Université Savoie Mont Blanc, 2022.
[30] W. Weiss, M. Spork-Dur, Solar Heat Worldwide 2018, 2018. https://www.iea-shc.org/Data/Sites/1/publications/Solar-Heat-Worldwide-2018.pdf.
[31] A. Altamirano, N. Le Pierrès, B. Stutz, Review of small-capacity single-stage continuous absorption systems operating on binary working fluids for cooling: Theoretical, experimental and commercial cycles, Int. J. Refrig. 106 (2019) 350–373. https://doi.org/10.1016/j.ijrefrig.2019.06.033.
[32] S. Braccio, H.T. Phan, N. Tauveron, N. Le Pierrès, Study of a cold and electric cogeneration machine using a low temperature heat source., in: SFT 2021, 2021. https://doi.org/10.25855/SFT2021-036.
[33] N. Voeltzel, H.T. Phan, Q. Blondel, B. Gonzalez, N. Tauveron, N.T. N. Voeltzel, H.T. Phan, Q. Blondel, B. Gonzalez, Steady and dynamical analysis of a combined cooling and power cycle, Therm. Sci. Eng. Prog. 19 (2020) 100650. https://doi.org/10.1016/j.tsep.2020.100650.
[34] E. Fanelli, S. Braccio, G. Pinto, G. Cornacchia, G. Braccio, Small scale Organic Rankine Cycle testing for low grade heat recovery by using refrigerants as working fluids, Model. Meas. Control C. 79 (2018) 70–78. https://doi.org/10.18280/mmc-c.790302.
[35] M. Akbari Kordlar, S.M.S. Mahmoudi, Exergeoconomic analysis and optimization of a novel cogeneration system producing power and refrigeration, Energy Convers. Manag. 134 (2017) 208–220. https://doi.org/10.1016/j.enconman.2016.12.007.
[36] V. Zare, A comparative thermodynamic analysis of two tri-generation systems utilizing low-grade geothermal energy, Energy Convers. Manag. 118 (2016) 264–274. https://doi.org/https://doi.org/10.1016/j.enconman.2016.04.011.
[37] V. Novotny, M. Kolovratnik, Absorption power cycles for low-temperature heat sources using aqueous salt solutions as working fluids, Int. J. Energy Res. 41 (2017) 952–975. https://doi.org/10.1002/er.3671.
[38] D.S. Ayou, J.C. Bruno, R. Saravanan, A. Coronas, An overview of combined absorption power and cooling cycles, Renew. Sustain. Energy Rev. 21 (2013) 728–748. https://doi.org/10.1016/j.rser.2012.12.068.
[39] A. Khaliq, Energetic and exergetic performance investigation of a solar based integrated system for cogeneration of power and cooling, Appl. Therm. Eng. 112 (2017) 1305–1316. https://doi.org/10.1016/j.applthermaleng.2016.10.127.
[40] F. Xu, D. Yogi Goswami, S. S. Bhagwat, A combined power/cooling cycle, Energy. (2000). https://doi.org/10.1016/S0360-5442(99)00071-7.
[41] G.P. Kumar, R. Saravanan, A. Coronas, Experimental studies on combined cooling and power system driven by low-grade heat sources, Energy. 128 (2017) 801–812. https://doi.org/10.1016/j.energy.2017.04.066.
[42] J. Wang, Y. Dai, T. Zhang, S. Ma, Parametric analysis for a new combined power and ejector-absorption refrigeration cycle, Energy. 34 (2009) 1587–1593. https://doi.org/10.1016/j.energy.2009.07.004.
[43] S. Braccio, H.T. Phan, N. Tauveron, N. Le Pierrès, Study of the integration of a supersonic impulse turbine in a NH3/H2O absorption heat pump for combined cooling and power production from a low temperature heat source, in: A.T.I.I.T. Association, A.T.I.I.T. Association (Eds.), E3S Web Conf., 2021: p. 8018. https://doi.org/10.1051/e3sconf/202131208018.
[44] F. Boudéhenn, S. Bonnot, H. Demasles, A. Lazrak, Comparison of Different Modeling Methods for a Single Effect Water-Lithium Bromide Absorption Chiller, in: ISES Conf. Proc., 2014. https://doi.org/10.18086/eurosun.2014.07.04.
[45] D. Triche, Numerical and experimental study of coupled mass and heat transfers in the absorber of an ammonia-water absorption chiller. PhD thesis., Université Grenoble Alpes, 2016. https://tel.archives-ouvertes.fr/tel-01696252.
[46] C.M. Invernizzi, D. Bonalumi, 5 - Thermal stability of organic fluids for Organic Rankine Cycle systems, in: Org. Rank. Cycle Power Syst. Technol. Appl., Woodhead Publishing, 2017: pp. 121–151. https://doi.org/https://doi.org/10.1016/B978-0-08-100510-1.00005-3.

[47] H. Fang, J. Xia, K. Zhu, Y. Su, Y. Jiang, Industrial waste heat utilization for low temperature district heating, Energy Policy. 62 (2013) 236–246. https://doi.org/https://doi.org/10.1016/j.enpol.2013.06.104.
[48] C. Haddad, C. Périlhon, A. Danlos, M.-X. François, G. Descombes, Some Efficient Solutions to Recover Low and Medium Waste Heat: Competitiveness of the Thermoacoustic Technology, Energy Procedia. 50 (2014) 1056–1069. https://doi.org/https://doi.org/10.1016/j.egypro.2014.06.125.
[49] H. Jouhara, N. Khordehgah, S. Almahmoud, B. Delpech, A. Chauhan, S.A. Tassou, Waste heat recovery technologies and applications, Therm. Sci. Eng. Prog. 6 (2018) 268–289. https://doi.org/10.1016/j.tsep.2018.04.017.
[50] P. Durcansky, R. Nosek, J. Jandacka, Use of stirling engine for waste heat recovery, Energies. 13 (2020). https://doi.org/10.3390/en13164133.
[51] K.A.A. Khalid, T.J. Leong, K. Mohamed, Review on Thermionic Energy Converters, IEEE Trans. Electron Devices. 63 (2016) 2231–2241. https://doi.org/10.1109/TED.2016.2556751.
[52] M. Yari, S.M.S. Mahmoudi, Utilization of waste heat from GT-MHR for power generation in organic Rankine cycles, Appl. Therm. Eng. 30 (2010) 366–375. https://doi.org/https://doi.org/10.1016/j.applthermaleng.2009.09.017.
[53] E. Macchi, Theoretical basis of the Organic Rankine Cycle, in: Org. Rank. Cycle Power Syst. Technol. Appl., Woodhead Publishing, 2016. https://doi.org/10.1016/B978-0-08-100510-1.00001-6.
[54] K. Rahbar, S. Mahmoud, R.K. Al-Dadah, N. Moazami, S.A. Mirhadizadeh, Review of organic Rankine cycle for small-scale applications, Energy Convers. Manag. (2017). https://doi.org/10.1016/j.enconman.2016.12.023.
[55] S. Quoilin, M. Van Den Broek, S. Declaye, P. Dewallef, V. Lemort, Techno-economic survey of organic rankine cycle (ORC) systems, Renew. Sustain. Energy Rev. 22 (2013) 168–186. https://doi.org/10.1016/j.rser.2013.01.028.
[56] S. Quoilin, Sustainable energy conversion through the use of Organic Rankine Cycles for waste heat recovery and solar applications. PhD Thesis, 2011.
[57] M. Astolfi, 3 - Technical options for Organic Rankine Cycle systems, in: Org. Rank. Cycle Power Syst., Woodhead Publishing, 2017: pp. 67–89. https://doi.org/https://doi.org/10.1016/B978-0-08-100510-1.00003-X.
[58] S. Karellas, A. Schuster, A.-D.D. Leontaritis, Influence of supercritical ORC parameters on plate heat exchanger design, Appl. Therm. Eng. 33–34 (2012) 70–76. https://doi.org/https://doi.org/10.1016/j.applthermaleng.2011.09.013.
[59] O.A. Oyewunmi, S. Ferré-Serres, S. Lecompte, M. van den Broek, M. De Paepe, C.N. Markides, An Assessment of Subcritical and Trans-critical Organic Rankine Cycles for Waste-heat Recovery, Energy Procedia. 105 (2017) 1870–1876. https://doi.org/https://doi.org/10.1016/j.egypro.2017.03.548.
[60] M. Astolfi, D. Alfani, S. Lasala, E. Macchi, Comparison between ORC and CO2 power systems for the exploitation of low-medium temperature heat sources, Energy. 161 (2018) 1250–1261. https://doi.org/https://doi.org/10.1016/j.energy.2018.07.099.
[61] B. Saleh, G. Koglbauer, M. Wendland, J. Fischer, Working fluids for low-temperature organic Rankine cycles, Energy. 32 (2007) 1210–1221. https://doi.org/https://doi.org/10.1016/j.energy.2006.07.001.
[62] G. Qiu, Selection of working fluids for micro-CHP systems with ORC, Renew. Energy. (2012). https://doi.org/10.1016/j.renene.2012.06.006.
[63] H. Chen, D.Y. Goswami, E.K. Stefanakos, A review of thermodynamic cycles and working fluids for the conversion of low-grade heat, Renew. Sustain. Energy Rev. 14 (2010) 3059–3067. https://doi.org/https://doi.org/10.1016/j.rser.2010.07.006.
[64] I. Dincer, M.E. Demir, 4.8 Steam and Organic Rankine Cycles, in: Compr. Energy Syst., Elsevier, Oxford, 2018: pp. 264–311. https://doi.org/https://doi.org/10.1016/B978-0-12-809597-3.00410-7.
[65] S.M. Besarati, D.Y. Goswami, Supercritical CO2 and other advanced power cycles for concentrating solar thermal (CST) systems, in: Adv. Conc. Sol. Therm. Res. Technol., Woodhead Publishing, 2017: pp. 157–178. https://doi.org/10.1016/B978-0-08-100516-3.00008-3.
[66] A.I. Kalina, Combined-Cycle System With Novel Bottoming Cycle, J. Eng. Gas Turbines Power. 106 (1984) 737–742. https://doi.org/10.1115/1.3239632.
[67] R. Shankar, T. Srinivas, Performance investigation of Kalina cooling cogeneration cycles, Int. J. Refrig. (2018). https://doi.org/10.1016/j.ijrefrig.2017.11.019.
[68] J. Bao, L. Zhao, A review of working fluid and expander selections for organic Rankine cycle, Renew. Sustain. Energy Rev. 24 (2013) 325–342. https://doi.org/https://doi.org/10.1016/j.rser.2013.03.040.
[69] S. Dixon, C. Hall, Fluid Mechanics and Thermodynamics of Turbomachinery, Seventh Ed, Butterworth-Heinemann, 2014. https://doi.org/https://doi.org/10.1016/C2011-0-05059-7.
[70] G. Persico, M. Pini, 8 - Fluid dynamic design of Organic Rankine Cycle turbines, in: Org. Rank. Cycle Power Syst., Woodhead Publishing, 2017: pp. 253–297. https://doi.org/https://doi.org/10.1016/B978-0-08-100510-1.00008-9.

[71] E. Macchi, M. Astolfi, 9 - Axial flow turbines for Organic Rankine Cycle applications, in: Org. Rank. Cycle Power Syst., Woodhead Publishing, 2017: pp. 299–319. https://doi.org/https://doi.org/10.1016/B978-0-08-100510-1.00009-0.
[72] D.Y. Kim, Y.T. Kim, Preliminary design and performance analysis of a radial inflow turbine for ocean thermal energy conversion, Renew. Energy. 106 (2017) 255–263. https://doi.org/10.1016/j.renene.2017.01.038.
[73] G. Persico, M. Pini, V. Dossena, P. Gaetani, Aerodynamics of Centrifugal Turbine Cascades, J. Eng. Gas Turbines Power. 137 (2015). https://doi.org/10.1115/1.4030261.
[74] I. Smith, N. Stosic, A. Kovacevic, Screw Expanders Increase Output and Decrease the Cost of Geothermal Binary Power Plant Systems, Trans. - Geotherm. Resour. Counc. 29 (2005).
[75] M.G. Read, I.K. Smith, N. Stosic, Optimisation of two-stage screw expanders for waste heat recovery applications, in: IOP Conf. Ser. Mater. Sci. Eng., 2015. https://doi.org/10.1088/1757-899X/90/1/012058.
[76] V. Lemort, A. Legros, 12 - Positive displacement expanders for Organic Rankine Cycle systems, in: Org. Rank. Cycle Power Syst., Woodhead Publishing, 2017: pp. 361–396. https://doi.org/https://doi.org/10.1016/B978-0-08-100510-1.00012-0.
[77] V. Vodicka, V. Novotny, J. Mascuch, M. Kolovratnik, Impact of major leakages on characteristics of a rotary vane expander for ORC, Energy Procedia. 129 (2017) 387–394. https://doi.org/10.1016/j.egypro.2017.09.249.
[78] M. Tahir, N. Yamada, Thermodynamic Analysis of Expansion Profile for Displacement-type Expander in Low-temperature Rankine Cycle, J. Therm. Sci. Technol. - J THERM SCI TECHNOL. 5 (2010) 61–74. https://doi.org/10.1299/jtst.5.61.
[79] O. Badr, S.D. Probert, P. O'Callaghan, Performances of multi-vane expanders, Appl. Energy. 20 (1985) 207–234. https://doi.org/https://doi.org/10.1016/0306-2619(85)90024-8.
[80] D. Seher, T. Lengenfelder, J. Gerhardt, N. Eisenmenger, M. Hackner, I. Krinn, Waste Heat Recovery for Commercial Vehicles with a Rankine Process, 21 St Aachen Colloq. Automob. Engine Technol. (2012) 1–15.
[81] S. Clemente, D. Micheli, M. Reini, R. Taccani, Performance analysis and modeling of different volumetric expanders for small-scale organic rankine cycles, ASME 2011 5th Int. Conf. Energy Sustain. ES 2011. (2011) 375–384. https://doi.org/10.1115/ES2011-54302.
[82] J.L. Bouvier, V. Lemort, G. Michaux, P. Salagnac, T. Kientz, Experimental study of an oil-free steam piston expander for micro-combined heat and power systems, Appl. Energy. 169 (2016) 788–798. https://doi.org/10.1016/j.apenergy.2016.01.122.
[83] R. Dickes, Design and fabrication of a variable wall thickness two-stage scroll expander to be integrated in a micro-solar power plant. MSc Thesis., Université de Liège, 2013. https://doi.org/10.13140/2.1.1893.3760.
[84] M. Deligant, E. Sauret, R. Persky, S. Khelladi, F. Bakir, 3D CFD simulation of a turbocharger compressor used as a turbo expander for Organic Rankine cycle, Proc. 21st Australas. Fluid Mech. Conf. AFMC 2018. (2018) 1–4.
[85] O.E. Balje, A Study on Design Criteria and Matching of Turbomachines: Part A - Similarity relations and Design Criteria of Turbines, J. Eng. Gas Turbines Power. 84 (1962) 83–102. https://doi.org/https://doi.org/10.1115/1.3673386.
[86] A. Landelle, N. Tauveron, P. Haberschill, R. Revellin, S. Colasson, Organic Rankine cycle design and performance comparison based on experimental database, Appl. Energy. (2017). https://doi.org/10.1016/j.apenergy.2017.04.012.
[87] A. Landelle, Experimental and numerical study of transcritical Organic Rankine Cycles for low-grade heat conversion into electricity from various sources. PhD Thesis., Université de Lyon, 2017. https://hal.archives-ouvertes.fr/tel-01731123/document.
[88] P. Whittaker, Corrosion in the Kalina cycle An investigation into corrosion problems at the Kalina cycle geothermal power plant in Húsavík , Iceland. MSc Thesis., University of Akureyri, 2009.
[89] V. Lemort, S. Quoilin, C. Cuevas, J. Lebrun, Testing and modeling a scroll expander integrated into an Organic Rankine Cycle, Appl. Therm. Eng. 29 (2009) 3094–3102. https://doi.org/10.1016/j.applthermaleng.2009.04.013.
[90] T. Tartière, M. Astolfi, A World Overview of the Organic Rankine Cycle Market, Energy Procedia. 129 (2017) 2–9. https://doi.org/10.1016/j.egypro.2017.09.159.
[91] C. Wieland, F. Dawo, C. Schifflechner, M. Astolfi, Market report on Organic Rankine Cycle power systems: recent developments and outlook, Proc. 6th Int. Semin. ORC Power Syst. (2021). https://doi.org/10.14459/2021mp1636584.
[92] IEA, Energy Technology Perspectives 2012 Pathways to a Clean Energy System, Energy Technol. Perspect. 2012 Pathways to a Clean Energy Syst. (2012). https://doi.org/10.1787/energy_tech-2012-en.
[93] X. Wang, H.T. Chua, Absorption Cooling: A Review of Lithium Bromide-Water Chiller Technologies,

Recent Patents Mech. Eng. 2 (2010) 193–213. https://doi.org/10.2174/1874477x10902030193.
[94] R.M. Tozer, R.W. James, Fundamental thermodynamics of ideal absorption cycles, Int. J. Refrig. (1997). https://doi.org/10.1016/S0140-7007(96)00061-8.
[95] H. Perez-Blanco, Absorption heat pump performance for different types of solutions, Int. J. Refrig. (1984). https://doi.org/10.1016/0140-7007(84)90024-0.
[96] J. Sun, L. Fu, S. Zhang, A review of working fluids of absorption cycles, Renew. Sustain. Energy Rev. (2012). https://doi.org/10.1016/j.rser.2012.01.011.
[97] M. de Vega, J.A. Almendros-Ibañez, G. Ruiz, Performance of a LiBr–water absorption chiller operating with plate heat exchangers, Energy Convers. Manag. 47 (2006) 3393–3407. https://doi.org/https://doi.org/10.1016/j.enconman.2006.01.005.
[98] H. Demir, M. Mobedi, S. Ülkü, A review on adsorption heat pump: Problems and solutions, Renew. Sustain. Energy Rev. (2008). https://doi.org/10.1016/j.rser.2007.06.005.
[99] A. Lima, G. Leite, A. Ochoa, C. Dos Santos, J. da Costa, P. Michima, A. Caldas, Absorption refrigeration systems based on ammonia as refrigerant using different absorbents: Review and applications, Energies. 14 (2021). https://doi.org/10.3390/en14010048.
[100] E. Dai, T. Jia, Y. Dai, Theoretical and experimental investigation on a GAX-Based NH3-H2O absorption heat pump driven by parabolic trough solar collector, Sol. Energy. (2020). https://doi.org/10.1016/j.solener.2020.01.011.
[101] K.E. Herold, R. Radermacher, S.A. Klein, Applications of Absorption Chillers and Heat Pumps, in: Absorpt. Chill. Heat Pumps, Second Ed., CRC Press, 2016: pp. 265–270. https://doi.org/10.1201/b19625-14.
[102] W. Wu, B. Wang, W. Shi, X. Li, Absorption heating technologies: A review and perspective, Appl. Energy. (2014). https://doi.org/10.1016/j.apenergy.2014.05.027.
[103] B. C. VON PLATEN ET AL, United States Patent Office, ACM SIGGRAPH Comput. Graph. 28 (1994) 131–134. https://doi.org/10.1145/178951.178972.
[104] K.R. Patil, S.K. Chaudhari, S.S. Katti, Thermodynamic design data for absorption heat pump systems operating on water-lithium iodide—part I. Cooling, Heat Recover. Syst. CHP. 11 (1991) 341–350. https://doi.org/https://doi.org/10.1016/0890-4332(91)90002-L.
[105] T.K. Gogoi, D. Konwar, Exergy analysis of a H2O–LiCl absorption refrigeration system with operating temperatures estimated through inverse analysis, Energy Convers. Manag. 110 (2016) 436–447. https://doi.org/https://doi.org/10.1016/j.enconman.2015.12.037.
[106] J. Patel, B. Pandya, A. Mudgal, Exergy Based Analysis of LiCl-H2O Absorption Cooling System, Energy Procedia. 109 (2017) 261–269. https://doi.org/https://doi.org/10.1016/j.egypro.2017.03.061.
[107] M.B. Shiflett, A. Yokozeki, United States Patent: 8506839 - Absorption cycle utilizing ionic liquids and water as working fluids, 2013. https://patft.uspto.gov/netacgi/nph-Parser?Sect1=PTO1&Sect2=HITOFF&p=1&u=/netahtml/PTO/srchnum.html&r=1&f=G&l=50&d=PALL&s1=8506839.PN.
[108] W. Wu, B. Wang, W. Shi, X. Li, An overview of ammonia-based absorption chillers and heat pumps, Renew. Sustain. Energy Rev. 31 (2014) 681–707. https://doi.org/https://doi.org/10.1016/j.rser.2013.12.021.
[109] D.-W. Sun, Comparison of the performances of NH3-H2O, NH3-LiNO3 and NH3-NaSCN absorption refrigeration systems, Energy Convers. Manag. 39 (1998) 357–368. https://doi.org/https://doi.org/10.1016/S0196-8904(97)00027-7.
[110] P.J. Scammells, J.L. Scott, R.D. Singer, Ionic Liquids: The Neglected Issues, Aust. J. Chem. 58 (2005) 155–169. https://doi.org/10.1071/CH04272.
[111] M. Cvjetko Bubalo, K. Radošević, I. Radojčić Redovniković, J. Halambek, V. Gaurina Srček, A brief overview of the potential environmental hazards of ionic liquids, Ecotoxicol. Environ. Saf. 99 (2014) 1–12. https://doi.org/https://doi.org/10.1016/j.ecoenv.2013.10.019.
[112] J. Cerezo, R.J. Romero, J. Ibarra, A. Rodríguez, G. Montero, A. Acuña, Dynamic simulation of an absorption cooling system with differentworking mixtures, Energies. 11 (2018). https://doi.org/10.3390/en11020259.
[113] R. Saravanan, M.P. Maiya, Thermodynamic comparison of water-based working fluid combinations for a vapour absorption refrigeration system, Appl. Therm. Eng. 18 (1998) 553–568. https://doi.org/10.1016/S1359-4311(97)00072-0.
[114] M. Bourouis, M. Vallès, M. Medrano, A. Coronas, Absorption of water vapour in the falling film of water–(LiBr+LiI+LiNO3+LiCl) in a vertical tube at air-cooling thermal conditions, Int. J. Therm. Sci. 44 (2005) 491–498. https://doi.org/https://doi.org/10.1016/j.ijthermalsci.2004.11.009.
[115] J.C. Delahanty, S. Garimella, M.A. Garrabrant, Design of compact microscale geometries for ammonia–water desorption, Sci. Technol. Built Environ. 21 (2015) 365–374. https://doi.org/10.1080/23744731.2015.1015906.

[116] M.A. Staedter, S. Garimella, Direct-coupled desorption for small capacity ammonia-water absorption systems, Int. J. Heat Mass Transf. 127 (2018) 196–205. https://doi.org/https://doi.org/10.1016/j.ijheatmasstransfer.2018.06.118.
[117] J.C. Delahanty, M. Hughes, S. Garimella, Desorber and rectifier geometries for ammonia-water absorption systems; Part I: Experimental approach and heat transfer, Int. J. Refrig. 123 (2021) 111–123. https://doi.org/https://doi.org/10.1016/j.ijrefrig.2020.10.020.
[118] S. Braccio, H. Trieu Phan, M. Wirtz, N. Tauveron, N. Le Pierrès, H.T. Phan, M. Wirtz, N. Tauveron, N. Le Pierrès, Simulation of an ammonia-water absorption cycle using exchanger effectivness., Appl. Therm. Eng. 213 (2022) 1. https://doi.org/https://doi.org/10.1016/j.applthermaleng.2022.118712.
[119] F. Boudéhenn, S. Bonnot, H. Demasles, F. Lefrançois, M. Perier-Muzet, D. Triché, Development and Performances Overview of Ammonia-water Absorption Chillers with Cooling Capacities from 5 to 100 kW, Energy Procedia. 91 (2016) 707–716. https://doi.org/https://doi.org/10.1016/j.egypro.2016.06.234.
[120] A. Landelle, N. Tauveron, R. Revellin, P. Haberschill, S. Colasson, V. Roussel, Performance investigation of reciprocating pump running with organic fluid for organic Rankine cycle, Appl. Therm. Eng. 113 (2017) 962–969. https://doi.org/10.1016/j.applthermaleng.2016.11.096.
[121] S. Karellas, T. Roumpedakis, N. Tzouganatos, K. Braimakis, Solar Cooling Technologies, CRC Press, 2018. https://doi.org/https://doi.org/10.1201/9781315163178.
[122] T.S. Ge, R.Z. Wang, Z.Y. Xu, Q.W. Pan, S. Du, X.M. Chen, T. Ma, X.N. Wu, X.L. Sun, J.F. Chen, Solar heating and cooling: Present and future development, Renew. Energy. 126 (2018) 1126–1140. https://doi.org/10.1016/j.renene.2017.06.081.
[123] Robur S.p.a., (n.d.). https://www.robur.com/en-us/ (accessed December 8, 2022).
[124] G. Besagni, R. Mereu, F. Inzoli, Ejector refrigeration: A comprehensive review, Renew. Sustain. Energy Rev. (2016). https://doi.org/10.1016/j.rser.2015.08.059.
[125] J.S. Lee, M.S. Kim, M.S. Kim, Experimental study on the improvement of CO2 air conditioning system performance using an ejector, Int. J. Refrig. 34 (2011) 1614–1625. https://doi.org/https://doi.org/10.1016/j.ijrefrig.2010.07.025.
[126] S. Elbel, N. Lawrence, Review of recent developments in advanced ejector technology, Int. J. Refrig. 62 (2016) 1–18. https://doi.org/10.1016/j.ijrefrig.2015.10.031.
[127] L.-T. Chen, A new ejector-absorber cycle to improve the COP of an absorption refrigeration system, Appl. Energy. 30 (1988) 37–51. https://doi.org/https://doi.org/10.1016/0306-2619(88)90053-0.
[128] S. Aphornratana, I. Eames, Experimental investigation of a combined ejector-absorption refrigerator., Int. J. Energy Res. 22 (1998) 195–207. https://doi.org/https://doi.org/10.1002/(SICI)1099-114X(19980310)22:3<195::AID-ER346>3.0.CO;2-A.
[129] G.K. Alexis, E.D. Rogdakis, Performance characteristics of two combined ejector–absorption cycles, Appl. Therm. Eng. 22 (2002) 97–106. https://doi.org/https://doi.org/10.1016/S1359-4311(01)00057-6.
[130] D. Hong, G. Chen, L. Tang, Y. He, A novel ejector-absorption combined refrigeration cycle, Int. J. Refrig. 34 (2011) 1596–1603. https://doi.org/https://doi.org/10.1016/j.ijrefrig.2010.07.007.
[131] A. Godefroy, N. Mazet, M. Périer-Muzet, Thermodynamic analysis and dynamic performances of hybrid cycles involving sorption processes, Analyse thermodynamique et performances dynamiques de cycles hybrides impliquant des procédés à sorption, Université de Perpignan, 2020. https://tel.archives-ouvertes.fr/tel-03051549.
[132] D.B. Boman, A.W. Raymond, S. Garimella, Adsorption Heat Pumps: Fundamentals and Applications, Springer International Publishing, 2021. https://doi.org/https://doi.org/10.1007/978-3-030-72180-0.
[133] L.W. Wang, R.Z. Wang, R.G. Oliveira, A review on adsorption working pairs for refrigeration, Renew. Sustain. Energy Rev. 13 (2009) 518–534. https://doi.org/https://doi.org/10.1016/j.rser.2007.12.002.
[134] W.R. R. Best, R. Best, W. Rivera, A review of thermal cooling systems, Appl. Therm. Eng. 75 (2015) 1162–1175. https://doi.org/10.1016/j.applthermaleng.2014.08.018.
[135] Y. Shi, M. Liu, F. Fang, Combined Cooling, Heating, and Power Systems, John Wiley & Sons, 2017. https://doi.org/10.1002/9781119283362.
[136] D.W. Wu, R.Z. Wang, Combined cooling, heating and power: A review, Prog. Energy Combust. Sci. 32 (2006) 459–495. https://doi.org/10.1016/j.pecs.2006.02.001.
[137] A. Godefroy, M. Perier-Muzet, P. Neveu, N. Mazet, Hybrid thermochemical cycles for low-grade heat storage and conversion into cold and/or power, Energy Convers. Manag. 225 (2020) 113347. https://doi.org/10.1016/j.enconman.2020.113347.
[138] I. Lee, J.W. Tester, F. You, Systems analysis, design, and optimization of geothermal energy systems for power production and polygeneration: State-of-the-art and future challenges, Renew. Sustain. Energy Rev. 109 (2019) 551–577. https://doi.org/https://doi.org/10.1016/j.rser.2019.04.058.
[139] Y. Liang, Z. Yu, W. Li, A Waste Heat-Driven Cooling System Based on Combined Organic Rankine and Vapour Compression Refrigeration Cycles, Appl. Sci. 9 (2019). https://doi.org/10.3390/app9204242.
[140] J. Bao, L. Zhang, C. Song, N. Zhang, X. Zhang, G. He, Comparative study of combined organic Rankine

cycle and vapor compression cycle for refrigeration: Single fluid or dual fluid?, Sustain. Energy Technol. Assessments. 37 (2020) 100595. https://doi.org/https://doi.org/10.1016/j.seta.2019.100595.
[141] L. Cao, J. Wang, H. Wang, P. Zhao, Y. Dai, Thermodynamic analysis of a Kalina-based combined cooling and power cycle driven by low-grade heat source, Appl. Therm. Eng. 111 (2017) 8–19. https://doi.org/https://doi.org/10.1016/j.applthermaleng.2016.09.088.
[142] E. Pastor-Martinez, C. Rubio-Maya, V.M. Ambriz-Díaz, J.M. Belman-Flores, J.J. Pacheco-Ibarra, Energetic and exergetic performance comparison of different polygeneration arrangements utilizing geothermal energy in cascade, Energy Convers. Manag. 168 (2018) 252–269. https://doi.org/https://doi.org/10.1016/j.enconman.2018.04.096.
[143] C. Schifflechner, L. Irrgang, F. Kaufmann, C. Apolinario, C. Wieland, S. Hartmut, Optimal integration of different absorption chillers in geothermal trigeneration systems with Organic Rankine Cycles, in: Proc. ECOS 2022, 2022: pp. 341–352. https://www.researchgate.net/profile/Christopher-Schifflechner-2/publication/361902513_Optimal_integration_of_different_absorption_chillers_in_geothermal_trigeneration_systems_with_Organic_Rankine_Cycles/links/62cbcc38cab7ba7426e4abc9/Optimal-integration-.
[144] C. Schifflechner, F. Kaufmann, L. Irrgang, L. Kuhnert, F. Dawo, C. Wieland, H. Spliethoff, Evaluation of Plant Configurations for Geothermal Trigeneration Systems with Organic Rankine Cycles, in: T.U. of Munich (Ed.), Proc. 6th Int. Semin. ORC Power Syst., Technical University of Munich, 2021: pp. 1–9. https://doi.org/10.14459/2021mp1632994.
[145] A. Kasaeian, A. Shamaeizadeh, B. Jamjoo, Combinations of Rankine with ejector refrigeration cycles: Recent progresses and outlook, Appl. Therm. Eng. 211 (2022) 118382. https://doi.org/https://doi.org/10.1016/j.applthermaleng.2022.118382.
[146] L. Wang, F. Ziegler, A.P. Roskilly, R. Wang, Y. Wang, A resorption cycle for the cogeneration of electricity and refrigeration, Appl. Energy. 106 (2013) 56–64. https://doi.org/https://doi.org/10.1016/j.apenergy.2013.01.041.
[147] H. Bao, Y. Wang, C. Charalambous, Z. Lu, L. Wang, R. Wang, A.P. Roskilly, Chemisorption cooling and electric power cogeneration system driven by low grade heat, Energy. 72 (2014) 590–598. https://doi.org/https://doi.org/10.1016/j.energy.2014.05.084.
[148] H. Bao, Z. Ma, A.P. Roskilly, An optimised chemisorption cycle for power generation using low grade heat, Appl. Energy. 186 (2017) 251–261. https://doi.org/https://doi.org/10.1016/j.apenergy.2016.06.080.
[149] L. Jiang, A.P. Roskilly, R.Z. Wang, L.W. Wang, Analysis on innovative resorption cycle for power and refrigeration cogeneration, Appl. Energy. 218 (2018) 10–21. https://doi.org/https://doi.org/10.1016/j.apenergy.2018.02.174.
[150] A. Godefroy, M. Perier-Muzet, N. Mazet, Thermodynamic analyses on hybrid sorption cycles for low-grade heat storage and cogeneration of power and refrigeration, Appl. Energy. 255 (2019) 113751. https://doi.org/https://doi.org/10.1016/j.apenergy.2019.113751.
[151] J. Wang, Y. Dai, Z. Sun, A theoretical study on a novel combined power and ejector refrigeration cycle, Int. J. Refrig. 32 (2009) 1186–1194. https://doi.org/https://doi.org/10.1016/j.ijrefrig.2009.01.021.
[152] X. Chen, Y. Su, S. Omer, S. Riffat, Theoretical investigations on combined power and ejector cooling system powered by low-grade energy source, Int. J. Low-Carbon Technol. 11 (2016) 466–475. https://doi.org/10.1093/ijlct/ctv015.
[153] Y. Zhao, J. Wang, L. Cao, Y. Wang, Comprehensive analysis and parametric optimization of a CCP (combined cooling and power) system driven by geothermal source, Energy. 97 (2016) 470–487. https://doi.org/https://doi.org/10.1016/j.energy.2016.01.003.
[154] H. Ghaebi, T. Parikhani, H. Rostamzadeh, B. Farhang, Thermodynamic and thermoeconomic analysis and optimization of a novel combined cooling and power (CCP) cycle by integrating of ejector refrigeration and Kalina cycles, Energy. 139 (2017) 262–276. https://doi.org/https://doi.org/10.1016/j.energy.2017.07.154.
[155] H. Ghaebi, T. Parikhani, H. Rostamzadeh, B. Farhang, Proposal and assessment of a novel geothermal combined cooling and power cycle based on Kalina and ejector refrigeration cycles, Appl. Therm. Eng. 130 (2018) 767–781. https://doi.org/https://doi.org/10.1016/j.applthermaleng.2017.11.067.
[156] J. Muye, D.S. Ayou, R. Saravanan, A. Coronas, Performance study of a solar absorption power-cooling system, Appl. Therm. Eng. 97 (2016) 59–67. https://doi.org/10.1016/j.applthermaleng.2015.09.034.
[157] L.C. Mendoza, D.S. Ayou, J. Navarro-Esbrí, J.C. Bruno, A. Coronas, Small capacity absorption systems for cooling and power with a scroll expander and ammonia based working fluids, Appl. Therm. Eng. 72 (2014) 258–265. https://doi.org/10.1016/j.applthermaleng.2014.06.019.
[158] Y. Zhang, L. Shi, H. Tian, L. Li, X. Wang, G. Huang, G. Shu, Experimental investigation on CO2-based combined cooling and power cycle, Energy Convers. Manag. 256 (2022) 115342. https://doi.org/https://doi.org/10.1016/j.enconman.2022.115342.
[159] Y. Goswami, Solar Thermal Power Technology: Present Status and Ideas for the Future, Energy Sources. 20 (1998) 137–145. https://doi.org/10.1080/00908319808970052.

[160] G. Tamm, D.Y. Goswami, Novel combined power and cooling thermodynamic cycle for low temperature heat sources, part II: Experimental investigation, J. Sol. Energy Eng. Trans. ASME. 125 (2003) 223–229. https://doi.org/10.1115/1.1564080.
[161] A.A. Hasan, D.Y. Goswami, S. Vijayaraghavan, First and second law analysis of a new power and refrigeration thermodynamic cycle using a solar heat source, Sol. Energy. 73 (2002) 385–393. https://doi.org/10.1016/S0038-092X(02)00113-5.
[162] V. Zare, S.M.S. Mahmoudi, M. Yari, M. Amidpour, Thermoeconomic analysis and optimization of an ammonia-water power/cooling cogeneration cycle, Energy. 47 (2012) 271–283. https://doi.org/10.1016/j.energy.2012.09.002.
[163] D. Zheng, B. Chen, Y. Qi, H. Jin, Thermodynamic analysis of a novel absorption power/cooling combined-cycle, Appl. Energy. 83 (2006) 311–323. https://doi.org/10.1016/j.apenergy.2005.02.006.
[164] J. López-Villada, D.S. Ayou, J.C. Bruno, A. Coronas, Modelling, simulation and analysis of solar absorption power-cooling systems, Int. J. Refrig. 39 (2014) 125–136. https://doi.org/10.1016/j.ijrefrig.2013.11.004.
[165] S.M.S. Mahmoudi, M. Akbari Kordlar, A new flexible geothermal based cogeneration system producing power and refrigeration, Renew. Energy. 123 (2018) 499–512. https://doi.org/10.1016/j.renene.2018.02.060.
[166] Z. Seyfouri, M. Ameri, M.A. Mehrabian, Exergo-economic analysis of a low-temperature geothermal-fed combined cooling and power system, Appl. Therm. Eng. 145 (2018) 528–540. https://doi.org/10.1016/j.applthermaleng.2018.09.072.
[167] V. Zare, S.M.S. Mahmoudi, M. Yari, An exergoeconomic investigation of waste heat recovery from the Gas Turbine-Modular Helium Reactor (GT-MHR) employing an ammonia-water power/cooling cycle, Energy. 61 (2013) 397–409. https://doi.org/10.1016/j.energy.2013.09.038.
[168] M. Puig-Arnavat, J.C. Bruno, A. Coronas, Modeling of trigeneration configurations based on biomass gasification and comparison of performance, Appl. Energy. 114 (2014) 845–856. https://doi.org/10.1016/j.apenergy.2013.09.013.
[169] D.S. Ayou, V. Eveloy, Energy, exergy and exergoeconomic analysis of an ultra low-grade heat-driven ammonia-water combined absorption power-cooling cycle for district space cooling, sub-zero refrigeration, power and LNG regasification, Energy Convers. Manag. 213 (2020) 112790. https://doi.org/10.1016/j.enconman.2020.112790.
[170] S. Ogriseck, Integration of Kalina cycle in a combined heat and power plant, a case study, Appl. Therm. Eng. 29 (2009) 2843–2848. https://doi.org/https://doi.org/10.1016/j.applthermaleng.2009.02.006.
[171] S. Vijayaraghavan, Y. Goswami, On Evaluating Efficiency of a Combined Power and Cooling, J. Energy Resour. Technol. 125 (2003) 221–227. https://doi.org/10.1115/1.1595110.
[172] S. Braccio, A. Arteconi, H.T. Phan, N. Tauveron, N. Le Pierrès, Energy and exergy analysis of a pilot plant for the combined production of cooling and electricity from a low temperature heat source through an absorption process., in: Proc. ECOS 2022, 2022: pp. 529–540.
[173] N. Lior, N. Zhang, Energy, exergy, and Second Law performance criteria, Energy. 32 (2007) 281–296. https://doi.org/10.1016/j.energy.2006.01.019.
[174] W. Han, Q. Chen, L. Sun, S. Ma, T. Zhao, D. Zheng, H. Jin, Experimental studies on a combined refrigeration/power generation system activated by low-grade heat, Energy. 74 (2014) 59–66. https://doi.org/https://doi.org/10.1016/j.energy.2014.02.097.
[175] D. Triché, S. Bonnot, M. Perier-Muzet, F. Boudéhenn, H. Demasles, N. Caney, Experimental and numerical study of a falling film absorber in an ammonia-water absorption chiller, Int. J. Heat Mass Transf. 111 (2017) 374–385. https://doi.org/10.1016/j.ijheatmasstransfer.2017.04.008.
[176] N. Tauveron, S. Colasson, J.A. Gruss, Available systems for the conversion of waste heat to electricity, in: ASME Int. Mech. Eng. Congr. Expo. Proc., 2014. https://doi.org/10.1115/IMECE2014-37984.
[177] L.C. Mendoza, J. Navarro-Esbrí, J.C. Bruno, V. Lemort, A. Coronas, Characterization and modeling of a scroll expander with air and ammonia as working fluid, Appl. Therm. Eng. 70 (2014) 630–640. https://doi.org/10.1016/j.applthermaleng.2014.05.069.
[178] H.G. Lee, J.H. Shin, C.H. Choi, E. Jeong, S. Kwon, Partial admission effect on the performance and vibration of a supersonic impulse turbine, Acta Astronaut. 145 (2018) 105–115. https://doi.org/10.1016/j.actaastro.2018.01.025.
[179] S.A. Ibrahim, O.M., Klein, Thermodynamic properties of ammonia-water mixtures., in: ASHRAE Trans. Symp. 21, 2, 1495, n.d.
[180] S. Braccio, H.T. Phan, N. Tauveron, N. Le Pierrès, Système de production de froid et d'électricité à partir d'une source thermique à basse température, permettant un réglage du rapport entre production de froid et production électrique. French Patent., FR2107442, n.d.
[181] A. Altamirano, N. Le Pierrès, B. Stutz, A. Coronas, Performance characterization methods for absorption chillers applied to an NH3-LiNO3 single-stage prototype, Appl. Therm. Eng. 185 (2021).

https://doi.org/10.1016/j.applthermaleng.2020.116435.
[182] J. Labus, J.C. Bruno, A. Coronas, Performance analysis of small capacity absorption chillers by using different modeling methods, Appl. Therm. Eng. 58 (2013) 305–313. https://doi.org/10.1016/j.applthermaleng.2013.04.032.
[183] J.M. Gordon, K.C. Ng, A general thermodynamic model for absorption chillers: Theory and experiment, Heat Recover. Syst. CHP. 15 (1995) 73–83. https://doi.org/10.1016/0890-4332(95)90038-1.
[184] C. Ziegler, F., Hellmann, H.M., Schweigler, An approximative method for modeling the operating characteristics of advanced absorption chillers., in: Int. Congr. Refrig., 1999. https://iifiir.org/en/fridoc/an-approximative-method-for-modeling-the-operating-characteristics-of-17861.
[185] E. Thorin, Comparison of correlations for predicting thermodynamic properties of ammonia-water mixtures, Int. J. Thermophys. 21 (2000) 853–870. https://doi.org/10.1023/A:1006658107014.
[186] S.S. Stecco, U. Desideri, A thermodynamic analysis of the Kalina cycles: Comparisons, problems and perspectives, Proc. ASME Turbo Expo. 4 (1989). https://doi.org/10.1115/89GT-149.
[187] R. Tillner-Roth, D.G. Friend, A Helmholtz free energy formulation of the thermodynamic properties of the mixture {water + ammonia}, J. Phys. Chem. Ref. Data. 27 (1998) 63–77. https://doi.org/10.1063/1.556015.
[188] F. Incropera, Fundamentals of Heat and Mass Transfer, John Wiley & Sons, Hoboken, NJ, USA, 2006.
[189] Y. Cengel, Introduction to Thermodynamics and Heat Transfer, Second, McGraw-Hill, 2004.
[190] M. Perier-Muzet, B. Stutz, Numerical study of the effectiveness of a vertical falling plate film absorber for an absorption chiller, Int. J. Refrig. 127 (2021) 221–229. https://doi.org/10.1016/j.ijrefrig.2021.02.013.
[191] Saravanamuttoo, Cohen, Rogers, Nix, Straznicky, Gas Turbine Theory, Seventh, Pearson, 2017.
[192] EES, Engineering Equation Solver, F-Chart, (n.d.). https://fchartsoftware.com/ees/.
[193] S. Braccio, N. Guillou, N. Le Pierrès, N. Tauveron, H. Trieu Phan, Mass-flowrate-maximization thermodynamic model and simulation of supersonic real-gas ejectors used in refrigeration systems, Therm. Sci. Eng. Prog. (2022) 101615. https://doi.org/https://doi.org/10.1016/j.tsep.2022.101615.
[194] Z. Ma, H. Bao, A.P. Roskilly, Thermodynamic modelling and parameter determination of ejector for ejection refrigeration systems, Int. J. Refrig. 75 (2017) 117–128. https://doi.org/https://doi.org/10.1016/j.ijrefrig.2016.12.005.
[195] M.H. Vavra, Aero-Thermodynamics and Flow in Turbomachines, John Wiley, 1960.
[196] Roelke, Miscellaneous Losses, in: AJ Glas. (Ed.), Turbine Des. Appl. NASA Cent. Aerosp. Information, Linthicum Height. Maryland, USA, 1994: pp. 225–248.
[197] R.H. Aungier, Turbine Aerodynamics: Axial-Flow and Radial-Flow Turbine Design and Analysis, ASME Press, 2005. https://doi.org/https://doi.org/10.1115/1.802418.
[198] J.P. Czapla, Investigation of Supersonic Impulse Turbines for Application to Geothermal Binary Power Stations. PhD Thesis., University of Queensland, 2015.
[199] S.Y. Cho, C.H. Cho, C. Kim, Performance prediction on a partially admitted small axial-type turbine, JSME Int. Journal, Ser. B Fluids Therm. Eng. 49 (2007) 1290–1297. https://doi.org/10.1299/jsmeb.49.1290.
[200] M. Li, J. Wang, L. Gao, X. Niu, Y. Dai, Performance evaluation of a turbine used in a regenerative Organic Rankine Cycle, in: Proc. ASME Turbo Expo, 2012: pp. 425–432. https://doi.org/10.1115/GT2012-68441.
[201] A. Capetti, Motori termici, UTET, 1964.
[202] D. Wilcox, Turbulence Modeling for CFD, DCW Industries, 2006.
[203] H.G. Berhane, G.G. Gonzalo, J. Laureano, B. Dieter, B.H. Gebreslassie, G. Guillén-Gosálbez, L. Jiménez, D. Boer, Design of environmentally conscious absorption cooling systems via multi-objective optimization and life cycle assessment, Appl. Energy. 86 (2009) 1712–1722. https://doi.org/https://doi.org/10.1016/j.apenergy.2008.11.019.
[204] R.D. Misra, P.K. Sahoo, A. Gupta, Thermoeconomic evaluation and optimization of an aqua-ammonia vapour-absorption refrigeration system, Int. J. Refrig. 29 (2006) 47–59. https://doi.org/10.1016/j.ijrefrig.2005.05.015.
[205] A. Bejan, G. Tsatsaronis, M.J. Moran, Thermal design and optimization, Wiley, 1995.
[206] G. Tsatsaronis, J. Pisa, Exergoeconomic evaluation and optimization of energy systems — application to the CGAM problem, Energy. 19 (1994) 287–321. https://doi.org/https://doi.org/10.1016/0360-5442(94)90113-9.
[207] M.A. Lozano, A. Valero, Theory of the exergetic cost, Energy. 18 (1993) 939–960. https://doi.org/https://doi.org/10.1016/0360-5442(93)90006-Y.
[208] A. Valero, M.A. Lozano, L. Serra, C. Torres, Application of the exergetic cost theory to the CGAM problem, Energy. 19 (1994) 365–381. https://doi.org/https://doi.org/10.1016/0360-5442(94)90116-3.
[209] C.A. Frangopoulos, Application of the thermoeconomic functional approach to the CGAM problem, Energy. 19 (1994) 323–342. https://doi.org/https://doi.org/10.1016/0360-5442(94)90114-7.
[210] J. Szargut, Exergy method: technical and ecological applications, Int. Ser. Dev. Heat Transf. 18 (2005)

164.
[211] A. Vidal, R. Best, R. Rivero, J. Cervantes, Analysis of a combined power and refrigeration cycle by the exergy method, Energy. 31 (2006) 3401–3414. https://doi.org/10.1016/j.energy.2006.03.001.
[212] V. Zare, S.M.S. Mahmoudi, M. Yari, On the exergoeconomic assessment of employing Kalina cycle for GT-MHR waste heat utilization, Energy Convers. Manag. 90 (2015) 364–374. https://doi.org/https://doi.org/10.1016/j.enconman.2014.11.039.
[213] D.A. Wood, M. Kulitsa, A review: Optimizing performance of Floating Storage and Regasification Units (FSRU) by applying advanced LNG tank pressure management strategies, Int. J. Energy Res. 42 (2018) 1391–1418. https://doi.org/https://doi.org/10.1002/er.3883.
[214] B.B. Kanbur, L. Xiang, S. Dubey, F.H. Choo, F. Duan, Thermoeconomic and environmental assessments of a combined cycle for the small scale LNG cold utilization, Appl. Energy. 204 (2017) 1148–1162. https://doi.org/10.1016/j.apenergy.2017.01.061.
[215] The Chemical Engineering Plant Cost Index, Chem. Eng. (2022). https://www.chemengonline.com/pci-home/.
[216] R. Turton, R.C. Bailie, W.B. Whiting, Analysis, Synthesis, and Design of Chemical Processes, Pearson Prentice Hall, 2012. https://books.google.fr/books?id=f6sbYJuFSycC.
[217] M. Taal, I. Bulatov, J. Klemeš, P. Stehlík, Cost estimation and energy price forecasts for economic evaluation of retrofit projects, Appl. Therm. Eng. 23 (2003) 1819–1835. https://doi.org/10.1016/S1359-4311(03)00136-4.
[218] S. Lemmens, Cost engineering techniques & their applicability for cost estimation of organic rankine cycle systems, Energies. 9 (2016). https://doi.org/10.3390/en9070485.
[219] G. Lillo, R. Mastrullo, A.W. Mauro, R. Trinchieri, L. Viscito, Thermo-economic analysis of a hybrid ejector refrigerating system based on a low grade heat source, Energies. 13 (2020). https://doi.org/10.3390/en13030562.
[220] P. Dorj, Thermoeconomic Analysis of a New Geothermal Utilization CHP Plant in Tsetserleg, Mongolia. MSc thesis, University of Iceland, 2005.
[221] A. Modi, Numerical evaluation of the Kalina cycle for concentrating solar power plants. PhD Thesis., DTU Mechanical Engineering, 2015. https://orbit.dtu.dk/en/publications/numerical-evaluation-of-the-kalina-cycle-for-concentrating-solar-.
[222] C.E.C. Rodríguez, J.C.E. Palacio, C.R. Sotomonte, M. Leme, O.J. Venturini, E.E.S. Lora, V.M. Cobas, D.M. dos Santos, F.R.L. Dotto, V. Giallucca, Exergetic and economic analysis of Kalina cycle for low temperature geothermal sources in Brazil, in: Proc. ECOS 2012, 2012: pp. 345–358. https://www.researchgate.net/publication/268268800_Exergetic_and_economic_analysis_of_Kalina_cycle_for_low_temperature_geothermal_sources_in_Brazil.
[223] C. Wu, S. Wang, X. Feng, J. Li, Energy, exergy and exergoeconomic analyses of a combined supercritical CO2 recompression Brayton/absorption refrigeration cycle, Energy Convers. Manag. 148 (2017) 360–377. https://doi.org/https://doi.org/10.1016/j.enconman.2017.05.042.
[224] L.S. Vieira, J.L. Donatelli, M.E. Cruz, Exergoeconomic improvement of a complex cogeneration system integrated with a professional process simulator, Energy Convers. Manag. 50 (2009) 1955–1967. https://doi.org/10.1016/j.enconman.2009.04.020.
[225] J.K. Jensen, W.B. Markussen, L. Reinholdt, B. Elmegaard, Exergoeconomic optimization of an ammonia–water hybrid absorption–compression heat pump for heat supply in a spray-drying facility, Int. J. Energy Environ. Eng. 6 (2015) 195–211. https://doi.org/10.1007/s40095-015-0166-0.
[226] N. Shokati, F. Ranjbar, M. Yari, A comparative analysis of rankine and absorption power cycles from exergoeconomic viewpoint, Energy Convers. Manag. 88 (2014) 657–668. https://doi.org/10.1016/j.enconman.2014.09.015.
[227] H. Rostamzadeh, M. Ebadollahi, H. Ghaebi, A. Shokri, Comparative study of two novel micro-CCHP systems based on organic Rankine cycle and Kalina cycle, Energy Convers. Manag. 183 (2019) 210–229. https://doi.org/10.1016/j.enconman.2019.01.003.
[228] S. Klein, G. Nellis, Mastering EES, F-Chart, 2014. https://fchart.com/ees/mastering-ees.php.
[229] J. Chen, H. Havtun, B. Palm, Investigation of ejectors in refrigeration system: Optimum performance evaluation and ejector area ratios perspectives, Appl. Therm. Eng. 64 (2014) 182–191. https://doi.org/10.1016/j.applthermaleng.2013.12.034.
[230] https://www.europeanbiogas.eu/eba-statistical-report-2021/, EBA Statistical Report, 2021. https://www.europeanbiogas.eu/eba-statistical-report-2021/.
[231] GSE, Rapporto Statistico 2020 Energia da fonti rinnovabili in Italia., 2020. https://www.gse.it/documenti_site/Documenti GSE/Rapporti statistici/Rapporto Statistico GSE - FER 2020.pdf.
[232] Arpa metheorological data, (n.d.). http://www.webgis.arpa.puglia.it/meteo/index.php.
[233] J. Ramsebner, P. Linares, R. Haas, Estimating storage needs for renewables in Europe: The correlation

between renewable energy sources and heating and cooling demand, Smart Energy. 3 (2021) 100038. https://doi.org/https://doi.org/10.1016/j.segy.2021.100038.
[234] Rhoss S.p.a., (n.d.). https://www.rhoss.it/.
[235] G. Kosmadakis, C. Arpagaus, P. Neofytou, S. Bertsch, Techno-economic analysis of high-temperature heat pumps with low-global warming potential refrigerants for upgrading waste heat up to 150 °C, Energy Convers. Manag. 226 (2020) 113488. https://doi.org/https://doi.org/10.1016/j.enconman.2020.113488.
[236] K. Braimakis, S. Karellas, Integrated thermoeconomic optimization of standard and regenerative ORC for different heat source types and capacities, Energy. 121 (2017) 570–598. https://doi.org/https://doi.org/10.1016/j.energy.2017.01.042.
[237] M. Papapetrou, G. Kosmadakis, F. Giacalone, B. Ortega-Delgado, A. Cipollina, A. Tamburini, G. Micale, Evaluation of the Economic and Environmental Performance of Low-Temperature Heat to Power Conversion using a Reverse Electrodialysis – Multi-Effect Distillation System, Energies. 12 (2019). https://doi.org/10.3390/en12173206.
[238] M.H. Ahmadi, M. Mehrpooya, F. Pourfayaz, Exergoeconomic analysis and multi objective optimization of performance of a Carbon dioxide power cycle driven by geothermal energy with liquefied natural gas as its heat sink, Energy Convers. Manag. 119 (2016) 422–434. https://doi.org/https://doi.org/10.1016/j.enconman.2016.04.062.
[239] Z. Aidoun, K. Ameur, M. Falsafioon, M. Badache, Current Advances in Ejector Modeling, Experimentation and Applications for Refrigeration and Heat Pumps. Part 2: Two-Phase Ejectors, Inventions. 4 (2019) 15. https://doi.org/10.3390/inventions4010016.
[240] E. Rusly, L. Aye, W.W.S. Charters, A. Ooi, CFD analysis of ejector in a combined ejector cooling system, Int. J. Refrig. 28 (2005) 1092–1101. https://doi.org/https://doi.org/10.1016/j.ijrefrig.2005.02.005.
[241] K. Pianthong, W. Seehanam, M. Behnia, T. Sriveerakul, S. Aphornratana, Investigation and improvement of ejector refrigeration system using computational fluid dynamics technique, Energy Convers. Manag. 48 (2007) 2556–2564. https://doi.org/https://doi.org/10.1016/j.enconman.2007.03.021.
[242] D. Li, E.A. Groll, Transcritical CO2 refrigeration cycle with ejector-expansion device, Int. J. Refrig. 28 (2005) 766–773. https://doi.org/10.1016/j.ijrefrig.2004.10.008.
[243] Ø. Wilhelmsen, A. Aasen, K. Banasiak, H. Herlyng, A. Hafner, One-dimensional mathematical modeling of two-phase ejectors: Extension to mixtures and mapping of the local exergy destruction, Appl. Therm. Eng. 217 (2022) 119228. https://doi.org/10.1016/j.applthermaleng.2022.119228.
[244] H. El-Dessouky, H. Ettouney, I. Alatiqi, G. Al-Nuwaibit, Evaluation of steam jet ejectors, Chem. Eng. Process. Process Intensif. 41 (2002) 551–561. https://doi.org/https://doi.org/10.1016/S0255-2701(01)00176-3.
[245] S. Balamurugan, M.D. Lad, V.G. Gaikar, A.W. Patwardhan, Hydrodynamics and mass transfer characteristics of gas–liquid ejectors, Chem. Eng. J. 131 (2007) 83–103. https://doi.org/https://doi.org/10.1016/j.cej.2006.12.026.
[246] S. He, Y. Li, R.Z. Wang, Progress of mathematical modeling on ejectors, Renew. Sustain. Energy Rev. 13 (2009) 1760–1780. https://doi.org/https://doi.org/10.1016/j.rser.2008.09.032.
[247] J.H. Keenan, E.P. Neumann, A Simple Air Ejector, J. Appl. Mech. 9 (1942) A75–A81. https://doi.org/10.1115/1.4009187.
[248] J.H. Keenan, E.P. Neumann, F. Lustwerk, An Investigation of Ejector Design by Analysis and Experiment, J. Appl. Mech. 17 (1950) 299–309. https://doi.org/10.1115/1.4010131.
[249] F. Khoury, M. Heyman, W. Resnick, Performance Characteristics of Self-Entrainment Ejectors, Ind. Eng. Chem. Process Des. Dev. 6 (1967) 331–340. https://doi.org/10.1021/i260023a013.
[250] S. Aphornratana, S. Chungpaibulpatana, P. Srikhirin, Experimental investigation of an ejector refrigerator: Effect of mixing chamber geometry on system performance, Int. J. Energy Res. (2001). https://doi.org/10.1002/er.689.
[251] J. Fabri, R. Siestrunck, Supersonic Air Ejectors, in: Adv. Appl. Mech., Elsevier, 1958: pp. 1–34. https://doi.org/https://doi.org/10.1016/S0065-2156(08)70016-4.
[252] I.W. Eames, S. Aphornratana, H. Haider, A theoretical and experimental study of a small-scale steam jet refrigerator, Int. J. Refrig. 18 (1995) 378–386. https://doi.org/https://doi.org/10.1016/0140-7007(95)98160-M.
[253] B.J. Huang, J.M. Chang, C.P. Wang, V.A. Petrenko, A 1-D analysis of ejector performance, Int. J. Refrig. 22 (1999) 354–364. https://doi.org/https://doi.org/10.1016/S0140-7007(99)00004-3.
[254] J.T. Munday, D.F. Bagster, A New Ejector Theory Applied to Steam Jet Refrigeration, Ind. Eng. Chem. Process Des. Dev. 16 (1977) 442–449. https://doi.org/10.1021/i260064a003.
[255] I.W. Eames, S. Wu, M. Worall, S. Aphornratana, An experimental investigation of steam ejectors for applications in jet-pump refrigerators powered by low-grade heat, Proc. Inst. Mech. Eng. Part A J. Power Energy. 213 (1999) 351–361. https://doi.org/10.1243/0957650991537734.
[256] Y.-M. Chen, C.-Y. Sun, Experimental study of the performance characteristics of a steam-ejector

refrigeration system, Exp. Therm. Fluid Sci. 15 (1997) 384–394. https://doi.org/https://doi.org/10.1016/S0894-1777(97)00006-X.
[257] W. Chen, C. Shi, S. Zhang, H. Chen, D. Chong, J. Yan, Theoretical analysis of ejector refrigeration system performance under overall modes, Appl. Energy. 185 (2017) 2074–2084. https://doi.org/https://doi.org/10.1016/j.apenergy.2016.01.103.
[258] A. Metsue, R. Debroeyer, S. Poncet, Y. Bartosiewicz, An improved thermodynamic model for supersonic real-gas ejectors using the compound-choking theory, Energy. 238 (2022). https://doi.org/10.1016/j.energy.2021.121856.
[259] A. Bernstein, W.H. Heiser, C. Hevenor, Compound-Compressible Nozzle Flow, J. Appl. Mech. 34 (1967) 548–554. https://doi.org/10.1115/1.3607742.
[260] O. Lamberts, P. Chatelain, N. Bourgeois, Y. Bartosiewicz, The compound-choking theory as an explanation of the entrainment limitation in supersonic ejectors, Energy. 158 (2018) 524–536. https://doi.org/https://doi.org/10.1016/j.energy.2018.06.036.
[261] H. Hoge, R. Segars, Choked flow - A generalization of the concept and some experimental data., AIAA J. 3 (1965) 2177–2183. https://doi.org/10.2514/3.3343.
[262] N. Ruangtrakoon, T. Thongtip, S. Aphornratana, T. Sriveerakul, CFD simulation on the effect of primary nozzle geometries for a steam ejector in refrigeration cycle, Int. J. Therm. Sci. 63 (2013) 133–145. https://doi.org/10.1016/j.ijthermalsci.2012.07.009.
[263] F. Mazzelli, A. Milazzo, Performance analysis of a supersonic ejector cycle working with R245fa, Int. J. Refrig. 49 (2015) 79–92. https://doi.org/10.1016/j.ijrefrig.2014.09.020.
[264] S. Croquer, Y. Fang, A. Metsue, Y. Bartosiewicz, S. Poncet, Compound-choking theory for supersonic ejectors working with real gas, Energy. 227 (2021) 120396. https://doi.org/10.1016/j.energy.2021.120396.
[265] Y. Zhu, Y. Li, Novel ejector model for performance evaluation on both dry and wet vapors ejectors, Int. J. Refrig. 32 (2009) 21–31. https://doi.org/https://doi.org/10.1016/j.ijrefrig.2008.08.003.
[266] S. Braccio, A. Di Nardo, G. Calchetti, H.T. Phan, N. Le Pierrès, N. Tauveron, Performance evaluation of a micro partial admission impulse axial turbine in a combined ammonia-water cooling and electricity absorption cycle. Sumbitted to Energy Journal May 2022, 2022.
[267] H. Saravanamuttoo, G. Rogers, H. Cohen, P. Straznicky, Gas Turbine Theory, 6th ed., Pearson Prentice Hall, Harlow, England; New York, 2009.
[268] M. Khennich, N. Galanis, M. Sorin, Effects of design conditions and irreversibilities on the dimensions of ejectors in refrigeration systems, Appl. Energy. 179 (2016) 1020–1031. https://doi.org/https://doi.org/10.1016/j.apenergy.2016.07.053.
[269] F. Liu, E.A. Groll, Study of ejector efficiencies in refrigeration cycles, Appl. Therm. Eng. 52 (2013) 360–370. https://doi.org/https://doi.org/10.1016/j.applthermaleng.2012.12.001.
[270] J. Liu, L. Wang, L. Jia, X. Wang, Thermodynamic model for all modes performance analysis of supersonic ejector considering non-uniform distribution of flow field, Int. J. Refrig. 96 (2018) 17–24. https://doi.org/https://doi.org/10.1016/j.ijrefrig.2018.08.023.
[271] D. Butrymowicz, K. Śmierciew, J. Karwacki, J. Gagan, Experimental investigations of low-temperature driven ejection refrigeration cycle operating with isobutane, Int. J. Refrig. 39 (2014) 196–209. https://doi.org/10.1016/j.ijrefrig.2013.10.008.
[272] A. Hakkaki-Fard, Z. Aidoun, M. Ouzzane, A computational methodology for ejector design and performance maximisation, Energy Convers. Manag. 105 (2015) 1291–1302. https://doi.org/https://doi.org/10.1016/j.enconman.2015.08.070.
[273] K. Cizungu, A. Mani, M. Groll, Performance comparison of vapour jet refrigeration system with environment friendly working fluids, Appl. Therm. Eng. 21 (2001) 585–598. https://doi.org/https://doi.org/10.1016/S1359-4311(00)00070-3.
[274] A. Selvaraju, A. Mani, Analysis of an ejector with environment friendly refrigerants, Appl. Therm. Eng. 24 (2004) 827–838. https://doi.org/https://doi.org/10.1016/j.applthermaleng.2003.08.016.
[275] J. Chen, H. Havtun, B. Palm, Screening of working fluids for the ejector refrigeration system, Int. J. Refrig. 47 (2014) 1–14. https://doi.org/https://doi.org/10.1016/j.ijrefrig.2014.07.016.
[276] R.E. Henry, H.K. Fauske, The Two-Phase Critical Flow of One-Component Mixtures in Nozzles, Orifices, and Short Tubes, J. Heat Transfer. 93 (1971) 179–187. https://doi.org/10.1115/1.3449782.
[277] A. Leyzerovich, Wet-steam Turbines for Nuclear Power Plants, PennWell Books Ed., 2005.
[278] G. Lhermet, N. Tauveron, N. Caney, Q. Blondel, F. Morin, A Recent Advance on Partial Evaporating Organic Rankine Cycle: Experimental Results on an Axial Turbine, Energies. 15 (2022) 7559. https://doi.org/10.3390/en15207559.
[279] C. Herer, Éléments de thermohydraulique et applications aux réacteurs nucléaires, (2017). https://doi.org/10.13140/RG.2.2.12982.50243.
[280] J.C. Leung, Easily size relief devices and piping for two-phase flow, Chem. Eng. Prog. 92 (1996). https://www.osti.gov/biblio/419821.